

# **UNIVERSIDAD DE CANTABRIA**

PROGRAMA INTERUNIVERSITARIO DE DOCTORADO EN  
TECNOLOGÍAS DE LA INFORMACIÓN Y COMUNICACIÓN EN REDES  
MÓVILES POR LAS UNIVERSIDADES DE A CORUÑA, OVIEDO,  
CANTABRIA, PAIS VASCO Y ZARAGOZA



## **TESIS DOCTORAL**

**CONTRIBUCIONES AL DESARROLLO DE  
SENSORES DISTRIBUIDOS BASADOS EN LA  
DISPERSIÓN ESTIMULADA DE BRILLOUIN**

## **PHD THESIS**

**CONTRIBUTIONS TO THE DEVELOPMENT OF  
DISTRIBUTED SENSORS BASED ON  
STIMULATED BRILLOUIN SCATTERING**

AUTOR: RUBÉN RUIZ LOMBERA

DIRECTORES: JOSÉ MIGUEL LÓPEZ HIGUERA  
JESÚS MIRAPEIX SERRANO

Escuela de Doctorado de la Universidad de Cantabria

Santander 2019



*When you make the finding yourself  
- even if you're the last person on Earth to see the light -  
you'll never forget it.*

*Carl Sagan*



---

# Acknowledgments

---

This work has been supported by the funding of the following entities and actions:

- Universidad de Cantabria through the research grant *Programa de Personal Investigador en Formación Predoctoral* and research stays grants in Pamplona, Spain and in Aversa, Italy.
- Agencia Estatal de Investigación through research project *Sensores fotónicos para seguridad y protección* (TEC2016-76021-C2-2-R).
- Ministerio de Economía y Competitividad through research project *Sensores de fibra óptica para seguridad y protección* (TEC2013-47264-C2-1-R).
- Gobierno de Cantabria through research project *Detección de fugas en autovías del agua mediante sensores ópticos* (FASO).
- Fundación TTI through a research grant *Patrocinio de actividades formativas en investigación científica y técnica*.
- Cost action td1001: *Novel and reliable optical fibre sensor systems for future security and safety applications* (OFSESA) through a research grant for a short term scientific mission to Aversa, Italy and through two grants for summer schools.

I would also like to thank the Università della Campania “Luigi Vanvitelli” and Universidad Pública de Navarra, for the help received during the research stays I carried out there, which have contributed greatly to the development of this thesis.



---

# Resumen

---

La sociedad actual exige cada día más servicios en una amplia variedad de sectores: medios de transporte, energía, salud o telecomunicaciones, entre otros. Para poder conseguir que todos estos servicios funcionen a la perfección se requieren de muchas infraestructuras tales como carreteras, puentes, ferrocarriles, túneles, presas o tuberías, que ahora mismo son indispensables para cubrir las necesidades de la sociedad actual. Sin embargo, todo este tipo de infraestructuras lleva asociado un riesgo debido al deterioro que van sufriendo con el tiempo, dando lugar a la aparición de grietas, procesos de corrosión u otros problemas que pueden desembocar en su colapso. En este sentido, cada vez se es más consciente de los potenciales riesgos que implica para la población la aparición de defectos en dichas estructuras, apareciendo la necesidad de realizar la monitorización de su integridad estructural para tratar de detectar prematuramente estas situaciones antes de que puedan repercutir en la sociedad. De esta manera, hay un número creciente de estructuras que están siendo monitorizadas utilizando todo tipo de enfoques tecnológicos.

En este sentido, el desarrollo de los sensores de fibra óptica ha permitido la monitorización de la integridad de las estructuras gracias a ciertas propiedades que presentan estos sensores pudiendo ser empleados en multitud de aplicaciones. Algunas de sus ventajas con respecto a otros sensores más convencionales son su capacidad de medir a larga distancia, su inmunidad electromagnética, la posibilidad de ser embebidos en las estructuras o en diferentes materiales y el hecho de que no necesitan de una fuente de energía cerca de la zona que se quiera medir. Existe una gran variedad de sensores de fibra óptica basados en diferentes fenómenos, como por ejemplo la difracción, interferometría, polarización o dispersión. Centrándonos en este último efecto, existe

un tipo de sensor de fibra óptica conocido como sensores distribuidos. Estos sensores presentan unas propiedades muy interesantes para su utilización en aplicaciones de monitorización, especialmente cuando las estructuras tienen unas dimensiones relativamente grandes. En este sentido hay que considerar tres procesos de dispersión diferentes, conocidos como Rayleigh, Brillouin y Raman. Este tipo de sensores permite obtener miles de puntos de medidas distribuidas a lo largo de la fibra óptica con una resolución espacial definida. Una importante ventaja de este tipo de sensores es que la fibra es el propio sensor, no siendo necesario realizar ninguna modificación sobre ella para poder medir variaciones de temperatura y/o las deformaciones que sufre. Concretamente, los sensores distribuidos basados en la dispersión estimulada de Brillouin emplean típicamente resoluciones espaciales de 1 m midiendo a lo largo de fibras de decenas de kilómetros de largo. Además, es posible aumentar sus capacidades aplicando algunas mejoras propuestas, alcanzando distancias de más de 100 km o resoluciones espaciales por debajo del metro, entre otras.

El objetivo de esta tesis es contribuir al desarrollo de sensores distribuidos basados en la dispersión de Brillouin. Con este propósito, en primer lugar, se realiza un estudio teórico de la dispersión Brillouin, centrandó el análisis teórico en la utilización de este efecto para el desarrollo de sensores. Dado que la mayoría de las contribuciones propuestas durante la tesis se basan en el empleo de sensores distribuidos basados en el efecto Brillouin y trabajando en el dominio del tiempo, se realiza una amplia explicación de los conceptos más relevantes que este tipo de sensores utiliza. En este apartado también se identifican las principales limitaciones que este tipo de sensores presenta como son la presencia de efectos no locales, el elevado tiempo de medida, la limitada resolución espacial o el agotamiento del bombeo.

Una vez aclarados los conceptos teóricos más relevantes, se continúa con la explicación de las contribuciones que se han propuesto durante la tesis. Esta parte está dividida en tres grandes grupos dependiendo de la naturaleza de la solución propuesta. De este modo se explican las contribuciones realizadas que tratan sobre nuevas configuraciones experimentales, sobre la aplicación de técnicas de procesado en sensores BOTDA y, por último, sobre demostraciones a escala de laboratorio de aplicaciones de monitorización reales. De este modo, las contribuciones del primer grupo tratan de resolver problemas como los efectos no locales en sensores BOTDA, aumentar el rendimiento de sensores de Brillouin trabajando en el dominio de la frecuencia y también el uso de otro tipo de fuentes láser en los esquemas BOTDA. En el segundo tema

---

se proponen soluciones basadas en el uso de redes neuronales artificiales para discriminar entre medidas de temperatura y deformación, y el uso de algoritmos subpíxel tratando de mejorar el rendimiento de los sensores BOTDA estimando la frecuencia de Brillouin. Por último, las demostraciones de laboratorio están centradas en encontrar soluciones para la monitorización en ambientes hostiles como lo son zonas expuestas a altas temperaturas, el análisis modal de paneles de materiales compuestos permitiendo la localización de defectos en ellos y la detección de fugas de agua en tuberías.

De manera resumida, se puede decir que las propuestas incluidas en esta tesis buscan mejorar el rendimiento de estos sensores por medio de evitar ciertas de sus limitaciones como son los efectos no locales o a la aparición de los sub-picos en los esquemas BOFDA, la discriminación entre temperatura y deformación, o su empleo en ambientes hostiles.



---

# Abstract

---

Nowadays, society demands more and more services in a wide range of different sectors: transport, energy, health or communications, among others. To have all these services working properly, many infrastructures are required. Roads, bridges, railways, tunnels, dams, industrial factories or pipelines are examples of these indispensable infrastructures to satisfy our needs. However, they are not perfect and exhibit deterioration with time, with the appearance of cracks, corrosion processes or other problems that can give rise to their collapse. Accordingly, monitoring the integrity of structures has become a task that concerns society due to the potential risks that they imply on the population. In this way, there is a growing number of monitored structures using all kinds of technological approaches.

In this regard, the development of fiber optic sensors has enabled a wide range of solutions to be employed in structural health monitoring due to their unique properties. Optical fiber sensors present some advantages such as long distance monitoring, electromagnetic immunity, the possibility of multiplexing more than one sensor in a fiber, the capability of being embedded on structures or not requiring electricity near the measurement point. They are based on different physical phenomena, such as diffraction, interferometry, polarization or scattering, among others. Based on the latter effect, there is a kind of optical fiber sensor that has very interesting properties to be employed with monitoring purposes, especially when the structure is large. They are known as distributed fiber sensors and are based on different scattering phenomena: Rayleigh, Brillouin or Raman. They enable to perform distributed measurements along large optical fibers with a defined spatial resolution, obtaining thousands of measurement points. Moreover, these sensors present the advantage that the optical fiber

itself is the sensing element, not requiring any modifications to measure temperature and strain variations surrounding the optical fiber. Specifically, these sensors based on stimulated Brillouin scattering typically employ 1 m spatial resolution measuring along tenths of kilometers long fibers, although it is possible to increase their performance by applying some proposed improvements, reaching more than 100 km or sub-meter spatial resolutions, among others.

This thesis aims to contribute to the development of distributed sensors based on Brillouin scattering. With this purpose, first of all, a theoretical study of Brillouin scattering is carried out, focusing on the employment of this effect with sensing objectives. Especially, a deep understanding of Brillouin optical time domain sensors is considered, given that most of the proposed contributions are based on their employment. Once the main limitations of these systems are identified, such as non-local effects, high measurement time, limited spatial resolution or pump depletion, the proposed contributions of the thesis are explained.

The contributions are divided into three main groups depending on the proposed approaches: new experimental configurations, processing techniques applied to BOTDA sensors and laboratory demonstrations of field applications. In this way, proposals aiming to overcome non-local effects in BOTDA, to increase the performance of Brillouin distributed sensors based on the frequency domain and to use other kinds of laser sources in BOTDA are included in the first group. The second group contains proposals based on using artificial neural networks to discriminate temperature and strain measurements and the use of subpixel algorithms to improve the BOTDA performance when estimating the Brillouin frequency shift. Finally, the laboratory demonstrations are focused on providing solutions for high-temperature environments and water leakage detection, and also to analyse the modal shapes of a composite panel to allow the location of defects.

In summary, the solutions presented in this thesis seek to contribute to the field of Brillouin distributed sensors through the proposal of new approaches. They try to overcome some limitations detected in the literature such as non-local effects, the detrimental effect of sub-peaks in BOFDA sensors, the temperature and strain discrimination or their employment in harsh environments.

---

# Contents

---

<b>Resumen</b>	<b>vii</b>
<b>Abstract</b>	<b>xi</b>
<b>List of figures</b>	<b>xvii</b>
<b>List of tables</b>	<b>xxiii</b>
<b>Acronyms</b>	<b>xxv</b>
<b>List of variables</b>	<b>xxix</b>
<b>I. Preliminary</b>	<b>1</b>
<b>1. Introduction</b>	<b>3</b>
1.1. Motivation . . . . .	3
1.2. Objectives of the thesis . . . . .	5
1.3. Structure of the thesis . . . . .	6
<b>2. Optical fiber sensors based on Brillouin scattering</b>	<b>9</b>
2.1. Introduction . . . . .	10
2.2. Scattering effects in optical fibers . . . . .	11
2.2.1. Rayleigh, Brillouin and Raman scattering . . . . .	13
2.3. Spontaneous Brillouin scattering . . . . .	17
2.4. Stimulated Brillouin scattering . . . . .	23
2.4.1. Electrostriction . . . . .	24

2.4.2.	Stimulated Brillouin scattering induced by electrostriction . . .	26
2.4.3.	Theoretical model of SBS . . . . .	27
2.4.4.	Steady-state solution . . . . .	29
2.4.5.	SBS threshold . . . . .	31
2.5.	Distributed sensing using Brillouin scattering . . . . .	33
2.5.1.	Introduction . . . . .	33
2.5.2.	Brillouin sensing principle . . . . .	35
2.5.3.	Brillouin distributed sensors. Types and main characteristics .	38
2.5.3.1.	Brillouin optical correlation domain analysis . . . . .	39
2.5.3.2.	Brillouin optical correlation domain reflectometry . .	41
2.5.3.3.	Brillouin optical frequency domain analysis . . . . .	43
2.5.3.4.	Brillouin optical time domain reflectometry . . . . .	46
2.5.3.5.	Brillouin optical time domain analysis . . . . .	49
<b>II.</b>	<b>Contributions</b>	<b>71</b>
<b>3.</b>	<b>New techniques and configurations for Brillouin distributed sensors.</b>	<b>73</b>
3.1.	Overcoming Non-local effects in Brillouin optical time domain analysis sensors . . . . .	74
3.1.1.	Description of the technique . . . . .	75
3.1.2.	Experimental setup . . . . .	78
3.1.3.	Experimental results . . . . .	79
3.2.	Brillouin optical frequency domain reflectometry . . . . .	85
3.2.1.	Principle of operation . . . . .	86
3.2.2.	Experimental setup . . . . .	87
3.2.3.	Experimental measurements . . . . .	89
3.2.3.1.	Experimental tests over uniform fibers . . . . .	89
3.2.3.2.	Experimental tests over nonuniform fibers . . . . .	91
3.3.	Study of a fiber ring laser working on the SLM regime in a BOTDA sensor . . . . .	96
3.3.1.	Experimental setup . . . . .	99
3.3.2.	Experimental results . . . . .	100
3.4.	Conclusions . . . . .	107

---

<b>4. Processing techniques applied to BOTDA sensors</b>	<b>111</b>
4.1. Discrimination ANN . . . . .	112
4.1.1. Principle of operation . . . . .	113
4.1.2. Experimental issues . . . . .	117
4.1.3. Results . . . . .	123
4.2. Brillouin frequency shift estimation in BOTDA via subpixel processing	127
4.2.1. Principle of operation . . . . .	127
4.2.2. Experimental issues . . . . .	129
4.3. Conclusions . . . . .	131
<b>5. Laboratory demonstrations of field applications</b>	<b>133</b>
5.1. High temperature monitoring with gold-coated fibers . . . . .	134
5.1.1. Fundamentals . . . . .	136
5.1.2. Experimental setup . . . . .	137
5.1.3. Experimental issues . . . . .	138
5.2. Modal analysis of a composite panel by means of slope-assisted BOTDA	143
5.2.1. Experimental demonstration . . . . .	143
5.3. Experimental demonstration of a leakage monitoring system for large diameter water pipes . . . . .	149
5.3.1. Experimental setup . . . . .	150
5.3.2. Experimental results . . . . .	150
5.4. Conclusions . . . . .	155
<b>III. Conclusions and open lines</b>	<b>157</b>
<b>6. Conclusions</b>	<b>159</b>
<b>7. Open lines</b>	<b>165</b>
<b>IV. References</b>	<b>167</b>
<b>8. References by chapter</b>	<b>169</b>
8.1. References of Chapter 2 . . . . .	169
8.2. References of Chapter 3 . . . . .	182
8.3. References of Chapter 4 . . . . .	187

8.4. References of Chapter 5 . . . . .	190
<b>List of publications</b>	<b>195</b>
1. Related to the thesis work . . . . .	196
1.1. International journals . . . . .	196
1.2. International conferences . . . . .	197
2. Additional contributions . . . . .	198
2.1. International journals . . . . .	198
2.2. International conferences . . . . .	199

---

## List of figures

---

2.1. Representation of scattering mechanisms . . . . .	14
2.2. Typical observed spectrum of light scattering . . . . .	17
2.3. Illustration of Stokes scattering. . . . .	21
2.4. Illustration of anti-Stokes scattering. . . . .	21
2.5. Brillouin gain spectrum as a function of temperature . . . . .	37
2.6. Brillouin gain spectrum as a function of strain . . . . .	38
2.7. BOCDA operation principle . . . . .	41
2.8. BOCDR operation principle . . . . .	43
2.9. BOFDA experimental setup . . . . .	46
2.10. BOTDR operation principle . . . . .	47
2.11. BOTDA operation principle . . . . .	50
2.12. Brillouin gain and loss configurations . . . . .	51
2.13. Normalized probe signal versus fiber distance . . . . .	52

LIST OF FIGURES

---

2.14. Definition of spatial resolution . . . . .	53
2.15. Distributed Brillouin gain spectrum . . . . .	54
2.16. Brillouin gain spectrum at a specific fiber position . . . . .	55
2.17. Experimental setup of a BOTDA sensor . . . . .	56
2.18. Evolution of the Brillouin gain signal affected by modulation instability	62
2.19. Types of pulses employed in BOTDA . . . . .	65
3.1. Fundamentals of the technique employed to overcome non-local effects	76
3.2. Experimental setup employed to overcome non-local effects in BOTDA	78
3.3. Pulses at the output of the fiber for a conventional dual-probe BOTDA	79
3.4. Measured Brillouin gain spectra for a conventional dual-probe BOTDA	80
3.5. Measured Brillouin gain spectra at the end of the fiber . . . . .	81
3.6. Pulses at the output of the fiber, raw measurement data and measured Brillouin spectra for the FM dual-probe BOTDA . . . . .	82
3.7. Measured BGS at the end of the fiber with the FM BOTDA system .	83
3.8. Comparison of measured BFS for the FM technique and for the conventional dual-probe . . . . .	84
3.9. Measured rms noise using the conventional dual-probe and the FM technique . . . . .	84
3.10. Experimental setup of BOFDR system . . . . .	88
3.11. Gain map acquired over a uniform 100 m long fiber . . . . .	90
3.12. BGSs acquired using the proposed BOFDR method for different filters	91

---

3.13. Frequency domain data acquired using the proposed BOFDR method or the BOFDA method . . . . .	92
3.14. Brillouin gain map of a 100 m fiber with two cold spots . . . . .	92
3.15. BFS reconstruction obtained by processing the BOFDR and BOFDA measurements . . . . .	93
3.16. BGS acquired by the employment of BOFDR and BOFDA techniques	94
3.17. BFS profile reconstruction along a 5 km fiber spool . . . . .	95
3.18. Fiber ring laser configuration employed to achieve a SLM output . . .	99
3.19. BOTDA system used in the experimental tests . . . . .	100
3.20. Optical output spectra of DFB and EDFRL lasers . . . . .	101
3.21. Electrical output spectra of DFB and EDFRL lasers . . . . .	102
3.22. Optical spectral stability of DFB and EDFRL lasers after 4 hours . .	103
3.23. Fiber ring laser configuration employed to achieve a better wavelength stability . . . . .	103
3.24. Optical spectral stability of DFB and EDFRL lasers after 4 hours using the climatic chamber . . . . .	104
3.25. Brillouin gain map measured employing the EDFRL . . . . .	105
3.26. Estimated BFS over the last 10 km of the sensing fiber . . . . .	105
3.27. Standard deviation of the estimated BFS . . . . .	106
4.1. Schematic representation of an artificial neural network . . . . .	116
4.2. Schematic representation of the proposed solution based on ANN . .	118

LIST OF FIGURES

---

4.3.	BOTDA setup employed in the experimental tests . . . . .	119
4.4.	Evolution of the BGS linewidth for different pump pulse widths . . . . .	120
4.5.	Setup designed and implemented for the development of the simultaneous temperature and strain measurements . . . . .	121
4.6.	BFS evolution for simultaneous measurements of temperature and strain . . . . .	123
4.7.	Network cross-entropy for the best classification . . . . .	125
4.8.	Working principle of the CDA algorithm . . . . .	128
4.9.	Comparison of the BFS profiles obtained with Lorentzian fitting and subpixel CDA processing . . . . .	130
5.1.	Fiber under test configuration employed . . . . .	137
5.2.	BOTDA system used to monitor the gold-coated fiber . . . . .	138
5.3.	BFS distribution along the fiber for temperatures from 50 to 600°C. . . . .	139
5.4.	BFS distribution along the fiber for temperatures from 600 to 50°C . . . . .	140
5.5.	Brillouin frequency shift vs. temperature at the hot spot section . . . . .	141
5.6.	Evolution of the BGS for increasing and decreasing temperatures . . . . .	142
5.7.	Experimental slope assisted BOTDA setup . . . . .	144
5.8.	Schematic view of the aluminum composite plate employed for the experiments . . . . .	145
5.9.	First three strain modal shapes of the plate. Experimental and simulated shapes . . . . .	146
5.10.	Strain modal shape of the first bending mode of the plate . . . . .	148

---

5.11. Images illustrating the experimental facility employed . . . . .	151
5.12. Sensing fiber installation in each laboratory scenario . . . . .	152
5.13. Water leakage detection in the first scenario with 1 m spatial resolution	152
5.14. Water leakage detection in the first scenario (temporal evolution) . .	153
5.15. Longitudinal expansion of the temperature variation with time . . . .	154
5.16. Verification of the spatial resolution by means of multiple leakage de- tection . . . . .	154



---

## List of tables

---

4.1. BFS standard deviation ( $\sigma$ ) (MHz) for different temperatures and pump pulse widths. . . . .	120
4.2. BFS standard deviation ( $\sigma$ ) (MHz) for different strains and pump pulse widths. . . . .	121
4.3. BFS error (MHz) for different temperatures and strains and a pump pulse width of 20 ns. . . . .	122
4.4. ANN classification results via PCA. . . . .	124
4.5. Noise variance ( $\sigma^2$ ) for the intensity-normalized BGSs (a.u. $\cdot 10^{-4}$ ) . .	126
5.1. Averaged BFS values, estimated temperature and mean error for each temperature. . . . .	141
5.2. Experimental and simulated resonance frequencies. . . . .	147
5.3. Defect localization (the coordinates refer to the center of the added element). . . . .	147



---

# Acronyms

---

- **ALP:** Adaptive Linear Prediction
- **ANN:** Artificial Neural Network
- **AWG:** Arbitrary Waveform Generator
- **BFS:** Brillouin Frequency Shift
- **BGS:** Brillouin Gain Spectrum
- **BLS:** Brillouin Loss Spectrum
- **BOCDA:** Brillouin Optical Correlation Domain Analysis
- **BOCDR:** Brillouin Optical Correlation Domain Reflectometry
- **BOFDA:** Brillouin Optical Frequency Domain Analysis
- **BOFDR:** Brillouin Optical Frequency Domain Reflectometry
- **BOSA:** Brillouin Optical Spectrum Analyzer
- **BOTDA:** Brillouin Optical Time Domain Analysis
- **BOTDR:** Brillouin Optical Time Domain Reflectometry

- **BPF:** Bandpass Filter
- **c.c.:** Complex Conjugate
- **CDA:** Centroid Detection Algorithm
- **DFB:** Distributed Feedback
- **DOFS:** Distributed Optical Fiber Sensor
- **DPP:** Differential Pulse-width Pair
- **DRA:** Distributed Raman Amplification
- **DSF:** Dispersion Shifted Fibers
- **DTS:** Distributed Temperature Sensor
- **EDFA:** Erbium-Doped Fiber Amplifier
- **EDFRL:** Erbium-Doped Fiber Ring Laser
- **EMA:** Experimental Modal Analysis
- **EOM:** Electro-Optic Modulator
- **ER:** Extinction Ratio
- **ESA:** Electrical Spectrum Analyzer
- **FBG:** Fiber Bragg Grating
- **FDM:** Frequency Division Multiplexing
- **FM:** Frequency Modulation
- **FoM:** Figure-of-Merit
- **FUT:** Fiber Under Test

- 
- **FWHM:** Full Width at Half Maximum
  - **IF:** Intermediate Frequency
  - **IFFT:** Inverse Fast Fourier Transform
  - **LEAF:** Large Effective Area Fiber
  - **LO:** Local Oscillator
  - **LPR:** Landau-Placzek Ratio
  - **MI:** Modulation Instability
  - **OTDR:** Optical Time Domain Reflectometer
  - **PCA:** Principal Component Analysis
  - **PCF:** Photonic Crystal Fiber
  - **PS:** Polarization Scrambler
  - **RBW:** Resolution Bandwidth
  - **RF:** Radio Frequency
  - **SBS:** Stimulated Brillouin Scattering
  - **SHB:** Spatial Hole Burning
  - **SHM:** Structural Health Monitoring
  - **SLM:** Single Longitudinal Mode
  - **SMF:** Single-Mode Fiber
  - **SNR:** Signal-to-Noise Ratio
  - **SOA:** Semiconductor Optical Amplifier

- **SOP:** State of Polarization
- **SpBS:** Spontaneous Brillouin Scattering
- **TDM:** Time Division Multiplexing
- **VNA:** Vector Network Analyzer
- **WDM:** Wavelength Division Multiplexing

---

## List of variables

---

- $I_{sc}$ : Intensity of the scattered light
- $I_0$ : Intensity of the incident light
- $\lambda_0$ : Wavelength of the incident light
- $N$ : Number of scatterers
- $\alpha_m$ : Molecular polarizability
- $\theta$ : Scattering angle
- $R$ : Distance from the scatterer
- $N_0$ : Population of the starting ground level
- $\sigma_R$ : Raman cross section
- $\Delta\lambda$ : Wavelength variation
- $\Gamma'$ : Damping parameter of the material
- $V_A$ : Acoustic velocity in the medium
- $K_S$ : Bulk modulus

- $\rho$ : Material density
- $C_S$ : Adiabatic compressibility
- $\Delta p$ : Pressure wave variation
- $p$ : Pressure wave
- $q$ : Propagation constant of acoustic wave
- $\Omega$ : Angular frequency of acoustic wave
- $\Gamma_B$ : Phonon decay rate
- $\alpha_s$ : Sound absorption coefficient
- $\tau_p$ : Phonon lifetime
- $E$ : Electric field
- $E_0$ : Amplitude of electric field
- $k$ : Wave vector of the incident light
- $\omega$ : Angular frequency of the incident light
- $k'$ : Wave vector of the scattered light
- $\omega'$ : Angular frequency of the scattered light
- $n$ : Refractive index of medium
- $c$ : Speed of light in vacuum
- $\epsilon_0$ : Dielectric permittivity in vacuum
- $P$ : Polarization of the medium
- $\Delta\chi$ : Fluctuation of the dielectric susceptibility

- 
- $\Delta\epsilon$ : Fluctuation of the dielectric constant
  - $\Delta\rho$ : Density variation
  - $\Delta s$ : Entropy variation
  - $\gamma_e$ : Electrostrictive constant
  - $\Omega_B$ : Angular Brillouin frequency shift
  - $\nu_B$ : Brillouin frequency shift
  - $g_B$ : Brillouin gain spectrum
  - $g_0$ : Brillouin gain coefficient
  - $\nu$ : Optical frequency
  - $\Delta\nu_B$ : Brillouin linewidth
  - $\rho_{12}$ : Longitudinal elasto-optic coefficient
  - $m$ : Dipole moment
  - $U$ : Energy
  - $F$ : Force
  - $\Delta U$ : Energy variation
  - $\Delta w$ : Work variation
  - $p_{st}$ : Strictive pressure
  - $V$ : Volume
  - $\Delta V$ : Volume variation
  - $k_p$ : Wave vector of the pump wave

- $k_S$ : Wave vector of the Stokes wave
- $q_B$ : Wave vector of the acoustic wave
- $\omega_p$ : Frequency of pump wave
- $\omega_S$ : Frequency of Stokes wave
- $E_p$ : Electric field of the pump wave
- $E_S$ : Electric field of the Stokes wave
- $\rho_0$ : Mean density of the material
- $f$ : Force per unit of volume
- $P_{NL}$ : Non-linear polarization
- $A_p$ : Amplitude of the pump wave
- $A_S$ : Amplitude of the Stokes wave
- $I_p$ : Intensity of the pump wave
- $I_S$ : Intensity of the Stokes wave
- $L$ : Fiber length
- $\alpha$ : Attenuation coefficient of the medium
- $P_0$ : Pump power at the input of the optical fiber
- $A_{eff}$ : Effective area
- $L_{eff}$ : Effective length
- $P_{th}$ : Power threshold
- $\Delta_T$ : Temperature variation

- 
- $\Delta_\varepsilon$ : Strain variation
  - $C_T$ : Temperature coefficient
  - $C_\varepsilon$ : Strain coefficient
  - $T_0$ : Reference temperature
  - $\varepsilon_0$ : Reference strain
  - $\delta z$ : Spatial resolution
  - $f_{max}$ : Maximum frequency modulation
  - $f_{min}$ : Minimum frequency modulation
  - $L_{max}$ : Maximum measuring range
  - $\Delta f_m$ : Modulation frequency step
  - $z$ : Fiber location
  - $t_0$ : Pulse width
  - $\sigma_\nu$ : Brillouin frequency error
  - $\delta f$ : Frequency step
  - $N_{Av}$ : Number of averages
  - $N_{Tr}$ : Number of traces
  - $f_1$ : Fiber configuration
  - $\eta$ : Peak fraction level
  - $\sigma$ : Noise amplitude
  - $\Delta\nu_L$ : Detuning of the Brillouin loss spectra

- $\nu_{SL}$ : Frequency of the lower probe sideband
- $\nu_p$ : Frequency of the pump
- $\Delta\nu_G$ : Detuning of the Brillouin gain spectra
- $\nu_{SU}$ : Frequency of the upper probe sideband
- $T_{acq}$ : Acquisition time
- $N_{Av,eff}$ : Effective number of averages
- $\mathbf{ce}$ : Cross-entropy
- $\sigma^2$ : Noise variance
- $f_{sub}$ : Subpixel frequency
- $f_j$ : Frequency of a pixel
- $i_j$ : Intensity of a pixel

# Part I

## Preliminary

Monitoring the health of structures with optical fiber sensors has become an extensive research field over recent years. A brief motivation of the employment of optical fiber sensors in structural health monitoring, the objectives proposed to increase the performance of distributed sensors and the structure of this document are presented in this part.

Moreover, a state of the art of distributed optical fiber sensors, especially those based on Brillouin scattering, has been included in order to explain the most relevant characteristics of this kind of sensors.

The chapters included in this part are:

- Chapter 1: Introduction
- Chapter 2: Optical fiber sensors based on Brillouin scattering



# Chapter 1

---

## Introduction

---

### 1.1. Motivation

Over the last two decades, structural health monitoring (SHM) has become an emerging research area where many developments have been achieved. The main reason for the growth of this field of expertise lies in the continuous new requirements that the current society requires. People do not only want more and more services around them, they also demand safer infrastructures associated with those services: the integrity of sport facilities or big buildings, roads and tunnels, industrial factories or planes are some examples. As a result, new devices are required to check the real state of those structures. Apart from gathering information on those facilities, it is also very important that the analysis could be in real time. Many solutions are based on supervising structures from their outside, but in this way, it is very difficult to efficiently measure the strain and/or internal stress that they are suffering. Many times this is only noticed when cracks are evident, thus being too late for the integrity of the structure. Moreover, if situations leading to crack formation were detected before they physically appear in infrastructures, some operations could be adopted to prevent those malfunctions.

These situations evidence that analysis techniques enabling the health monitoring of those structures are crucial, measuring on a distributed way temperature and deforma-

tion. One particular characteristic of SHM is that the existing infrastructures around the world are very different. This requires the employment of versatile devices able to being adapted to a wide range of different scenarios/situations. Some interesting examples of these infrastructures are pipelines; power energy cables; long roads; water dams; radioactive scenarios; high-temperature emplacements or facilities where these monitoring devices might be surrounded by electromagnetic fields.

With this purpose, optical fiber sensors have been developed to help on this complicated task. Optical fiber sensors constitute a big sensing category where different sensor technologies are considered. They are based on different physical phenomena such as interferometry, diffraction, light polarization and scattering, among others. Sensors based on the latter are one of the most relevant due to their unique characteristics to provide distributed information along the optical fiber, especially those based on Brillouin scattering. These sensors have the ability to distributively measure both strain and temperature over long fiber distances, reaching more than 100 km. They also show very high spatial resolutions: sub-meter spatial resolutions have been reached with different experimental configurations, providing over 1 million effective sensing points. These optical sensors are based on analysing the backscattering light that it is generated within optical fibers when the optical waves propagating within the fiber interact with an acoustic wave. Distributed sensors have the advantage that lots of point sensors, e.g. fiber Bragg grating (FBG), can be replaced by only one distributed system. The main difference between these two optical fiber sensor categories is that in distributed systems all the optical fiber is the sensor and the number of measurement points depends on the spatial resolution and the length of the employed optical fiber. Meanwhile, point sensors employ the optical fiber to propagate some waves that interact with the sensors that have been previously generated in the fiber. So, the number of measurement points depends on the number of sensors manufactured on the fiber, thus complicating the installation process and measurements on large structures. This is the main reason why distributed sensors are the best solution to install on big infrastructures where lots of points need to be analysed. These sensors have the advantage that it is only necessary to attach the measuring optical fiber, generally, a single-mode fiber (SMF), to the structure and use an interrogator to monitor it, thus being possible to replace lots of point sensors with only a single distributed system.

Research efforts in the field of optical fiber sensors have considerably increased over recent years. This has led Brillouin distributed sensors to show nowadays a good

performance measuring temperature and strain, allowing them to be used in some applications related to the field of SHM. In this regard, detection of leakages on gas or oil pipelines, temperature control of power cables and monitoring of bridges or dams stand out. Their employment in these fields fits perfectly due to the long measurement range and good spatial resolutions that some solutions can achieve. Typically, Brillouin distributed sensors have a good accuracy on temperature and strain, making it possible to measure repetitively strain variations of few microstrains ( $2\text{-}5 \mu\epsilon$ ) and about  $0.1^\circ\text{C}$  of uncertainty in temperature measurements. These values depend considerably on the configuration of the distributed interrogator employed, and also on the fiber sensing distance.

## 1.2. Objectives of the thesis

The main objective of this thesis dissertation is to contribute to the development and improvement in the performance of distributed sensors based on Brillouin scattering. Different areas of improvement have been considered during the development of this work. First of all, various different experimental configurations have been proposed to overcome some traditional limitations of these sensors, such as non-local effects on Brillouin optical time domain analysis (BOTDA) sensors or appearance of sub-peaks on the Brillouin gain measured with systems based on the frequency domain. Another main objective of this work is applying different processing approaches in an attempt to solve open problems such as the discrimination between temperature and strain measurements obtained with Brillouin sensors. Additionally, it would be interesting to provide some faster and alternative methods to estimate the Brillouin shift in comparison to traditional method based on applying Lorentzian fittings. Finally, this work has also tried to contribute to the validation of the acquired knowledge by performing validations in real scenarios, such as high-temperature applications or leakage detection in pipelines.

### 1.3. Structure of the thesis

This thesis dissertation has been divided into seven different chapters, covering from a review of the associated state of the art to the contributions developed within the framework of this work.

This first chapter is an introduction to the thesis dissertation, where the motivation and objectives of the work are explained.

The second chapter presents a state of the art of Brillouin distributed sensors. This chapter introduces different scattering processes that take place into optical fibers, distinguishing between spontaneous and stimulated scattering, and highlighting Brillouin effect. Some concepts regarding Brillouin scattering, such as the stimulated Brillouin scattering (SBS), the Brillouin gain spectrum (BGS) or the Brillouin frequency shift (BFS) among others, are described there. Moreover, it is also explained how to use this phenomenon to develop distributed sensors using optical fibers to measure both temperature and strain. After the sensing concept is introduced, the different kinds of Brillouin sensors are defined, as well as their most relevant parameters, like spatial resolution, measurement range or accuracy in terms of temperature and strain. Finally, the most remarkable advances developed for these sensors in recent years are explained and also the existing limitations to be overcome.

These first two chapters belong to Part I of this thesis dissertation. After this preliminary part, where some limitations or detrimental behaviours of these sensors are detected, Part II is then focused on how to solve them in order to achieve a better final performance. In this regard, three different approaches, each one of the following chapters, are detailed in the contributions part.

According to this classification, the third chapter is focused on using new experimental configurations of Brillouin sensors to improve their final performance. The first approach is to use frequency modulation (FM) on the probe wave of BOTDA sensors in an attempt to overcome a detrimental behaviour typically present on these sensors known as non-local effects. This harmful effect arises when the probe optical power exceeds a certain threshold, and it produces an increase in the pump pulse peak power during its propagation along the optical fiber. This proposal enables to overcome this limitation on the optical probe power than can be injected into the fiber without

the appearance of these non-local effects. The second contribution is the employment of a new Brillouin configuration based on the frequency domain. With this new experimental setup, access to only one end of the optical fiber is required to perform the measurements, thus helping an easy installation of the system in real applications. Moreover, this technique also enables the distributed measurements along optical fibers without the presence of a detrimental effect known as sub-peak. This effect appears in conventional Brillouin frequency domain analysis based sensors and it makes necessary the application of more complex processing algorithms on the measured data to avoid it and, consequently, to obtain correct measurements. Finally, a feasibility study on the employment of a fiber laser acting as the source of a BOTDA sensor is analysed. In this study, the most relevant parameters of the laser are analysed and its employment in a distributed sensor is demonstrated. Moreover, its performance is compared with the one achieved if the optical source is a commercial distributed feedback (DFB) laser.

The fourth chapter is focused on the employment of processing strategies to improve the performance of Brillouin-based sensors, a research area exhibiting a clearly growing trend. Most of the advances that are published on Brillouin distributed sensors are based on the employment of new experimental configurations or modifications of the conventional systems, thus trying to improve the final performance of these sensors. This is generally achieved via upgrading the signal-to-noise ratio (SNR), the spatial resolution or the measurement range, among others. However, the interest in applying different processing techniques to the retrieved data obtained with these sensors has increased over recent years. In this fourth chapter, efforts are focused on applying different processing algorithms to data obtained using BOTDA sensors. The first proposal is based on applying artificial intelligence approaches to enable the automatic discrimination between the measurement of temperature and/or strain. Another solution presented in this chapter is the proposal of an algorithm to estimate the BFS of a measured BGS without applying the traditional Lorentzian fitting. The idea of using this kind of algorithms over the measured BGS lies in the elevated processing time that it is necessary to correctly estimate the BFS when Lorentzian fitting is applied. This alternative method allows a significant improvement in this regard.

This part focused on the contributions developed during this thesis ends with the fifth chapter that deals with the application of these sensors in some industrial fields. The idea is to experimentally validate in the laboratory the feasibility of employing them to perform different types of distributed measurements in some real scenarios, such as

industrial environments. Firstly, some distributed measurements are performed using a gold-coated fiber acting as the sensing fiber. This experimental validation demonstrates the feasibility of using this kind of optical coated fiber in some scenarios where temperatures could reach up to 600°C. Another section of the chapter demonstrates how it is possible to analyse the modal shape of metal panels via the analysis of strain measurements when the slope-assisted BOTDA technique is used. The viability of this application is demonstrated comparing the obtained experimental results with those simulated using a commercial software for this purpose. Finally, the last section of this chapter presents the experimental results obtained trying to detect leakages on large-diameter water pipelines. Part II ends with this experimental demonstration.

The third and final part of this work is the closing of the thesis dissertation where conclusions and open lines are discussed. Here, chapter six and seven are clearly separated. The sixth chapter reports the main conclusions derived from this thesis' contributions and the seventh discusses the future open lines that this work has opened.

## Chapter 2

---

# Optical fiber sensors based on Brillouin scattering

---

In this chapter, a brief introduction to optical fiber sensors is presented, paying special attention to those based on light scattering effects. It starts with the explanation of the two different scattering processes present in optical fiber: linear and non-linear effects. Moreover, the distinction between elastic and inelastic scattering processes is also mentioned here, briefly explaining the three main scattering effects in terms of these classifications: Rayleigh, Brillouin and Raman. Afterwards, the focus changes to the scattering effect concerning this thesis dissertation: Brillouin scattering. Both processes are explained, spontaneous and stimulated, but as a consequence of the contributions presented in Part II, where the latter is the most relevant process, the stimulated Brillouin scattering (SBS) is explained in more detail. With this purpose, the main concepts of SBS are explained, such as the physical phenomenon needed for the stimulation of the process (electrostriction), their theoretical model and other concepts related to its properties, such as Brillouin gain spectrum (BGS), Brillouin frequency shift (BFS) or the SBS threshold, among others. Finally, a big section of the chapter is focused on the use of Brillouin scattering as the sensing mechanism for distributed sensors. Different kinds of distributed sensors based on different approaches, such as time, frequency or correlation domains are presented. Among all of them, the sensor based on the analysis of the Brillouin gain in the time domain is explained with more

details given that this thesis is mainly focused on this type of sensor. To finish this chapter, some limitations of these systems are discussed here, thus referring to Part II where some contributions are proposed to solve them.

## 2.1. Introduction

Sensors can be understood as devices that provide information about the real world, interacting with electronic systems to enable the processing and recording of the acquired data, thus also enabling actuation according to that information. Sensors are devices that have some property sensitive to the magnitude to be measured (of a certain medium): when this magnitude changes, that specific property will also change. It is possible to define a sensor as the device that converts some magnitude, such as temperature or strain, coming from the medium into data that can be read in electronic form [1].

Nowadays, optical fiber sensors occupy a privileged place within the field of sensors. The main reason for this is that they have some unique characteristics that give them great advantages over other sensing technologies, e.g. electrical sensors. These advantages are summarized as follows: (i) they are able to sense and transmit the measured information by the fiber link itself; (ii) it is possible to sense over long distances due to their low attenuation coefficient (0.2 dB/km in the third telecommunication window, around 1550 nm); (iii) they are a dielectric medium, and consequently, they are not affected by electromagnetic interferences; and lastly, (iv) their small size and low weight make them perfect to be embedded into composite materials, or to be attached easily onto the surface of structures [2].

It is also worth noting that optical fiber sensors are systems that can be employed to measure many different physical quantities. The optical properties of the optical waves suffer variations during the propagation of the light within the optical fibers when a physical magnitude interacts with the fiber. Some of the most important examples are temperature, strain, humidity, vibration, rotation, acoustic field, electric field or magnetic field, among others [3, 4]. Depending on the type of magnitude to be measured, different approaches are available. For example, the state of polarization (SOP) of light propagating in the fiber is rotated when a magnetic field is parallel to

the fiber longitudinal axis. This is due to the Faraday effect, and the rotated angle will be proportional to the strength of the applied field, allowing the development of electrical current sensors [2].

Given that optical fiber sensors are based on different technological approaches, some categories have been proposed to organize them according to the employed monitoring mechanism:

- Point sensors: they are employed to measure changes on a specific section of the optical fiber.
- Quasi-distributed sensors: they are capable of performing measurements on different points along the optical fiber. They are based on the employment of multiplexing strategies applied over FBGs sensors.
- Distributed sensors: with them, it is possible to measure thousands of different points along the sensing fiber without modifying it. They are based on different scattering phenomena.

The work developed in this thesis is focused on the latter, specifically on those based on Brillouin effect. For a better knowledge of this type of sensors, the next sections of this chapter explain their most important aspects, starting from the scattering concept, and describing the different types of scattering and the Physics involved. It continues with the employment of the Brillouin scattering for developing distributed sensors, going through its most relevant aspects, such as the spatial resolution, the measurement range or their dynamic behaviour. Moreover, different techniques employed to improve their performance are also explained. To end this part, limitations found on these sensors are mentioned, thus allowing to establish a connection between this part and Part II where some contributions are proposed trying to solve them.

## **2.2. Scattering effects in optical fibers**

Scattering is a physical process that light suffers during its propagation through any material due to the interaction between the radiation and the non-uniformities

in the molecular structure of the medium. This effect provokes a deviation from the original trajectory of the incident light beam. The different scattering processes could be divided into two big groups depending on the intensity of the propagating light. These two groups are known as linear or spontaneous scattering, and non-linear or stimulated scattering. Spontaneous scattering is present in optical fibers when the incident light propagating through them has a power below a certain threshold. In this type of light scattering, the medium does not suffer any modifications in their optical properties by the presence of the optical wave [5, 6]. On the other hand, when the power of the incident light exceeds the power threshold, the process generated within the optical fiber is known as stimulated scattering. This effect is caused as a consequence of the high power injected into the fiber that produces some modifications on the properties of the material, making the scattering process becoming non-linear. Both types of scattering will be explained in more detail in sections 2.3 and 2.4, respectively.

Additionally, scattering processes can be divided into elastic or inelastic, attending to the existence (or not) of an energy transfer during the process between the inhomogeneous medium, that in the concerning case is the optical fiber, and the scattered photons. When an incident wave is propagating through the medium, some of their photons can be removed by the scattering process generating the mentioned scattered photons. The resulting direction, frequency or phase of those scattered photons might suffer a shift depending on the medium properties and the scattering process employed to generate them.

Depending on this energy transfer, the two main categories are:

- **Elastic scattering:** the energy of the scattered photons is equal to the energy of the photons injected into the medium, therefore the frequency of the scattered wave is also the same. In this type of scattering, no energy exchange occurs between the medium and the wave. The main example in this category is the Rayleigh scattering.
- **Inelastic scattering:** the frequency of the scattered photons is shifted with respect to the frequency of the incident photons during the scattering process. This is a consequence of the energy transfer produced between the medium and the photons. There are two possible cases depending on whether the scattered photons lose or gain energy during the energy transfer that provokes the frequency

shift. If the scattered photons lose part of their energy, they are down-shifted in frequency with respect to the incident light, giving rise to the Stokes components. The other case produces the anti-Stokes components, where photons gain energy from the medium, and consequently, they are up-shifted in frequency. There are two important scattering effects that belong to this type of scattering: Brillouin and Raman scattering. Both of them present an energy transfer, represented with the appearance of Stokes and anti-Stokes components in their spectra.

This organization of the scattering processes is based on the energy transfer between the medium and the scattered photons; nevertheless, it is possible to extend this, pulling away the different scattering processes that appear on optical fibers. The main characteristics of the three mentioned scattering effects, i.e. Rayleigh, Brillouin and Raman, are discussed in detail in the following section.

### **2.2.1. Rayleigh, Brillouin and Raman scattering**

As mentioned before, Rayleigh, Brillouin and Raman are the three main scattering processes to be considered in optical fibers. Mie scattering could also be considered here, but Rayleigh and Mie scattering processes are not very different, and it can be said that both are different models to approximate the scattering process applicable at different wavelengths. Each one of the mentioned scattering processes could take place in an optical fiber when any incident wavelength is propagating through it. However, the intensity of the scattering effect will vary depending on the scattering type and its intrinsic wavelength dependence.

Figure 2.1 is a schematic illustration of the different mechanism that gives rise to scattering processes via interactions between the incident photons and molecules in a transmitting medium. In summary, it is possible to explain Rayleigh scattering as the small portion of light that suffers a deviation from its original trajectory due to the physical interaction between the incident photons and inhomogeneities in the medium. These inhomogeneities can include voids, density variations, impurities, composition fluctuations, structural variations, and other microscopic and nanoscopic variations divergent from the average of the surrounding medium. On the other hand, the inelastic scattering processes, Brillouin and Raman, are generated via the interaction of the

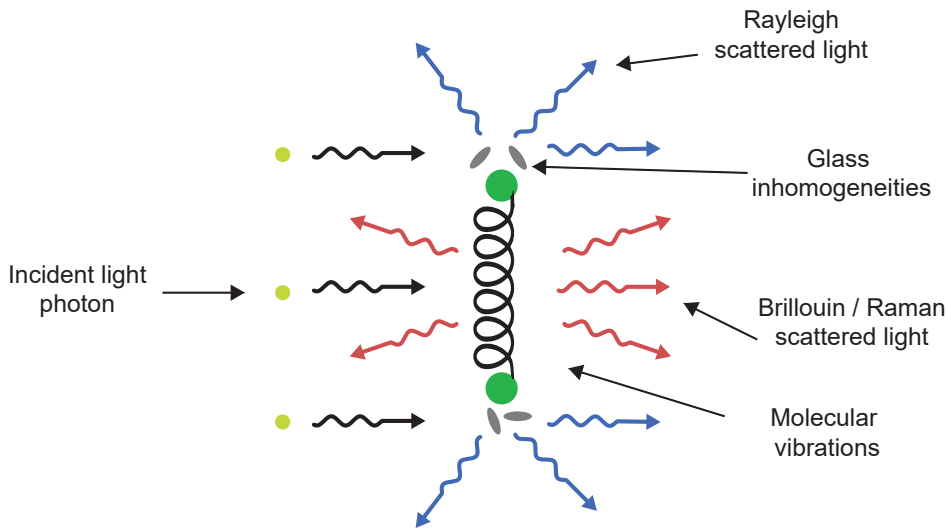


Fig. 2.1. Representation of scattering mechanisms (elastic and inelastic). Rayleigh scattering is caused by inhomogeneities in the fiber. Raman/Brillouin scattering are caused by molecular vibrations [7].

incident light with molecular vibrations. In the former, the scattered photons are the result of the interaction of photons with acoustic waves, meanwhile, in the latter (Raman effect), the interaction is produced between photons and thermally excited molecular vibrations [7].

- **Rayleigh scattering:** Rayleigh scattering is an elastic process, thus exhibiting no energy exchange and no frequency shift, caused by random inhomogeneities present in the core of the transmitting medium. These inhomogeneities appear as microscopic refractive index variations producing the scattering of incident photons. Inhomogeneities are a particularity within the manufacturing process of optical fibers, and they appear in the glass during the cooling process of the fabrication of optical fibers. Some examples of them are density variations, compositional variations, impurities and other irregularities.

For Rayleigh scattering, it is essential that the stationary inhomogeneities have a physical size much smaller than the wavelength of the incident photons. Rayleigh scattering is described as a light scattering in all directions from the scattering center with a radiation pattern like that of an electric dipole. This effect is characterized by a decreasing intensity with increasing wavelengths, thus being the scattering stronger at shorter wavelengths. Specifically, the intensity of the

scattered light ( $I_{sc}$ ) is given by Rayleigh's formula [8]

$$I_{sc} = I_0 \frac{8\pi^4 N \alpha_m^2}{\lambda_0^4 R^2} (1 + \cos^2 \theta) \quad (2.1)$$

where  $I_0$  and  $\lambda_0$  is the intensity and wavelength of the incident light,  $\theta$  is the scattering angle,  $N$  is the number of scatterers,  $\alpha_m$  is the molecular polarizability, and  $R$  is the distance from the scatterer.

This intensity dependence with the wavelength was employed by Lord Rayleigh to explain the blue colour of the sky via the Rayleigh scattering from water molecules in the air. This is due to the fact that blue is the visible colour with the lowest wavelength, and consequently, the intensity of its scattered light is higher than the intensity of the others. Rayleigh scattering has a very interesting application in optical fibers, especially in the field of telecommunications, known as optical time domain reflectometer (OTDR). This device is a practical and very useful fiber optic test and measurement instrument that enables the measurement of attenuation profiles of long fiber optic links. It is based on the detection of the backscattered Rayleigh signal generated when a pulse is propagating through the optical fiber. The recorded signal suffers an exponential decay with distance, which is related to the attenuation that the pulse suffers during its propagation.

As previously mentioned, the other elastic scattering process is known as Mie. This type of scattering is very similar to Rayleigh, but it occurs when the size of the inhomogeneities is similar to the wavelength of the incident light. Energy pattern radiations is a main difference between them, being more pronounced for Mie in the forward direction.

- **Raman scattering:** Raman scattering is one of the two inelastic scattering phenomena present in optical fibers. It is the result of the interaction between the incident light and thermally excited vibrational modes of the glass molecules [7]. This process can turn optical fibers into broadband Raman amplifiers [9–11] and tunable Raman lasers [12], but at the same time, this scattering effect limits the performance of some multichannel lightwave communications systems due to the possibility of energy transfer between different channels [6]. When the optical incident radiation interacts with molecules, the Raman effect takes place, and consequently, part of the energy of the incident wave is absorbed, thus generating molecular vibrations. This process can be understood as an electron transition

process where the incident photon is absorbed and produces a transition from a vibrational-rotational level of the ground state to a virtual (time-dependent) excited state, followed by a transition back down to a level adjacent to the starting level. The scattered photons generated by Raman scattering are characterized by a change of energy, and therefore a wavelength shift to longer or shorter wavelengths than the incident wavelength. In this process, a simultaneous transition between two vibrational states is experienced, provoking the scattered photons to be up/down-shifted, generating the usually known as Stokes and anti-Stokes components, respectively. Anti-Stokes components are very sensitive to temperature, changing their intensity with temperature changes. This property of Raman scattering makes it perfect to be used in distributed temperature fiber sensors [13, 14].

The emission of scattered photons by the Raman effect is propagated in both directions, forward and backward, with a wide spectrum formed by many lines and separated a considerable distance with respect to the incident wavelength. Raman scattering has the particularity that it can be generated by employing any pump wavelength, but its intensity decreases when the wavelength of the incident signal increases. This intensity is expressed as follows

$$I_{sc} = I_0 \frac{N_0 \sigma_R}{(\lambda_0 \pm \Delta\lambda)^4} \quad (2.2)$$

being  $I_0$  and  $\lambda_0$ , as in the case of Rayleigh scattering expressed in Eq.2.1, the intensity and the wavelength of the pump light injected into the optical fiber, respectively. Besides,  $N_0$  refers to the population of the starting ground level,  $\sigma_R$  is the Raman cross section and  $\Delta\lambda$  the wavelength variation. The resulting intensity of Raman scattering is typically at least three orders of magnitude less than the intensity of Rayleigh scattering.

Figure 2.2 depicts the spectrum of the main types of light scattering that appear when a monochromatic wave of wavelength  $\lambda_0$  is propagating through an optical fiber. The spectrum, in which Rayleigh, Brillouin and Raman features are presented, has a certain symmetry between the optical components. As mentioned before, the light components that are shifted to higher wavelengths are known as Stokes components, and those shifted to lower frequencies are known as anti-Stokes components [5]. In the specific case that the injected light has a wavelength of  $\lambda_0 = 1550$  nm and it is propagating along a single-mode fiber (SMF), the Brillouin scattering produces a

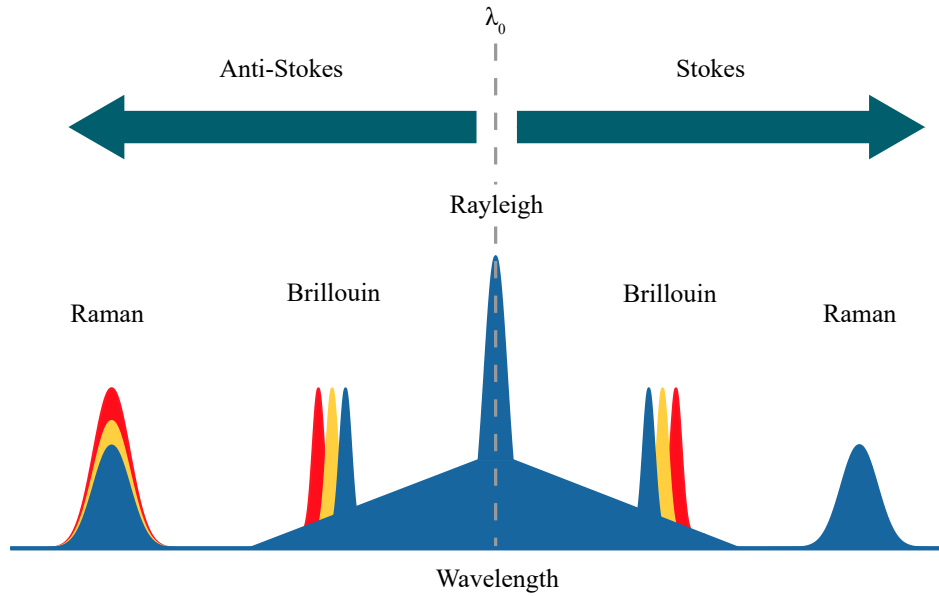


Fig. 2.2. Typical observed spectrum of the three main light scattering processes in optical fibers.

change on the wavelength of the scattered signal of about 80 pm, and in the case of Raman scattering, this shift is bigger, around 100 nm. This difference is basically based on the fact that the Raman effect is characterized by a higher energy transfer between the medium and the scattered wave. This causes the shift of the wavelength of the scattered wave to become larger.

The following sections are focused on the Brillouin scattering, the main topic of the contributions presented in Part II of this thesis dissertation. During the next sections, both spontaneous and stimulated Brillouin scattering processes will be explained in detail.

## 2.3. Spontaneous Brillouin scattering

As previously explained in section 2.1, light scattering occurs as a result of fluctuations in the optical properties of the medium. If those fluctuations are excited by thermal or by quantum-mechanical zero-point effects, the scattering process is known as spontaneous scattering. Meanwhile, if the fluctuations are induced by the presence of light, it is considered to be stimulated. In the specific case of Brillouin scattering,

it is caused by the collective acoustic oscillations of the solid matter [5]. The presence of thermally excited acoustic waves in the medium gives rise to density fluctuations in the medium, which provokes the appearance of Spontaneous Brillouin scattering (SpBS). According to the evidence that an acoustic wave is fundamental for the appearance of SpBS, it is necessary to start with the analysis of the behaviour of the acoustic wave in optical fibers to understand it. The equation of motion for a pressure wave ( $p$ ) is well-known from the field of acoustics, and it is given by [5]

$$\frac{\partial^2 \Delta \tilde{p}}{\partial t^2} - \Gamma' \nabla^2 \frac{\partial \Delta \tilde{p}}{\partial t} - V_A^2 \nabla^2 \Delta \tilde{p} = 0 \quad (2.3)$$

where  $\Gamma'$  is the damping parameter of the material and  $V_A$  is the acoustic velocity in the medium, which can be expressed in terms of thermodynamic variables as

$$V_A = \sqrt{\frac{K_s}{\rho}} = \sqrt{\frac{1}{C_S \rho}} \quad (2.4)$$

being  $\rho$  the material density,  $K_S$  the bulk modulus and  $C_S$  the adiabatic compressibility.

A simple solution for a one-dimensional propagating wave could be employed for a better understanding of the nature of the acoustic wave [15]

$$\Delta \tilde{p}(r, t) = \Delta p e^{i(qr - \Omega t)} + c.c. \quad (2.5)$$

where *c.c.* stands for complex conjugate, and  $q$  and  $\Omega$  are the propagation constant and the angular frequency of the acoustic wave, respectively. They are related by a dispersion relation of the form

$$\Omega^2 = q^2 (V_A^2 - i\Omega\Gamma') \quad (2.6)$$

This equation is easily rewritten, resulting in the following expression

$$q^2 = \frac{\Omega^2}{V_A^2 - i\Omega\Gamma'} \simeq \left( \frac{\Omega}{V_A} \right)^2 \left( 1 + i \frac{\Omega\Gamma'}{V_A^2} \right) \quad (2.7)$$

showing that

$$q \simeq \frac{\Omega}{V_A} + \frac{i\Gamma_B}{2V_A} \quad (2.8)$$

where the concept of the phonon decay rate  $\Gamma_B = \Gamma'q^2$  has been introduced. This parameter is employed to calculate the sound absorption coefficient  $\alpha_s = \Gamma_B/V_A$ . The phonon decay rate is inversely proportional to the acoustic phonon lifetime in the

medium,  $\tau_p$ , a parameter which is very important in Brillouin distributed systems given that it limits the spatial resolution of the sensor.

In order to calculate the interaction between an incident light wave and the acoustic wave, a monochromatic laser wave propagating through the optical fiber is assumed and it can be described by

$$E(r, t) = E_0 e^{i(kr - \omega t)} + c.c. \quad (2.9)$$

where  $k$  is the wave vector of the light,  $\omega$  its angular frequency, and  $E_0$  the amplitude. The scattered light satisfies the wave equation

$$\nabla^2 E - \frac{n^2}{c^2} \frac{\partial^2 E}{\partial t^2} = \frac{1}{\epsilon_0 c^2} \frac{\partial^2 P}{\partial t^2} \quad (2.10)$$

where  $n$  is the refractive index of medium,  $c$  is the speed of light in vacuum,  $\epsilon_0$  is the dielectric permittivity in vacuum and  $P$  is the polarization of the medium. According to the equation

$$P = \Delta\chi E = \Delta\epsilon E \quad (2.11)$$

the polarization of the medium is related to the fluctuation of the dielectric susceptibility  $\Delta\chi$  or to the fluctuation of the dielectric constant  $\Delta\epsilon$ . The latter can be represented as

$$\Delta\epsilon = \left( \frac{\partial\epsilon}{\partial\rho} \right) \Delta\rho \quad (2.12)$$

and, at the same time, the variation in density  $\Delta\rho$  can be expressed as

$$\Delta\rho = \left( \frac{\partial\rho}{\partial p} \right)_s \Delta p + \left( \frac{\partial\rho}{\partial s} \right)_p \Delta s \quad (2.13)$$

where  $\Delta p$  and  $\Delta s$  are the incremental pressure and entropy, respectively. The two terms of this equation refer to two different density fluctuations, the adiabatic (acoustic waves) and the isobaric (entropy or temperature fluctuations), respectively. Both terms lead to different spectral contributions of the scattered light. The first is responsible for Brillouin contribution, and the second for Rayleigh-center scattering. For the analysis of Brillouin scattering, only variations in density given by the adiabatic density fluctuations are considered. Then, applying the first term of Eq.2.13 into Eq.2.12, the resulting expression can be employed in Eq.2.11 to obtain the following equation

$$P(r, t) = \epsilon_0 \left( \frac{\partial\epsilon}{\partial\rho} \right) \left( \frac{\partial\rho}{\partial p} \right)_s \Delta p(r, t) E(r, t) = \epsilon_0 \gamma_e C_S \Delta p(r, t) E(r, t) \quad (2.14)$$

where  $\gamma_e = \rho(\partial\epsilon/\partial\rho)|_{\rho=\rho_0}$  is the electrostrictive constant, and the adiabatic compressibility is expressed as  $C_S = \rho^{-1}(\partial\rho/\partial p)|_S$ .

Finally, combining the pressure disturbance expressed in Eq.2.5 with Eq.2.9, the final expression for the polarization of the medium is obtained

$$P(r, t) = \epsilon_0\gamma_e C_S (\Delta p e^{i(qr-\Omega t)} + c.c.) (E_0 e^{i(kr-\omega t)} + c.c.) \quad (2.15)$$

The wave equation employed to define the scattered field is obtained via combining Eq.2.15 and the wave equation given by Eq.2.10, thus obtaining

$$\begin{aligned} \nabla^2 E - \frac{n^2}{c^2} \frac{\partial^2 E}{\partial t^2} = & -\frac{\gamma_e C_S}{c^2} [(\omega - \Omega)^2 E_0 \Delta p^* e^{i(k-q)r-i(\omega-\Omega)t} \\ & + (\omega + \Omega)^2 E_0 \Delta p e^{i(k+q)r-i(\omega+\Omega)t} + c.c.] \end{aligned} \quad (2.16)$$

Each one of the two terms of this expression represents one of the two different contributions: Stokes and anti-Stokes components. The first, the Brillouin Stokes, has a component with a wave vector and frequency that can be expressed with the following expressions

$$k' = k - q \quad (2.17)$$

$$\omega' = \omega - \Omega \quad (2.18)$$

On the other hand, the second term of Eq.2.16 describes the Brillouin anti-Stokes process and its wave vector and frequency can be expressed according to these other expressions

$$k' = k + q \quad (2.19)$$

$$\omega' = \omega + \Omega \quad (2.20)$$

In both contributions, the wave vector  $k$  and the frequency  $\omega$  of the incident optical field are related according to

$$\omega = |k| \frac{c}{n} \quad (2.21)$$

and the same occurs in the case of the wave vector  $k'$  and the frequency  $\omega'$  of the scattered wave

$$\omega' = |k'| \frac{c}{n} \quad (2.22)$$

In addition, according to Eq.2.8 the wave vector  $q$  and the frequency  $\Omega$  of the acoustic wave are also related by

$$\Omega = |q|V_A \quad (2.23)$$

During the scattering process, the energy and momentum conservation must be satisfied. This means that the sound-wave frequency and wave vector must each have a particular value for any scattering direction.

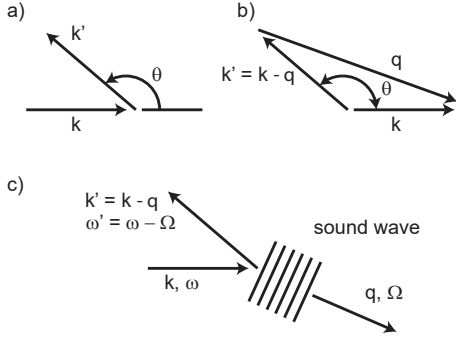


Fig. 2.3. Illustration of Stokes scattering.

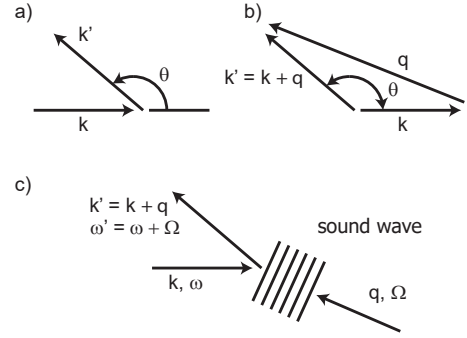


Fig. 2.4. Illustration of anti-Stokes scattering.

Both contributions of spontaneous Brillouin scattering, Stokes and anti-Stokes, are depicted in Figure 2.3 and Figure 2.4, respectively, for the case of scattering at angle  $\theta$ . Part a) of both figures shows the wave vectors of the incident and scattered fields. Meanwhile, part b) of the figures illustrates the relation between the incident and scattered optical wave vectors with the wave vector of the acoustic disturbance. The last part of these figures, c), corresponds to the different behaviour that the acoustic wave presents with respect to the incident light in both Stokes and anti-Stokes processes, respectively. In the case of the Stokes components, it can be analysed as the scattering of light from a co-propagating acoustic wave, meanwhile, in the anti-Stokes case, the acoustic wave is counter-propagating to the incident light.

Given that the frequency of the incident wave  $\omega$  is much higher than the frequency of the acoustic wave  $\Omega$ , it is possible to assume that  $|k|$  is practically the same than  $|k'|$  for both, Stokes and anti-Stokes scattering. Then, according to Figure 2.3 b) and Figure 2.4 b), the length of the wave vector of the acoustic field can be expressed as follows

$$|q| = 2|k| \sin\left(\frac{\theta}{2}\right) \quad (2.24)$$

and applying it to Eq.2.23, the acoustic frequency is given by

$$\Omega = 2|k|V_A \sin\left(\frac{\theta}{2}\right) = 2n\omega \frac{V_A}{c} \sin\left(\frac{\theta}{2}\right) \quad (2.25)$$

In the specific case that the media are optical fibers, light propagation is only possible in two directions (forward and backward) due to the fiber geometry, so the unique possible values for  $\theta$  are 0 or 180°. Consequently, and according to Eq.2.25, that relates the angle of the scattered light with the frequency shift, two main assertions can be defined: the frequency shift is equal to zero for forward scattering and it is maximized for backward propagation

$$\Omega_{max} = \Omega_B = 2n \frac{V_A}{c} \omega \quad (2.26)$$

This explains the reason why the Brillouin effect is a backscattering process, in opposition to other scattering processes such as Raman whose propagation is in both directions. This maximum frequency shift is generally known as BFS, and it is usually represented as ( $\nu_B = \Omega_B/2\pi$ ). In the specific case of a light propagating through a SMF with a wavelength  $\lambda_0 = 1550$  nm, the BFS is around 10.8 GHz.

The Brillouin components in the frequency domain are not completely monochromatic due to the finite duration of the phonon lifetime. So, the Brillouin gain spectrum,  $g_B$ , exhibits a Lorentzian spectral profile given by [6]

$$g_B(\nu) = g_0 \frac{(\Delta\nu_B/2)^2}{(\nu - \nu_B)^2 + (\Delta\nu_B/2)^2} \quad (2.27)$$

where  $g_0$  is the Brillouin gain coefficient,  $\nu$  is the optical frequency, and  $\Delta\nu_B = \Gamma_B/2\pi$  is the full width at half maximum (FWHM) Brillouin linewidth.

The peak value of the Brillouin gain spectrum is equal to the Brillouin gain coefficient when the frequency  $\nu$  is at the Brillouin frequency  $\nu_B$  of the fiber, and it is given by

$$g_0 = g_B(\nu_B) = \frac{2\pi^2 n^7 \rho_{12}^2}{c \lambda_0^2 \rho V_A \Delta\nu_B} \quad (2.28)$$

where  $\rho_{12}$  is the longitudinal elasto-optic coefficient.

## 2.4. Stimulated Brillouin scattering

As previously discussed in section 2.1, fluctuations in the optical properties of a material give rise to the effect known as light scattering. This process is considered stimulated when the mentioned fluctuations, that produces the scattering of the incident light, are excited by the presence of a strong optical field. This shows a clear contrast with the concept of spontaneous light scattering described in section 2.3, which is typically observed under low optical intensity conditions. Accordingly, the fluctuations on the optical properties of the medium are generated by thermal or by quantum-mechanical zero points effects. Stimulated light scattering is typically much more efficient than spontaneous light scattering.

SBS is a non-linear process that appears on optical fibers when the power of the injected optical field reaches a certain level known as Brillouin threshold. SBS was first observed in 1964 by Chiao et al. [16], meanwhile, spontaneous Brillouin scattering was predicted in 1922 by Leon Brillouin [17]. It was necessary the development of the laser in 1960 to enable the appearance of the stimulated Brillouin process. SBS is a non desired effect in optical communications due to the significant part of light that it is scattered, propagating in the backward direction. This produces a harmful and undesirable effect, as the signal power received at the detector is much lower when SBS is present in the link. Nevertheless, it is a very interesting phenomenon to be exploited in the field of optical fiber sensors, especially on distributed systems. The dependence of this effect on temperature and strain conditions surrounding the optical fiber makes it perfect to be employed in different sensing applications, such as structural health monitoring [18]. This non-linear effect is also commonly used for the development of fiber-based Brillouin lasers and amplifiers [19–21].

The SBS process is a non-linear interaction between the pump and Stokes fields through an acoustic wave. There are two different physical mechanisms, electrostriction and optical absorption, that enable the presence of the sound wave via the interference of the pump and Stokes waves. The first physical effect, electrostriction, can be briefly explained as the mechanism that provokes density variations in a material by means of an optical field. This effect will be explained in detail in section 2.4.1. The second mechanism, optical absorption, is not so commonly employed, given that it only appears in lossy optical media. This absorption in regions of high optical intensities produces

heat, motivating the expansion of the material in those regions. In this case, the acoustic wave needed for the SBS process is excited by the density variations of the material provoked by this absorption.

At the same time, the SBS process can be presented on two different configurations, as a generator or as an amplifier. The main difference between them is whether the Stokes signal is externally applied. In the generator configuration, only the laser pump is externally applied. Then, noise within the interaction region is responsible for the growth of both fields, the acoustic and Stokes waves. This noise is typically the scattering of the laser light from thermal phonons. As a consequence of this kind of configuration, the Stokes signal is generated at frequencies close to the one that maximized the Brillouin gain. On the other hand, the SBS amplifier configuration needs both optical fields, the laser pump and Stokes, to be externally applied with a counter-propagating direction. In this configuration, SBS produces an amplification of the Stokes wave when the frequency difference between the pump and Stokes is equal to the Brillouin frequency of the material. In the context of this thesis dissertation, this counter-propagating Stokes wave is usually known as the probe wave.

### 2.4.1. Electrostriction

Electrostriction is a physical mechanism present in some materials such as silica. It appears when a strong electric field is applied to the material and, as a result, it suffers a compression on it. From a practical point of view, electrostriction is a very interesting effect due to the following two main properties. Firstly, it is a mechanism leading to a third-order non-linear optical response; secondly, it is a coupling mechanism that leads to stimulated Brillouin scattering. To explain the origin of this effect it is necessary to analyse the behaviour of a dielectric slab when it is in the fringing field of a plane-parallel capacitor. At this situation, the slab will experience a force trying to move the slab into the region where the field strength is maximum [5].

Considering this electrostrictive force acting on each individual molecule under the presence of an electric field  $E$ , the molecule develops the dipole moment  $m = \epsilon_0 \alpha_m E$ . Consequently, the energy of the molecule is given by

$$U = -\frac{1}{2} \epsilon_0 \alpha_m E^2 \quad (2.29)$$

and the force is

$$F = -\nabla U = \frac{1}{2}\epsilon_0\alpha_m\nabla E^2 \quad (2.30)$$

The molecular displacement caused by the electrostrictive force leads to an increase in the material density in this region. As a consequence of this increase in the density of the material, its dielectric permittivity is also modified according to Eq.2.12. So, the changes in the field energy density are given by

$$\Delta U = \frac{1}{2}\epsilon_0 E^2 \Delta\epsilon = \frac{1}{2}\epsilon_0 E^2 \left( \frac{\partial\epsilon}{\partial\rho} \right) \Delta\rho \quad (2.31)$$

This change in the energy corresponds to the same work needed to compress the material. This work performed per unit volume  $\Delta w$  is expressed by

$$\Delta w = p_{st} \frac{\Delta V}{V} = -p_{st} \frac{\Delta\rho}{\rho} \quad (2.32)$$

where  $p_{st}$  is the strictive pressure,  $V$  is the volume and  $\Delta V$  its variation. It can be explained as the increase of the material pressure due to the presence of an electric field.

The electrostrictive pressure can be expressed with the help of Eq.2.31 and Eq.2.32, and with the internal equilibrium condition. It establishes that  $\Delta U = \Delta w$ , in such a way that the pressure is given by

$$p_{st} = -\frac{1}{2}\epsilon_0\rho \left( \frac{\partial\epsilon}{\partial\rho} \right) E^2 = -\frac{1}{2}\epsilon_0\gamma_e E^2 \quad (2.33)$$

It is necessary to remark that the assumed equilibrium condition is only valid if the electrostrictive energy is totally employed for the medium compression, and not for other purposes such as heating (adiabatic regime hypothesis) [22].

According to the sign of this equation, a reduction of the total pressure results in regions of high field strength. So, the medium structure tends to be drawn into these regions, and the density tends to be increased. Replacing  $\Delta p$  by the electrostrictive pressure in Eq.2.13, the variations of density now follow the following expression

$$\Delta\rho = -\rho \left( \frac{1}{\rho} \frac{\partial\rho}{\partial p} \right) p_{st} = -\rho C_S p_{st} \quad (2.34)$$

In previous equations, the electric field has been assumed to be static, but in the concerning case, the variations of the medium density are generated by optical fields, which propagating period within the medium is faster than the molecular mass displacement. In such case, combining Eq.2.33 with Eq.2.34 and replacing the electric field by the time average over optical periods denoted with angular brackets, the resulting expression is given by

$$\Delta\rho = \frac{1}{2}\epsilon_0\rho C\gamma_e\langle E \cdot E \rangle \quad (2.35)$$

As explained in Eq.2.11, the non-linear polarization of the medium is related to the changes in susceptibility through the expression  $P = \Delta\chi E$ , where  $\Delta\chi$  represents the changes in the susceptibility in the presence of an optical field. These changes are related to the fluctuations of the dielectric constant as  $\Delta\chi = \Delta\epsilon$ . Moreover, remembering Eq.2.12, where the variation of the dielectric constant is related with density fluctuations, and with the help of the expression obtained in Eq.2.35, the changes in susceptibility can be expressed as

$$\Delta\chi = \epsilon_0 C\gamma_e^2 E \cdot E^* \quad (2.36)$$

and, consequently, the complex amplitude of the non-linear polarization results in

$$P = \epsilon_0 C\gamma_e^2 |E|^2 E \quad (2.37)$$

Once the final expression of the polarization field is detailed, it is possible to obtain the coupled-wave field equations for the two optical waves present in the SBS process, pump and Stokes, taking into account the influence of the acoustic wave. For this purpose, it is necessary to use the electrostrictive pressure expressed by Eq.2.33 and the acoustic wave equation of Eq.2.3.

### 2.4.2. Stimulated Brillouin scattering induced by electrostriction

In the previous section, the physical mechanism of electrostriction has been explained. This process is necessary for the generation of the SBS phenomenon in optical fibers, given that the optical field employed as pump signal generates the acoustic wave via it. During the SBS process, a non-linear interaction is produced between the two counter-propagating optical fields, pump and Stokes, through the generated acoustic

wave. This acoustic wave is responsible of the modulation of the refractive index of optical fibers, which scatters the pump light through Bragg diffraction. This scattered light is downshifted in frequency. This shift in frequency corresponds to the Brillouin frequency shift of the medium, and it is due to the Doppler effect associated with the acoustic velocity  $V_A$  of the wave moving through the medium. To enhance the SBS process, the frequency difference between the counter-propagating Stokes and pump waves must be equal to the BFS of the medium, that in the case of SMFs is around 10.8 GHz. During the process, the intensity of the Stokes wave grows during its propagation through the optical fiber. This effect is due to the generated scattered photons of the pump wave that reinforce the Stokes wave. This enables its use as an optical amplification mechanism.

The SBS process can also be understood from the quantum-mechanical point of view. This way, it is possible to obtain a Stokes photon and an acoustic phonon simultaneously with only one pump photon. As previously mentioned in section 2.3, the energy and the quantum momentum of the three waves must be conserved [6] during the scattering process. These waves are related by

$$\Omega_B = \omega_p - \omega_S \quad (2.38)$$

$$q_B = k_p - k_S \quad (2.39)$$

where the frequencies of the pump and Stokes signals are  $\omega_p$  and  $\omega_S$ , respectively, and in the same way  $k_p$  and  $k_S$  are their respective wave vectors. The acoustic wave is represented by its frequency  $\Omega_B$  and its wave vector  $q_B$ , and they satisfy the standard dispersion relation given by

$$\Omega_B = V_A |q_B| \approx 2V_A |k_p| \sin(\theta/2) \quad (2.40)$$

where  $\theta$  is the angle between both optical signals and it is assumed that  $|k_p| \approx |k_s|$ .

### 2.4.3. Theoretical model of SBS

The non-linear process of SBS in optical fiber needs the analysis of the three waves that are simultaneously propagating through the fiber. Wave propagation only occurs in optical fibers along the axial direction, so the non-linear coupling among pump,

Stokes and acoustic waves can be modelled as a one-dimensional interaction

$$E_p(z, t) = A_p(z, t)e^{i(k_p z - \omega_p t)} + c.c. \quad (2.41)$$

$$E_s(z, t) = A_s(z, t)e^{i(-k_s z - \omega_s t)} + c.c. \quad (2.42)$$

$$\tilde{\rho}(z, t) = \rho_0 + [\rho(z, t)e^{i(qz - \Omega t)} + c.c.] \quad (2.43)$$

These three equations describe the two optical fields, pump and Stokes, respectively, and the acoustic field in terms of the material density distribution, where  $\Omega = \omega_p - \omega_s$ ,  $q = 2k_p$ ,  $\rho_0$  is the mean density in the fiber and,  $A_p$  and  $A_s$  are the amplitude of the pump and Stokes waves, respectively.

As previously explained in section 2.4.1, the stricitive pressure  $p_{st}$  is given by Eq.2.33, in this case the optical field  $E = E_p + E_s$ . The divergence of the force per unit of volume is given by  $f = \nabla p_{st}$ , knowing the expression of the homogeneous acoustic wave given by Eq.2.3, and adding the contribution of the interference of the optical fields through electrostriction in the form of a pressure source term, the acoustic wave is now expressed by

$$\frac{\partial^2 \tilde{p}}{\partial t^2} - \Gamma' \nabla^2 \frac{\partial \tilde{p}}{\partial t} - V_A^2 \nabla^2 \tilde{p} = \nabla \cdot f \quad (2.44)$$

Now, it is possible to introduce the expressions of the acoustic field detailed in Eq.2.43 and the optical fields of Eq.2.41 and Eq.2.42 into the previous acoustic wave equation, obtaining

$$-2i\Omega \frac{\partial \rho}{\partial t} + (\Omega_B^2 - \Omega^2 - i\Omega \Gamma_B) \rho - 2iqV_A^2 \frac{\partial \rho}{\partial z} = \epsilon_0 \gamma_e q^2 A_p A_s^* \quad (2.45)$$

where  $\Gamma_B = q^2 \Gamma'$  is the phonon decay rate.

Some simplifications can be performed to the previous equation to obtain a reduced expression. Firstly, the term that describes the propagation of phonons (the last term on its left-hand side) in the medium can be omitted. Phonons are strongly damped during their propagation, and they vanish after propagation over very short distances. This distance is typically small compared to the distance needed for any change in the optical fields to significantly vary.

The optical fields are described by the wave equation

$$\frac{\partial^2 E_i}{\partial z^2} - \frac{n^2}{c^2} \frac{\partial^2 E_i}{\partial t^2} = \frac{1}{\epsilon_0 c^2} \frac{\partial^2 P_i^{NL}}{\partial t^2} \quad (2.46)$$

being  $E_i = E_p$  for the pump field and  $E_i = E_s$  for the Stokes field. The same case occurs for the non-linear polarization, being  $P_i^{NL} = P_p^{NL}$  and  $P_i^{NL} = P_s^{NL}$  for the pump and Stokes fields, respectively.

By introducing the optical waves expressed in Eq.2.41 and Eq.2.42 into the previous optical wave equation Eq.2.46, the following equations are obtained

$$\frac{\partial A_p}{\partial z} + \frac{n}{c} \frac{\partial A_p}{\partial t} = \frac{i\omega_p \gamma_e}{2nc\rho_0} \rho A_s \quad (2.47)$$

$$\frac{\partial A_s}{\partial z} - \frac{n}{c} \frac{\partial A_s}{\partial t} = -\frac{i\omega_s \gamma_e}{2nc\rho_0} \rho^* A_p \quad (2.48)$$

To reach these equations it is necessary to take into account the following considerations: the slowly-varying amplitude approximation is made, the non-linear polarization is described as  $P^{NL} = \epsilon_0 \Delta \chi E = \epsilon_0 \Delta \epsilon E$  and the linear attenuation in the fiber is not included.

The resulting equations for the two optical fields and the acoustic wave describe the interaction between the two counter-propagating optical waves and the acoustic wave they excite. These equations can be simultaneously solved through numerical integration or analytically with some preliminary simplifications. For instance, it is interesting to solve them in some cases, such as distributed sensors based on the time domain. In this case the pump is generally pulsed, and, as a consequence, the interaction is taking place over a very short time, typically shorter than the lifetime of the phonons  $\tau_p$ , which is about 6 ns in silica [23]. Nevertheless, in most cases, the system can be analytically solved by assuming the steady-state solution.

#### 2.4.4. Steady-state solution

The steady-state conditions are applicable only if the variables of the equation system are constant in time. In this case it concerns the pump, Stokes and acoustic waves, where the partial derivatives with respect to time in their respective wave equations vanish.

Considering the simplification previously explained affecting the term which describes the propagation of phonons in the acoustic wave, and assuming steady-state

conditions so that  $\partial\rho/\partial t$  in Eq.2.45 is set equal to zero. The acoustic amplitude is given by

$$\rho(z, t) = \epsilon_0 \gamma_e q^2 \frac{A_p A_s^*}{\Omega_B^2 - \Omega^2 - i\Omega\Gamma_B} \quad (2.49)$$

This expression shows that the acoustic wave amplitude is related to the amplitudes of the pump and Stokes fields.

The same simplifications can be made to the optical wave equations Eq.2.47 and Eq.2.48. Partial time derivatives appearing in them can be also omitted under the steady-state conditions, and knowing that the frequency of pump and Stokes waves are similar, it can be assumed that  $\omega = \omega_p \approx \omega_s$ . Taking into account these assumptions in the mentioned equations, and including the acoustic wave given by Eq.2.49 in them, the coupled-amplitude equations are now expressed as

$$\frac{dA_p}{dz} = \frac{i\epsilon_0 \omega q^2 \gamma_e^2}{2nc\rho_0} \frac{|A_s|^2 A_p}{\Omega_B^2 - \Omega^2 - i\Omega\Gamma_B} \quad (2.50)$$

$$\frac{dA_s}{dz} = \frac{-i\epsilon_0 \omega q^2 \gamma_e^2}{2nc\rho_0} \frac{|A_p|^2 A_s}{\Omega_B^2 - \Omega^2 + i\Omega\Gamma_B} \quad (2.51)$$

The SBS is a pure gain process, whose gain is very dependent on the amplitudes of both pump and Stokes waves, in agreement with the obtained equations. If the intensity is defined as  $I = 2nc\epsilon_0 AA^*$ , the coupled intensity equations for the two interacting optical waves can be expressed as

$$\frac{dI_p}{dz} = \frac{dI_s}{dz} = -g_B I_p I_s \quad (2.52)$$

where  $I_p$  and  $I_s$  are the intensities of the pump and Stokes fields, respectively, and  $g_B$  is the Brillouin gain factor which it is given by Eq.2.27. Assuming the case of a constant pump intensity  $I_p$ , the previous differential equation can be solved, coming to the following expression

$$I_s(z) = I_s(L) e^{g_B I_p (L-z)} \quad (2.53)$$

where  $L$  is the fiber length.

The previous analysis has been reached under the assumption that light does not suffer any loss during its propagation through the medium. However, the fact is that when light is propagating through optical fibers, it has an attenuation that could not

be neglected, especially for long distances. In the specific case of distributed sensors based on Brillouin scattering, the pump and Stokes waves typically propagate along tens of kilometres, reaching hundreds of them in some configurations. Accordingly, it is possible to rewrite the coupled equations given by Eq.2.52 taking into account the fiber loss. Given that the frequencies of both pump and Stokes waves are very close, the fiber loss are defined as  $\alpha = \alpha_p \approx \alpha_s$ , and the coupled equations are given by

$$\frac{dI_p}{dz} = -g_B I_p I_s - \alpha I_p \quad (2.54)$$

$$\frac{dI_s}{dz} = -g_B I_p I_s + \alpha I_s \quad (2.55)$$

In these equations, the pump and Stokes waves are assumed to be linearly polarized along the same direction and, in addition, their polarization state must be the same during the light propagation. Typically, the polarization state of the waves varies randomly when they are propagating along conventional fibers, except when they are polarized along a principal axis, and they are propagating along a polarization-maintaining fiber. These changes on the polarization state give rise to a reduction of the Brillouin gain by a factor of 1.5 compared to the perfect case where the pump and Stokes are completely aligned [24].

### 2.4.5. SBS threshold

An analytical solution for the previously described coupled equations is useful for a complete description of SBS, including pump depletion. For others analyses, such as the estimation of the Brillouin threshold, it is better to consider that pump depletion is neglected. This way, the intensity of the pump wave only suffers an exponential decay with distance due to the optical attenuation  $I_p(z) = I_p(0)e^{-\alpha z}$ . Employing it in Eq.2.55, and integrating over the fiber length  $L$ , it results in the expression of the intensity of the Stokes wave given by

$$I_s(0) = I_s(L) e^{\frac{g_B P_0 L_{eff}}{A_{eff}} - \alpha L} \quad (2.56)$$

where  $I_s(L)$  is the intensity of the Stokes wave at the input of the fiber ( $z = L$ ),  $P_0 = I_p(0)A_{eff}$  is the pump power at the input of the optical fiber,  $A_{eff}$  is the effective

core area, and  $L_{eff}$  is the effective interaction length that it is given by

$$L_{eff} = \frac{1 - e^{-\alpha L}}{\alpha} \quad (2.57)$$

For long fibers such as  $\alpha L \gg 1$ , it is possible to approximate it to  $L_{eff} \approx 1/\alpha$ . At  $\lambda_0 = 1550$  nm the fiber attenuation is minimum, about 0.2 dB/km, so the effective length is around 20 km.

The Stokes signal, incident at  $z = L$ , suffers amplification and attenuation during its propagation along the optical fiber as described in Eq.2.56. The first is due to the Brillouin amplification resulting of the SBS process, and it provokes the exponential growth of the Stokes signal in the backward direction. On the other hand, its intensity is also reduced due to the loss of the optical fiber.

When the Stokes signal is not fed, the case of the Brillouin generator configuration, this wave grows from spontaneous Brillouin scattering. In this process, the thermal agitation in the fiber is responsible for the appearance of the phonons that initiate the scattering effect. Another way to describe this is as a fictitious photon per mode that is injected at a distance where the gain exactly equals the fiber loss [6].

The Brillouin threshold  $P_{th}$  to generate the SBS process is given by the following expression

$$P_{th} = 21 \frac{A_{eff}}{g_B L_{eff}} \quad (2.58)$$

This power level needed for the stimulation of the scattering process is much lower than the one required for the other non-linear scattering process, the Raman effect. If the typical values for optical fibers working at  $\lambda_0 = 1550$  nm are employed here, such as  $A_{eff} = 50 \mu m^2$ ,  $L_{eff} = 20$  km and  $g_B = 5 \cdot 10^{-11} m/W$ , the Brillouin threshold will be  $P_{th} \approx 1$  mW. This low threshold value makes SBS the predominant non-linear effect in optical fibers. The predicted threshold level is an approximation, given that the effective Brillouin gain can be reduced by different factors. One of the most predominant is the state of the polarization: if the polarization of the pump field is scrambled, the SBS threshold can increase by 50% [24]. Other factors that affect the threshold are the variations in the doping levels used to make the fiber, changes in the Brillouin frequency shift along the fiber or the presence of inhomogeneities on the fiber [6].

## 2.5. Distributed sensing using Brillouin scattering

### 2.5.1. Introduction

As previously commented, sensors are very powerful and useful devices whose functionality is to convert some physical magnitudes into information that can be recorded and analysed using electronic devices. In the particular case of distributed optical fiber sensors (DOFSs), an optical fiber is used as the sensing element via scattering processes. Thousands of points can be measured along the fiber with these sensors, enabling the possibility to have a representation of the spatial distribution of the measured magnitude along large distances. This characteristic makes them perfect for some applications such as the monitoring of large infrastructures. To achieve similar results with other alternative sensing mechanisms, it would be necessary to use lots of individual point sensors to provide similar information, with all the associated inconveniences. Their assembly and subsequent analysis of the recorded data would be very complex and tedious. In distributed sensors, it is commonly employed a technique based on sending the pump signal in the form of a pulse, and, as a consequence, the backscattered retrieved signal provides information on the time domain about the different positions along the optical fiber. Once the temporal data is recorded, it is easy to translate to fiber distance via the employment of the time-of-flight technique, commonly used for example in radar systems [23]. Another great advantage of these sensors is that the optical fiber employed as the sensing element can be used at the same time for other purposes, such as in communication systems to carry optical signals [1]. This feature provides distributed sensors a strong advantage with respect to other fiber sensors due to the possibility of employing them in old fiber links previously installed with communications purposes without performing any modifications in the fiber, it would only be necessary to connect the interrogator system to the optical fiber.

The first distributed measurements were performed in 1976 by Barnoski and Jensen [25] demonstrating the concept of OTDR. Moreover, almost at the same time, Personick et al. [26] provided an expression for the signal levels that are received in these systems. Since the appearance of these contributions, the OTDR technique has been applied in optical fibers to evaluate losses, to measure their uniformity and to check their attenuation profile over large distances, trying to identify defects and performing quality controls. OTDR was one of the first applications where a phenomenon, in this

case Rayleigh scattering, previously seen as a harmful effect for communications due to the losses it produces on the optical signals during the propagation of light through the optical fiber, was turned into a very useful mechanism to be employed in the field of sensors. This approach has proved to be the general rule for the development of distributed fiber sensors.

The first distributed sensor based on Brillouin scattering appeared in 1989. This was proposed as an alternative method to the existing OTDR technique to estimate the loss along fiber optics [27]. Almost at the same time, another contribution was proposed demonstrating that this technique had a great potential in the field of sensing, employing the shift of the Brillouin frequency as a mechanism for the development of temperature distributed sensors [28]. After these first contributions, different sensor configurations were proposed demonstrating new features and improvements to the technique. Here, it is possible to highlight two of the first different contributions, one for the distributed measurement of the fiber temperature using the analysis of Brillouin scattering in the time domain [29], and the other for the distributed measurement of strain in the fiber via the Brillouin scattering [30]. Both contributions were based on the employment of the technique known as BOTDA, the main topic of this thesis dissertation. During the following years, these configurations were improved, making better sensors: more accurate, faster, capable of measuring along longer distances and more stable for field applications [23].

Distributed fiber sensors based on Brillouin scattering can be classified into two different and separated groups. This classification corresponds to the two existing physical phenomena to obtain the Brillouin backscattering signal: spontaneous Brillouin scattering or stimulated Brillouin scattering. In a simple way, it is possible to differentiate them paying attention to the number of optical waves present in the fiber under test (FUT) at the same time. In the case of SpBS based sensors, only the pump wave is injected into the fiber, meanwhile, in SBS based sensors it is necessary the presence of another counter-propagating wave, the probe or Stokes signal. When the two waves interact into the fiber, the SBS appears, and, as a consequence, the probe suffers the amplification related to the scattering of the pump. Another distinction may be applied to Brillouin distributed sensors, depending on the technique employed to obtain the Brillouin gain, and consequently, the frequency shift along the fiber. There are three main techniques: time domain, frequency domain and correlation domain. If the process is stimulated, sensors employing these techniques are known as BOTDA sensors,

Brillouin optical frequency domain analysis (BOFDA) sensors and Brillouin optical correlation domain analysis (BOCDA) sensors, respectively. On the other hand, when the process is spontaneous, the sensors are known as Brillouin optical time domain reflectometry (BOTDR) sensors and Brillouin optical correlation domain reflectometry (BOCDR) sensors.

It is worth noting that there are no spontaneous solutions based on the frequency domain. This issue has tried to be solved in this thesis with the proposal of a Brillouin optical frequency domain reflectometry (BOFDR) sensor.

During the following subsections, a brief description of the mechanism enabling the measurement of temperature and strain using the Brillouin scattering is presented. This section continues with more detailed explanations about the typical configurations of the different Brillouin sensors, especially those based on the analysis in the time domain, main subject of this thesis. Finally, some typical problems exhibited by these sensors, such as the discrimination between temperature and strain when both are simultaneously present along the fiber are addressed.

## 2.5.2. Brillouin sensing principle

As previously mentioned, Brillouin scattering is a non-linear phenomenon present in optical fibers, which it is very dependent on the thermodynamic conditions surrounding the medium. This characteristic makes Brillouin scattering perfect to be employed in the development of distributed optical fiber sensors, given that changes in temperature or strain in the optical fiber imply some modifications in the behaviour of the scattering phenomenon.

As previously explained in section 2.3, the Brillouin frequency shift has a linear dependency with the acoustic velocity and the refractive index of the optical fiber as it can be seen in the following expression

$$\nu_B = \frac{2nV_A}{\lambda_0} \quad (2.59)$$

This linear dependence enables the use of Brillouin scattering for fiber sensors, as both parameters fluctuate with the environmental variations surrounding the opti-

cal fiber, modifying the BFS according to them. These variations are mainly due to changes in temperature or strain, making it possible to have estimations of these two measurands along the optical fiber via recording the changes of the BFS. Nevertheless, both temperature and strain variations have an almost equal impact on the resulting BFS value, making it very complex the process to discern whether the perturbation on the fiber is due to temperature changes or some strain has been applied to it. Although there are a few techniques capable of discerning between them, in most cases one of the two quantities is supposed to be constant, assuming that changes in the BFS are provoked by the other. The relation between the resulting BFS, the local temperature variation  $\Delta_T$  and the applied strain conditions  $\Delta_\varepsilon$  can be expressed as follows [31]

$$\nu_B(T, \varepsilon) = C_\varepsilon \Delta_\varepsilon + C_T \Delta_T + \nu_B(T_0, \varepsilon_0), \quad (2.60)$$

where  $C_\varepsilon$  and  $C_T$  are the strain (MHz/ $\mu\varepsilon$ ) and temperature (MHz/ $^\circ\text{C}$ ) coefficients, respectively, and  $T_0$  and  $\varepsilon_0$  are the temperature and strain references. These values are mainly determined by the fiber composition and external protections (coatings and jackets) [32]. Nevertheless, this equation is only valid when the temperature is not very high. Results provided by other authors suggest that the best fitting may be accomplished by means of a negative exponential when dealing with high-temperature measurements [33]. In recent years, different experimental results have demonstrated this linear dependency between the Brillouin frequency and the temperature/strain conditions surrounding the optical fiber. This is the case of Figures 2.5 and 2.6, where it is depicted the increase of the Brillouin frequency when the temperature and the strain increase, respectively. These results were obtained employing a method to measure the Brillouin gain spectrum in optical fibers via the use a unique laser source to generate both the pump and the probe waves and an external modulator to generate the needed frequency shift between them [34]. As can be observed in both figures, there is another parameter in addition to the BFS that it is also related to the variations in temperature and strain: the linewidth of the Brillouin gain. These measurements demonstrate that the behaviour of this linewidth is different when the BFS changes due to variations in temperature or when these variations are due to strain. For the former, the linewidth suffers a decrease of its value, meanwhile, when the BFS changes are due to strain, the linewidth remains constant. Additionally, the peak value of the BGS tends to increase with increasing temperatures and, on the contrary, it decreases with increasing strain. This different behaviour of these two parameters can be employed to try to distinguish between fiber perturbations provoked by changes in temperature or strain. They can be a good tool for some specific applications; however, the most relevant parameter in

the field of distributed Brillouin fiber sensors is the Brillouin frequency shift.

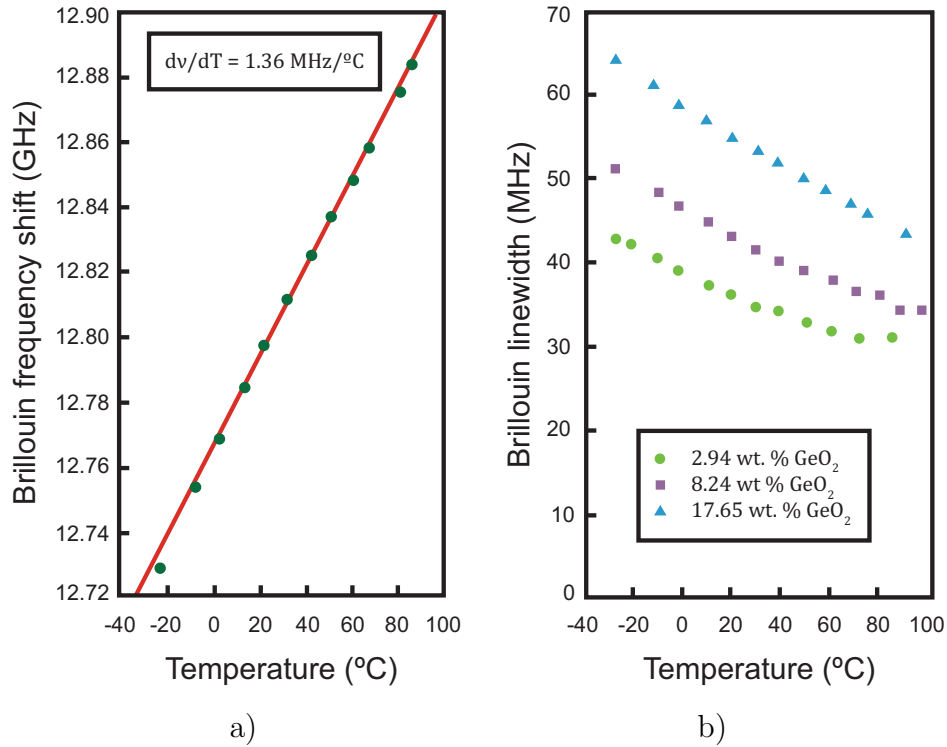


Fig. 2.5. Central frequency a) and linewidth b) of the Brillouin gain spectrum as a function of temperature. Linewidth measurements are shown for fibers with different  $\text{GeO}_2$ -core content [34].

For the specific case of the figures depicted, they show a linear dependence with a temperature coefficient of  $1.36 \text{ MHz}/^\circ\text{C}$  and a strain coefficient very close to  $600 \text{ MHz}$  per cent of elongation, both coefficients working at a wavelength of  $1.32 \mu\text{m}$ . Nowadays, BOTDA sensors typically work at  $1550 \text{ nm}$  wavelength, showing a Brillouin shift of around  $10.8 \text{ GHz}$  for SMF and a temperature and strain coefficients of around  $1 \text{ MHz}/^\circ\text{C}$  and  $50 \text{ kHz}/\mu\epsilon$ , respectively. As expressed in Eq.2.59, the BFS is inversely proportional to the injected wavelength, and according to this concept, Minardo et al. investigated the effect of Brillouin distributed sensors when the incident wavelength propagating through the optical fiber is at  $850 \text{ nm}$ . In their studies, they conclude that the Brillouin shift is nearly increased by a factor of 2 with respect to the typical shift of  $10.8 \text{ GHz}$  when working at the mentioned wavelength [35]. Not only does the BFS show this behaviour, but the temperature and strain coefficients are also affected in a similar way, showing coefficients of around  $1.99 \text{ MHz}/^\circ\text{C}$  for temperature and  $85.78 \text{ kHz}/\mu\epsilon$  for strain [36]. These studies were proposed with the idea of dealing with the

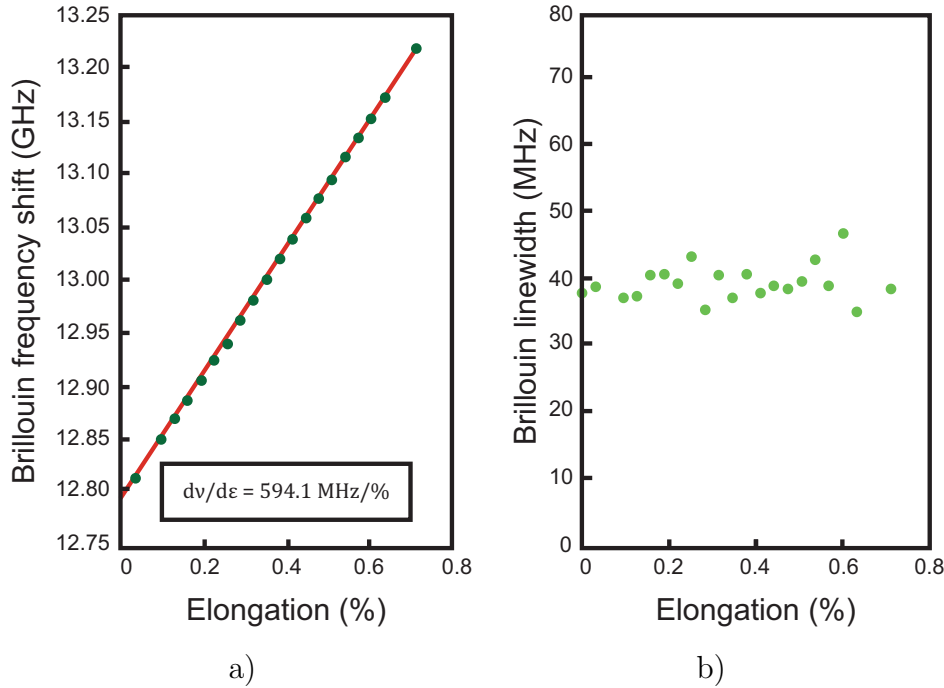


Fig. 2.6. Central frequency a) and linewidth b) of the Brillouin gain spectrum as a function of strain [34].

still unsolved problem of strain and temperature discrimination in BOTDA sensors.

### 2.5.3. Brillouin distributed sensors. Types and main characteristics

As previously mentioned, Brillouin distributed sensors can be classified according to their different properties, being one of the most recognizable categorizations whether they are based on spontaneous or stimulated Brillouin scattering. Additionally, the other most relevant characteristic to classify them is related to the domain employed to retrieve the variations on Brillouin frequency shift along the optical fiber, i.e. temperature or strain variations. In this regard, three different domains are employed to acquire the backscattered Stokes wave: correlation, frequency and time domains. According to these two main classifications, five different fundamental optical setups appear to describe Brillouin distributed sensors: BOCDR and BOTDR when the employed scattering phenomenon is spontaneous, and BOCDA, BOFDA, and BOTDA when it is stimulated. A brief description of all of them will be detailed in the following, with a special focus on the last one, the BOTDA sensor, given that it is the

predominant technique employed to perform the contributions that appear in this thesis.

### **2.5.3.1. Brillouin optical correlation domain analysis**

The first sensors based on the correlation domain were proposed by Hotate et al. in 2000 [37]. These sensors employed a sensing technique that had a great advantage over other Brillouin sensing technologies known at that moment. It enabled the possibility to perform distributed measurements of temperature or strain with very high spatial resolutions, in the order of tens of centimeters ( $\sim 40$  cm in the first proposal made by Hotate) over short optical fibers. Nowadays, this technique has been developed, improving their final performance to the point of achieving spatial resolutions of 1.6 mm [38]. This new typology of distributed sensors based on stimulated Brillouin is known as BOCDA, and, in addition to the previously mentioned advantage of the high spatial resolution, these sensors have other useful features such as sampling speeds in the kHz range, random accessibility to arbitrary multiple points, and discriminative and distributed measurement of strain and temperature [39]. Their working principle is based on the selective generation of the SBS effect at a specific position along the optical fiber. This is achieved by means of the control of the interference properties between the continuous waves propagating through the optical fiber, pump and probe. In agreement with this, to scan the different positions along the fiber it is necessary to generate the SBS effect progressively in all points of the fiber. This is solved by manipulating the modulation frequency of the continuous waves employed to stimulate the scattering process [40].

To generate the SBS in optical fibers, BOCDA sensors use two counter-propagating signals, pump and probe, that are identically frequency modulated with a frequency difference near the Brillouin frequency shift of the fiber. The modulation signal applied to the laser must be a periodical signal, such as a sinusoidal function, in order to achieve the position selective nature of the generated SBS along the fiber [39]. These selected positions where both counter-propagating waves have a constant frequency difference are known as “correlation peaks”. At these points, the SBS process appears enabling the energy transfer between the pump and the probe waves, but only if they are correctly frequency-shifted by the BFS of the fiber. The resulting spatial resolution of the sensor is defined by the width of these correlation peaks. On the other hand, the frequency

difference between both waves in the remaining positions of the fiber fluctuates faster than the time required to excite the acoustic wave, and therefore, the appearance of the Brillouin gain effect is not achieved. Then, it is necessary to sweep the frequency difference between the probe and the pump around the BFS of the fiber to obtain the full Brillouin gain spectrum at the correlation peak. Due to the periodic nature of the modulation waveform employed, multiple correlation peaks could appear in the fiber at the same time making it impossible to extract the BFS. So, the correlation peak interval defines the measurement range of the sensor. This operation principle is explained in Figure 2.7, where the mechanism that enables the appearance of the correlation peaks along the fiber and the effect when the waves are not correlated is depicted. According to this explanation, to perform distributed measurements along the optical fiber it is necessary that the correlation peak moves from one end of the fiber to the other to scan the BGS consecutively in all the points. This analysis is easily performed first by sweeping the modulation frequency of the signals, getting them correlated in other positions, and once the correlated peak is selected, sweeping the pump-probe frequency difference to scan the BGS at each one of the mentioned locations [40].

As mentioned at the beginning, the most remarkable feature of this kind of sensor is the high spatial resolution that it can reach, higher than those offered by other techniques. Nevertheless, this carries some limitations or weaknesses, such as the high associated measuring time or the maximum fiber length that it is possible to scan. The first is directly proportional to the chosen spatial resolution and also the fiber length, the smaller the resolution and the longer fibers, the larger is the time needed to scan the BGS in all the consecutive correlated peaks. Regarding the second parameter, there must be a trade-off between the total length of the sensing fiber and the chosen spatial resolution, given that only one correlation peak can appear in the fiber at the same time. This is the reason why the length of the fiber must be shorter than the distance between two correlative correlation peaks [2]. Some approaches have been proposed to solve this issue, such as the employment of temporal gating schemes to select only one localized position, reaching distributed measurements over 1 km with a spatial resolution of 7 cm [41]. To summarize the main characteristics of BOCDA sensors, it can be said that they are capable of performing distributed measurements with spatial resolutions in the order of mm and with measurement speeds in the kHz range. Also, it is important to highlight the random accessibility that BOCDA sensors have to measure at arbitrary multiple points along the fiber.

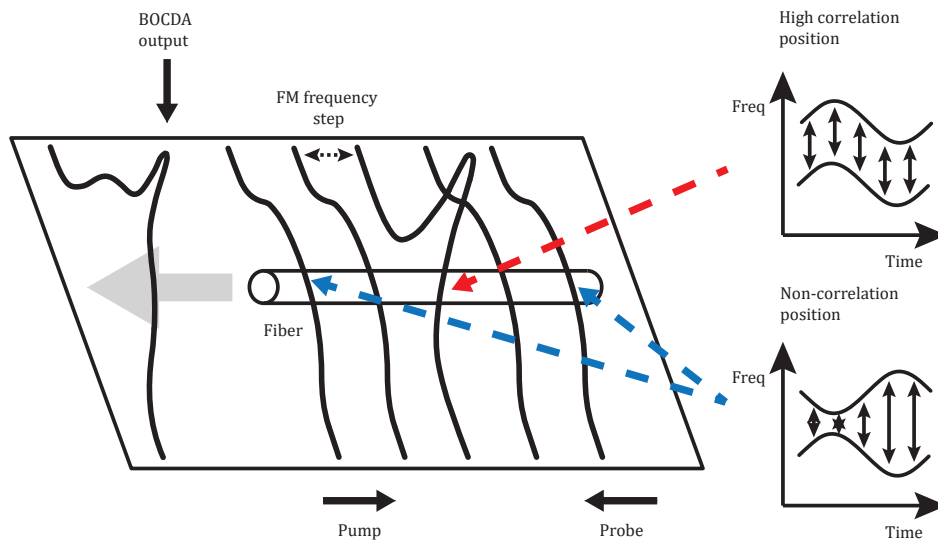


Fig. 2.7. Operation principle of BOCDA sensors [40].

### 2.5.3.2. Brillouin optical correlation domain reflectometry

An alternative method also based on the correlation domain appeared some years later than the first proposal of a BOCDA sensor: the BOCDR sensor, also proposed by the same research group that originally proposed the first BOCDA implementation [42]. The main difference between these two approaches is that BOCDR is based on the measurement of the generated spontaneous Brillouin scattering, rather than in the stimulated one. This feature makes BOCDR sensors to exhibit a significant advantage in comparison with BOCDA: it is possible to employ Brillouin sensors to perform distributed measurements over fibers where only one end is accessible. Their working principle is similar to other Brillouin sensors, the light of a laser source, typically a distributed feedback (DFB) laser used as a frequency tunable light source, is divided into two branches. One is employed as a pump wave, which is launched into the accessible end of the FUT, and as a consequence, a Stokes backscattered signal is obtained due to the spontaneous Brillouin scattering caused along all the fiber. The light of the other branch is used as a reference signal, and it is mixed at the output of a coupler with the Stokes signal to obtain the interference between the back-scattered generated signal and the reference. Finally, with the help of a photodetector and an electrical spectrum analyzer (ESA), the beat frequency between the Stokes and the reference signal is measured [39]. This kind of implementation has an identical

behaviour as BOCDA sensors. The final signal detected with the ESA is position-selective, so it is necessary to scan all positions of the FUT to perform distributed measurements. This is done through the modulation of the laser frequency so that the generation of successive correlated peaks along the fiber is obtained. Sweeping the frequency modulation of the laser, the Stokes signal generated through SpBS at a unique position is highly correlated with the reference, causing the beating of the signals. At this situation, the frequency difference between the Stokes signal and the reference is constant and equal to the BFS of the fiber at that location. Meanwhile, the rest of the fiber positions, the non-correlated ones, are in the opposite situation. There is no frequency synchronism between the Stokes backscattered signal and the reference since the frequency difference fluctuates too much, therefore the resulting beating signal has a broadened spectrum. This working principle is depicted in Figure 2.8, where both the detection (left side) and not detection (right side) of the mixed signals are explained [40]. According to this, the value of the BFS along the FUT can be retrieved by measuring the peak frequencies of the resulting spectra acquired with the ESA in the correlative selected positions.

Applying small variations to the original setup presented by Mizuno et al. [42], it is possible to improve the basic features of these sensors. For example, Manotham et al. proposed reducing the background noise spectrum by applying an additional intensity modulation to the laser synchronized with the frequency modulation (FM). As a consequence, this modification in the setup provokes the improvement of the spatial resolution of the sensor, and also a huge increase of the dynamic range in the strain measurement, reaching 10 mm of spatial resolution, and about 7000  $\mu\epsilon$  of strain dynamic range, respectively [43]. Moreover, as happens in BOCDA, it is possible to apply temporal gating schemes to increase the measurement range of these sensors, solving the existing trade-off between spatial resolution and measurement range. In this way, distributed strain measurements employing a sampling rate of 50 Hz have been performed, reaching spatial resolutions of 66 cm along 1 km long fibers [44]. Using this same sampling rate of 50 samples/s, another contribution to the development of BOCDR has achieved the measurement of the BFS along a 3 cm long fiber with a 13 mm spatial resolution [45], being at that moment the highest spatial resolution obtained by a Brillouin distributed sensor based on spontaneous scattering.

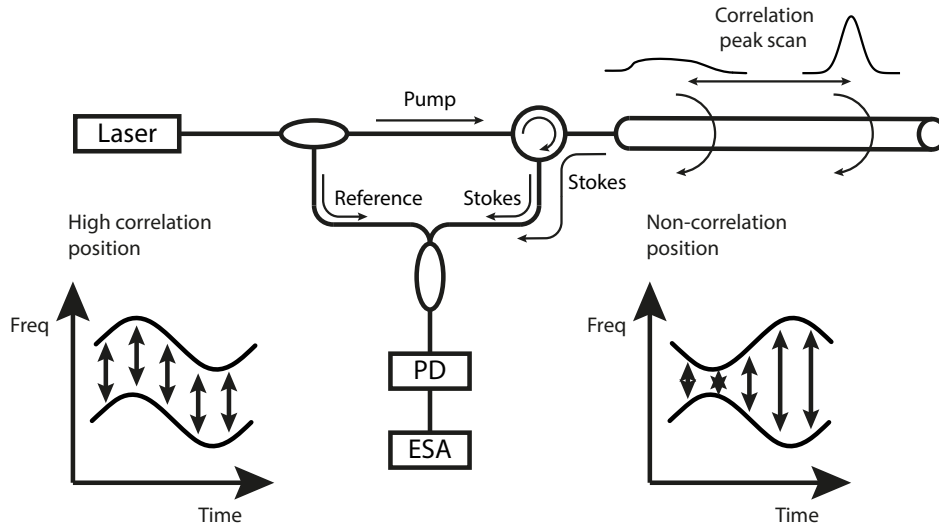


Fig. 2.8. Conceptual setup of BOCDR sensor [40].

### 2.5.3.3. Brillouin optical frequency domain analysis

The first proposal of a Brillouin-based distributed sensor not based on the time domain to retrieve the Brillouin frequency shift was performed in 1996 [46]. This alternative method to the well-known BOTDA sensor employed to perform distributed measurements was based on the analysis of the SBS generated in the frequency domain. In agreement with the previous nomenclature, it was named as Brillouin optical frequency domain analysis. This kind of sensors rests on the measurement of a complex baseband transfer function of the fiber given by the relation between the amplitudes of the two optical waves involved in the SBS process along the fiber length. Explaining this working principle in a more detailed way, these sensors also employ two counter-propagating signals, a pump signal and a probe wave frequency-shifted around the BFS of the fiber, as it happens in the sensors based on the time domain analysis. The main difference lies in the fact that in this approach the pump is a continuous wave rather than pulsed, and the amplitude of the shifted probe is modulated by a sinusoidal function. The fact that both Stokes and pump signals are continuous waves promotes a stationary acoustic wave. This implies that the linewidth of the Brillouin gain keeps its natural linewidth of 30 MHz during all the process accomplishing a higher accuracy in the BFS determination [47]. After the interaction between both signals, the resulting optical signal is converted to the electrical domain via the action of two photodetectors. Then, the resulting wave is acquired with a network analyzer. Once this operation is

finished, as happens with the other Brillouin based distributed sensors, the frequency difference between the probe and pump waves must be swept around the BFS of the fiber to acquire the remaining transfer functions. To enable the analysis of the distributed measurement performed, it is required to obtain the BGS at each location, i.e. it is necessary to apply the inverse Fourier transform to the retrieved baseband transfer function of the sensing fiber.

In comparison with traditional BOTDA sensors, BOFDA exhibits an important advantage. This is the possibility of narrow-band operation. This is because the previously mentioned baseband transfer function employed in BOFDA is determined point-wise for each modulation frequency. This means that the network analyzer only has to measure a single frequency component with a narrow resolution bandwidth at each time. Meanwhile in BOTDA, to resolve the rising time of pulses (several nanoseconds), broadband measurements are necessary [22]. Another advantage of these sensors is their high spatial resolution, resolving spots in the order of centimeters when distributed measurements are carried out [48]. In these sensors, the spatial resolution and the maximum measuring range are completely related to the signal employed to modulate the pump wave [49, 50]. According to this, the spatial resolution of the system, expressed as  $\delta z$ , can be calculated using the following equation

$$\delta z = \frac{c}{2n} \frac{1}{f_{max} - f_{min}} \quad (2.61)$$

where  $f_{max}$  and  $f_{min}$  denote the maximum and minimum modulation frequencies, respectively. Another relevant parameter of these sensors is the modulation frequency step  $\Delta f_m$ , which determines the maximum measuring range  $L_{max}$  according to

$$L_{max} = \frac{c}{2n} \frac{1}{\Delta f_m} \quad (2.62)$$

On the other hand, these systems show some drawbacks that are not present in conventional time domain based sensors, or at least are not so limiting. The most relevant is related to the excessive time needed to perform distributed measurements. To obtain the BFS with a high spatial resolution it is necessary to acquire the baseband transfer function with a large range of frequencies. Moreover, the frequency steps employed to cover all the selected frequency range can not be very long since this would reduce the full length of the sensing fiber. Both situations increase the required measuring time. This implies that during this time temperature and strain conditions

around the fiber must be constant; otherwise, measurement errors may appear when the BFS is calculated [22]. Apart from this factor, these sensors have another problem introducing errors in the final estimation of temperature or strain. When the pump and the modulated component of the acoustic field interact, some artifacts appear in the acquired BGS. This unwanted behaviour is remarkable when the BFS along the fiber is not completely uniform, introducing a detrimental effect leading to a loss of spatial resolution that reduces the accuracy of the sensors [47]. Nevertheless, this loss of spatial resolution can be mitigated with the help of processing algorithms. Bernini et al. experimentally demonstrated the capacity of BOFDA sensors to perform distributed sensing at 29 mm spatial resolution using an algorithm. This is employed to mitigate the negative effect that the presence of artifacts in the measurements causes in the final correct determination of the BFS along the fiber [48]. This algorithm enables a more accurate reconstruction of the BFS via filtering out the spurious effects associated with acoustic wave modulation employing an iterative method that corrects the acquired data.

As mentioned before, the high spatial resolution of these sensors is a good feature; however, the sensing range was limited to not very long distances. Until recently, BOFDA sensors had only been successfully tested over distances of about 5 and 11 km [51–53]. But in recent times, new implementations of BOFDA sensors have been proposed to overcome this sensing limitation. This is the case of the studies of Kapa et al., in which in a first approach they demonstrated a sensor capable of monitoring temperature and strain along 63 km using a fiber loop of 100 km with an accuracy of 5.8 °C and a spatial resolution of 26 m. In that work, they could measure a 100 m hot spot (37°C) located at 51.7 km without needing the use of image processing or Raman amplification [54]. The experimental setup employed to extend the sensing range is depicted in Figure 2.9.

The same researchers also proposed an improvement to their previous work, reaching 100 km of sensing range using a 200 km fiber loop. They have obtained these results by implementing distributed Raman amplification (DRA) and a digital high-pass filter. Applying these modifications over the experimental setup described in Figure 2.9, they have detected temperature changes of 5°C with a spatial resolution of 12.5 m over sensing distances of 75 km. Additionally, they have been able to measure a temperature variation of 30°C at a distance of 99.5 km with the same previous spatial resolution [55].

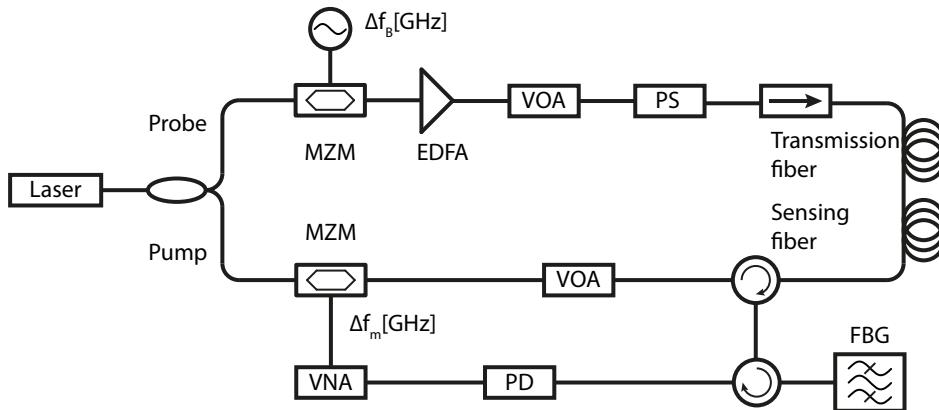


Fig. 2.9. Experimental setup of a BOFDA sensor [54].

#### 2.5.3.4. Brillouin optical time domain reflectometry

The first approach of a distributed sensor based on SpBS was proposed in 1993 [56]. Basically, BOTDR sensors worked launching an optical pulse into the sensing fiber and measuring the frequency shift of the backscattered Brillouin signal with a coherent self heterodyne detection system. The measuring method of these sensors works in a similar way to the conventional OTDR technique, although the employed setup is a little more complicated. In this first approach, the Brillouin spectrum profile of a 10 km long fiber was measured using a spatial resolution of 100 m. Being a sensor based on SpBS, the probe wave is not externally generated and launched into the other end of the fiber. Rather than this, the interaction of the pump with thermally excited phonons generates the Stokes wave, as explained in section 2.3.

The working principle of these sensors, depicted in Figure 2.10, is based on launching a pump to one end of the fiber, then, through SpBS a Stokes wave is generated. The pump is a pulsed wave that defines a very short Brillouin interaction wave and whose temporal width fixes the spatial resolution of the sensor. Typically, the chosen width is around a few tens of nanoseconds, being the minimum width employed around 10 ns due to the existing limitation of the phonon lifetime present in Brillouin scattering processes, driving to a minimum theoretical spatial resolution of 1 m. This limitation has a detrimental effect on the final performance of sensors based on the time domain [6]. While the pump is propagating from one end of the fiber to the other and interacting with thermally excited phonons, the generated Stokes wave is back-propagating in the opposite direction. So, with the employment of a photodetector, it is possible to

monitor at the accessible end of the fiber the backscattered signal as a function of time that is generated at each point along the fiber by the pump through SpBS. At this point, it is important to notice that, as mentioned before, this sensing mechanism is very similar to the one used in OTDR systems, being the difference between them that in BOTDR the measured signal is the backscattered Stokes wave, meanwhile in OTDR it is the backscattered Rayleigh wave. This provokes that a filtering strategy must be considered to avoid the simultaneous measurement of both waves. The resulting monitoring signal has a frequency shift with respect to the frequency of the launched pump, giving information about the BFS at each location of the fiber [57, 58].

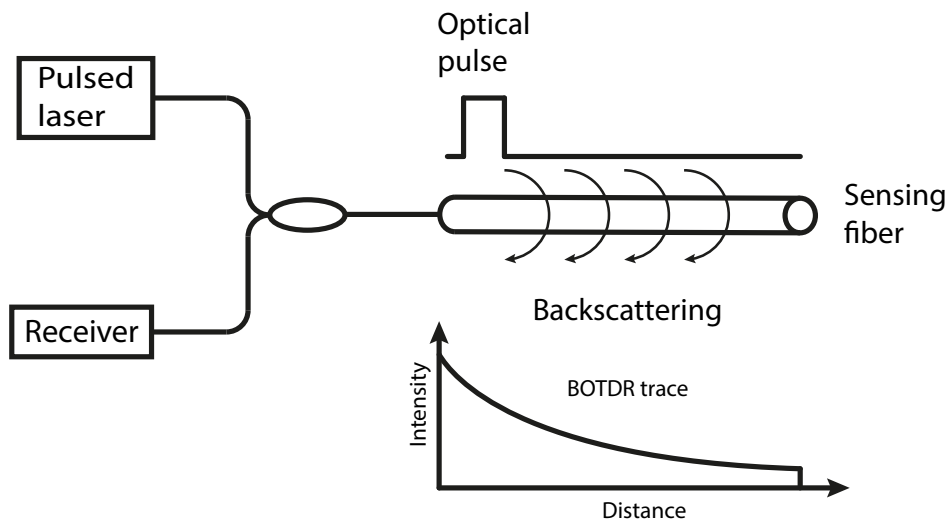


Fig. 2.10. Operation principle of BOTDR sensors [58].

Since the first appearance of BOTDR sensors, two different main approaches have been proposed by researchers. The first is known as BOTDR sensors based on the Landau-Placzek Ratio (LPR) [59]. This approach is based on the use of the OTDR technique in addition to the simple direct-detection of the Brillouin backscattered signal to measure the total SpBS intensity versus distance. Once the Stokes intensity is measured, the variations in temperature or strain of the distributed profile along the fiber are retrieved by quantifying the relative changes in the Stokes intensity at each fiber location [58, 59]. On the other hand, the second approach scans the SpBS spectrum via the measurement of the different BOTDR traces related to the different SpBS spectral components. So, in contrast to the LPR approach, the spectrum of SpBS is measured, rather than its intensity. These measurements are acquired via the employment of an optical coherent detection scheme in addition to the use of electrical demodulation [56, 60]. Using this measurement technique, a full map of the SpBS

spectral shape for each position of the fiber is obtained, enabling the extraction of the BFS distributed profile via the fitting and analysis of the measured Brillouin gain spectrum at each fiber position.

In comparison to other Brillouin distributed sensors, BOTDR systems have some advantages. The main advantage might be the possibility of performing distributed measurements accessing only one end of the fiber, enabling their use in applications where both ends of the fiber are not available. An additional advantage is the simplified setup needed to make measurements, being less complex than other solutions such as the setups employed in BOFDA or BOTDA sensors. Nevertheless, these sensors show some limitations that limit their use. In addition, as these sensors are based on the spontaneous Brillouin scattering, where the interaction required to give rise to the Stokes wave is made between the pump and the thermal phonons, the generated backscattered Stokes wave is very weak and noisy. Accordingly, the SNR is not very high, resulting in sensors with low performance. This is the reason why this implementation is less extended than other sensors such as conventional BOTDA sensors.

To overcome these disadvantages, some advanced configurations have been proposed over recent years to improve their final performance [2]. Most of them are focused on increasing the backscattered Stokes wave, which implies an increase of the SNR, and, as a consequence an increase in the final performance of the sensor [61]. For instance, solutions based on different amplifying strategies have been developed. Wang et al. proposed to add a pumped Erbium-doped fiber amplifier (EDFA) in the sensing fiber to extend the sensing distance [62]. In this study, different pump power and direction of EDFA were employed to analyze the performance of BOTDR sensors. They concluded that the dynamic range and the BFS estimation of BOTDR with backward pumped EDFA were better than using forward pumped EDFA, achieving experimental results showing a temperature error of 0.5°C using a spatial resolution of 10 m over a 80 km long sensing fiber [62]. Another proposal based on amplifying strategies is the employment of Raman distributed amplification [63]. It is well known that during their propagation, both the pulsed light and the Stokes wave become weaker as the sensing fiber goes farther. An unidirectionally pump Raman amplifier is adopted to overcome this. In general, an optical fiber Raman amplifier produces a distributed gain along the fiber that compensates the losses suffered by a given wave. In this case, the Raman pump, introduced before the sensing fiber, provokes

an amplification of both the pulse pump and the backscattered Stokes wave during its propagation through the optical fiber. This implies an increase in the sensing range of the sensor. With this experimental configuration, an enlargement of the sensing range was demonstrated, reaching a distance of 100 km with a temperature resolution of  $\pm 3^\circ\text{C}$ . Other proposed solutions are based on the use of coding techniques, such as the use of Golay complementary sequences that improves the measured SNR without introducing detrimental effects in the spatial resolution [64]; or the application of post-processing techniques to improve different features of the sensors, such as the iterative subdivision algorithm that improves considerably the spatial resolution [65]; or the fast digital envelope detection method that improves the existing trade-off between the sensor accuracy, the spatial resolution and the measurement speed [66].

#### **2.5.3.5. Brillouin optical time domain analysis**

Since the appearance in 1989 of a primitive distributed sensing technique that employed stimulated Brillouin scattering in schemes based on the time domain, Brillouin optical time domain analysis has remarkably evolved to the point of achieving great performances in many different applications. This first proposal was initially employed to measure the optical fiber attenuation [27], and shortly after that to calculate the temperature [28, 29] and strain [30] variations via retrieving the Brillouin frequency shift along the fiber in the time domain. During the last 30 years, these sensors have been widely studied, leading to the appearance of different proposals and developments trying to increase their final performance. These solutions usually have the main objective of improving some of the features of these sensors, such as their spatial resolution, sensing distance or measuring time. As a consequence of these researching efforts, BOTDA is nowadays the Brillouin-based technique most employed in distributed sensing, allowing temperature and strain distributed measurements with around 1 m of spatial resolution over tens of kilometers of sensing fiber. These systems are usually employed in different fields such as pipeline leakage detection [67]; structural health monitoring of bridges [68]; geotechnical monitoring [69] or railway traffic monitoring [70].

The operation principle of BOTDA sensors, depicted in Figure 2.11, is based on the measurement of the Brillouin scattering generated through the interaction that takes place in the optical fiber between a pulsed pump wave and a counter-propagating

continuous wave. This continuous wave is usually referred to as probe or Stokes wave, and it is frequency shifted around the BFS of the fiber.

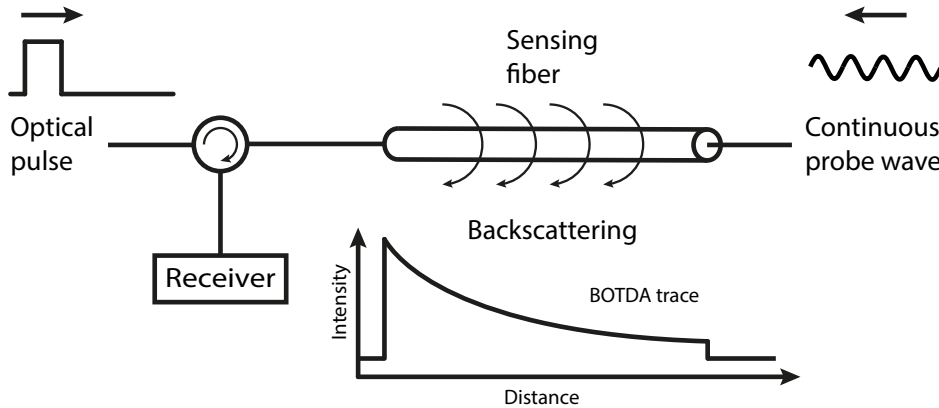


Fig. 2.11. Operation principle of BOTDA sensors.

When the pulsed pump and the probe are in the same position of the fiber, an acoustic wave is locally generated at that point. The specific characteristics of this acoustic wave will depend on the fiber location where both optical waves have met. When the three waves are present in the fiber at the same location, an energy transfer happens. At this scenario, two possibilities appear: the probe wave can receive energy from the pump (amplified probe) or in the other case, it can transfer energy to the pump (depleted probe). This is determined by the optical frequency difference existing between the two optical waves. This principle is depicted in Figure 2.12, where the two possible configurations of BOTDA sensors have been represented [58]:

- Brillouin gain configuration: This is present when the optical frequency of the pump is higher than the frequency of the probe. In this case, the energy transfer occurs from the pulsed pump to the continuous probe wave. Consequently, the probe wave is amplified and, accordingly, the pump is depleted. This energy transfer is shown in Figure 2.12 a).
- Brillouin loss configuration: This represents the opposite situation: the optical frequency of the probe is higher than the frequency of the pump. As a consequence, the energy transfer happens from the continuous probe wave to the pulsed pump, so the probe wave is attenuated during its propagation due to the SBS effect. This transfer of energy is also depicted in Figure 2.12 b). This loss of the probe wave provides distributed information about the local Brillouin spec-

tral shape. According to the previous nomenclature used to refer to the BGS, this is referred to as Brillouin loss spectrum (BLS).

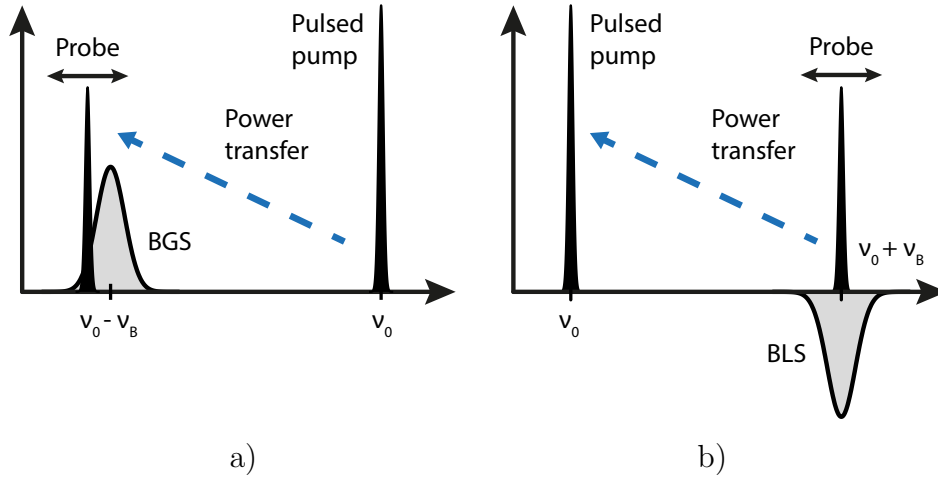


Fig. 2.12. Energy transfer between the pump and the probe in a) Brillouin gain configuration and b) Brillouin loss configuration [58].

Once the scattering effect is generated, the amplified or depleted probe wave must be detected and converted to the electrical domain to enable a future data analysis. The detection scheme used is similar to the one employed in other time domain approaches: the intensity of the continuous probe wave is recorded as a function of time. Considering the existing relation between the fiber location and the pulse time of flight given by the following expression

$$z = \frac{c}{2n}t \quad (2.63)$$

it is easy to translate the temporal trace acquired to fiber distance. This provides a distributed signal containing information along the optical fiber with a specific spatial resolution. This signal is typically known as BOTDA trace, as represented in Figure 2.13.

The mentioned spatial resolution is a sensor parameter that establishes the minimum fiber length needed to detect any temperature or strain variation. In distributed fiber optic sensors based on time domain, (e.g. BOTDA implementations), this parameter is defined by the temporal width of the employed pulse signal. Both are related through

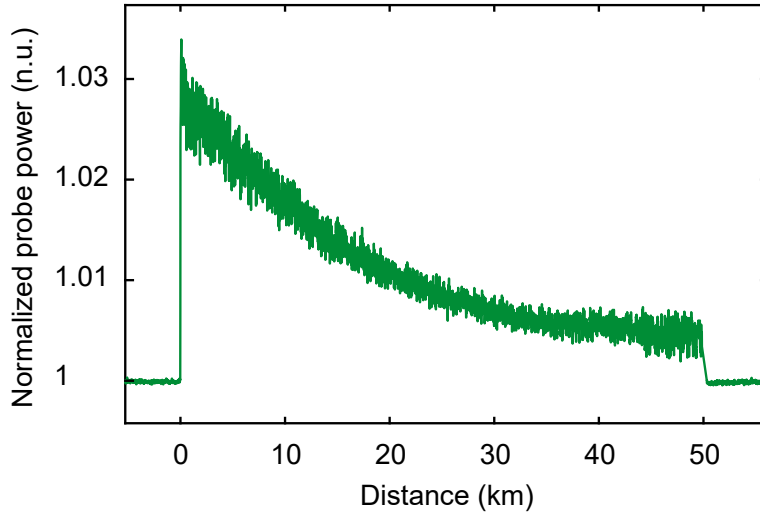


Fig. 2.13. An example of a typical normalized probe signal acquired during the frequency swept of a BOTDA sensor versus fiber length.

the following expression

$$\delta z = \frac{c}{2n} t_0 \quad (2.64)$$

being  $t_0$  the pulse width. Hence, it defines a ratio of around 1 m of spatial resolution for every 10 ns of pulse width. As happens in BOTDR systems, in conventional BOTDA schemes this time duration of 10 ns represents a limitation due to the phonon lifetime. Furthermore, in distributed sensors, it is common to experimentally estimate the spatial resolution using the 10-90% technique, establishing the spatial resolution of the sensor as the fiber distance existing between these two points. Figure 2.14 illustrates this technique, representing the real variation of temperature or strain (solid line), and the response of the sensor (dashed line). The dots over the sensor response represent the sampling interval employed during the acquisition [1].

This acquired BOTDA trace represents the gain that the probe wave suffers at different locations of the sensing fiber when the counter-propagating waves have a fixed frequency difference. The gain at each fiber position can be different depending on the local temperature and/or strain conditions surrounding the fiber. Accordingly, the acquired probe signal can also suffer some gain fluctuations at different positions. In order to obtain the full 3D map of the Brillouin gain spectrum, as illustrated in Figure 2.15, it is necessary to sweep the existing frequency difference between the

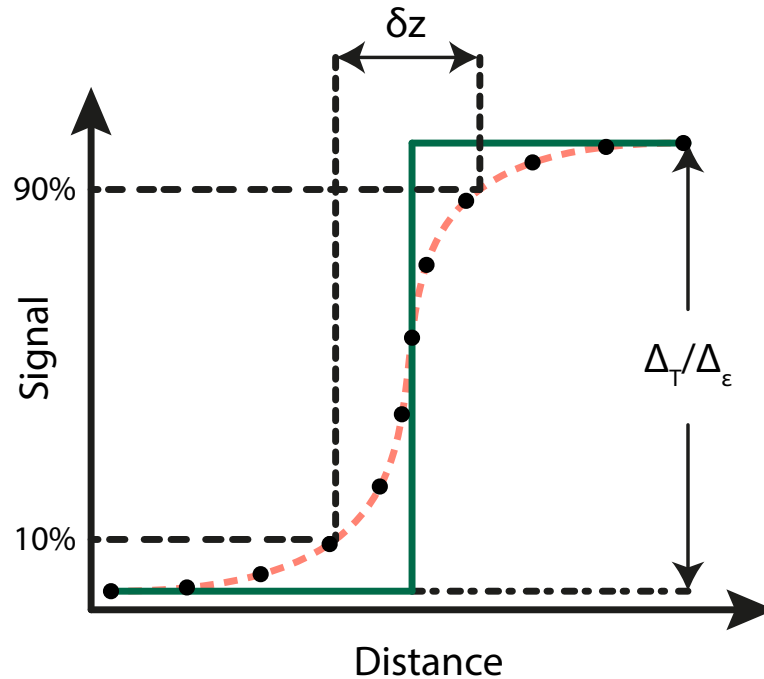


Fig. 2.14. Definition of spatial resolution of a distributed fiber sensor [1].

pump and probe signals around the BFS of the sensing fiber, and acquire the resulting time domain probe wave for each frequency offset. This swept is typically performed fixing the frequency of the pump wave and changing the frequency of the probe around the BFS of the fiber with a fixed step.

It is worth noticing that this frequency swept employed in BOTDA systems gives rise to slow measurements, making them not the best option for dynamic measurements. In general, the measurement time of BOTDA sensors is in the order of a few minutes. This also depends on other parameters, such as the fiber distance or the averaging employed, but the sensor parameters related to the frequency swept are the ones that most influence the measurement time, being the higher the number of scanned frequencies, the greater the time taken to perform the analysis.

The different monitoring requirements of the application where the sensor will be used will define the frequency steps and the range employed to perform the swept. To evidence this, two different monitoring applications where these sensors are employed can be compared: a high temperature environment where the temperature range can be from 20°C to 650°C and a leakage detection system. The first one will need to employ

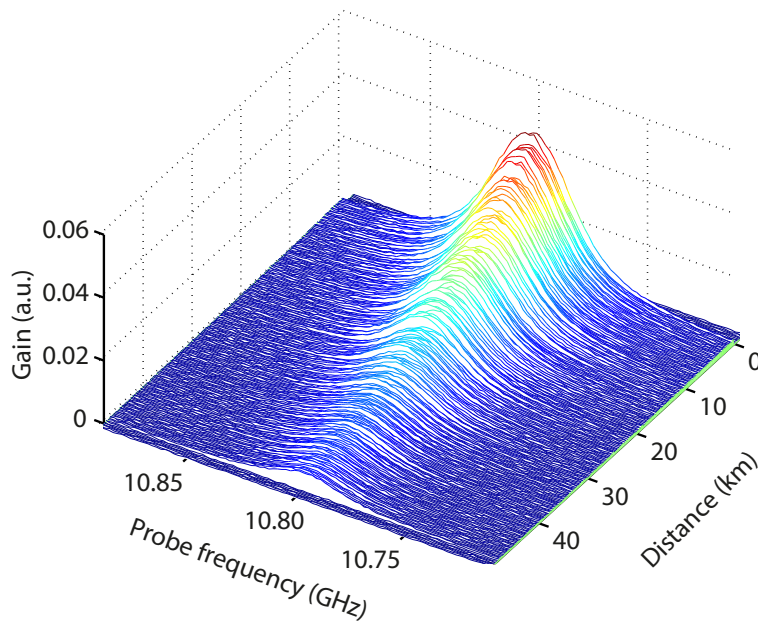


Fig. 2.15. Distributed Brillouin gain spectrum

a very wide frequency shift where lots of frequencies would be scanned; meanwhile, the number of scanned frequencies would be considerably lower in the latter, due to the measurement temperature and strain ranges.

Once the 3D Brillouin gain map is obtained, the resulting BFS for every position of the fiber must be calculated. This reconstruction is performed by applying a fitting method to the measured BGSs along the fiber. The number of BGSs obtained depends on the sampling interval employed to acquire the BOTDA traces during the measurement process, and also on the fiber distance to monitor. Figure 2.16 shows a normalized BGS obtained from the previous 3D gain map depicted in Figure 2.15 at a random fiber position. Applying a fitting processing algorithm, normally either Voigt or Lorentzian fitting [71, 72] to the measured Brillouin gain data for each one of the different positions along the fiber, the peak value of the measured data is obtained. These values are commonly known as the BFS of the fiber, and it is linearly related to the temperature and strain variations surrounding the optical fiber as expressed in Eq.2.60 [34].

As mentioned before, the first implementations of BOTDA systems appeared in the early 90s. Both those that were used to measure the fiber attenuation [27] and subsequent ones that were employed to measure temperature [28] or strain [30] variations

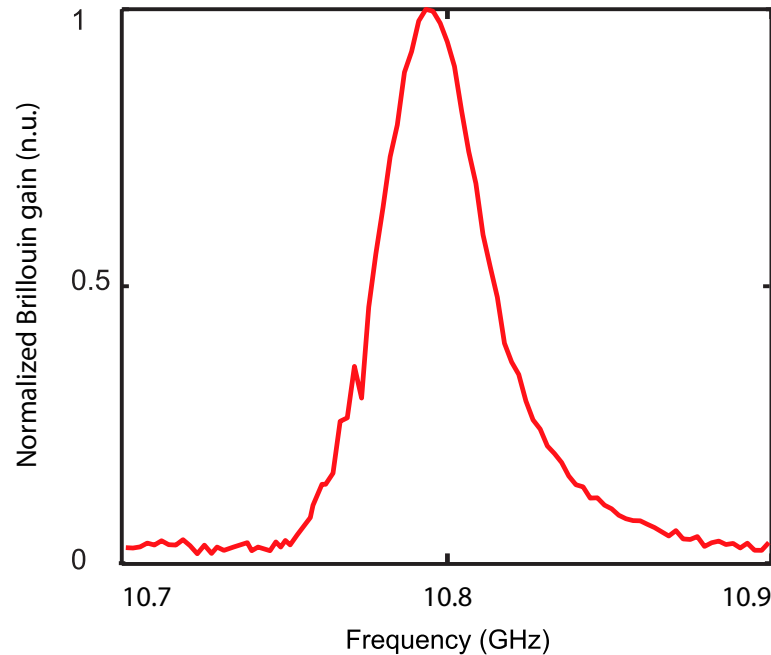


Fig. 2.16. Brillouin gain spectrum at a specific fiber position.

along the fiber shared a common characteristic. They required the employment of two laser sources to produce the two counter-propagating waves needed to generate the SBS effect. Nevertheless, this led to complex experimental setups with significant drawbacks such as the difficulty to simultaneously have the same wavelength and power stability in both lasers with the lowest possible drift, and also with accurate tunability around the BFS of the fiber [34].

A very promising implementation to avoid the requirement of using two different laser sources to perform BOTDA measurements was proposed by Nikles et al. few years later. This novel solution was a distributed Brillouin fiber sensor based on the pump-and-probe technique only employing a laser source and an electro-optic modulator to generate the required optical waves [73]. This was one of the most significant advances achieved in BOTDA techniques, as it implies a remarkable simplification in the instrumental setup with also high stability and excellent reliability. Moreover, this had the benefit of avoiding any relative error due to laser drifts. This improvement on the sensing capabilities of these sensors generated a greater interest in them, making their way to a wide market of monitoring applications. Nowadays, most of the BOTDA systems employed are based on this original setup.

This is the case of the experimental setup that has been mostly employed to perform distributed measurements during the elaboration of this thesis dissertation. It is a conventional dual-probe sideband BOTDA setup [52], as illustrated in Figure 2.17.

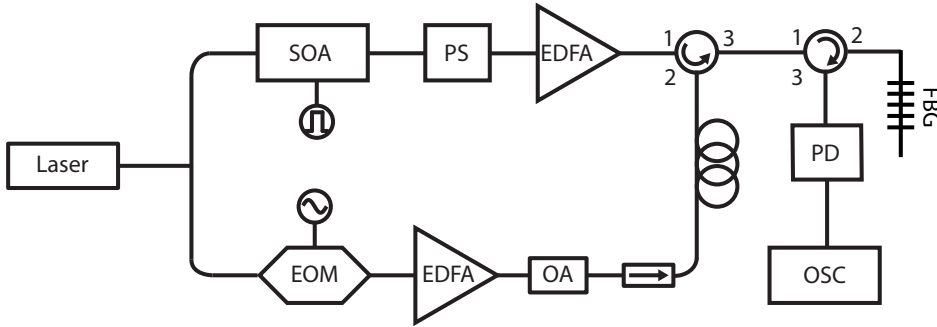


Fig. 2.17. Experimental setup of a BOTDA sensor.

The light from a narrowband laser source is divided into two separate branches to generate the two optical waves. In the setup represented in Figure 2.17, the upper branch is responsible for generating the pulsed pump wave. The continuous wave coming from the laser is transformed into a pulsed wave either by using a semiconductor optical amplifier (SOA) or an electro-optic modulator. The SOAs provide higher extinction ratios (ER) than conventional modulators, typically around 50dB. The ER of the pulsed wave have consequences on the final performance of the sensor. For instance, when a low ER device is employed, the pump wave is not only a pulsed signal, moreover, it also has a continuous wave, known as the pulse pedestal. It appears due to the leaks of the continuous wave that the pulsing device suffers. This pump wave, formed by the pulse and the pedestal, when propagating through the fiber leads to an extra amplification of the probe wave due to the interaction between the two continuous waves that introduces errors in the final measurements [74, 75]. There are other possibilities to obtain the pulsed pump wave, but their use is not extended. For instance, there is a BOTDA configuration allowing the shaping of the pump pulses in the radio frequency instead of the optical domain [76]. This technique provides pulses with 60 dB extinction ratios and also suppressing of the leakage.

As mentioned in section 2.4, the polarization state of the waves involved on the SBS process has a remarkable effect in the resulting Brillouin gain [24]. According to this, it is necessary to employ strategies to overcome this dependence. The most employed solution is the use of a polarization scrambler that continuously varies the polarization state of one of these waves. In the setup represented in Figure 2.17, the polariza-

tion scrambler (PS) is located after the SOA employed to generate the pump pulses. Therefore, each pulse is launched into the fiber with a different polarization state, producing BOTDA traces with different Brillouin gains, but once they are averaged this polarization dependence is minimized.

Once the pulsed pump signal is generated and its polarization scrambled, it is necessary to boost the peak power of the pulses by using an EDFA before the sensing fiber.

The other branch of the setup, at the bottom, represents the generation of the probe wave. This branch is responsible of the implementation of the previously mentioned frequency sweep around the BFS of the fiber. In this case, as the setup employed is based on the conventional dual-probe sideband configuration, a radio frequency (RF) generator and an electro-optic modulator are employed to generate a double-sideband suppressed carrier continuous probe wave. Then, the probe wave is launched into the other end of the sensing fiber.

The last part of the setup is the detection and acquisition stage. Once the SBS effect takes place inside the fiber, the probe wave is circulated to a filtering phase. This is typically formed by a FBG or a Fabry-Perot filter; or a wavelength division multiplexing (WDM) solution, in which one of the two sidebands is filtered out, while the other one is driven to a photodetector, enabling the recording of the BOTDA trace with an acquisition system. Depending on the acquired sideband, the BOTDA sensor can use a Brillouin gain/loss configuration, as explained in Figure 2.12 [77].

### **Techniques to improve the performance of BOTDA**

Over recent years, the research focus on BOTDA sensors has been positioned to increase their performance in different ways. The ideal performance of these sensors might be defined as a system that could obtain temperature or strain profiles with the minimum possible error, measuring the highest number of measurement points along the largest possible fiber distance, and employing the lowest possible measurement time. This should be the ideal situation in general for all types of distributed sensors, but reality is quite different for BOTDA sensors as previously commented. For instance, the sensing distance is limited by the pump and the probe powers injected into the fiber

that could drive to non-local effects or modulation instability, the spatial resolution is theoretically limited by the lifetime of the acoustic phonons and the measurement time depends on the frequency sweep and the fiber distance. All these sensor parameters affect the final performance of BOTDA sensors.

Due to the difficulty to compare the performance of two different implementations of a BOTDA sensor, a mathematical expression was proposed by Soto et al. to obtain a value enabling a better and easier comparison between them [77]. This sensor variable is known as figure-of-merit (FoM), and it provides an objective metric to evaluate the resulting performance of any Brillouin distributed sensor. This value can be obtained through an equation that considers some of the parameters of the sensor. Depending on the working domain of the sensor, time, correlation or frequency, the expression is a little different, but it can be easily adapted. The FoM of BOTDA sensors can be obtained through the following equation

$$FoM = \frac{(\alpha L_{eff})^2 \exp[(2 + f_1)\alpha L] \sqrt{\delta f \Delta \nu_B}}{\delta z \sqrt{N_{Tr} N_{Av}} \sigma_\nu} \quad (2.65)$$

being  $f_1$  a parameter that takes into account the fiber configuration. It is 0 for the standard fiber configuration and, it is equal to 1 for the fiber loop configuration, in which only the half of the total fiber length is employed for sensing. This FoM turns out to be equal to 1 for a typical commercial sensor, when the fiber distance is 30 km, it employs 1 m spatial resolution  $\delta z$ , the error on the Brillouin frequency ( $\sigma_\nu$ ) is 1 MHz, the averaging ( $N_{Av}$ ) is set to 1024, the number of employed traces ( $N_{Tr}$ ) is equal to 1, the frequency step ( $\delta f$ ) is 1 MHz, and the sensing fiber is a standard fiber with  $\Delta \nu_B = 27$  MHz and 0.2 dB/km attenuation.

This expression of the FoM is obtained employing the BOTDA theoretical model and considering the limitations imposed by other nonlinear effects such as Raman scattering [78] and also pump depletion [79]. To calculate the FoM it is necessary to estimate the error made when the Brillouin frequency shift is calculated.

This frequency uncertainty propagated when calculating the Brillouin peak gain frequency can be considered as a value that evidences the precision of a sensor, and it

can be estimated through the following expression

$$\sigma_\nu(z) = \sigma(z) \sqrt{\frac{3\delta f \Delta\nu_B}{8\sqrt{2}(1-\eta)^{3/2}}} = \frac{1}{SNR(z)} \sqrt{\frac{3\delta f \Delta\nu_B}{8\sqrt{2}(1-\eta)^{3/2}}} \quad (2.66)$$

being  $\eta$  the peak fraction level over which a quadratic least-square fitting is performed. As expressed in the previous equation, the local SNR of the trace at the peak gain frequency is directly inverse to the noise amplitude  $\sigma$  that it is here defined as a fraction of a normalized response. Here it is assumed a normalized gain response, as depicted in Figure 2.16, being 1 the response at the peak gain frequency, and 0 (absence of gain) the response at frequencies far from the central peak gain.

This expression determines the actual accuracy that BOTDA sensors have estimating the BFS, and it demonstrates the dependence of BOTDA sensors on the different measurement parameters, such as Brillouin gain linewidth, frequency scanning step and signal-to-noise ratio on the frequency error.

Analysing this equation, it can be noticed that the final performance of distributed sensors will be better if the resulting signal-to-noise ratio at the receiver is higher, or if the pair formed by the frequency sweeping step and the estimated Brillouin linewidth of the resonance is lower. Therefore, it could be possible to change some parameters of the sensor to improve its final performance, although this is not always viable. For instance, an increase in the probe or pump power implies a higher SNR at the receiver, but this also brings some other undesirable effects. The first can lead to the appearance of non-local effects and the amplification of spontaneous Brillouin scattering [79]. The latter is limited by the generation of Raman scattering and pump depletion effects induced by modulation instability [80]. The other possibility previously mentioned is to make the frequency sweeping step to be lower; however, this implies an increase in the measurement time.

Trying to overcome these mentioned undesirable effects that can finally reduce the resulting performance of these sensors, and other well-known restrictions such as the limited spatial resolution, the sensing length or the high measurement time required, lots of different solutions have been proposed since the appearance of the first BOTDA implementation. All these new approaches have the same objective: increase the BOTDA performance. To achieve it, on the one hand, there are some proposals trying to avoid

the appearance of these detrimental effects and, on the other hand, there are others that only try to mitigate their influence in the final sensor performance as much as possible. Some of the most relevant solutions proposed are going to be explained in the following.

As previously mentioned, one possibility to increase the performance of BOTDA is to have a better SNR. This can be achieved increasing the power of the probe wave injected into the fiber, but it can not be raised too high, as this would also imply the appearance of other problems such as the non-local effects and the spontaneous Brillouin scattering.

Non-local effects are a detrimental effect that implies a limitation, especially in long-range BOTDA sensors. They can be understood as an effect provoking that the measurement performed at a specific position of the fiber depends on the conditions surrounding the previous locations of the fiber. As explained before, BOTDA sensors are based on a gain process generated due to the interaction between the probe and the pulse waves. During this process, the pump pulse transfers part of its energy to the probe provoking its amplification. As a consequence, the pulse suffers a depletion during its propagation along the optical sensing fiber that depends on the power and on the optical frequency of the probe wave. If the power of the probe wave is too high, the depletion suffered by the pulse will also be higher and, consequently, it will affect the measurements, introducing errors on the estimation of the Brillouin frequency peak due to the distortion that the pump depletion provokes in the measured Brillouin gain spectra [79].

Therefore, it is a relevant effect in BOTDA sensors due to the limitation that implies in the power of the probe wave and, as a consequence, in the SNR detected at the receiver. Some techniques have been proposed to reduce or overcome this [52, 81–85]. The most employed approach to solve this issue is the implementation of BOTDA sensors using a dual-probe sideband wave [52]. By using this technique, the generated probe wave has two equally spaced frequency sidebands, the Stokes and anti-Stokes components, provoking the interaction between this probe wave and the pulse to be balanced. In this situation, the pump pulse does not suffer the previously commented depletion due to the interaction of the waves during the Brillouin gain process. Nevertheless, this technique is not completely perfect given that it can only compensate the first order of the non-local effects, but not the other distortion that the pulse wave

suffers due to both gain and loss spectra generated by the dual-probe sideband wave [86].

Other proposals to mitigate this effect are based on sectioning the fiber [81–83], such as the case of an approach that pulses not only the pump but also the probe wave providing a reduction of the effective interaction length between the waves [81]. As a consequence of a shorter interaction, the probe power can be raised leading to a better SNR without affecting the pulse. However, this technique presents a drawback: the measuring time will increase proportionally to the number of the pulses employed to generate the probe wave. Other solutions are based on the use of BOTDA configurations where the probe wave is phase modulated and the detection is RF phase-shifted [84] or to employ a scanning scheme where the frequency separation between the two probe sidebands is fixed achieving a flat zero net gain [85].

An alternative method to these proposals will be explained as a contribution of this thesis dissertation in the following chapter. It can be summarized as a new approach that employs a frequency modulated dual-probe sideband wave along the fiber that avoids the spectral distortion of the pulses.

Apart from non-local effects, pump depletion can be caused by other undesirable effects such as modulation instability (MI) [80] and Raman scattering [78]. As previously commented, the SNR can also be improved by increasing both the pump and the probe power. However, when the pump pulse power is too high, these other effects can appear and provoke the depletion of the pulses, causing a distortion on BOTDA traces limiting the resolution and the measurement range and giving raise errors in the final measurements. MI appears in optical fibers when there is an interaction between the Kerr effect, a third-order nonlinear effect, and the anomalous dispersion, leading to the generation of a train of solitons self-building from noise. At this situation, the pulse wave presents a spectrum with sidebands symmetrically spread around the initial frequency of the pulse. It has been demonstrated that MI increases with the pump power, leading to the presence of broaden sidebands around the pump frequency for higher pump powers, and consequently a higher pump depletion. This pump pulses spectral broadening can produce the suppression of the Brillouin gain at certain distances. The consequences of the MI effect on BOTDA sensors are represented in Figure 2.18. It shows the changes suffered by the BOTDA traces due to MI for different pump pulses in a 25.5 km long fiber. It can be appreciated how the gain of BOTDA traces goes

suddenly down after a certain distance, being shorter for higher pump powers [78]. This effect can be avoided using dispersion shifted fibers (DSF) with normal dispersion instead of standard SMF. This solution allows to increase the pump power above the threshold imposed by MI, but despite this Raman scattering may still appear if the pump power is too high, being its critical power 5 times larger than MI [87]. Another possibility is the employment of orthogonally-polarized pulses [88]. This technique reduces the influence of the MI effect and, additionally, the four-wave mixing present in systems employing pulses with parallel polarizations.

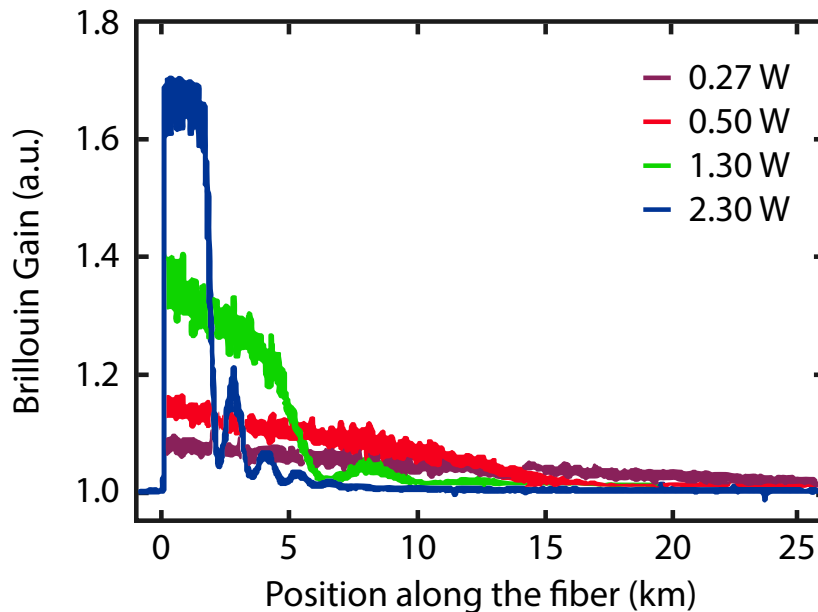


Fig. 2.18. Evolution of the Brillouin gain signal affected by modulation instability when increasing the peak pump power [78].

Not all the solutions that have been proposed to improve the SNR are based on modifications of the experimental setup. Recently, a novel processing strategy has been proposed to improve the associated SNR. It is based on the use of the high level of similitude and redundancy that the information of the measured 3D map of the Brillouin gain spectrum exhibits. Taking advantage of conventional image (2D) and video (3D) processing, the resulting SNR at the receiver is greatly increased, obtaining a good measurement contrast [89]. Based on this study, another approach has been proposed, and the performance of a BOTDA sensor that employs it has been analyzed. Here, linear and nonlinear 2-D image processings are employed over the distributed acquired measurements performed with a BOTDA sensor to eliminate the noise. Specifically, it has been analyzed the performance of the non-local means

(NLM), a nonlinear image denoising method. Using this processing technique in a conventional BOTDA, 2 m spatial resolution measurements are reached along 100 km of sensing distance over a 200 km fiber loop with a frequency uncertainty of 0.77 MHz, reaching a FoM of 222500, the highest at that moment for a conventional BOTDA implementation [90].

Other interesting points to enhance are the improvement of two fundamental parameters of distributed fiber sensors: spatial resolution and sensing distance range. In Brillouin sensors working on time domain, the first is determined by the temporal duration of the pulse, as explained in Eq.2.64. As this equation shows, shorter pulses lead to a better spatial resolution, but it is conventionally limited to 1 m due to the phonon lifetime. If the pulses employed have a duration below this, the Brillouin gain spectrum suffers a spectral broadening that implies measurement errors when estimating the Brillouin peak frequency. This is because the BGS is the result of the convolution between the natural Brillouin spectrum and the pulse spectrum. Moreover, shorter pulses also lead to shorter interactions between the waves, and consequently a lower Brillouin gain.

To get over this limitation, several solutions have been proposed giving rise to systems with high spatial resolutions. These solutions typically employ a common technique: the pre-excitation of the acoustic wave. The advantage of the pre-excitation is that the BGS does not suffer a broadening effect. The first proposal that demonstrated that it was possible to obtain distributed measurements using pulses under 10 ns was developed by X.Bao et al., employing pulses of 2 ns and measuring strain variations on a 400 mm section of strained fiber [91].

Some of the proposed techniques are outlined in Figure 2.19. Section a) shows the standard pulses employed in BOTDA sensors, in which the spatial resolution is fixed by the width of the pulse. Part b) represents a technique called dark pulse [92, 93]. In this proposal, two continuous waves are launched into the fiber so that the acoustic wave is excited all time along the fiber. At a certain moment, one of the two waves is switched off for a small interval of time, provoking the lack of Brillouin gain. Through this change on the gain, it is possible to obtain the Brillouin gain spectrum along the fiber. This interval where one wave is switched off defines the width of the dark pulse and hence the spatial resolution of the system. The third scheme, c), shows a pre-excitation technique known as pulse pre-pump [94]. Here, the pulse is composed of two clearly differentiable

parts. One is a low power long pedestal used for the excitation of the acoustic wave that it is immediately followed by the second: a narrow high power pulse. The latter defines the spatial resolution of the sensor. Finally, part d) depicts the differential pulse-width pair (DPP) technique [95, 96]. Here, two consecutive pulses with a slightly different temporal width are injected into the fiber. Accordingly, two BOTDA traces are obtained for each scanned frequency, and therefore two Brillouin gain spectra. To obtain the final measurement it is necessary to subtract both contributions. Hence, the common information is removed in the resulting new signal, remaining only the information that it is different. This subtracted signal has the temperature or strain information distributed along the fiber with a spatial resolution fixed by the temporal difference between both pulses. Among the techniques described above to increase the spatial resolution, this is the most employed. Moreover, it is possible to find it in combination with other proposals to improve BOTDA sensors, such as its use in phase BOTDA sensors [97] or in BOTDA systems with optical pre-amplification [98].

In addition to improving the spatial resolution, enlarge the sensing distance is another key point of improvement, as commented before. Typically, the sensing range of BOTDA sensors is around tens of kilometers, which allows covering a wide range of applications. However, there are some facilities that need to be monitored along larger distances, such as long pipelines or long power cables. This implies a problem for BOTDA sensors given that both probe and pump waves suffer losses during their propagation due to fiber attenuation, being higher with distance. This provokes errors in the determination of the BFS due to a very low SNR at the receiver. Moreover, as explained before, the probe power can not be as large as desired due to the associated detrimental effects [80]. Therefore, some alternative configurations have been proposed with the idea of enlarging the measuring range, increasing it above 100 km.

There are three basic different approaches to meet this goal: discrete amplification[99]; distributed amplification [21, 100–102] and pump coding[103]. The first is based on the employment of EDFAs along the sensing fiber working as discrete repeaters [99]. In this proposal a 650 km fiber loop was employed, corresponding to 325 km of sensing distance, using a repeater each 65 km. The main drawback of this type of solutions is that the employment of EDFAs along the fiber requires to have access to an electrical power supply at these points as EDFAs are active devices. The second approach is the employment of distributed amplification strategies along the fiber. Here, it is possible to find solutions based on first order Raman [100, 101], second order Raman [102],

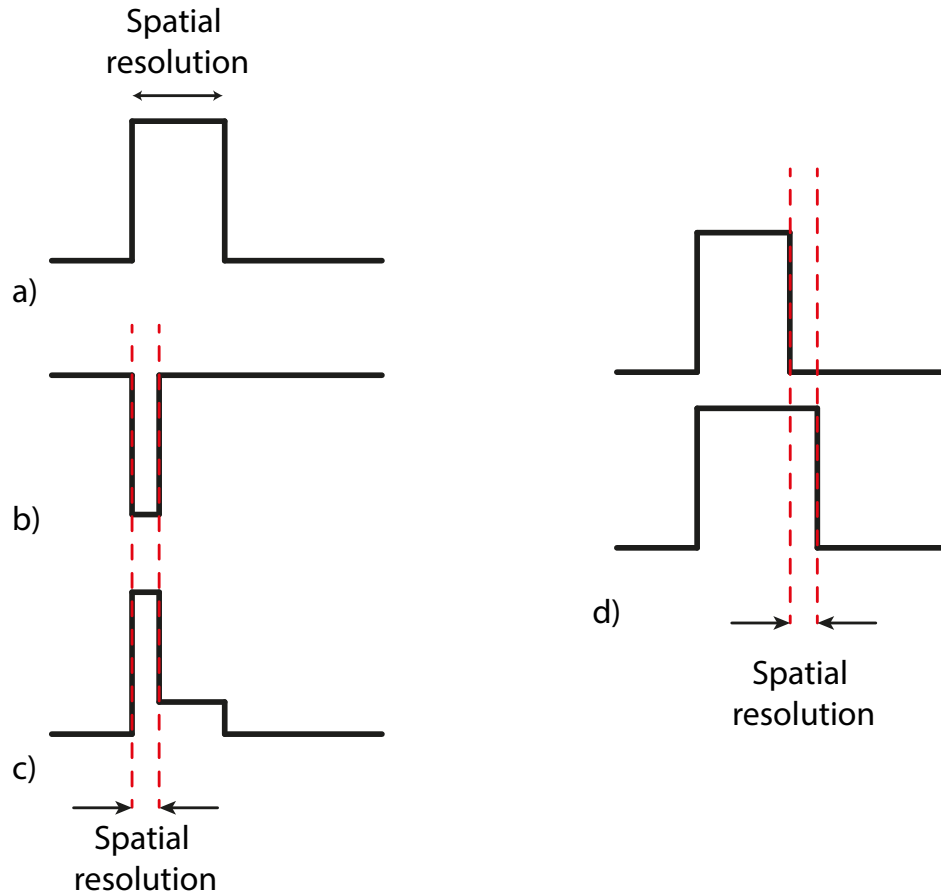


Fig. 2.19. Types of pulses employed in BOTDA sensors to improve the spatial resolution. a) Standard pulse, b) dark pulse, c) pulse pre-pump and d) differential pulse-width pair.

and also Brillouin amplification [21]. These techniques are based on the use of the distributed gain amplification generated using these non-linear effects to amplify the waves involved in the SBS process along the fiber. Being a distributed gain process, the BOTDA waves are amplified over the whole length of the fiber, compensating in a distributed way the losses they accumulate during their propagation. Therefore, the SNR at the receiver increases, allowing to employ these sensors in larger distances. The last approach is known as pump coding techniques [103]. It is based on the use of sequence of pulses to spread the pump energy over a relatively long time, instead of the employment of a single pulse. Different pulse sequences can be employed, such as the bipolar [104] or cyclic pulse codings [105]. Pulse coding approaches require to decode the detected signal to retrieve a conventional BOTDA trace. This solution results in an increase of the SNR at the end of the fiber without a detriment in the spatial resolution. Moreover, it is possible to combine it with other techniques, such

as its use in BOTDA sensors assisted by Raman amplification [106] achieving BOTDA sensors capable of measuring along 120 km with 1 m spatial resolution.

Finally, another characteristic of BOTDA sensors that has been significantly improved in recent years is the measuring time. The time required to carry on distributed measurements in conventional BOTDA systems is typically high, due to the trace averaging required to improve the SNR and the frequency swept. This makes them perfect to be employed in static or quasi-static applications, but very inefficient in other types of applications. Hence, in order to extend their applicability to a wider range of applications, some alternative solutions have been proposed to enable their utilization as dynamic sensors for diverse applications, e.g. the monitoring of the railway traffic [70].

The first proposal to measure dynamic strain was carried out by Bernini et al. in 2009, 20 years after the first proposal of a Brillouin distributed sensor. The proposed technique is known as slope-assisted BOTDA, and it is based on fixing the frequency of the probe wave in the center of the slope of the natural BGS of the fiber, rather than perform the conventional frequency swept [107]. In these systems, strain (or temperature) variations on the fiber produce changes on the local Brillouin frequency provoking the shift of the BGS. This frequency change implies variations on the probe wave due to changes in the Brillouin gain, therefore measuring the amplitude of the probe wave along time it is possible to detect the distributed strain variations. This technique can exploit the relation between the pulse duration and the BGS width employing shorter pulses that imply the broadening of BGS. This impact on the sensitivity of the sensor, but on the other hand, the dynamic range is larger. In [108], a similar concept was proposed. It uses a variable optical frequency probe wave so that it varies along the fiber enabling its use in fibers with different BGSs along their length. Slope-assisted solutions can produce measurements error if any of the waves suffer some losses due to the decrease of the measured probe intensity. To avoid this limitation, the employment of the two slopes is proposed [109]. Measuring the amplitude of the probe wave for both frequencies it is possible to compensate this error. Another novel approach to perform dynamic measurements was made using a system based on Brillouin phase-shift in addition to the conventional Brillouin gain [110]. As it is based on the measurement of the RF phase-shift spectrum, it is immune to variations of the Brillouin peak gain, attenuation of the fiber, or changes in the power of the pump pulses.

The other two solutions present in the literature are fast BOTDA [111] and sweep free

BOTDA [112]. The first is based on the replacement of the slow RF generator employed to generate the frequency swept of the probe wave by an arbitrary waveform generator (AWG) that is quite faster. Hence, the frequency swept is accelerated, launching into the fiber the probe waves consecutively. The latter is a method that employs multiple pump tones to generate multiple downshifted Brillouin gains; in addition, multiple probe tones are injected into the other fiber end, also downshifted around the BFS but with a narrow frequency spacing between them, locating each one at a different section of the BGS.

Apart from the mentioned hardware solutions proposed to reduce the measurement time, there are also other solutions based on processing approaches that can help in this regard. There are some proposals that try to reduce the measuring time by reducing the number of averages employed. This reduction of the averaging implies a degradation of the SNR. The purpose of the employment of these algorithms is to try to compensate this SNR degradation. For instance, one proposal suggests using wavelet shrinkage techniques to remove the noise of the distributed signal measured. Hence, here the denoising is performed via the algorithm rather than the typical averaging. Therefore, if the resulting signal is good enough using a reduced number of averages, the measurement time of the sensor will be lower, allowing faster distributed measurements [113]. Another approach based on the same concept of reducing the number of averages is the employment of a method using the adaptive linear prediction (ALP) technique. The use of this processing algorithm, like the previous one, eliminates part of the noise of the acquired BOTDA trace before averaging, smoothing parts of the trace and keeping abrupt changes [114]. Moreover, the ALP technique has been used in addition to optical pulse coding in a BOTDA sensor for long range measurements, achieving distributed strain measurements with only 20 averages of the BOTDA trace [115].

The last proposal is based on a different approach, it uses an artificial neural network (ANN) to estimate the temperature of the sensing fiber. With this solution, the temperature distribution along the fiber is calculated without the necessity of previously calculating the BFS, and then of translating it to temperature variation. In this study, the training stage of the ANN is performed using theoretical Brillouin gain spectrum with different linewidth, and the performance obtained is better than the one obtained with classical methods, with higher accuracy, lower errors and with a reduced computing time [116].

### Techniques to discriminate between temperature and strain

One of the problems of Brillouin distributed sensors yet to be resolved is the discrimination between strain and temperature. As indicated in section 2.5.2, the BFS of the sensing fiber depends on both magnitudes, and if they occur at the same time in the same location of the fiber, the resulting BFS is composed by both contributions, being very complicated to isolate one from the other. There are some proposals that try to be independent of this limitation. This is the case of a proposal where half the fiber is installed in a way that it only is affected by temperature changes; meanwhile, the remaining fiber is bonded or embedded into the structure to monitor. In this way, one fiber is only dependent on temperature changes, enabling the temperature compensation of the other fiber that has a dependency with both magnitudes [117]. Based on a similar idea, there are some companies that have developed special fiber cables to monitor only one magnitude, for instance, it is possible to find fiber cables where the fiber is loose inside a strong tube or cable, making it insensitive to strain variations, and there are also cables that have more than one fiber inside, being some fibers bonded inside the cable and the others free, enabling the discrimination of both magnitudes.

Another solution uses the dependence of the linewidth and the Brillouin gain with temperature and strain conditions surrounding the fiber in addition to the Brillouin frequency shift. This dependence is depicted previously on Figures 2.5 and 2.6 [34]. Using all these parameters, simultaneous temperature and strain measurement were demonstrated using a distributed Brillouin loss system and polarization-maintaining fibers [118]. A novel method also using polarization-maintaining fibers has been recently proposed. It employs the Brillouin frequency and the birefringence of the optical fiber, demonstrating that the BFS and the birefringence have the same signs for strain but opposite signs for temperature [119]. Other solutions that take advantage of the use of non-standard SMF are proposals that employ large-effective-area fiber (LEAF) that is nonzero-dispersion-shifted, [120] and photonic crystal fibers (PCF) [121]. When the SBS process is generated in these fibers, the Brillouin gain spectrum presents multiple-peaks with different temperature and strain coefficients for each one, allowing the measurement of temperature and strain at the same time.

The last proposal to discriminate between temperature and strain is a solution based on the employment of two different wavelengths to generate the SBS in BOTDA sensors

[36]. As mentioned before, BOTDA sensors typically work in the 1550 nm range due to the well-known characteristics that this wavelength has during its propagation through optical fibers. This solution proposes a system working at 850 nm in addition to the standard wavelength at 1550 nm. Each wavelength produces a different relationship between the BFS and the temperature and strain, so that it is possible to discriminate them due to their different sensitivity.



# Part II

## Contributions

This is the main part of this thesis dissertation. This part details some contributions to the development of distributed optical fiber sensors based on Brillouin scattering. The first chapter is about new experimental setups for Brillouin distributed sensors. These solutions have been proposed with the idea of improving the previous performance of these sensors, and also, to explore the viability of new approaches. Secondly, some processing techniques have been applied to the data acquired using BOTDA sensors. The objectives of applying the processing solutions are to provide an intelligent tool for the decision making of these sensors and also to enable faster ways to estimate the Brillouin frequency shift than the standard Lorentzian fitting. Finally, the feasibility of using these sensors in some real applications such as high temperature scenarios, water leakage detection or modal analysis is analyzed on experimental setups inside the laboratory. The chapters included in this part are:

- Chapter 3: New techniques and configurations for Brillouin distributed sensors
- Chapter 4: Processing techniques applied to BOTDA sensors
- Chapter 5: Laboratory demonstrations of field applications



## Chapter 3

---

# Contributions to the improvement of the performance of Brillouin distributed sensors via new techniques and configurations

---

The first proposal to measure distributed temperature using the non-linear Brillouin effect was published in 1989 [1]. In this research, it was demonstrated that the SBS process taking place inside the optical fiber may be employed to reconstruct a distributed temperature profile along the fiber with a sensitivity of approximately 5.5 MHz/°C (relationship between the Stokes frequency and the measured temperature). Since this contribution, different approaches have been proposed to increase the performance of Brillouin sensors in terms of signal-to-noise ratio (SNR) enhancement [2], spatial resolution [3] or sensing range [4], among others.

In this chapter, different implementations of distributed sensors based on Brillouin scattering that have been proposed and implemented, will be discussed. These implementations try to increase their performance by improving some of their key characteristics or trying to avoid their limitations. The first solution that will be explained is focused on overcoming a detrimental effect that takes place in Brillouin optical time do-

main analysis (BOTDA) sensors, known as non-local effects. The second is a proposal of a new technique based on the frequency domain and optical reflectometry. This technique has been named Brillouin optical frequency domain reflectometry (BOFDR), and it presents some advantages in comparison with traditional Brillouin optical frequency domain analysis (BOFDA) sensors. For instance, only one fiber end is needed in order to perform distributed measurements and, in addition, this system has the advantage that its measurements are free from the distorting components related to acoustic wave modulation, a detrimental effect that appears in BOFDA, known as sub-peaks. The last contribution of the chapter is based on a feasibility study of the employment of an Erbium-doped fiber ring laser (EDFRL) as the optical laser source of BOTDA sensors.

### **3.1. Overcoming Non-local effects in Brillouin optical time domain analysis sensors**

One of the main limitations to the deployment of such long-range BOTDAs comes from the so-called non-local effects. They are due to the interaction of the two optical waves that counter-propagate in a BOTDA sensor: the pump pulse and the probe wave. BOTDA measurements are based on characterizing the gain spectra that the pump pulse provides to the probe wave at each position of the fiber. However, this gain comes from an energy transfer that leads to the depletion of the pump pulse during its propagation along the sensing fiber. The higher the probe wave that is amplified, the larger the pump depletion that the pulses suffer. Moreover, the pump depletion depends on the optical frequency of the probe, which introduces a distortion in the measured Brillouin gain spectrum (BGS) and, hence, a systematic error in the estimation of the Brillouin frequency shift (BFS) [5]. Altogether, this implies a limitation to the maximum probe power that can be launched into the fiber and, hence, a reduction in the resulting SNR.

Several methods have been proposed to counteract this limitation [5–10]. For instance, the use of a BOTDA sensor deploying phase modulation of the probe and RF phase-shift detection [7]. Other approaches are based on the use of different techniques that divide into several sections the entire sensing fiber to reduce the effective Brillouin amplification length so that the Brillouin interaction length only takes place in a

portion of the fiber. Examples of this are techniques based on frequency division multiplexing (FDM) [8], time division multiplexing (TDM) [9] or pulsing the probe wave [10]. Nevertheless, the most popular method to compensate this detrimental effect to date has been the use of a dual-probe sideband setup, in which two sidebands equally spaced from the pulse wavelength provide a complementary interaction. Therefore, the energy that the pulse transfers to the lower optical frequency probe is compensated by that transferred from the upper optical frequency probe to the pulse [5, 6]. However, it has been demonstrated that the probe power that can be deployed in such dual-probe sideband setup is rather limited. It is because non-local effects are compensated only to first order, but there is an additional distortion of the pump pulse spectra that is brought by the combined gain and loss spectra generated by the two probe waves [11].

Therefore, the limitation to long-range BOTDAs coming from non-local effects is yet to be resolved. Furthermore, even though non-local effects were completely overcome, another limit for the probe power would remain: the Brillouin threshold of the fiber. This threshold defines the maximum power that can be launched into the sensing fiber before the amplification of thermally-induced spontaneous Brillouin scattering (SpBS) leads to depletion of the probe wave and addition of noise to the detected signal [12, 13].

To get over this limitation, a new method is proposed to greatly expand the probe power that can be deployed in BOTDA sensors. This improvement in BOTDA setups implies that previous non-local effect limits and even the Brillouin threshold limit have been overcome. It is based on modulating the optical frequency of the probe waves in a dual-probe BOTDA setup. Moreover, this technique avoids the need to sweep the frequency of the probe waves by changing the microwave frequency applied to the modulator used to generate those waves. Instead, the Brillouin gain spectra are characterized by changing the delay between the pump pulse and the probe wave optical frequency modulation.

### **3.1.1. Description of the technique**

Figure 3.1 shows the fundamentals of the technique by depicting the spectra of the various optical waves involved. A BOTDA setup with two probe waves counter-propagating to the pump pulse was assumed. As it is highlighted in the figure, the optical frequency of the probe waves is modulated in the time domain. Moreover,

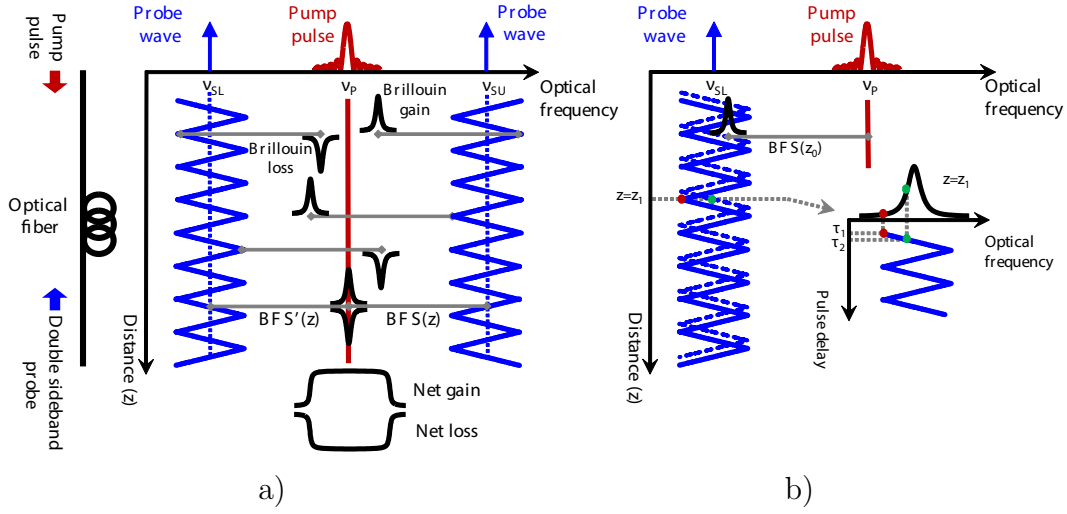


Fig. 3.1. Fundamentals of the technique employed to overcome non-local effects: details of the Brillouin interaction on the pump pulse a) and on the probe wave b).

this frequency modulated (FM) signal is synchronized to the pump pulses so that a sequence of pulses experiences the same wavelength of the probe waves at any given location. Therefore, the modulation of the optical frequency of the probe waves leads to a variation of the Brillouin interaction frequency along the fiber that follows the same profile of this modulation.

This has important implications for the Brillouin interaction generated by both probe waves onto the pump pulse, as it is schematically depicted in Figure 3.1 a). The modulation of the optical frequency of the probe waves makes the Brillouin interaction induced by them upon the optical pulse to spread over a large frequency range, so that non-local effects cease to be significant. This can be understood by taking into account that the lower-frequency probe induces a loss spectrum to the pulse that changes its central frequency along the fiber. The interaction at a particular location is given by the detuning of the Brillouin loss spectra from the pulse,  $\Delta\nu_L$

$$\Delta\nu_L(z) = \nu_{SL}(z) - \nu_P(z) + BFS(z) \quad (3.1)$$

where  $\nu_P$  and  $\nu_{SL}$  are the optical frequencies of the pump pulse and the lower-frequency probe sideband, respectively. The change in  $\nu_{SL}$  along the fiber mimics the shape of the FM modulation imposed on the probe wave. The integration of this loss interaction along the fiber gives a flat wideband total depletion spectrum that does not distort the pulse spectrum, provided that an adequate shape is chosen for the frequency modulation. Similarly, the upper-frequency probe wave induces a gain spectrum that has a

variation along the fiber given its detuning from the pulse,  $\Delta\nu_G$

$$\Delta\nu_G(z) = \nu_P(z) - \nu_{SU}(z) + BFS(z) \quad (3.2)$$

where  $\nu_{SU}$  is the optical frequency of the upper-frequency probe sideband. Again, integration of this gain along the fiber gives a flat wideband total gain spectrum that compensates the pulse depletion. Therefore, the gain and loss spectra perfectly compensate for all the frequency components of the pulse, and, hence non-local effects are fully avoided.

A triangular modulation of the probe waves frequency is assumed in Figure 3.1. However, other modulation shapes are possible to optimize the objective of having the flattest possible total gain and depletion spectra so that no distortion is introduced to the pulse.

In detection, just one of the probe waves is detected, typically the lower frequency one, while the other is filtered out. In order to measure the Brillouin spectra experienced by the chosen probe wave at any given location, it is necessary to scan the frequency of the probe wave at that location. This is done by sweeping the frequency of the probe wave in a conventional BOTDA.

However, in FM BOTDA systems this can be done in a much simpler way by sequentially changing the relative delay between the pump pulses and the FM wave, as it is schematically depicted in Figure 3.1 b). This changes the relative location of the optical frequency profile of the probe wave along the fiber so that at any given location all frequencies are sequentially scanned.

This new technique of using FM modulation of the probe waves can be regarded as an evolution of a previous proposal to generate virtual BFS profiles along a sensing fiber [14]. However, in that case, the method was based on modulating the wavelength of the laser source used to generate the optical waves needed in a self-heterodyne BOTDA setup, rather than directly modulating the probe wave frequency. Moreover, in that previous work the pulse depletion was not compensated but simply made flatter in terms of its frequency dependence to avoid BFS measurement errors.

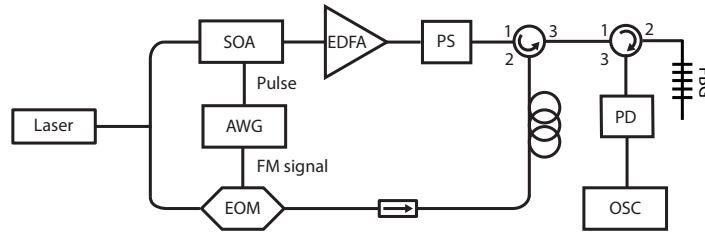


Fig. 3.2. Experimental setup employed to overcome non-local effects in BOTDA.

### 3.1.2. Experimental setup

Figure 3.2 depicts the assembled setup used to demonstrate this technique. The output of a laser source is divided into two branches to generate the pump and probe waves. In the upper branch, the pump signal is pulsed using a semiconductor optical amplifier (SOA). Then, the pulse power is boosted to a peak of 140 mW using an Erbium-doped fiber amplifier (EDFA) and its polarization state is randomized using a polarization scrambler (PS) before being launched into 50 km of standard single-mode fiber (SMF).

In the lower branch, a dual-probe sideband wave is generated using a Mach-Zehnder electro-optic modulator (EOM) driven by an arbitrary waveform generator (AWG) and biased at the minimum transmission point of its transfer curve. The AWG provides an FM microwave signal whose instantaneous frequency varies around the average BFS of the fiber following a triangular shape. This induces an identical modulation of the optical frequency of the probe waves. The microwave signal has been designed to have a carrier frequency of 10.8 GHz and a peak frequency deviation of 75 MHz. The modulation frequency is 40 kHz, which yields a total of 20 cycles of triangular variation of the local probe frequency along the 50 km long sensing fiber.

When the Brillouin interaction provided by such FM modulated probe waves is integrated along the fiber, it gives Brillouin gain and loss spectra with a bandwidth of around 150 MHz, which is more than enough to avoid distortion in 10 ns pulses for 1 m resolution. Shorter pulses can be accommodated simply by increasing the peak frequency deviation. In the particular proof-of-concept experiments described here, 50 ns pulses are deployed.

Finally, after Brillouin interaction of these probe signals with the pump pulse, they

are directed to a fiber Bragg grating (FBG) to filter out the upper sideband. The remaining probe wave is detected, captured in a digital oscilloscope and processed in a computer.

### 3.1.3. Experimental results

The experiments started by confirming that, indeed, in the conventional dual-probe BOTDA there is a serious problem with non-local effects as the probe power is increased. This is done by simply switching off the FM modulation on the AWG so that it generates tunable continuous microwave tones, and sweeping the optical frequency of the probe waves to scan the Brillouin spectra along the fiber.

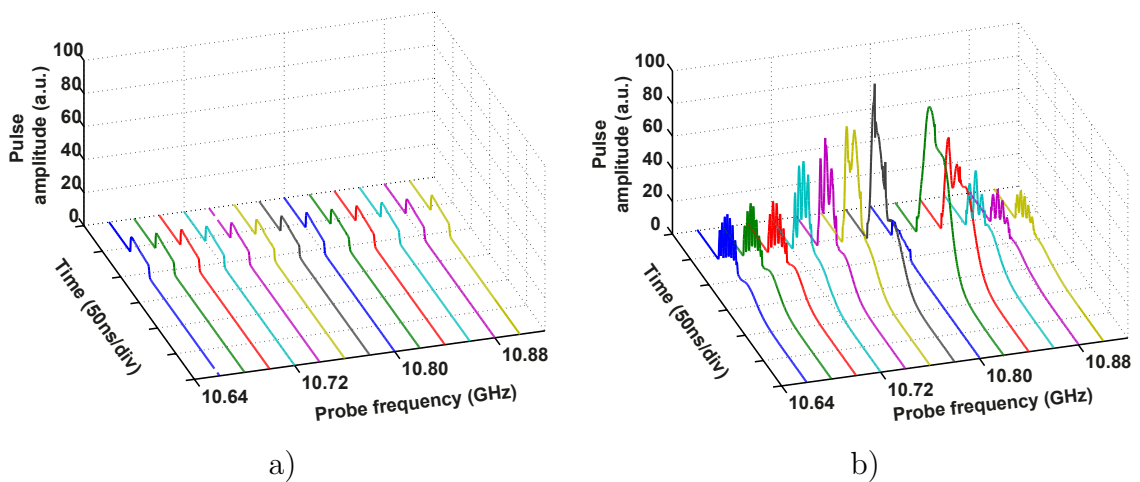


Fig. 3.3. Pulses at the output of the fiber for a conventional dual-probe BOTDA in two cases: for probe wave powers of -6 dBm a) and 5 dBm b).

Figure 3.3 shows the pulses that are measured at the output of the fiber as the microwave frequency is swept to measure the Brillouin spectra for two cases: a) with low probe power (-6 dBm) and b) with high probe power (5 dBm). Notice that, when the probe power is low, non-local effects are negligible so the pulse remains constant and undistorted for all optical frequencies of the probe.

However, when the probe power is increased the pulses are greatly distorted depending on the probe frequency. This distortion has been previously reported in the literature, but the effect was found to be rather mild due to the deployment of lower

probe powers than the one used here [11]. However, it can be seen that the distortion is much more pronounced as the probe wave power is increased. In Figure 3.3 b), it can be seen that the gain and depletion induced by both probe waves upon the pulse compensate just when the microwave frequency coincides with average BFS of the fiber (around 10.8 GHz). However, for small departures of the microwave frequency from that value, the pulse gets distorted as its spectral components get differential amplification or depletion [11]. This makes the pulse peak power to greatly increase around the BFS frequency. The temporal duration of the pulses at those frequencies are also increased.

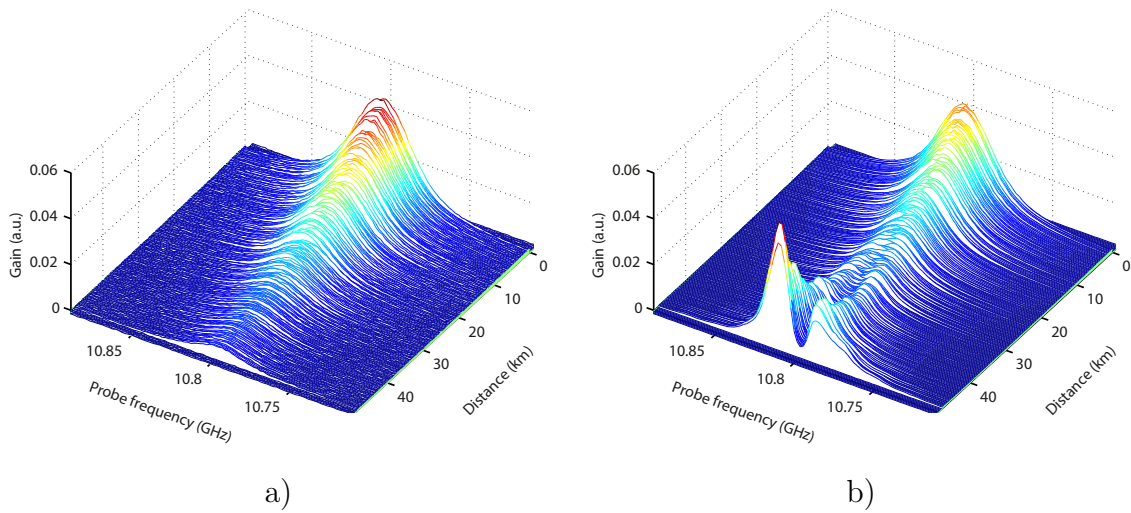


Fig. 3.4. Measured Brillouin gain spectra for a conventional dual-probe BOTDA in two cases: a) for probe wave powers of -6 dBm, and b) 5 dBm.

The distortion of the pulses has a strong impact on the measured Brillouin spectra along the fiber. Figure 3.4 shows a 3D view of the Brillouin spectra measured for the two cases considered before. It is clearly appreciated that for larger probe powers at the far away locations of the fiber, where the pulse arrives with great distortion, the measured spectra are also greatly distorted. Note that in Figure 3.4 b) the spectra at the end of the fiber have two peaks around the mean BFS of the fiber that correspond to the probe frequencies at which the pulse is shown to be amplified in Figure 3.3 b).

A more detailed view of the spectra at the end of the fiber is highlighted in Figure 3.5. It shows how the spectra are affected by the distortion of the pulse spectra due to non-local effects when the probe power is increased. These spectra have lost his Lorentzian shape and two peaks have appeared around its center due to the amplification of the

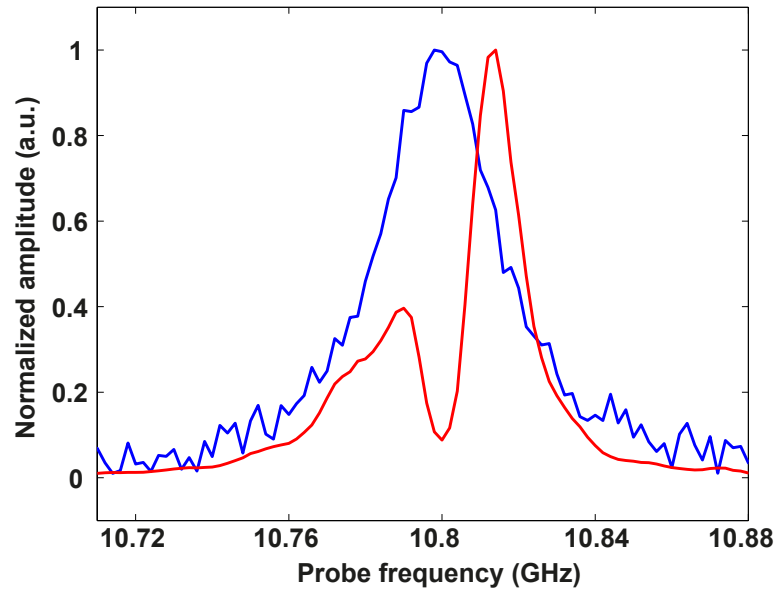


Fig. 3.5. Measured Brillouin gain spectra at the end of the fiber for -6 dBm (blue line) and 5 dBm (red line) probe power.

pulse at those frequencies.

In contrast to the conventional technique, Figure 3.6 depicts measurements done using this new technique with FM modulation of the probe waves. Figure 3.6 a) depicts the pulses measured at the output of the fiber with and without probe wave applied. Notice that the pulse shape remains almost identical for both cases with negligible distortion and just some added noise, which is attributed to SpBS amplified by the probe waves. Also note that the deployed probe power is larger than for previous measurements, i.e., 8 dBm, which was the largest probe power ever demonstrated in a long-range BOTDA sensor without errors induced by non-local effects.

The raw measurement data, obtained as the delay between the pulse and the FM modulation, is depicted in Figure 3.6 b). Note that it follows the shape of the FM modulating signal. This raw data is post-processed to compensate the frequency shift in the measurement introduced by FM modulation of the probe wave along the fiber. With this purpose, at each location  $z$ , the frequencies in the measured spectra are reordered to account for the delay changes that are introduced between the pulses and the FM signal during the measurement process, as it was explained in Figure 3.1 b). This is a simple and immediate operation that does not introduce any significant calculation delay, resulting in the measurement of the well-behaved spectra in Figure

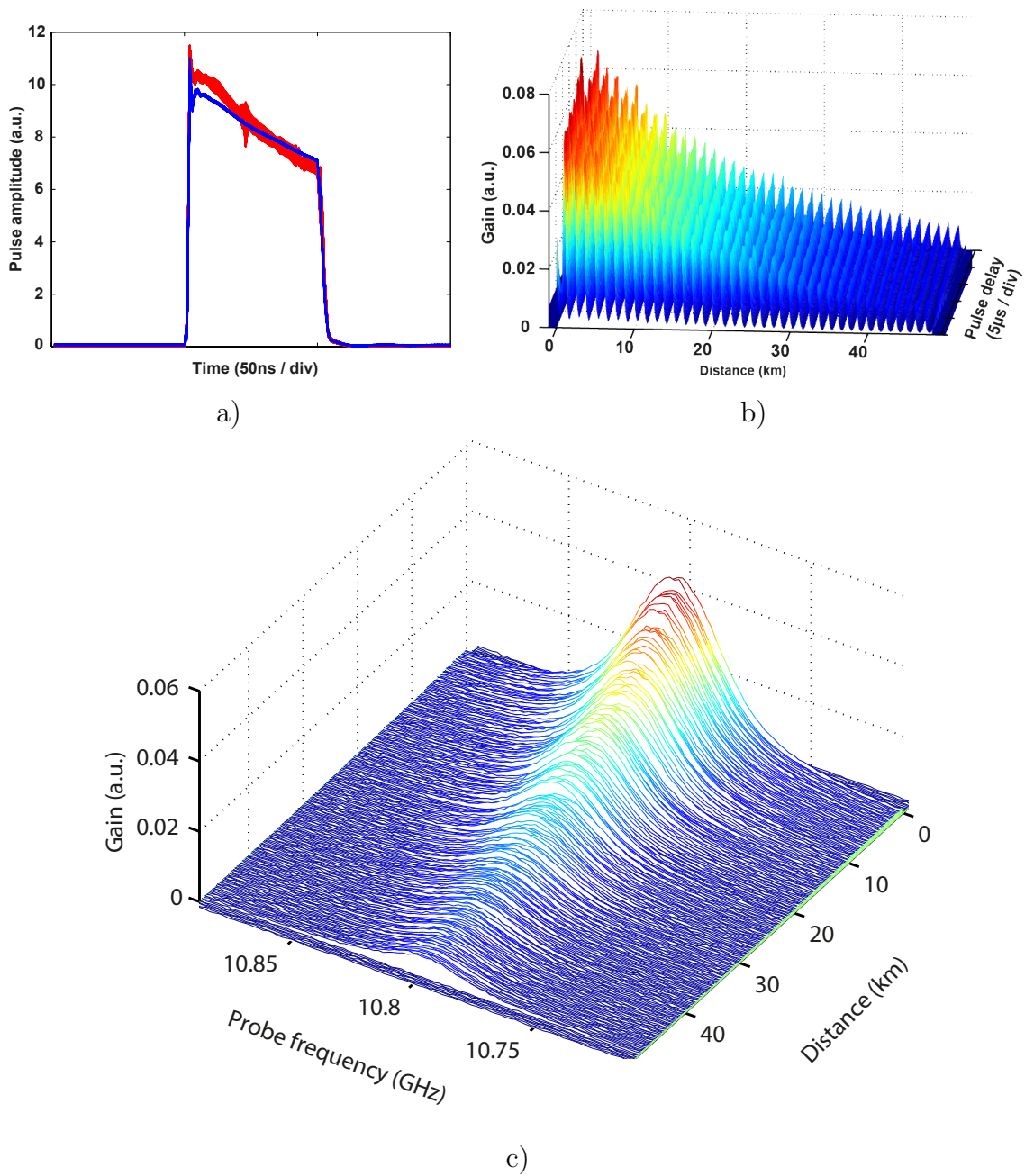


Fig. 3.6. a) Pulses at the output of the fiber in two cases for probe wave power of 8 dBm (red line) and without probe power (blue line), b) raw measurement data for the FM dual-probe BOTDA with 8 dBm probe power and c) measured Brillouin gain spectra.

3.6 c). The spectra are completely normal, not suffering any distortion at the end of the fiber.

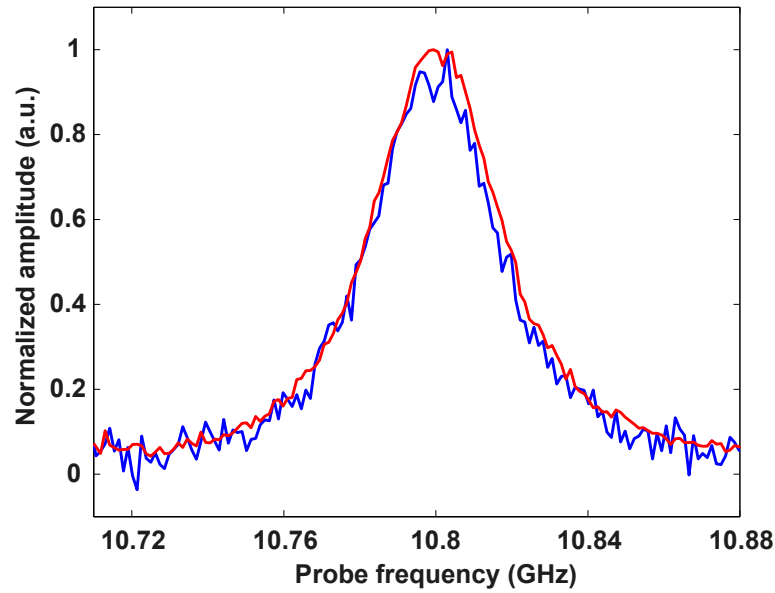


Fig. 3.7. Measured Brillouin gain spectra at the end of the fiber for -6 dBm (blue line) and 8 dBm (red line) probe powers with the FM dual-probe BOTDA system.

Figure 3.7 compares the spectra measured at the output of the fiber for the FM technique with low and high powers of the probe wave. It can be seen that, indeed, the larger power measurement is not distorted at all. The only difference between the measurements is that the higher power one is significantly less noisy, as it was expected, due to the higher probe wave reaching the receiver. Moreover, there is no systematic error in the BFS measurement given by both spectra. Note that the full potential improvement in SNR generated with the presented technique is limited, for this particular case, by the maximum optical power injected to the receiver (-13 dBm).

Therefore, with this technique there is no systematic error in the BFS measurement when the probe power is increased. This is confirmed by Figure 3.8 that displays the BFS measured for the conventional dual-probe BOTDA and for this system for different powers of the probe wave. Notice that, as it was explained before, there is a large systematic measurement error as the probe power is increased for the conventional dual-probe BOTDA, while for the FM system, the BFS measurement remains error-free even for larger probe powers.

Finally, it must be pointed out that the FM BOTDA setup is operating with a probe power above the Brillouin threshold, which was measured to be 6 dBm for the deployed sensing fiber. This is made possible by a side effect of the FM modulation,

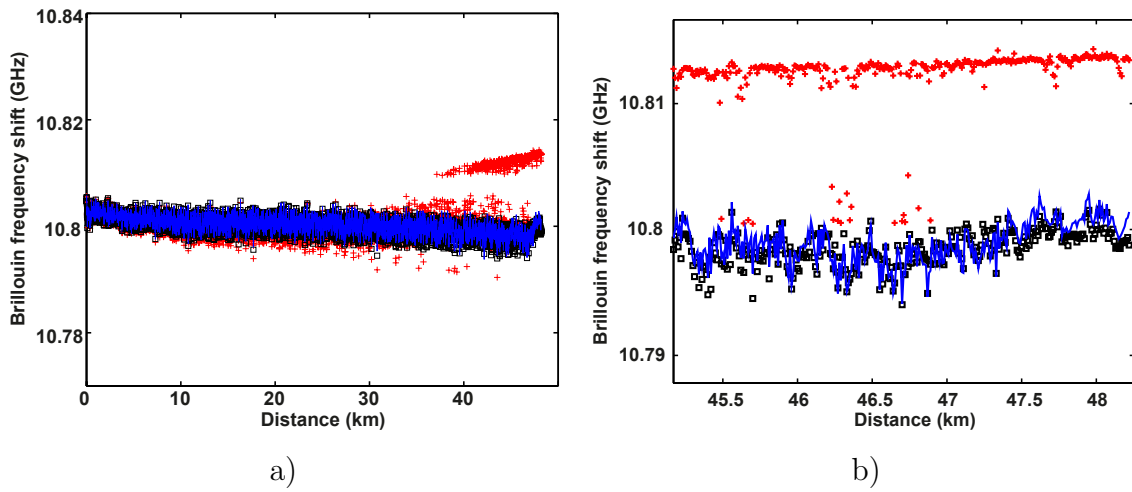


Fig. 3.8. Comparison of measured BFS for the FM technique with 8 dBm probe power (blue solid line) and for the conventional dual-probe with 5 dBm (red crosses) and -6 dBm (black squares) probe power for a) all the fiber and b) in the last kilometers.

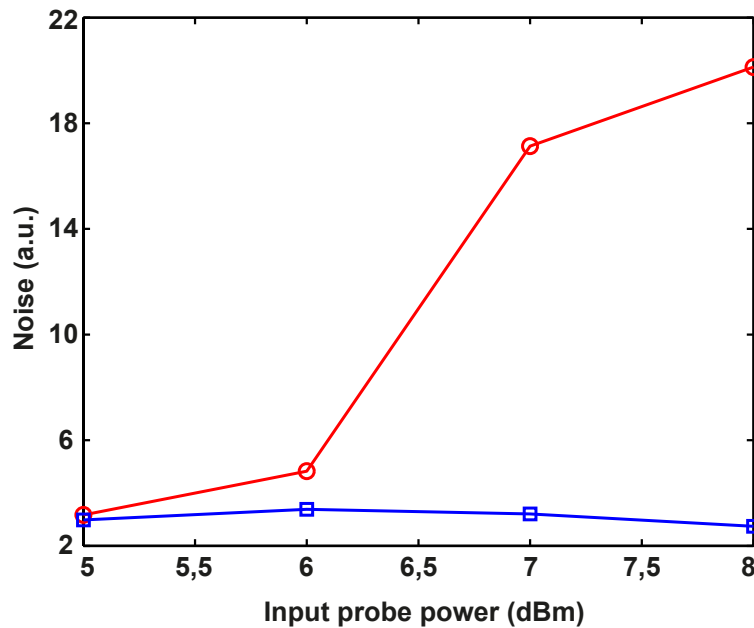


Fig. 3.9. Comparison of measured rms noise at the detector for different probe powers injected in the fiber using the conventional dual-probe system (red line with circles) and the FM technique (blue line with squares).

which has been previously shown to increase the effective Brillouin threshold [15]. This is confirmed by measuring the rms noise at the detector for different probe powers injected into the fiber but using an attenuator to keep a constant received power. As it

is shown in Figure 3.9, in the conventional dual-probe system there is a larger than six times increment in rms noise as the probe power is increased from 5 dBm to 8 dBm, whereas with the FM technique the noise level remains stable. This is confirmed by measuring the rms noise at the detector for different probe power injected in the fiber but using an attenuator to keep a constant received power.

These experimental results have demonstrated that the proposed technique based on a dual-probe sideband BOTDA sensor with FM modulation of the probe waves permits a much larger power injected in the sensing fiber than it was previously possible. This fact opens the way to a substantial enhancement in the performance of BOTDA sensors. This will come in the form of enhanced SNR in the detectors at the end of the fiber as more optical power reaches them, which in turn leads to an enhanced sensor performance in terms of precision or measurement time.

## 3.2. Brillouin optical frequency domain reflectometry

As mentioned in 2.5.3.2 and 2.5.3.4, distributed optical fiber sensors based on spontaneous Brillouin scattering attract interest because of their capability to perform distributed strain and temperature measurements accessing only one end of the fiber. Traditionally, these sensors use the Brillouin optical time domain reflectometry (BOTDR) method, where a pulsed light is injected into the fiber while the SpBS backscattered light is detected as a function of time [16].

BOTDR operates based on the fact that the BGS and therefore the BFS depends on temperature and strain conditions surrounding the optical fiber. In order to improve the spatial resolution, shorter pump pulses must be injected into the fiber. However, the spectra of the backscattered Stokes (and anti-Stokes) wave broadens rapidly when the pump pulse duration is reduced below the phonon lifetime, resulting in a loss of accuracy in the BFS estimation [17]. Consequently, it is typically limited to 1 m in conventional BOTDR sensors, although advanced configurations have been proposed to improve the spatial resolution, such as the differential pulse-width pair (DPP) method that may reach submeter resolutions [3]. An alternative approach, known as Brillouin optical correlation domain reflectometry (BOCDR), synthesizes a single correlation peak within the range of the fiber by modulating the frequency of the injected pump

light [18]. Owing to the continuous wave nature of the pump light, the technique is capable of spatial resolution in the centimeters range, while keeping a narrowband Brillouin spectrum, and moreover with the single ended sensing capability. However, the method allows for a limited number of measuring points, owing to the requirement of having one single correlation peak into the fiber, unless complex modulation schemes are adopted [19–21].

Therefore, this section describes the proposal of a novel reflectometry technique that can be known as Brillouin optical frequency domain reflectometry, in concordance with other similar acronyms. Compared to BOTDR, the proposed method inherits the advantages of frequency domain configurations: narrowband operation, averaging effect of inverse Fourier transform and reduced power levels [22, 23]. Moreover, it will be demonstrated with the experimental results that the proposed technique avoids the corruption of the acquired data observed in BOFDA sensors and caused by acoustic wave modulation [24], thus simplifying the extraction of the BFS from the acquired BGS.

### 3.2.1. Principle of operation

BOFDR is a distributed Brillouin sensor based on SpBS and optical reflectometry. Its working principle is based on the use of a pump light whose amplitude is sinusoidally modulated with a variable frequency. The corresponding modulation in the backscattered light is detected by the use of a vector network analyzer (VNA). In analogy to the other frequency sensor, BOFDA that it is based on SBS, the spatial resolution and the sensing range are determined by the frequency scan of the VNA [22].

As explained in section 2.3, the SpBS effect is caused by the nonlinear interaction between light launched into an optical fiber and thermally excited acoustic phonons in the medium. During the interaction, the scattered light undergoes a spectral shift equal to the BFS and travels backwards. As it happens in other Brillouin distributed sensors, the BFS changes linearly with temperature and strain, allowing the extraction of these parameters from BFS measurements. In these sensors, the spatial resolution is achieved by impressing some form of modulation into the pump light. The operation of the proposed BOFDR method is very similar to the BOTDR, except from the use of a sinusoidally modulated, rather than pulsed pump light. When the modulated pump

light is travelling through the fiber, it experiences loss due to fiber attenuation and a phase shift. Note the low-pass filtering due to fiber dispersion is negligible in this case, as the bandwidth-length product in single-mode fibers at 1550 nm amounts to tens of GHz · km [23]. The backscattered wave due to SpBS comprises both Stokes and anti-Stokes components, originating at each section of the fiber and propagating back to the fiber input. The modulated backscattered Stokes and anti-Stokes waves experience power loss and a phase shift, as well. After propagating back to the fiber input, one of the two backscattered waves is filtered out (the anti-Stokes wave in these measurements), while the other one is converted into an electrical signal and finally sent to the VNA. The latter also provides the frequency-scanning signal modulating the pump light. During the sweep of the modulation frequency, the amplitudes and the phases of the detected Stokes powers are successively measured by the VNA. After data acquisition, the fiber response is obtained by discrete inverse fast Fourier transform (IFFT), which provides the amplitude of the backscattered wave as a function of position. The modulation frequency scan determines the spatial resolution and the measuring range, according to [22, 25]

$$\delta z = \frac{c}{2n} \frac{1}{f_{max} - f_{min}} \quad (3.3)$$

$$L_{max} = \frac{c}{2n} \frac{1}{\Delta f_m} \quad (3.4)$$

where  $f_{min}$  and  $f_{max}$  denote the minimum and maximum modulation frequencies, respectively,  $\Delta f_m$  is the modulation frequency step,  $n$  is the refractive index of the fiber, and  $c$  is the speed of light in the vacuum. As in BOTDR, the information on local temperature and/or strain is achieved by spectrally analyzing the backscattered wave. As the latter is weak, its frequency is conveniently retrieved using a coherent detection scheme, as it will be described in the next section.

### 3.2.2. Experimental setup

Figure 3.10 shows the setup used for the experiments. The laser light from an external cavity diode laser ( $\lambda = 1550$  nm, power  $\simeq 40$  mW, linewidth  $\simeq 100$  kHz) is divided into the pump and reference light beams. The pump light is amplitude modulated by an electro-optic modulator, biased at the half-power point and driven

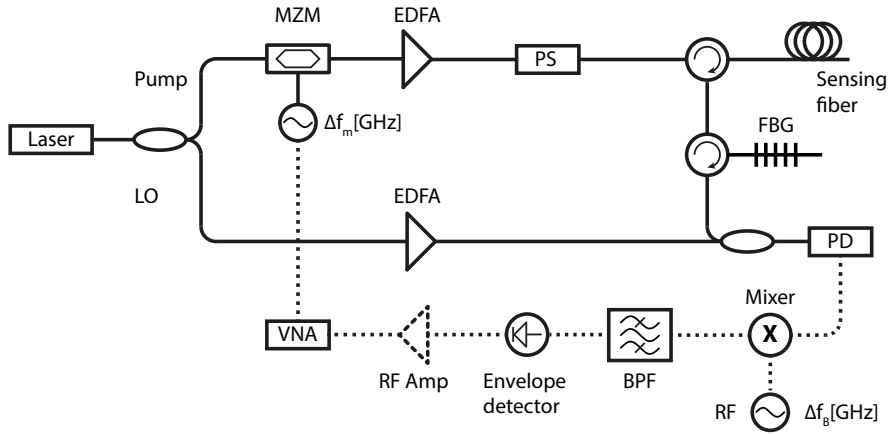


Fig. 3.10. Experimental setup of BOFDR system.

by the output of the VNA (Anritsu MS4630B). The modulated pump light is then amplified up to 5 dBm and sent to a polarization scrambler operating at a rate of 700 kHz, before being injected into the sensing fiber. Through both optical circulators, the backscattered light is directed to a narrowband ( $\simeq 5$  GHz) FBG, to reject all the optical components apart from the Stokes wave of the SpBS. After optical filtering, the backscattered field is mixed to a fraction of the laser light acting as an optical local oscillator (LO) amplified up to 8 dBm, producing a beat signal at the BFS frequency ( $\simeq 11$  GHz). After conversion to the electrical domain by the use of a 12 GHz photodetector (PD), the signal at the BFS frequency is downshifted to the intermediate frequency (IF) band, by mixing it with the RF signal provided by a tunable microwave generator. The IF signal is filtered by a custom-made electrical bandpass filter (BPF) with a center frequency of 700 MHz and a 3 dB bandwidth of 110 MHz, and then amplified. Finally, the baseband signal is recovered by passing the IF signal through an envelope detector (MACOM 2087-6001-13) and sent to the VNA. The latter acquires the frequency domain data and transfers them to a computer for processing and storage. To construct distributed spectra, the frequency of the microwave source is swept, in order to record the Brillouin fiber responses over a range of pump-probe frequency shifts. After conversion to the time domain by IFFT, the retrieved spectra are curve fitted to determine the BFS distribution.

### 3.2.3. Experimental measurements

#### 3.2.3.1. Experimental tests over uniform fibers

In order to demonstrate the capabilities of the proposed method, a first test was carried out over a 100 m uniform fiber, with the VNA operating at a resolution bandwidth (RBW) of 100 Hz and the modulation frequency  $f_m$  ranging from 100 kHz to 100 MHz, with 100 kHz steps. Both ends of the sensing fiber (i.e., also the one not connected to the setup) were terminated with FC/APC connectors in order to minimize Fresnel reflections. The choice of a maximum modulation frequency of 100 MHz, which corresponds to a spatial resolution of  $\simeq 1$  m, was dictated by the bandwidth of the bandpass filter in the heterodyne receiver stage. In fact, it was verified experimentally that the highest frequency component (100 MHz) of the acquired fiber responses was attenuated by  $\simeq 5$  dB due to the presence of the BPF. Higher modulation frequencies would experience higher losses, giving no real contribution to the spatial resolution of this sensor. Figure 3.11 shows the position frequency Brillouin gain map obtained by IFFT, with the frequency domain data acquired for a microwave frequency swept from 11250 MHz to 11650 MHz at 5 MHz step. Note that in Figure 3.11 the 700 MHz offset between the microwave source and the frequency shift between pump and Stokes light, owing to the center frequency of the electrical BPF, has been properly taken into account. The measured BFS is  $\simeq 10725$  MHz, with a standard deviation of  $\simeq 4$  MHz. It is interesting to observe that the BGS linewidth is  $\simeq 110$  MHz, thus larger than the typical BGS linewidth in SpBS ( $\simeq 80$  MHz, see e.g. [17]). This fact must be attributed to the bandwidth of the electrical bandpass filter used in the heterodyne receiver. In fact, it is known that the observed BGS linewidth increases with the BPF bandwidth [26].

As an example, a comparison of the BGS acquired at a generic position with the custom filter and the BGS acquired at the same position after replacing the BPF with a different one featuring a nominal full width at half maximum (FWHM) of 428 MHz (Minicircuits VBFZ-780-S+) is depicted in Figure 3.12. As expected, the BGS bandwidth increases with the BPF bandwidth. Obviously, using a narrower filter would result, instead, in a lower BGS linewidth, at the expenses of the achievable spatial resolution. It is important to notice that the accuracy of strain/temperature estimation is also related to the BGS linewidth; in particular, the BFS error increases

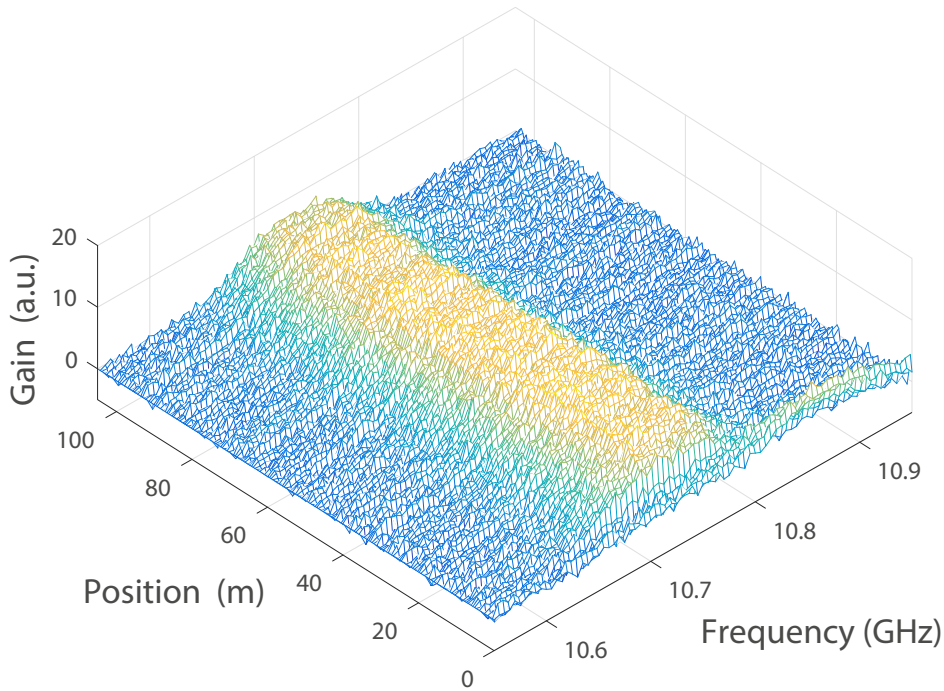


Fig. 3.11. Position frequency Brillouin gain map acquired over a uniform 100 m long fiber, for a modulation frequency ranging from 100 kHz to 100 MHz.

with the square root of the BGS linewidth [27]. Therefore, a trade-off exists between spatial resolution and strain/temperature resolution, in analogy to BOTDR systems.

A drawback of BOFDA sensors is the presence of artifacts in the acquired measurements, deriving from the ac modulation of the acoustic wave involved in the scattering process [24, 28]. Such artifacts generally lead to a loss of spatial resolution, unless proper algorithms are applied to filter out these terms from the acquired data [24]. Therefore, it is important to verify if these artifacts are present also in the newly proposed BOFDR. From a theoretical point of view, it must be considered that in BOFDR the acoustic wave is thermally (rather than optically) generated [29]; therefore, it may be argued that the acoustic wave is not modulated by the pump light as in BOFDA systems, with the consequence that no artifacts should be found in the acquired spectra. This argumentation can be conveniently verified, by analyzing the data directly in the frequency domain (i.e. as they are acquired by the VNA). In fact, in BOFDA measurements the acoustic wave sidebands are clearly identified as subpeaks in the frequency domain data, separated by the resonant peak by a quantity equal to the modulation frequency [28].

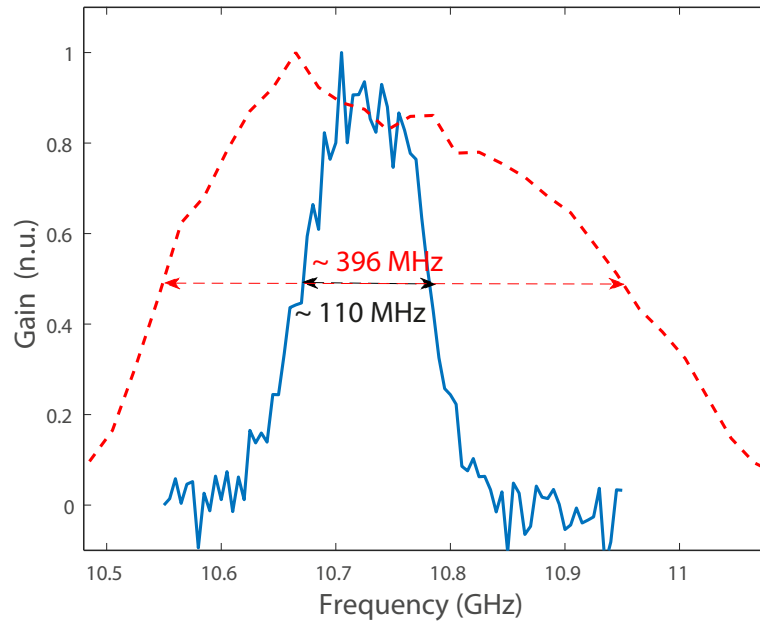


Fig. 3.12. BGSs acquired at a generic position of the fiber using the custom-made BPF (blue solid line), or the Minicircuits VBFZ780-S+ (note that both BGSs have been translated horizontally, by a quantity equal to the center frequency of the bandpass filter).

Figure 3.13 shows the magnitude of the frequency domain response of the 100 m fiber for the two different setups employed, the former is the magnitude acquired using the proposed BOFDR method, and it is represented in Figure 3.13 a) and the latter, the response when the conventional BOFDA configuration operated at the same modulation frequencies and RBW of the VNA, and when the same optical power levels are employed, depicted in Figure 3.13 b). The BOFDA configuration employed here is the same described in section 2.5.3.3 and also explained in [24]. Note that each dataset was normalized to its maximum. When the modulation frequency is larger than the natural BGS linewidth, the presence of three peaks in the frequency domain data is evident in BOFDA data [28], while the proposed BOFDR data show no subpeaks.

### 3.2.3.2. Experimental tests over nonuniform fibers

As a further demonstration of the absence of distorting features in the BOFDR data, a new test after immersing the 100 m fiber in a hot water bath ( $T \simeq 55^\circ\text{C}$ ) has been performed, while leaving out of the bath two fiber segments of lengths 2 m and 1 m, respectively. Still, BOFDR and BOFDA measurements are compared under the same

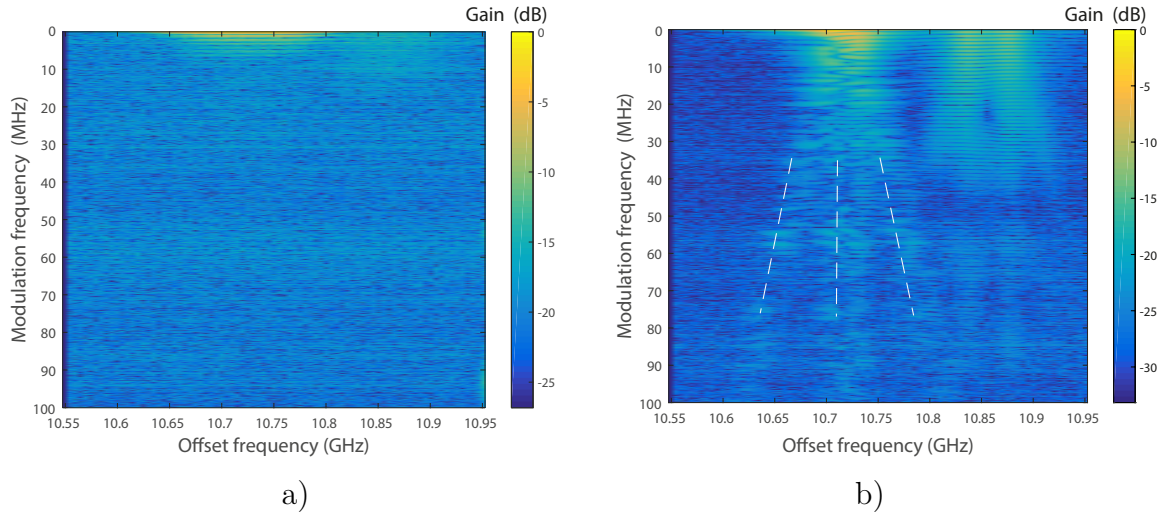


Fig. 3.13. Frequency domain data acquired using the proposed BOFDR method a) and the BOFDA method b). The white dashed lines in b) highlight the three peaks in the frequency domain Brillouin gain spectra. The gain visible at frequencies around 10860 MHz is due to the SBS occurring along short pigtailed spliced to the test fiber.

experimental conditions. Figure 3.14 shows the time domain raw data as obtained by IFFT-ing the acquired BOFDR data a) and BOFDA data b).

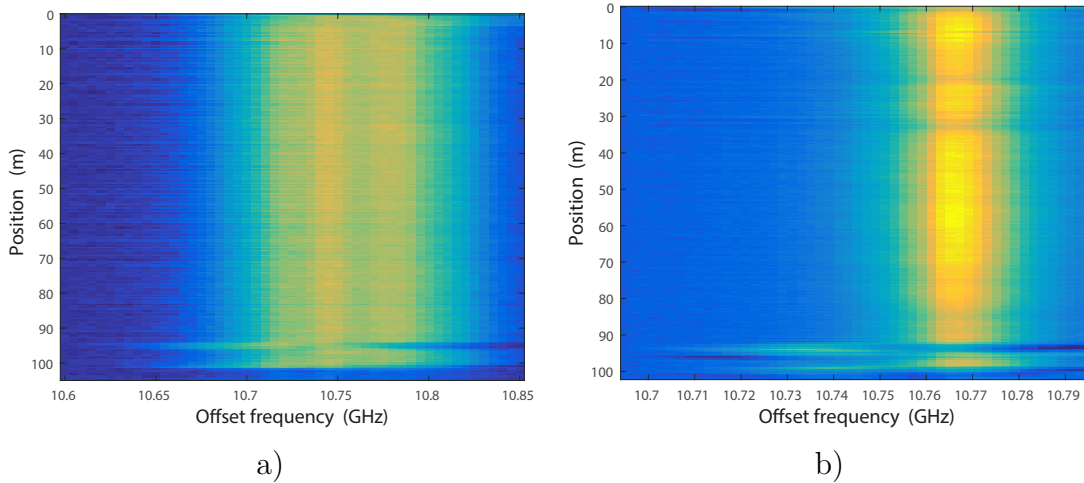


Fig. 3.14. Brillouin gain map of a 100 m fiber with two small fiber section at lower temperature. It is computed by applying the IFFT on the frequency domain data acquired using a) the BOFDR method and b) the BOFDA method.

Applying a curve fitting to the spectra shown in Figure 3.14, the two BFS profiles reported in Figure 3.15 are achieved. It is seen that, while the BOFDA measurements are characterized by a better signal-to-noise ratio (about 6.4 dB higher), the BFS

determined in the two cold spots is more accurate when processing the BOFDR data. This fact can be explained by recalling that the distorting features associated with the acoustic wave modulation degrade the spatial resolution in BOFDA sensors, because of the loss of spectral purity of the spectra at the perturbed sections [24]. Therefore, even though the spatial resolution of BOFDA measurements is nominally sufficient to detect the two cold spots, the rightmost perturbation is not correctly resolved.

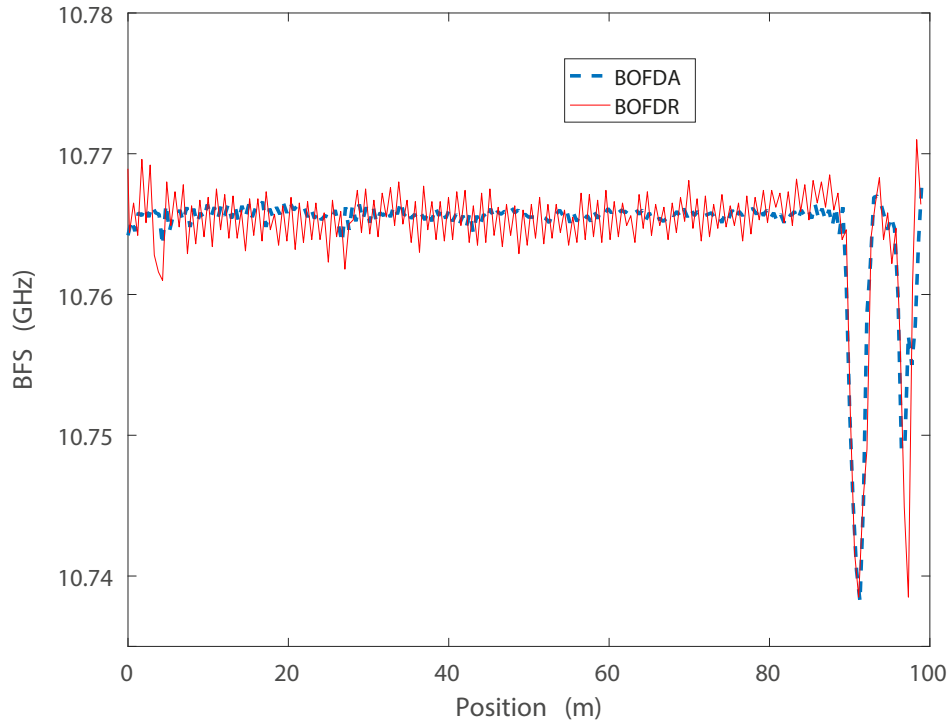


Fig. 3.15. BFS reconstruction obtained by processing the BOFDR and BOFDA measurements.

The loss of BGS spectral purity is evident in Figure 3.16, which shows the BGS acquired by the BOFDA system at the position of the rightmost cold spot (the BOFDR spectra in the same position and in the middle of two cold spots are also shown for comparison purposes). In the BOFDA case, it is possible to see that the BGS exhibits two peaks, one centered at the resonance of the cold spot ( $\simeq 10738$  MHz), and the other one at the resonance of the unperturbed fiber ( $\simeq 10766$  MHz). As discussed in [24], the spurious peak (the one centered at 10766 MHz in Figure 3.16) is due to the interaction between the modulated component of the electrostrictively-driven acoustic wave, and the pump wave. Vice versa, the BGS acquired at the same position by the BOFDR method, while being much wider than its BOFDA counterpart (partly because of the Brillouin linewidth narrowing effect discussed in [30] and partly because of the

electrical BPF), shows only one peak centered at the position of the cold spot.

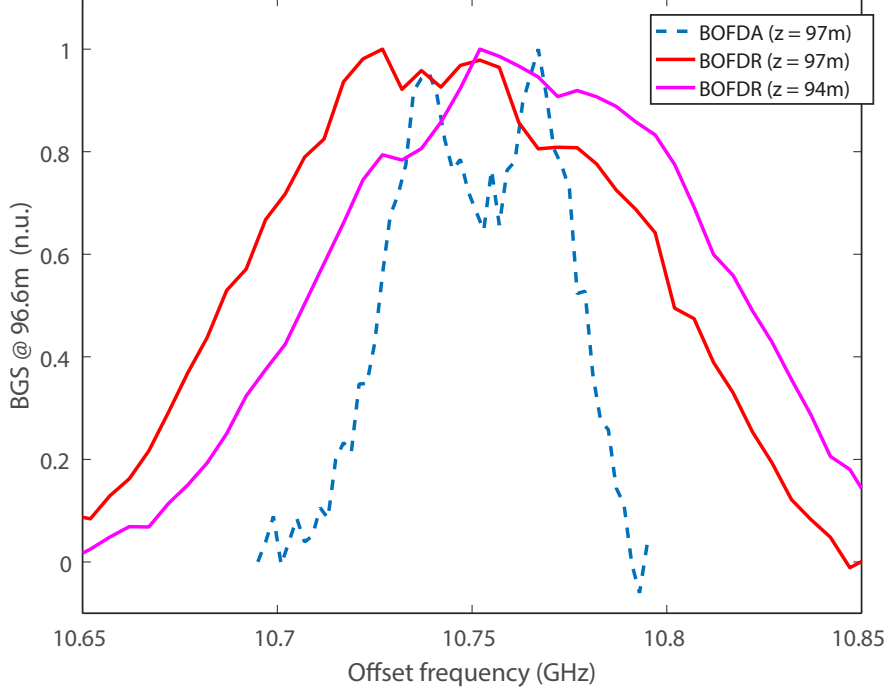


Fig. 3.16. BGS acquired by the BOFDA at the position of the second cold spot ( $z = 97$  m), and BGS acquired by the BOFDR at the same position and at an unperturbed position.

The final test was carried out on a 4970 m long fiber with a BFS of  $\simeq 10855$  MHz, followed by a 3.5 m long fiber with a BFS of  $\simeq 10690$  MHz. The resolution bandwidth of the VNA was set to 1 kHz, while the modulation frequency range was swept from 2 kHz to 100 MHz, with 2 kHz step. Figure 3.17 shows the BFS profile obtained by processing the fiber responses acquired over a microwave frequency range comprised between 11250 MHz to 11700 MHz, at 5 MHz step. It can be observed that the proposed method is able to retrieve the BFS variation after  $\simeq 5$  km of uniform fiber. Note that the standard deviation of the BFS along the uniform fiber is  $\simeq 5$  MHz.

In order to quantify the performance of the proposed method, it is useful to make use of the figure-of-merit (FoM) originally proposed in [27] and reported here for convenience:

$$FoM = \frac{(\alpha L_{eff})^2 \exp(2\alpha L) \sqrt{\delta f \Delta \nu_B}}{\delta z \sqrt{N_{Av}} \sigma_\nu} \quad (3.5)$$

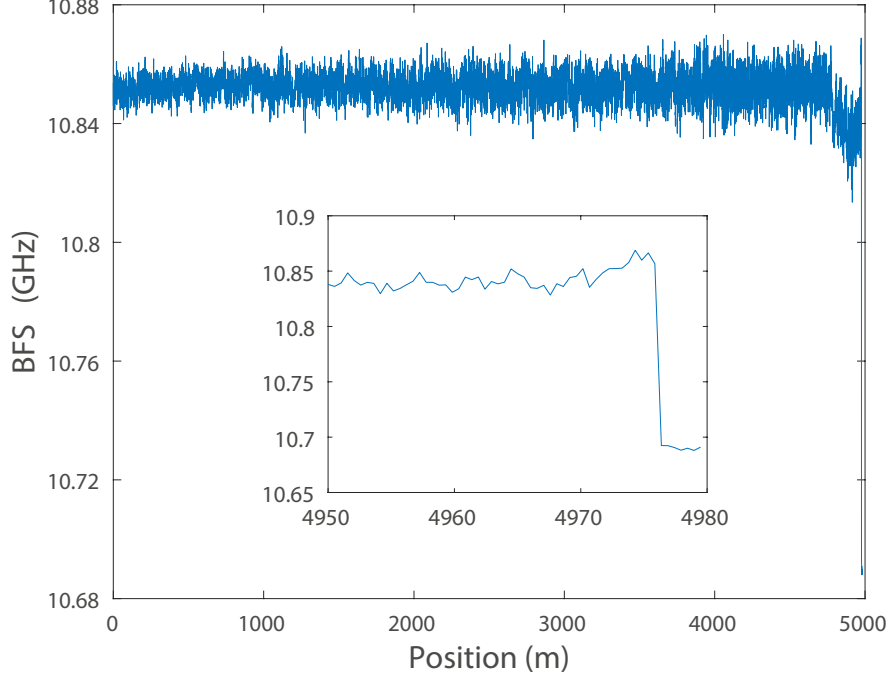


Fig. 3.17. BFS profile reconstruction along a 5 km fiber spool. The inset shows the zoomed view of the last 20 m of the reconstructed profile.

In Eq.3.5,  $\alpha$  is the linear fiber loss,  $L_{eff}$  is the effective nonlinear length of the fiber  $L_{eff} = (1 - e^{-\alpha L})/\alpha$ ,  $\delta z$  is the spatial resolution,  $N_{Av}$  is the number of averages,  $\delta f$  is the frequency sampling step used for the pump-probe frequency scan,  $\Delta\nu_B$  is the Brillouin linewidth, and  $\sigma_\nu$  is the error on the estimated BFS. In this case, a difficulty arises in applying the formulation of Eq.3.5, as it uses the time domain parameter  $N_{Av}$ , which represents the number of acquired traces (one for each launched pulse) that are averaged to increase the SNR. In BOFDR measurements, the SNR is controlled by the RBW parameter of the VNA, which represents the smallest frequency that the VNA can resolve. In order to use the definition of the FoM expressed in Eq.3.5, an “effective” number of averages, equivalent to the chosen RBW, must be found. This number can be found by equating the measurement time in the two methods. In time domain sensors, the (minimum) acquisition time per scanned frequency is given by

$$T_{acq}(time\ domain) = \frac{2nL}{c}N_{Av} \quad (3.6)$$

In BOFDR measurements, the sweep time of the VNA, and therefore the acquisition

time per scanned frequency, is given by [31]

$$T_{acq}(frequency\ domain) = 3 \frac{L}{\delta z} \frac{1}{RBW} \quad (3.7)$$

Equating Eq.3.6 and Eq.3.7, the effective number of averages can be found

$$N_{Av,eff} = \frac{c}{2n} \frac{3}{\delta z} \frac{1}{RBW} \quad (3.8)$$

Referring to the measurement data shown in Figure 3.17 ( $\delta z = 1$  m,  $RBW = 1$  kHz), the number of averages obtained using Eq.3.8 is  $N_{Av} \simeq 361,000$ . Substituting this value in Eq.??, the derived FoM is  $\simeq 6 \cdot 10^{-4} \text{ m}^{-1}$ . Compared to classical BOTDA configurations (FoM  $\simeq 1 \text{ m}^{-1}$ ), or the BOFDA results reported in [24] (FoM  $\simeq 0.07 \text{ m}^{-1}$ ), or even the advanced BOCDA configuration reported in [32] (FoM  $\simeq 0.08 \text{ m}^{-1}$ ), the derived performance for the BOFDR are quite poor.

However, it must be underlined here that the novel Brillouin sensor based on the reflectometry in the frequency domain has good advantages such as the one end accessibility, together with the submeter spatial resolution potentiality, and also the absence of distorting features in the acquired spectra in comparison with BOTDA. Experimental results have demonstrated the capability of these sensors based on SpBS to measure in a distributed way over at least 5 km optical fiber length, with a spatial resolution of 1 m.

### 3.3. Study of a fiber ring laser working on the SLM regime in a BOTDA sensor

As commented before, the research efforts in the field of optical fiber sensors have considerably increased over recent years due to their potential for monitoring long distance with high spatial resolution. A remarkable amount of proposals have been developed to improve the performance of these sensors, including those that use the time domain, highlighting BOTDA configurations, and also others based on the correlation or the frequency domain. These improvements are focused on the enhancement

of their fundamental characteristics, such as the monitoring distance [33, 34], the spatial resolution [3, 35], or the measuring time [36]. However, in this kind of sensors the main feature is the SNR, as it is directly related to the uncertainty in the estimation of the BFS along the fiber, which involves errors in the determination of the temperature and/or strain affecting the fiber. Therefore, the increase of the SNR is a main goal of these systems. Different approaches to achieve it have been proposed during these years. Typically, it can be done by increasing the signal, for instance injecting more power through the pump or the probe waves, or applying some techniques that enable to have more power at the receiver [2]. All of these solutions give rise to an increase of the SNR.

However, it is also important to analyze the impact of different noise sources and their influence on the resulting SNR in BOTDA sensors. These noise sources taking place on these sensors have been studied and modeled [37], concluding that they are very dependent on the fiber length and on the optical powers injected into the fiber, both pump and probe waves. The fiber length determines the nature of the dominating noise source, making it different for short and long sensing distances. The former is dominated by the phase-to-intensity noise conversion induced by the SBS process and the second is ought to a combination of sources, basically dominated by probe double Rayleigh scattering. In addition, the influence of some laser parameters on the noise of Brillouin sensors has been analyzed in other works. In [38], the effect of the laser phase noise has been studied when pump and probe are both continuous waves. It has also been analyzed how the laser linewidth has an effect on the noise system for different pump pulse durations and fiber lengths [39].

As explained in section 2.5, Brillouin distributed sensors based on the SBS process need the interaction of the counter-propagating probe and pump waves, where, in the case of time domain implementations, the latter is pulsed. The first BOTDA implementation was proposed in 1989 by Horiguchi et al. [40]. On this first approach, two independent laser sources were employed to generate the pump and the probe waves respectively and, by measuring the amplification of the probe, the BGS could be determined. This system presents the inconvenience that it is complex to simultaneously adjust both lasers in power and frequency to generate the SBS process. For this reason, a new configuration appeared with only one laser source to avoid these problems [41]. This configuration, with the laser source and an electro-optic modulator, has been the base in most of the new BOTDA configurations. Nowadays, it is possible to

find new implementations, in which more than one laser source is employed, but these proposals are related to amplification effects. For instance, there are different contributions based on using first [42] or second order [43] Raman amplification to improve the performance of BOTDA sensors. An alternative solution is based on injecting into the fiber the signal of a distributed Brillouin amplifier to compensate the attenuation, and amplify the BOTDA pump pulses to achieve larger measurement distances [34]. Finally, an additional study has been carried out using a modified Brillouin ring laser instead of using traditional techniques based on phase-locked loop or optical side-band generation methods with EOMs. This technique has the advantage of enabling a cost-effective solution given that more expensive and complex devices are not required, such as the RF generator. Using this approach it is possible to tune the probe wave for a tuning range of 200 MHz without modulators, enough to analyze the BGS of a fiber, and measure the BFS over a 10 km single-mode fiber with 4 m of spatial resolution [44].

On the other hand, Erbium-doped fiber ring lasers are devices that have attracted attention due to their potential applications in optical fiber sensing, sensor network multiplexing schemes, and instrument testing due to their advantages: they are simple structures with narrow linewidths and compatibility with other optical fiber components. Over recent years, several techniques have been proposed to achieve a stable single longitudinal mode (SLM) operation in fiber lasers, such as the employment of a laser configuration based on serial connection of FBGs using optical circulators [45], or saturable absorbers operating as autotracking ultranarrow-band filters, which always select the dominant mode [46].

Here, the feasibility study of the employment of a fiber laser working as the laser source of a Brillouin distributed sensor is presented. In this contribution, a stable configuration of an EDFRL structure works on the SLM regime, and the main parameters of the ring cavity are analyzed in terms of the laser requirements. Moreover, it is analyzed the BOTDA performance when this fiber laser is employed as the sensor light source.

### 3.3.1. Experimental setup

The proposed fiber laser configuration is depicted in Figure 3.18. The setup uses two sections of commercial Er-doped fiber (I25 from Fibercore). The first 4 m long Er-doped fiber is pumped with a 980 nm pump laser to generate an Erbium amplification around 1550 nm with a bandwidth of tens of nanometers. This amplified signal is launched through a 2 m non-pumped Er-doped fiber acting as saturable absorber to narrow the FBG response due to the spatial hole burning (SHB) effect [47] and reaching the single longitudinal mode regime. After that, the resulting signal returns to the ring configuration via an optical circulator. One of the arms of the 50/50 optical coupler is used for the propagation of the signal within the ring and the other branch is the output of the EDFRL that will be employed in the BOTDA setup.

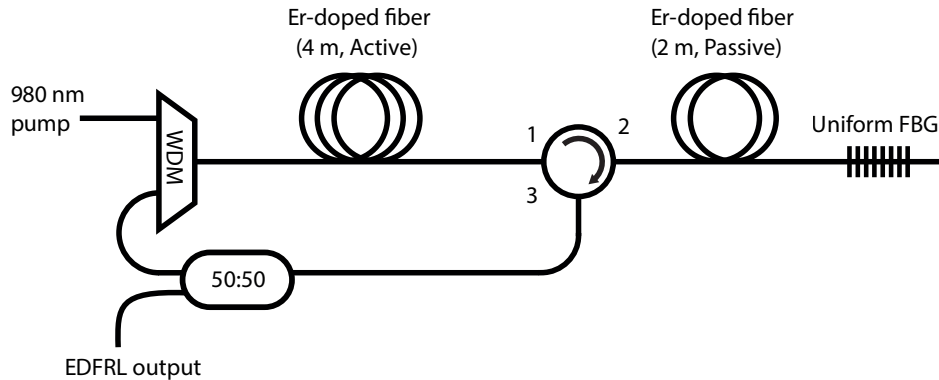


Fig. 3.18. Fiber ring laser configuration employed to achieve a SLM output. A 2 m section of Er-doped fiber is introduced before the FBG as saturable absorber to narrow the FBG response.

The system employed to validate the feasibility of the EDFRL as a laser source for distributed measurements is based on a conventional dual-probe sideband BOTDA implementation. Figure 3.19 shows the proposed setup. This sensor is the most popular BOTDA configuration employed in the literature, where the light from a laser source working around  $\lambda = 1550$  nm is divided using an optical coupler into two branches, obtaining the probe and pump waves. The upper branch of Figure 3.19 is responsible for generating the optical pump pulses. To achieve this, a SOA is employed with an external pulse generator. The duration of the electrical pulses determines the duration of the optical pulses that establish the spatial resolution of the sensor. The use of the SOA allows to reach extinction ratios above 40 dB. The frequency of the pulses defines the maximum length of the FUT, given that only one pump pulse can be transmitted within the fiber at any given moment. A PS and EDFA are used to avoid

the polarization dependence of the SBS gain along the fiber and to boost the pump pulse power, respectively. The probe wave, the lower branch of BOTDA depicted in Figure 3.19, employs an EOM driven by a RF generator to generate the modulated probe. It uses the double-sideband suppressed-carrier technique to generate the two sidebands. The probe is then amplified and afterwards attenuated with the help of an EDFA and a variable optical attenuator to establish a constant power and it is then launched into the FUT. For these measurements, the optical fiber employed to verify the performance of the sensor is a 50 km long SMF. The detection scheme employed is based on the direct detection of one of the two sidebands (Stokes or anti-Stokes) [48]. This means that, once the SBS process has taken place within the FUT, the resulting optical signals are circulated and filtered with a narrow FBG. In this case, the Stokes component is reflected by the FBG and detected with a 125 MHz photodetector. Finally, the electrical signal is acquired and averaged with an oscilloscope.

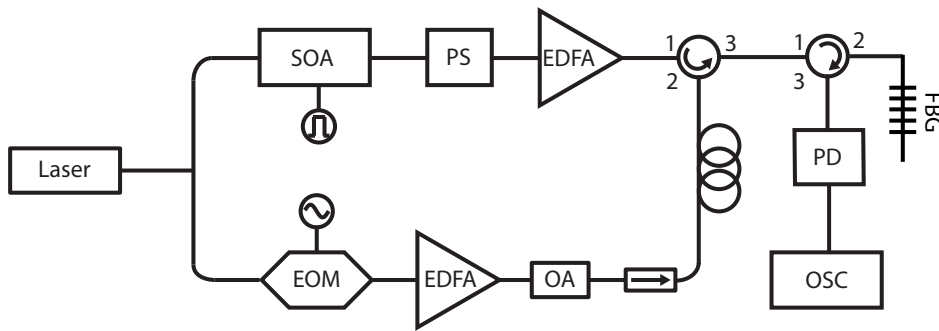


Fig. 3.19. Schematic setup of the BOTDA system used in the experimental tests.

### 3.3.2. Experimental results

A set of experimental tests was carried out to study the feasibility of using the proposed EDFRL to perform distributed measurements within a BOTDA sensor. Some key laser parameters have initially been measured, such as the optical and electrical output spectra and the wavelength and power stability in time, in order to check the SLM working regime of the EDFRL. These results have been compared with the results obtained using a commercial DFB laser diode manufactured by EMCORE, with both lasers working around 1550 nm. One of the advantages of the EDFRL structure is that the operating wavelength could be easily modified between 1500 to 1600 nm only by changing the chosen uniform FBG.

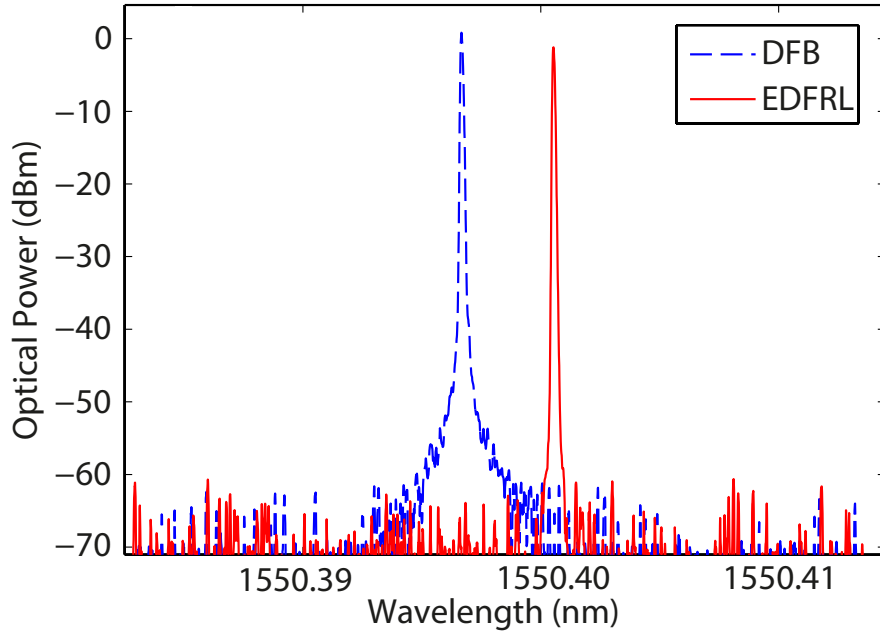


Fig. 3.20. Optical output spectra comparison between DFB (blue dashed line) and EDFRL (red solid line) lasers.

Figure 3.20 presents the comparison of the spectra associated with both lasers using a Brillouin optical spectrum analyzer (BOSA) with a high spectral resolution of 0.082 pm. In order to equalize the output power of both lasers, an optical attenuator has been employed with the DFB to reduce the optical power down to 0 dBm for a better comparison. It is important to note that the wavelength of the EDFRL is easily modifiable by simply changing the temperature/strain conditions of the FBG. For a fair comparison, the FBG has been tuned to achieve an EDFRL wavelength (red solid line) very close to the one produced by the EMCORE laser (blue dashed line). The results show a very similar optical spectrum for both lasers, with a narrow spectrum and monomode behavior.

As explained in [39], the phase noise of the laser is directly proportional to its linewidth, and the noise of a BOTDA sensor increases linearly with the power spectral density of the laser frequency noise, so a narrower laser source would enable an improved performance. In this regard, an analysis of the linewidth of each laser has been carried out with the help of an electrical spectrum analyzer (ESA).

In order to measure the FWHM linewidth of the emitted wavelength, the delayed self-heterodyne detection scheme [49] has been employed. The results, depicted in Figure

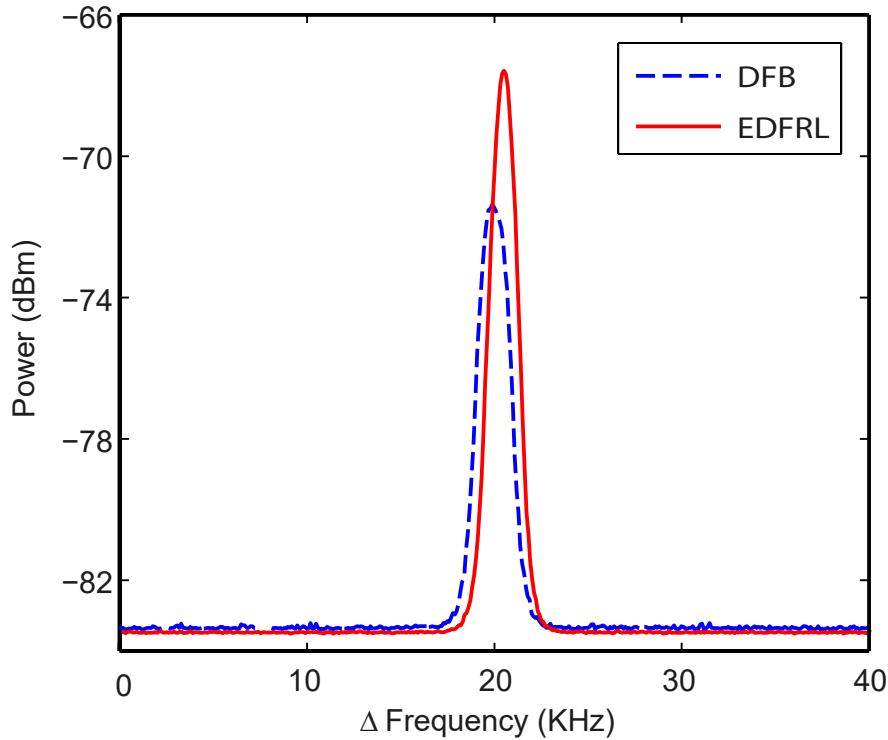


Fig. 3.21. Electrical output spectra of DFB (blue dashed line) and EDFRL (red solid line) lasers.

3.21, show that the EDFRL (red solid line) is slightly narrower than the commercial DFB (blue dashed line), 1 kHz and 1.5 kHz respectively.

Stability, in terms of wavelength and power, is another key parameter associated with laser performance. Some initial measurements, depicted in Figure 3.22, were carried out with the proposed setup explained in the previous section. With this setup, the output wavelength of the EDFRL (red solid line) was very variable during the 4 hours of the test, due to room temperature changes in the laboratory. The commercial DFB (blue dashed line) does not present this problem, as it is always thermally controlled.

The setup was modified to improve the stability. Both non-pumped Er-fiber and FBG were put into a climatic chamber where temperature is under control. The modification of the setup is shown in Figure 3.23.

With this new configuration, it might be feasible to use the EDFRL as source of a BOTDA sensor, given that a fixed and stable operation wavelength is required. In the BOTDA configuration employed for this study (dual-probe sideband implementation),

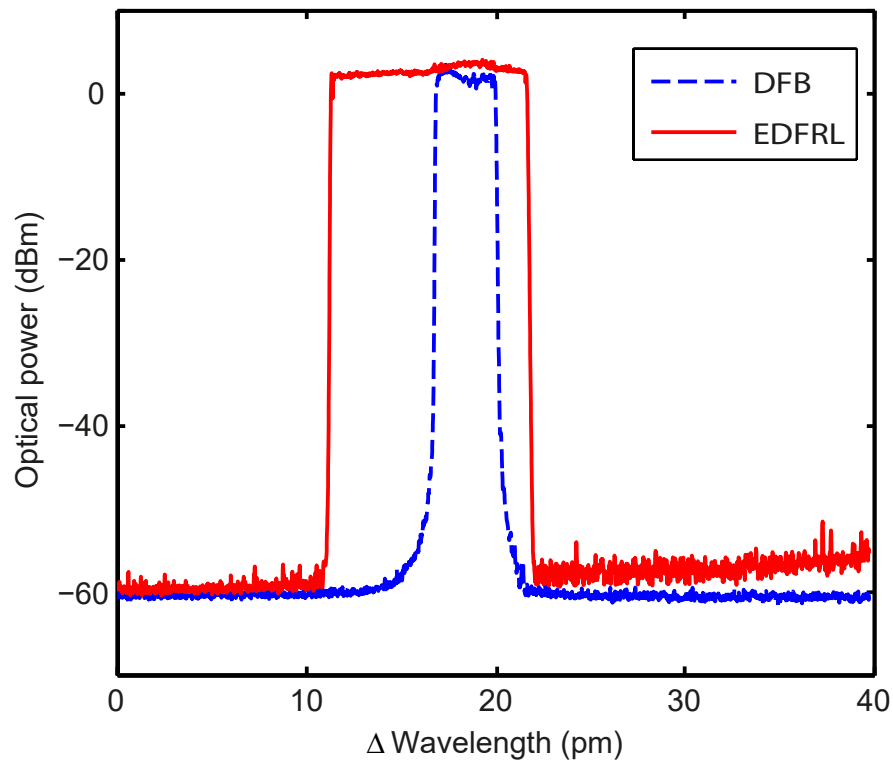


Fig. 3.22. Optical spectral stability of DFB (blue dashed line) and EDFRL (red solid line) lasers after 4 hours.

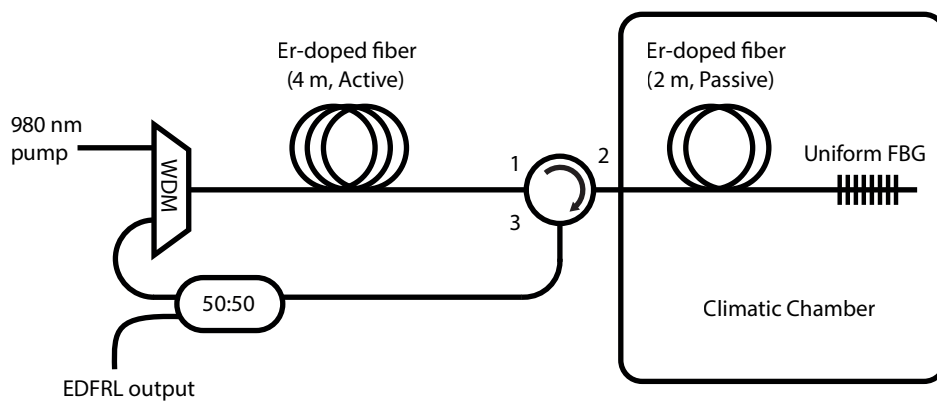


Fig. 3.23. Fiber ring laser configuration employed to achieve a better wavelength stability. A 2m section of Er-doped fiber and the FBG are inside a climatic chamber.

one of the sidebands is filtered out using a narrow FBG (after the interaction takes place) and the other is photodetected and analyzed. For this reason, it is essential that the wavelength of the probe wave, dependent on the laser source, and the filtering FBG exhibit wavelength consistency.

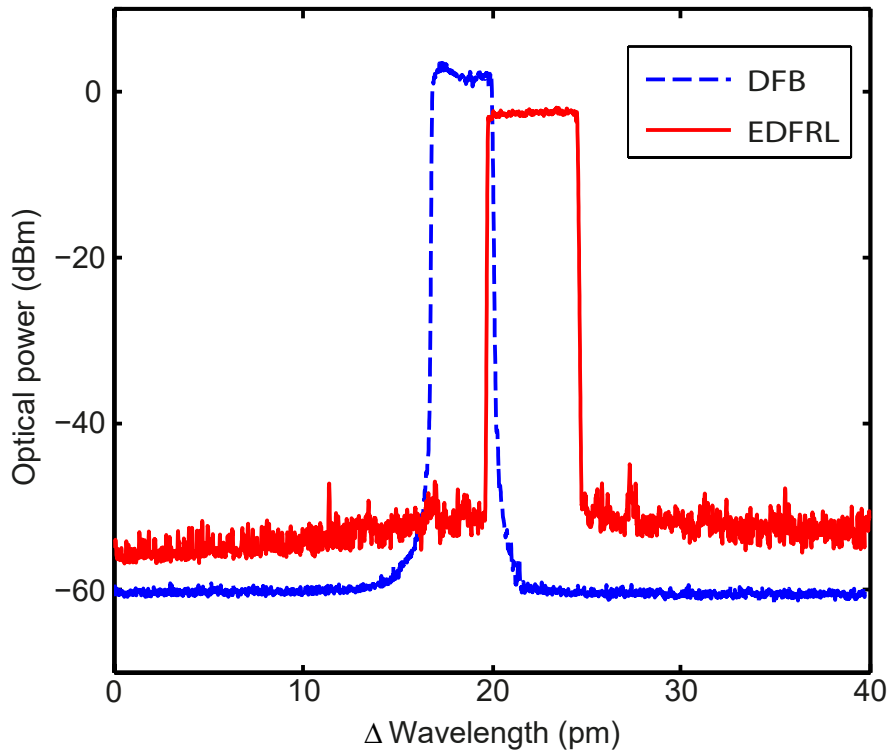


Fig. 3.24. Optical spectral stability of DFB (blue dashed line) and EDFRL (red solid line) lasers after 4 hours using the climatic chamber.

As can be appreciated in Figure 3.24, now the results present a similar behavior for both DFB (blue dashed line) and EDFRL (red solid line) lasers, with a fluctuation of approximately 5 pm with respect to the center wavelength. This value is measured by recording the optical spectra with the BOSA during 4 hours.

Once a suitable performance of the EDFRL was achieved, some distributed measurements were carried out over a long single-mode fiber to check the feasibility of the proposed solution. The sensing fiber is a uniform 50 km single-mode fiber at room temperature, where the last 20 m have been placed inside a climatic chamber at 50°C to measure a hot spot. The spatial resolution of the sensor was set to 5 m, and the frequency of the probe wave was swept from 10.55 to 10.85 GHz with a frequency step of 2 MHz.

Figure 3.25 a) shows the retrieved 3D data of the BGS measured using the BOTDA sensor with the EDFRL. Only the last 5 km of the sensing fiber are shown for a better understanding of the achieved results. The changes of the central frequency of the

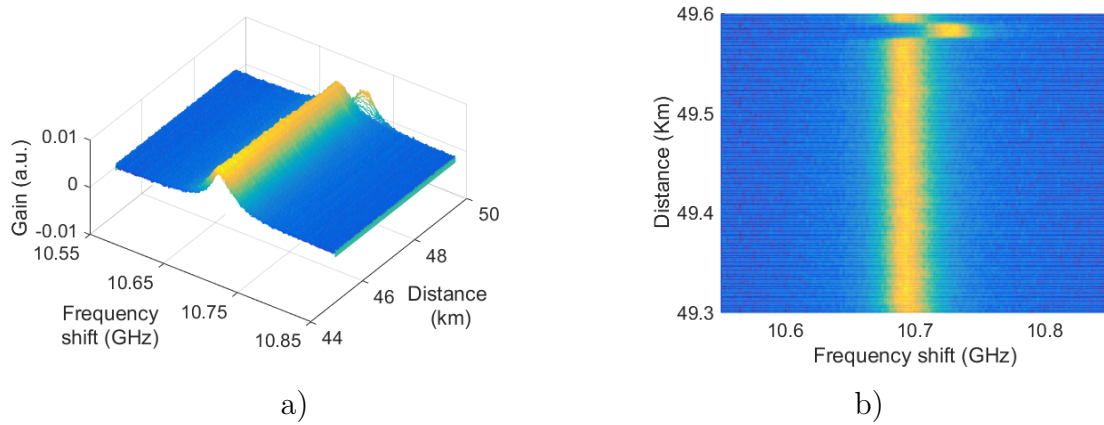


Fig. 3.25. a) 3D map of the last 5 km of the sensing fiber and b) top view of the last 300 m, where the hot spot can be better observed, of the Brillouin gain measured employing the EDFRL

BGS are clearly identified at the end of the fiber due to the presence of the hot spot. A zoomed version of the last 300 m of the gain data is shown in part b) of the same figure using a top view of the 3D map. The shift of the Brillouin frequency (around 30 MHz) can be easily identified at the hot spot section.

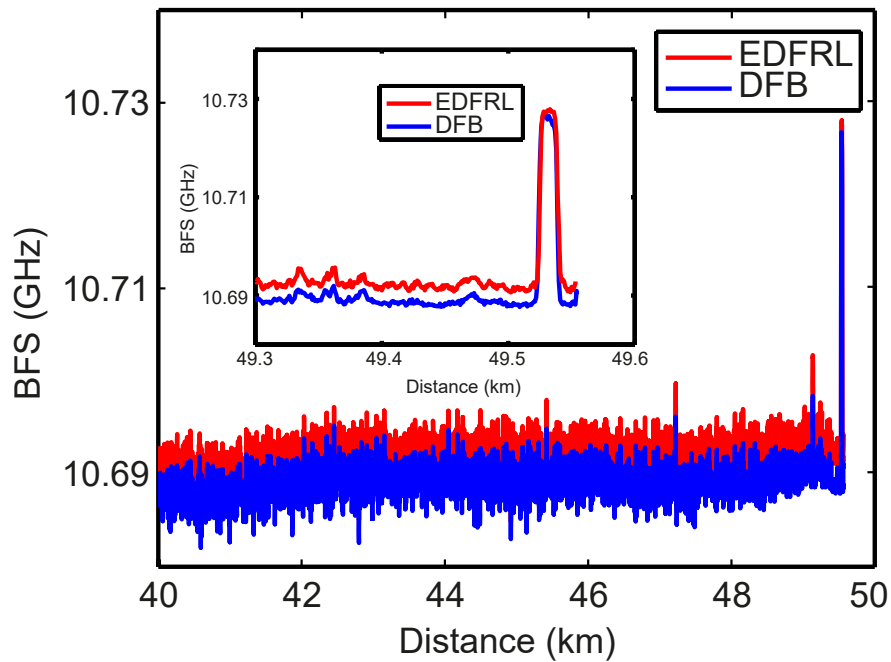


Fig. 3.26. Estimated BFS over the last 10 km of the sensing fiber. The inset only shows the BFS near the hot spot section. The red line represents the BFS measured with the EDFRL and the blue line with the DFB.

After the BOTDA traces are obtained, a Lorentzian fitting is applied to the BGS measured at each spatial point along the 50 km fiber estimating the resulting BFS. The same process is put into practice with other measurements made with the DFB laser at the same conditions, and the results are depicted in Figure 3.26. Again, the estimated BFS only presents the last 10 km of the FUT. As can be observed, the distribution of the BFS along the fiber is practically the same for both lasers, DFB and EDFRL (blue and red lines, respectively). An inset with the BFS over the last 300 meters has also been included in the figure to verify that the hot spot is correctly resolved, showing a difference of about 30 MHz, corresponding to a temperature change of about 30°C, as expected.

Figures 3.25 and 3.26 demonstrate that the EDFRL could be used as the laser source of a BOTDA sensor to perform distributed measurements with similar results than using a DFB laser diode.

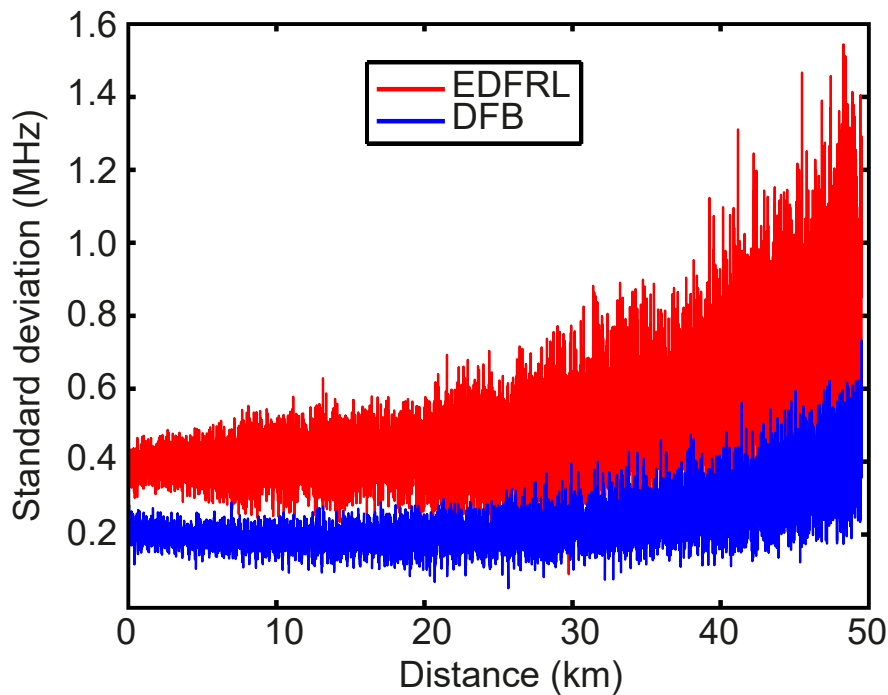


Fig. 3.27. Standard deviation of the estimated BFS vs fiber distance for both lasers (EDFRL in red and DFB in blue)

Finally, an analysis of the error in the determination of the BFS along the optical fiber is performed when the fiber spool is maintained at a constant temperature of 25°C. 10 measurements were performed with each BOTDA configuration always with

the same temperature and strain conditions. The error is calculated as the standard deviation of the BFS at each spatial point of the FUT. The results are not as good as expected, showing that the EDFRL setup exhibits an almost double BFS error estimation in comparison to the DFB. These results have been represented in Figure 3.27, where it is possible to appreciate the whole FUT length. The error varies from 0.4 to 1 MHz for the EDFRL (red line) and from 0.2 to 0.5 MHz when the resulting BFS is measured employing the DFB (blue line).

These experimental measurements, especially with the results of Figures 3.25 and 3.26, have demonstrated the feasibility of using a Erbium-doped fiber ring laser as the laser source of a BOTDA sensor. To verify this possibility, first the main laser features of the fiber laser structure were analyzed. In this analysis, some key parameters such as the output spectrum and the wavelength and power stability were measured and also compared with the commercial DFB. Once a good laser performance was achieved, its implementation on a BOTDA sensor was verified by measuring a hot spot of 20 m at 50°C at the end of a 50 km fiber spool and comparing the results with those provided by a commercial DFB laser. The results achieved at the hot spot section prove that the proposed laser implementation can correctly estimate the BFS, although it exhibits a higher noise level than the DFB, as depicted in Figure 3.27. Nevertheless, the results are promising and the viability of using a fiber laser on BOTDA implementations has been demonstrated. This could open up the possibility of improving the EDFRL configuration or using other Erbium fiber laser approaches to improve the final performance of the sensor. Among other possible advantages, the proposed structure can be tuned over a wide spectral range, from 1500 to 1600 nm, only by changing the uniform FBG, and also to be fine tuned modifying the temperature or strain conditions surrounding the FBG. Moreover, these structures are flexible structures allowing the possibility of including the laser modulation within the ring structure, thus giving rise to interesting solutions for some implementations.

### **3.4. Conclusions**

In this chapter, three contributions have been proposed in an attempt to improve the final performance of Brillouin distributed sensors. All of them are proposals affecting the experimental setups, mainly changing their working principle by modifying some

parts of the conventional implementations.

The first contribution deals with the problem associated with the employment of high probe powers. This proposal is based on the use of BOTDA sensors capable of measuring with a probe power larger than the Brillouin threshold of the deployed sensing fiber. Moreover, this proposed system is free from detrimental non-local effects. The proposed technique establishes their working principle on the use of a dual-probe sideband BOTDA setup in which an optical frequency modulation of the probe waves along the fiber is introduced. This makes the optical frequency of the Brillouin interactions induced by each probe wave on the pump to vary along the fiber so that two broadband Brillouin gain and loss spectra that perfectly compensate are created. As a consequence, the pulse spectral components remain undistorted avoiding non-local effects. Therefore, a very large probe power can be injected, which improves the SNR in detection for long-range BOTDA. Moreover, the probe power can even exceed the Brillouin threshold limit due to their frequency modulation, which reduces the effective amplification of spontaneous Brillouin scattering in the fiber. Experiments demonstrate the technique in a 50 km sensing link in which 8 dBm of probe power is injected.

The second contribution is a Brillouin distributed sensor based on SpBS working on the frequency domain and on optical reflectometry, and known as BOFDR. This system presents some advantages if compared to the other sensing system based on the frequency domain but in SBS: the BOFDA sensor. The most relevant is that they can measure the strain and/or temperature along an optical fiber with one end access given that they measure the SpBS generated from a sinusoidally modulated pump light. Moreover, these sensors are free from the distorting components related to acoustic wave modulation that appear in BOFDA, thus simplifying data processing. The experimental results demonstrated the measurement of the BFS along a fiber length of 5 km, allowing the detection of a 1 m hot spot.

Finally, the last contribution of this chapter is the proposal of a fiber laser to be employed as the optical source of a BOTDA sensor. The designed fiber laser is an Erbium-doped fiber ring laser working on the single longitudinal mode. This solution overcomes some typical fiber ring laser problems, such as multimode operation. Moreover, it presents a very narrow linewidth. To verify the feasibility of using it on a BOTDA setup, its main laser parameters have been analyzed. Once good results in terms of wavelength stability were achieved, it was tested on a dual-probe sideband

BOTDA setup. To verify its performance distributed measurements along a 50 km long fibers were performed, detecting a hot spot of 20 m at 50°C at the end of the sensing fiber. The obtained results have been compared with the ones obtained using the typical DFB laser source employed in BOTDA sensors, exhibiting a higher noise for this proposal. Despite this, the designed BOTDA source has demonstrated the feasibility of using other types of laser sources, such as fiber ring lasers and not only DFB ones, thus enabling the possibility of finding other EDFRL configurations that improve the final performance. Moreover, this kind of fiber ring laser has the advantage of a high spectral range adjustment, from 1500 to 1600 nm.



## Chapter 4

---

# Contributions to the improvement of the performance of BOTDA sensors via processing techniques

---

As explained in the previous chapter, distributed fiber sensors have experienced an intense research effort in the recent years, especially in Brillouin optical time domain analysis (BOTDA) sensors. Most of the advances made in this regard have been traditionally performed by applying modifications to the experimental setups, introducing new configurations or variations to improve their main characteristics. Their performance has been greatly improved in different areas due to the large amount of different proposals that have been appearing these years. For instance, the extension of the sensing range by means of coding techniques [1] or by distributed amplification [2, 3]. Also, there are proposals such as the ones presented in the previous chapter that try to overcome some limitations of the sensor, i.e. non-local effects in BOTDA sensors (Section 3.1) or the presence of sub-peaks in Brillouin optical frequency domain analysis (BOFDA) sensors (Section 3.2).

All of these approaches have something in common: all of them are based on modifying the experimental setup. However, there is a growing presence of proposals based on processing techniques over recent years. In this regard, the most ground-breaking

proposal was probably the one developed by Soto et al., where they employed conventional image (2D) and video (3D) processing strategies to improve the associated signal-to-noise ratio (SNR) [4]. Moreover, artificial intelligence strategies, in particular based on artificial neural networks (ANNs), have also been proposed to perform the Brillouin frequency shift (BFS) estimation [5].

During this chapter, two different approaches based on processing techniques will be proposed to solve or improve some limitations of these sensors, and as a consequence improve their final performance. The first proposal tries to find a solution to a problem yet to be solved of Brillouin sensors: the discrimination between temperature and strain effects. To achieve this, a processing strategy based on the use of ANN has been designed and experimentally validated with BOTDA measurements demonstrating the capability of the solution to discriminate between strain and temperature. On this way, this proposal could be employed to perform an automatic discrimination of both parameters without compromising the complexity or cost of the interrogation unit. The other proposal is the employment of subpixel algorithms to calculate the BFS instead of using classical approaches such as Lorentzian fitting, giving rise to an efficient solution in terms of computational performance.

## **4.1. Simultaneous temperature and strain discrimination in a conventional BOTDA via artificial neural networks**

As previously stated in section 2.5.2, one of the drawbacks of using Brillouin distributed sensors is their fundamental limitation to discriminate between temperature and strain measurements. Within this framework, some efforts are still being devoted to overcoming it. A simple solution, in fact the first proposed to solve this problem, is based on the use of a second sensing optical fiber, deployed to be insensitive to strain [6]. The simultaneous employment of Raman or Rayleigh-based [7] distributed systems in addition to a BOTDA may be a possible solution, although at the expense of increasing the complexity and cost of the final setup. Some authors have also proposed the use of large-effective-area (LEAF) [8] or photonic crystal (PCF) fibers [9]. In these cases several peaks with different temperature and strain dependences

appear in the Brillouin spectra, allowing the desired discrimination. Recently, discrimination of temperature and strain in distributed measurements has been achieved by means of a system combining standard coherent optical time-domain reflectometry and Rayleigh-based distributed birefringence measurements in an elliptical-core polarization-maintaining fiber [10]. A dual-BOTDA scheme has also been proposed, where the simultaneous measurement of temperature and strain is performed using the different wavelength scaling factor of temperature and strain coefficients at 850 and 1550 nm [11].

These proposals typically imply the use of more complex systems or special fibers, thus affecting the cost of the resulting systems. Trying to find an alternative solution to this discrimination, the use of a conventional BOTDA system has been proposed. This proposal considers a standard single-mode fiber as fiber under test (FUT), including an artificial intelligence solution, in particular an ANN, used to process the BOTDA data and perform the requested discrimination. Although the temperature and strain resolutions considered in the proposed solution are still clearly lower than those obtained in previous works, the resulting BOTDA setup complexity and its associated cost would remain unaltered. Distributed simultaneous temperature and strain measurements will demonstrate the feasibility of the proposed solution in the following sections.

#### 4.1.1. Principle of operation

As previously stated in section 2.5.2, the BFS of Brillouin distributed fiber sensors shows a linear dependence with the estimated temperature and strain surrounding the sensing fiber, which can be expressed as follows [12]

$$\nu_B(T, \varepsilon) = C_\varepsilon \Delta\varepsilon + C_T \Delta T + \nu_B(T_0, \varepsilon_0), \quad (4.1)$$

being  $C_\varepsilon$  and  $C_T$  the strain (MHz/ $\mu\varepsilon$ ) and temperature (MHz/ $^\circ\text{C}$ ) coefficients,  $\Delta T$  and  $\Delta\varepsilon$  the temperature and strain changes at a given fiber location and  $T_0$  and  $\varepsilon_0$  the reference temperature and strain. Apart from this widely known frequency dependency, there are some other subtle changes in the Brillouin gain spectrum (BGS) depending on the magnitude affecting the sensing fiber. As detailed by Nickles et al. in [13], the BGS shows a decrease in its linewidth and an increase in the associated Brillouin gain

for increasing temperatures. However, an increasing strain does not clearly affect the BGS width, while the resulting gain decreases in this case.

These subtle variations might be difficult to be used for simultaneous temperature and strain measurements in a conventional BOTDA scheme, but in this approach the use of an ANN is proposed to perform the requested temperature and strain classification or discrimination. However, some pre-processing strategies have been also considered adapting the acquired BOTDA data and trying to obtain a suitable performance, in an attempt to improve the classification rate achieved in a previous feasibility study [14].

The first step consists on a normalization of the amplitude of the acquired BGSs, as it has been assumed that they will not provide useful information for the temperature/strain discrimination, and they might even compromise the system performance. This normalization has been performed in all the experimental tests carried out. A so-called spatial filtering has also been considered to avoid the negative effect of excessive inhomogeneities in the estimated BFS. In particular, spectra of the same class (i.e. associated with the same temperature and strain) with a BFS deviation over 5 MHz have been removed from the dataset. These two processes have always been implemented, but there are some other stages whose influence in the system performance should be evaluated:

- Lorentzian-Gaussian fit: this process, usually employed in BOTDA systems, enables a better estimation of some key spectral features such as the BFS or the BGS linewidth. 251 spectral samples are considered for each frequency sweep.
- Manual selection of parameters: implies the possibility of directly using the estimated BFS and BGS linewidth of each new spectrum after a Lorentzian-Gaussian fitting process.
- Principal component analysis (PCA): a common solution to reduce the dimensionality of the data entering an ANN [15], this technique will be explained in more detail in the following.

PCA is a technique used to express a set of variables into a new orthogonal basis, where the new basis vectors are ordered in terms of the variance of the original data,

from high to low (i.e. these new vectors are the data directions containing the most relevant information). This transformation implies that the variables of the new dataset are uncorrelated. In this case, the original dataset used as input for the PCA algorithm will be a  $m \times n$  matrix ( $X$ ), where  $m$  denotes the number of frequencies in each individual BOTDA spectrum (251) and  $n$  the number of observations. The goal of PCA is to build the matrix  $W$  such that  $Y = WX$ , where  $Y$  is the resulting transformed data and  $W$  represents the linear operation needed to obtain  $Y$  from  $X$ . The process implemented by PCA to obtain  $W$  can be summarized as follows:

- Subtract the mean of each row in  $X$
- Calculate the covariance matrix  $C = XX^T = EDE^T$ , where  $D$  is a diagonal matrix containing the eigenvalues of  $C$  and  $E$  are the eigenvectors of the covariance matrix  $C$ .
- Calculate the eigenvectors and eigenvalues of the covariance matrix  $C = VDV^{-1}$ , where  $V$  is a matrix with the eigenvectors of  $C$ .
- Order the components in  $V$  in terms of the contribution of their associated eigenvalues to the total variance of the dataset.

After this last step  $W$ , the matrix that allows the desired transformation, is obtained as  $W = V$ . A criterion is now required to establish the number of principal components or columns in  $W$  to be used. Eq.4.2 defines the percentage of variance (information) that is kept after PCA, where  $I_K$  is this variance,  $K$  the number of chosen principal components (eigenvectors) and  $\beta_i$  the  $i_{th}$  eigenvalue:

$$I_K = \frac{\sum_{i=1}^K \beta_i}{\sum_{i=1}^m \beta_i} \cdot 100\% \quad (4.2)$$

It is worth noting that PCA has also been used in other BOTDA applications, for example to perform a pattern recognition for the extraction of temperature distributions [16]. With these possibilities of pre-processing the performance of the ANN can be evaluated, although the design of the network may also influence the final performance. ANNs are a computational approach that may solve a wide range of problems. They try to mimic, in a way, the behavior of the human brain, and they are formed by

neurons arranged in different layers. A standard implementation is constituted by an input layer, one or two hidden layers and an output layer. This arrangement is known as a feedforward implementation, where the input data are transmitted to the hidden layer and then to the output layer.

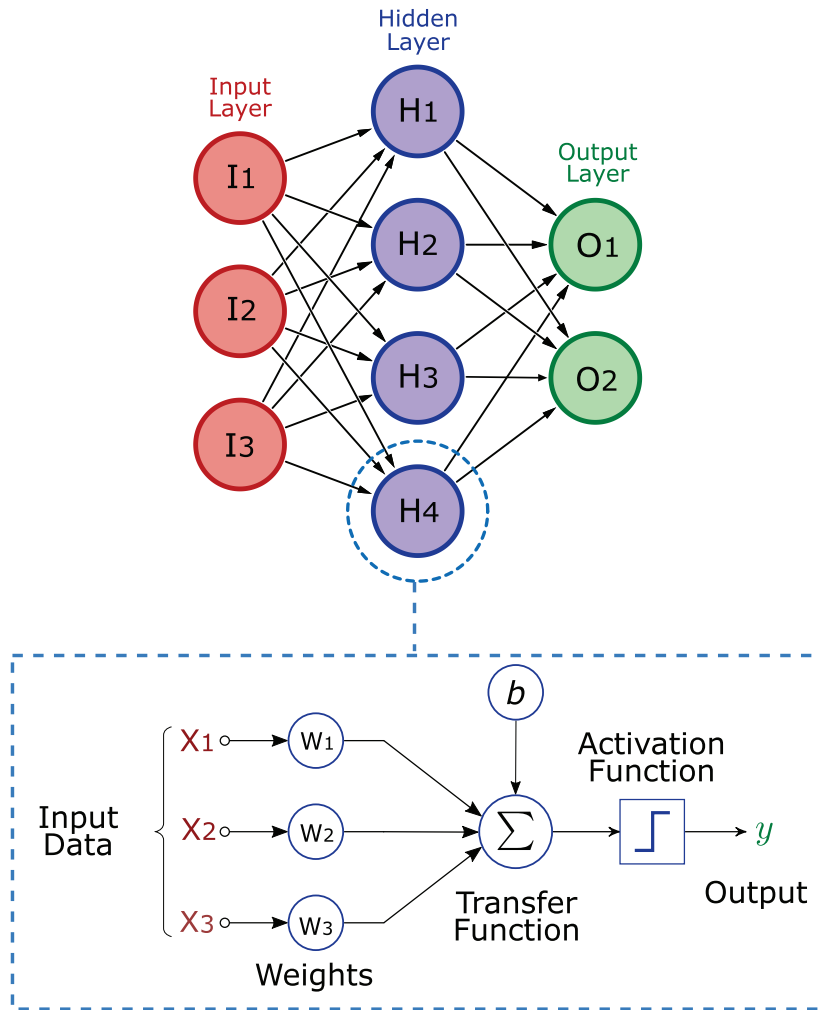


Fig. 4.1. Schematic representation of an artificial neural network.

In Figure 4.1, a simple ANN with 3 input neurons, 4 neurons in a single hidden layer and 2 output neurons has been represented as an example. As can be observed in the inset, a neuron receives several inputs ( $x_1$  to  $x_3$  in the example) that have an associated weight ( $w_1$  to  $w_3$ ) indicating the relevance of that input over the output. A weighted combination of inputs is then formed after the transfer function, and the corresponding output will be activated or not depending on the threshold established by the activation function. As ANNs work by activating a specific output neuron for

a given input, it is necessary to initially consider a training process where the weights will be determined by means of a given training algorithm. In this stage, the input training data are labeled so that the output neuron to be activated is known. Typically, a 70% of the whole dataset is devoted to the training process, while the remaining 30% is equally divided between the validation and test sets. The validation set is used to perform a final tuning of the parameters of the network, for example the number of hidden layers or neurons, but its associated classification rate might be biased as this set is used to select the final ANN model. Consequently, the test set is used only to evaluate the performance of a fully trained network.

It is important to note that two different stages can be considered in the implementation of the proposed solution for temperature and strain discrimination in a BOTDA system. The first stage, represented in Figure 4.2 a), can be understood as off-line, as it consists in the design and definition of the parameters of both pre-processing techniques and ANN. In this case, the former will be basically devoted to PCA, with the definition of the matrix  $W$  to apply the transformation to the original data and the definition of the number of principal components to be used. The most suitable ANN for the problem under analysis and the provided data will be completely defined once the training and validation steps have been performed. The computational cost derived from this stage will not penalize the on-line operation of the final system, schematically represented in Figure 4.2 b).

The specific parameters and ANN design selected to carry out the experimental analysis of the proposed solution will be discussed in the results section 4.1.3.

### 4.1.2. Experimental issues

The system used for the acquisition of the required measurements was based on a conventional dual-probe sideband BOTDA implementation. The setup is depicted in Figure 4.3. It can be observed that a conventional system was selected, where a distributed feedback laser (DFB) source working at  $\lambda = 1550.92$  nm generates the light employed. The optical coupler located at the output of the laser source divides the light into two branches, the probe and the pump. A semiconductor optical amplifier (SOA) is used in the upper (pump) branch to obtain high extinction-ratio pulses. The pump pulse is amplified via an Erbium-doped fiber amplifier (EDFA) and a polarization

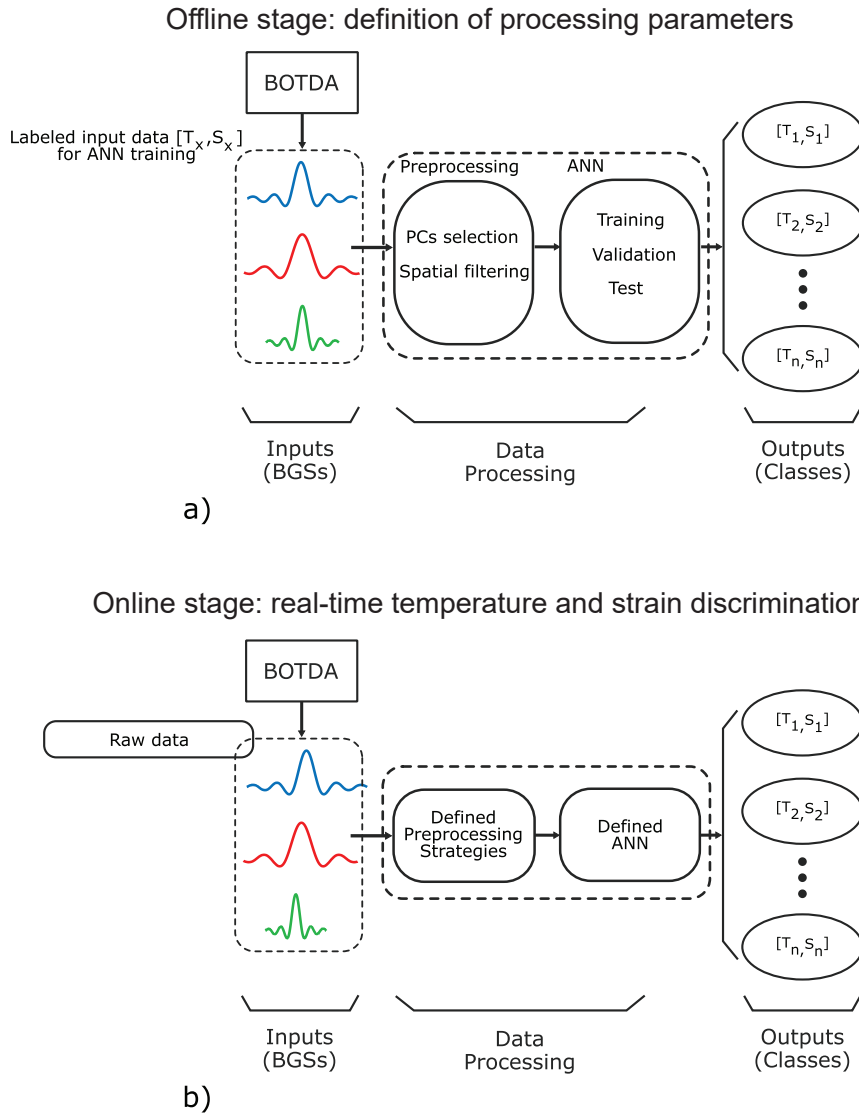


Fig. 4.2. Schematic representation of the proposed solution: a) off-line stage: definition of pre-processing and ANN parameters and architecture and b) online stage: real-time temperature and strain discrimination.

scrambler is also deployed in that branch to avoid the polarization dependence of the SBS gain along the fiber, while the probe wave is generated via a radio frequency generator and a electro-optic modulator (EOM), thus giving rise to two sidebands and a carrier that is suppressed by adjusting the bias voltage of the EOM. Both sidebands are transmitted to the FUT, where they will interact with the pump pulse. The detection stage is formed by two optical circulators, which allow to select the lower frequency sideband with a fiber Bragg grating (FBG). The BOTDA traces are detected with a

125 MHz photodetector and an acquisition card, once the probe signal is filtered.

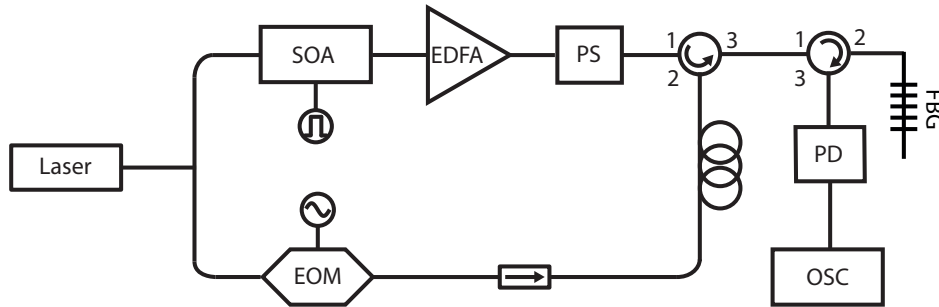


Fig. 4.3. BOTDA setup employed in the experimental tests.

Some initial tests were performed to verify that the hypothesis [13] described in the previous section was correct. In particular, the evolution of the BGS width was analyzed in terms of the temperature for various widths of the chosen pump pulse. Given that a fiber spool was used in this case, a constant tension close to 0 strain could be assumed, although the winding process will imply some residual stress. As can be observed in Figure 4.4 a) there is a clear decreasing trend in the BGS width for increasing temperatures from 0 to 80°C for all the pump pulse widths considered (from 10 to 100 ns). The tests were carried out using a climatic chamber. These results were obtained using a FUT of around 2.8 km and performing an average over 1000 BOTDA traces. A similar analysis for increasing strains (considering in this case a constant temperature of 22°C) is presented in Figure 4.4 b). In this case, only several tens of meters (about 40 m) were homogeneously strained due to the limitations imposed by the strain setup. This also limited the pump widths to be considered: 10, 15 and 20 ns. A frequency step of 2 MHz and a Lorentzian-Gaussian profile were considered in this case. The results shown in Figure 4.4 b) are in good agreement with those reported by Nickes et al. [13], as no clear trend can be derived from these tests. It is worth noting that the strain was measured in number of turns of the linear positioner employed to strain the fiber. Each turn corresponds to 384  $\mu$ strains.

For a further analysis of the acquired data, the BFS standard deviation for each pair of temperature/strain and pump pulse width has been calculated considering 10 consecutive measurements with the same environmental conditions. These results are presented in Tables 4.1 and 4.2.

Apart from the BOTDA setup, it was also necessary to design and implement a setup enabling to develop the required simultaneous temperature and strain measurements.

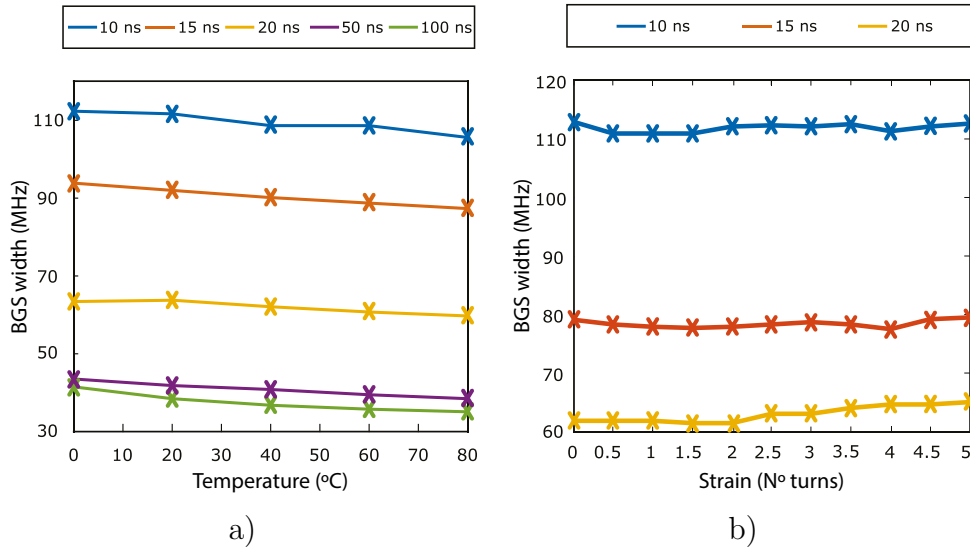


Fig. 4.4. Evolution of the BGS linewidth for different pump pulse widths for: a) increasing temperature and b) increasing strain.

Table 4.1.: BFS standard deviation ( $\sigma$ ) (MHz) for different temperatures and pump pulse widths.

Temperature (°C)	Pulse width (ns)				
	10	15	20	50	100
0	0.49	0.29	0.30	0.12	0.11
20	0.24	0.44	0.16	0.13	0.20
40	0.68	0.42	0.19	0.12	0.08
60	0.80	0.53	0.23	0.12	0.14
80	0.44	0.43	0.56	0.14	0.12

As it was impossible to perform distributed strain measurements within the climatic chamber, a setup similar to the one described in [14], where a feasibility study of this approach was presented, was chosen. The system (Figure 4.5) is an aluminium water tank covered by a thermal insulator material and formed by an air pump (1) used to get an homogeneous water temperature within the tank, an electrical resistance (2) to control the water temperature and two wheels (3 and 4) where the hot spot section of the FUT is deployed. Figures 4.5 b) and c) show details of the linear positioner used to strain the fiber coiled in the wheels (located under one of these wheels) and the control temperature unit used to established the desired temperature.

For the simultaneous temperature/strain tests, a range of temperatures between

Table 4.2.: BFS standard deviation ( $\sigma$ ) (MHz) for different strains and pump pulse widths.

Strain (N° Turns)	Pulse width (ns)		
	10	15	20
0	0.61	0.20	0.08
0.5	0.35	0.12	0.11
1	0.25	0.12	0.19
1.5	0.3	0.18	0.13
2	0.22	0.14	0.14
2.5	0.29	0.11	0.18
3	0.34	0.15	0.09
3.5	0.19	0.18	0.26
4	0.31	0.10	0.09

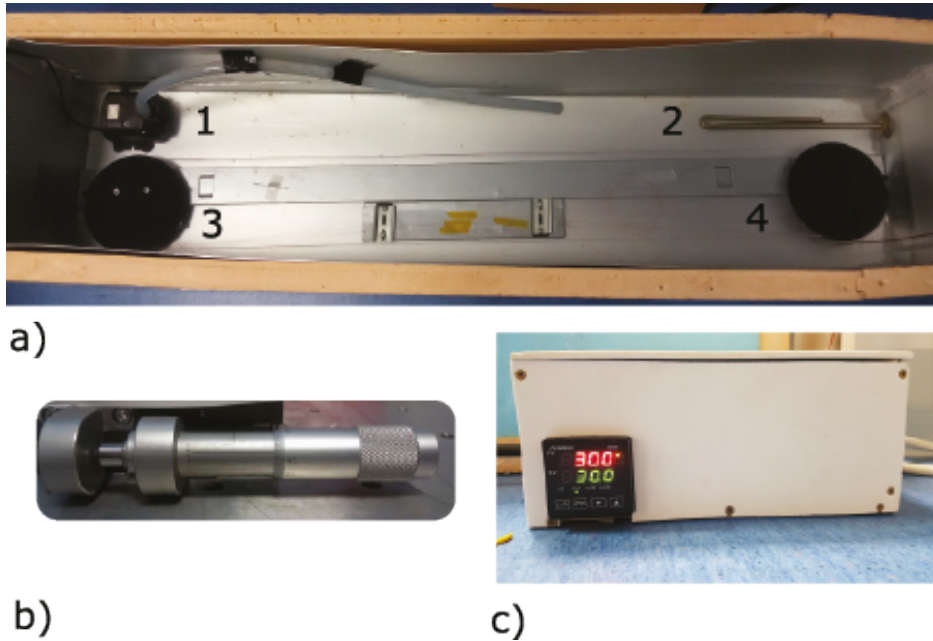


Fig. 4.5. Setup designed and implemented for the development of the simultaneous temperature and strain measurements: a) aluminium water tank; b) linear positioner and c) temperature control unit.

22 and 62°C (with steps of 10°C) was chosen to facilitate the development of the experiments. The strain range was in this case the one derived from considering 0 to 4 turns (with steps of 0.5 turns) of the linear positioner, thus from 0 to 1536  $\mu$ strains. While performing the simultaneous temperature/strain measurements, a study of the

BFS error in the hot spot section was performed for a pump pulse width of 20 ns (chosen for the subsequent analysis) and the results are presented in Table 4.3. Given the difficulty to obtain homogeneous temperature and strain distributions in the setup, the error was calculated in this case as the mean absolute deviation of the BFS associated with the hotspot section, i.e. the average distance between the BFS associated with each spatial sample within the hotspot and the BFS mean of the whole hotspot section. It can be noticed how for the same strain, the estimated error increases with increasing temperatures, given the difficulty to obtain a completely uniform water temperature distribution within the tank, especially for higher temperatures. It should be mentioned that the FUT is in this case formed by 70 m of fiber (the length of 1 turn in the strain setup is equivalent to approximately 1.1m), in comparison to the 40 m FUT used for Tables 4.1 and 4.2.

The evolution of the BFS for different strains (0 to 4 turns) at different temperatures (22 to 52°C) is depicted in Figure 4.6. It can be observed that the strain in the FUT is not homogeneous, but it exhibits some peaks associated with the manual deployment of the sensing fiber. This fact implies in fact a worse-case scenario for the proposed solution, as the ideal situation for an optimal performance of the ANN would be completely homogeneous BFSs.

Table 4.3.: BFS error (MHz) for different temperatures and strains and a pump pulse width of 20 ns.

Strain (N° Turns)	Temperature (°C)				
	22	32	42	52	62
0	4.41	5.29	5.57	5.64	5.98
0.5	4.51	5.68	5.64	5.67	6.1
1	4.60	5.74	5.65	5.68	6.13
1.5	4.75	5.69	5.76	5.90	6.35
2	4.68	5.69	5.85	5.93	6.49
2.5	4.81	5.83	5.86	5.94	6.52
3	4.85	5.84	5.88	5.97	6.74
3.5	4.87	5.86	5.96	5.96	6.76
4	4.94	5.84	5.93	5.98	6.97

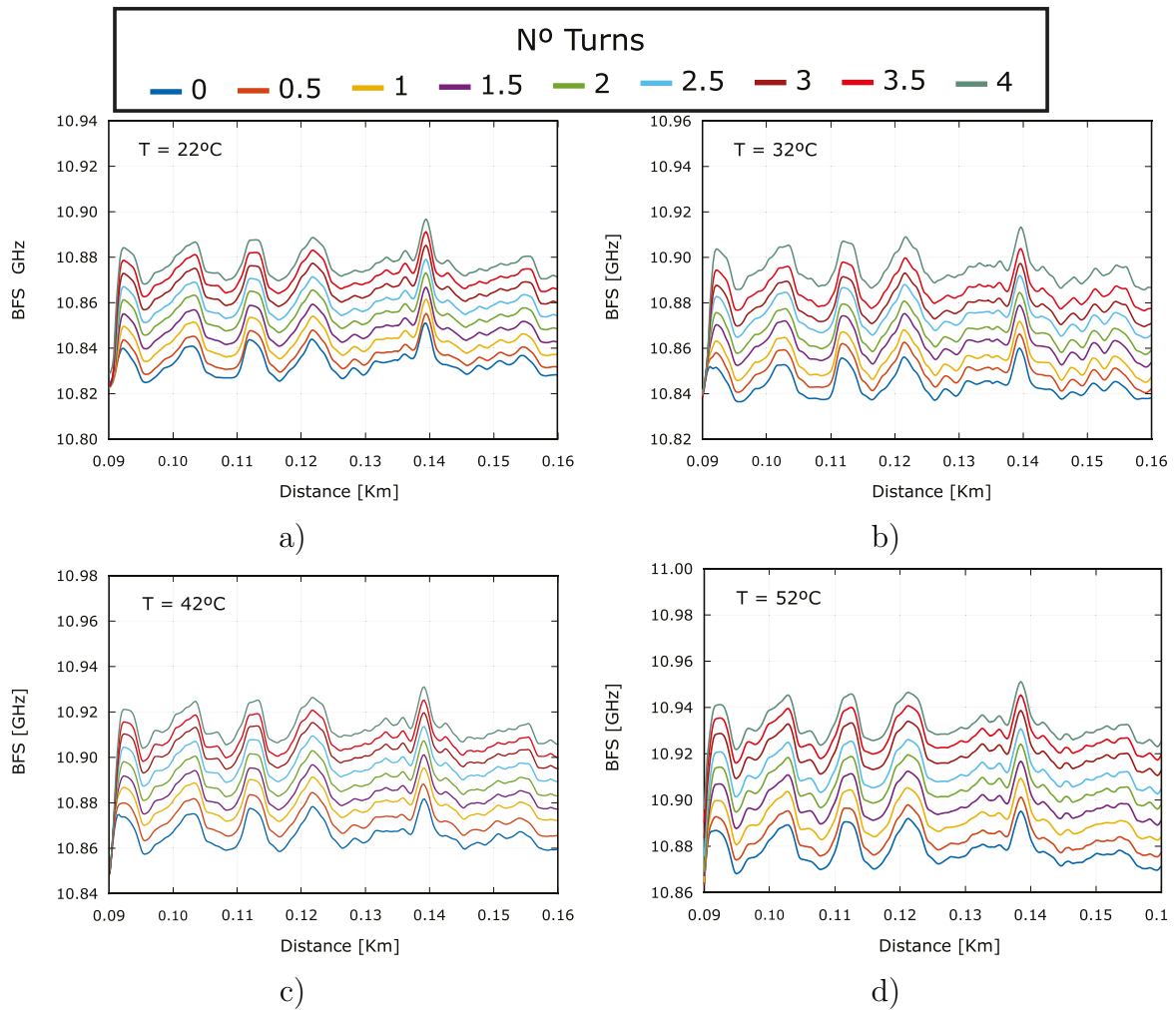


Fig. 4.6. BFS evolution for simultaneous measurements of temperature and strain.

### 4.1.3. Results

Once the experimental tests were performed, it was necessary to adapt the acquired data via the pre-processing strategies already introduced in Section 4.1.1. As already commented, the normalization of the BGS amplitude and the spatial filtering have always been considered, while the remaining three (Lorentzian-Gaussian fit, manual selection of parameters and PCA) have been independently evaluated. After applying PCA to the BOTDA data, 62 principal components were chosen using the criterion of obtaining the best classification rate for the ANN.

Regarding the ANN design, the number of neurons in the input layer will vary de-

pending on the pre-processing strategy considered: 251 input neurons for the Lorentzian-Gaussian fit, 2 for manual selection of parameters and 62 for PCA (same number as chosen principal components). The number of neurons in the hidden layer/s will be modified to analyze the performance of the network. The number of output neurons will remain constant at 40, the number of different classes (temperature and strain pairs) under analysis. The scaled conjugated gradient algorithm with backpropagation has been chosen for the training stage, given its high rate of convergence. A sigmoid activation function has also been considered.

For each pre-processing and ANN configuration, the whole dataset acquired during the experimental tests has been divided into training (70%), validation (15%) and test (15%) datasets. For each considered configuration, the data used for one of these classes have not been shared with the other two classes. After several studies, the best results in terms of the classification performance of the ANN were obtained via PCA, and also considering the normalization and spatial filtering processes described in the previous sections. The employment of the Lorentzian-Gaussian fit gave rise to a classification rate (number of correct associations of an input to its corresponding output over the whole number of inputs evaluated) of about 60%, while the manual selection of the input data to the network allowed to obtain a 70%. The classification results offered via PCA are presented in Table 4.4, where *Neurons* indicates the number of neurons in the hidden layer and *Training*, *Validation* and *Test* the corresponding classification results for each stage. The best result is obtained when 80 neurons are used in the hidden layer, offering a classification rate of 88.2% for the test set. A higher number of neurons in this layer gave rise to an overfitted solution.

Table 4.4.: ANN classification results via PCA.

<b>Neurons</b>	<b>Training (%)</b>	<b>Validation (%)</b>	<b>Test (%)</b>
20	86.9	77.5	<b>77.1</b>
25	88.3	78.7	<b>78.5</b>
30	88.1	80.4	<b>80</b>
35	88.9	81.4	<b>80.6</b>
40	91.3	82.2	<b>82.7</b>
50	93.8	83.6	<b>83.8</b>
80	96.8	87.7	<b>88.2</b>

The analysis of the network cross-entropy ( $ce$ ) also offers very interesting information about the process. This parameter calculates the difference between the network output and the expected result ( $target$ ). In this way, the cross-entropy highly penalizes those situations where the output  $y$  is far away from the target output  $t$ . It is calculated as  $ce = -t \cdot \log(y)$ , and lower values of  $ce$  imply a better performance of the network. Figure 4.7 shows the cross-entropy for the training, validation and test sets when the hidden layer is formed by 80 neurons. It can be observed how the cross-entropy associated with the training set decreases continuously, while this parameter remains constant for the validation and test sets from iteration #47. This is precisely where the training stage ends, given that the cross-entropy of the validation stage is no longer decreasing. It is also interesting to note that the cross-entropy training profile remains close to the other two curves, thus suggesting that there is no overfitting to the training set in this case.

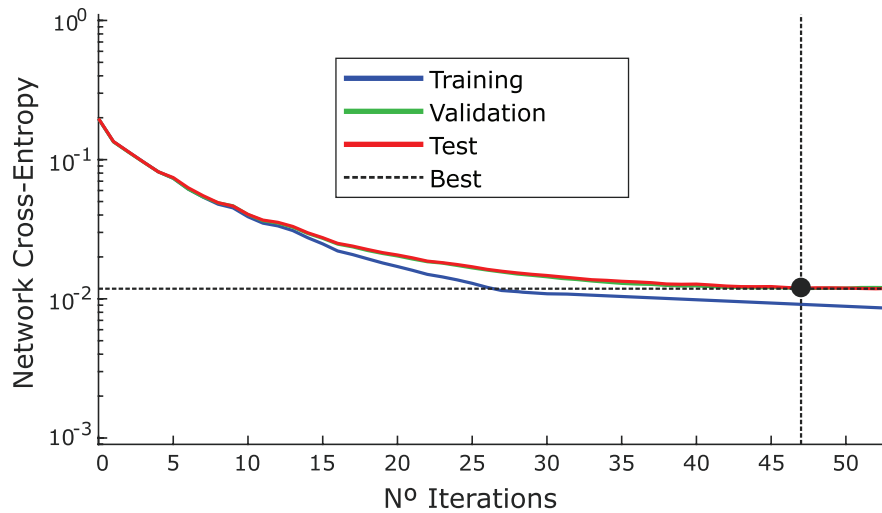


Fig. 4.7. Network cross-entropy for the best classification result achieved with 80 neurons in the hidden layer.

Finally, it is interesting to analyze the results derived from the use of the Lorentzian-Gaussian fit against the raw Brillouin spectra. Although the classification rates are lower in both cases in comparison to those presented in Table 4.4 using PCA, it is worth noticing that better classification rates (around 80%) were achieved when the classical fit to the acquired BGSs was not performed. This was initially surprising considering the starting premise considered in this work; however, an analysis of the intensity noise of the acquired spectra enables a possible explanation. Table 4.5 presents the variance of the noise associated with the spectra of different pairs of temperature/strain

considered, once the gain normalization was carried out. It can be observed how there is no clear trend between temperature and the noise variance, but the latter increases with increasing strain. It seems that the ANN might be using this feature to help in the classification process among the different categories, thus improving the classification results when that information is available (raw spectra) in comparison to the Lorentzian-Gaussian fit approach, where the intensity noise is removed.

Table 4.5.: Noise variance ( $\sigma^2$ ) for the intensity-normalized BGSs (a.u. $\cdot 10^{-4}$ )

Strain (N° Turns)	Temperature (°C)				
	22	32	42	52	62
<b>0.5</b>	1.9576	1.8351	1.9743	1.8224	1.9871
<b>1</b>	2.1673	1.9512	2.007	1.8938	2.0885
<b>1.5</b>	2.2137	1.9188	2.2070	1.9237	2.1870
<b>2</b>	2.2256	1.9824	2.2716	1.9418	2.3531
<b>2.5</b>	2.2463	2.0424	2.2187	2.1804	2.4302
<b>3</b>	2.4432	2.1137	2.3703	2.3396	2.5666
<b>3.5</b>	2.4577	2.3413	2.4951	2.4198	2.6631
<b>4</b>	2.5295	2.3853	2.5748	2.5391	2.6935

These obtained results demonstrate the feasibility of discriminating temperature and strain measurements in a BOTDA sensor via the employment of processing strategies. In this case, the use of PCA in addition to ANN has enabled to obtain a classification rate of around 90% even when the experimental tests have been not as good as they could have been due to the difficulties to perform good measurements affecting both parameters at the same time. Other pre-processing stages have been also employed, concluding that the use of PCA before ANN provided the best classification rates. Moreover, it is important to notice that the proposed solution does not need extra time for processing, achieving real-time processing times, due to the on-line stage (processing of each new measured BGS) only takes a few milliseconds.

## 4.2. Brillouin frequency shift estimation in BOTDA via subpixel processing

Another interesting aspect to explore in Brillouin distributed fiber sensors is the curve fitting process required to estimate the BFS of the sensor through analysis of the measured BGS data.

As previously explained in Section 2.5, Brillouin distributed sensors need to estimate the BFS previously to calculate the temperature or strain conditions of the sensing fiber. However, the BFS value is not a direct parameter obtained after performing a distributed measurement. To obtain this estimated BFS it is necessary to make the fitting of the measured BGS data that it is recovered after the interaction between the probe and the pump waves. This fitting process is typically done using a Lorentzian fit [17], but several works have dealt with this problem with more sophisticated proposals based on the Levenberg-Marquardt method [18], among others, trying to increase the accuracy and also the computational efficiency.

Within this framework, the feasibility of the employment of subpixel algorithms as an alternative solution for the curve fitting of the Brillouin scattering spectra and the associated frequency shift estimation has been studied. Their computational performance, as well as the resulting accuracy for different scanning granularities, will be analyzed for distributed BOTDA measurements over 50km.

### 4.2.1. Principle of operation

Brillouin distributed sensors usually need a large amount of time to perform the required measurements. This time depends on the frequency swept employed, the length of the optical fiber, the required averaging of the acquired traces, and also the time needed to process the measured data in order to obtain the frequency value for each point of the optical fiber. All of this implies a significant increase in the measurement time over the whole sensing fiber, thus avoiding dynamic measurements in the so-called standard BOTDA implementations. As explained in Section 2.5.3.5, different variations have been proposed in this regard to allow fast measurements,

such as the slope-assisted BOTDA [19] or the use of the Brillouin phase-shift and RF demodulation [20]. Although there are other factors limiting the measurement time, as the time of flight of the pump pulses, the frequency scanning is probably the most relevant. In addition, the above mentioned fitting process used for the BFS estimation is also time consuming, as it involves an iterative stage. So, trying to reduce this time related to the traditional approach based on the fitting of the BGS with a Lorentz profile, it is here substituted with the alternative processing technique based on the employment of subpixel algorithms. These algorithms have been extensively used for image processing [21], but they have been also applied in FBG applications [22] or plasma optical spectroscopy for welding diagnostics [23].

Specifically, the selected algorithm to explore the proposed solution is known as the centroid detection algorithm (CDA). It is one of the most widely used subpixel algorithms, and it is based on the estimation of the mass centre of the peak under analysis.

$$f_{sub} = \frac{\sum_j f_j i_j}{\sum_j i_j} \quad (4.3)$$

where  $f_{sub}$  is the subpixel estimation of the peak frequency and  $f_j$  and  $i_j$  the frequency and intensity associated with the pixel  $j$ . Figure 4.8 represent how this algorithm works.

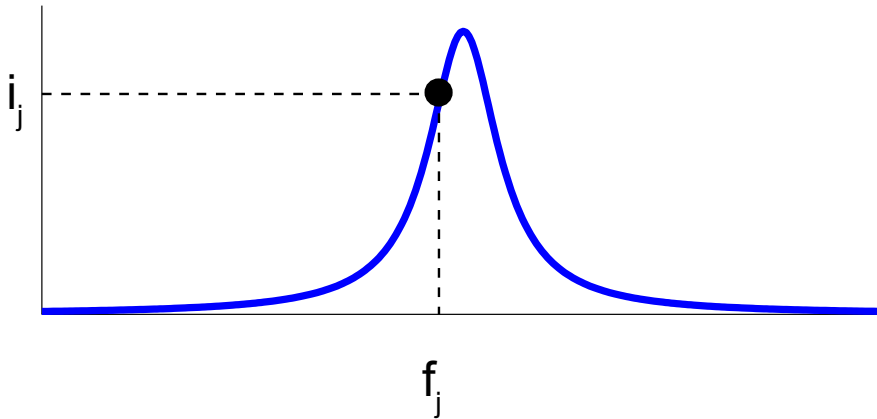


Fig. 4.8. Working principle of the CDA algorithm.

The code to perform the BFS estimation via CDA was implemented in MATLAB<sup>®</sup>, and compared to the conventional Lorentzian fitting.

### 4.2.2. Experimental issues

To perform the required experimental tests the same configuration described in Section 4.1.2 was used. It is a conventional dual-probe sideband BOTDA scheme, as depicted in Figure 4.3. In order to evaluate the corresponding performances of the different processing alternatives, a 50 km standard single-mode fiber was deployed with an estimated BFS of approximately 10.70 GHz. Several measurements were performed considering a frequency range between 10.59 and 10.79 GHz, and scanning granularities of 2, 4, 6, 8, 10 and 20 MHz. A 4096 averaging of the acquired BOTDA traces was performed to improve the SNR.

Figure 4.9 depicts BFS profiles derived from employing Lorentzian fitting and different scanning granularities: 2 MHz (black), 10 MHz (red) and 20 MHz (blue). As expected, the use of a smaller granularity gives rise to a less noisy profile, although the differences between the 2 and 10 MHz profiles are subtle. The BFS curve obtained with the 20 MHz granularity exhibits a clearly degraded SNR, as well as an error in the BFS estimation that increases with distance. For example, the standard deviation of the 2 MHz granularity BFS profile between 30 and 40 km is 1.33 MHz, while the one associated with the 20 MHz granularity is 1.69 MHz. The corresponding mean BFS values are 10.691 and 10.693 GHz.

Figure 4.9 b) presents the comparison of the worst case BFS profile (for a 20 MHz granularity) obtained via Lorentzian fitting and the result of substituting it with the CDA subpixel processing. It can be observed how the SNR clearly improves with the proposed solution, with a standard deviation, again evaluated within the 30 to 40 km section, of 0.86 MHz. The root mean square error over the whole FUT, computed using the 2 MHz granularity profile as a reference, is 2.68 MHz for the Lorentzian fitting and 1.80 MHz using CDA. It should be mentioned that the saturated profile obtained for the 20 MHz granularity (between  $x \simeq 10$  and 20 km) and Lorentzian fitting is precisely due to the chosen granularity and not to other effects to be found in BOTDA traces such as modulation instability.

Apart from these results, the main motivation for avoiding the conventional fitting process might lie in its high computational cost. The average processing time (over 10 tests) of the CDA processing was 0.241 s for the whole BFS of 2 MHz granularity, considering a data matrix of 101 (frequency) x 12000 (spatial) samples. In the same

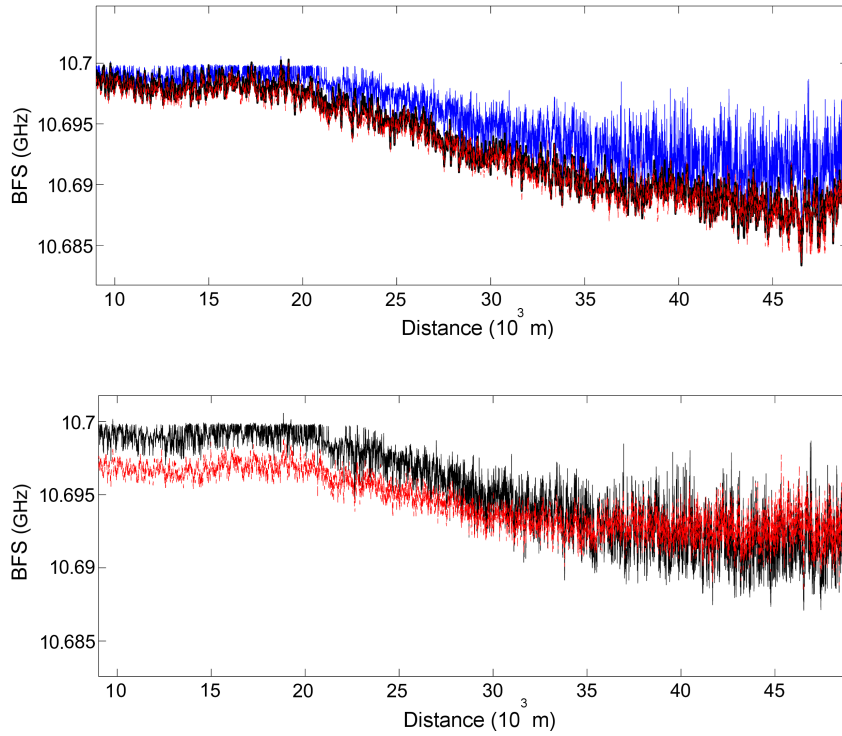


Fig. 4.9. a) Comparison of the BFS profiles obtained with Lorentzian fitting for the deployed fiber (9 to 49km) for different scanning granularities (2 MHz: black line; 10 MHz: red line; 20 MHz: blue line); b) Comparison of the BFS profiles for the deployed fiber (9 to 49km) for a scanning granularity of 20 MHz with Lorentzian fitting (black) and subpixel CDA processing (red).

scenario, the Lorentzian fitting gave rise to a processing time in the order of several minutes. These performance tests were carried out using MATLAB<sup>®</sup> in a conventional laptop (i5-2410M (2.30 GHz) processor with 4 GB RAM).

As a conclusion of these experimental results, it can be concluded that the proposed solution based on subpixel algorithms shows a good performance when the chosen frequency step for the required frequency sweep is high. If the improved computational efficiency in comparison to the traditional Lorentzian fitting is also considered, it can be concluded that this approach may be of great interest for applications where the measurement time must be reduced.

## 4.3. Conclusions

In this chapter, two different processing techniques have been applied to measured BOTDA data with different purposes trying to obtain some alternatives to classical approaches, either based on processing strategies or in setup modifications. Both proposed methods are not only valid for BOTDA sensors, but also it can be employed in other Brillouin distributed sensors configurations.

The first contribution is a new approach for the automatic discrimination of simultaneous temperature/strain measurements in a BOTDA sensor. The proposed solution bases its operating principle on the employment of a dual-probe sideband BOTDA sensor in addition to a processing stage formed by a pre-processing step and an ANN. With this experimental configuration, a classification rate of around 90% for temperature and strain discrimination has been demonstrated. Different pre-processing techniques have been applied before the ANN stage, obtaining the best results when PCA is chosen in addition to gain normalization and spatial filtering. Moreover, this solution has a relevant advantage in comparison with other proposed solutions: it does not involve a higher cost or complexity of the required setup. To demonstrate the classification rate of this solution an ANN has been implemented via MATLAB® in a conventional desktop PC, achieving real-time processing performance. The best classification results are associated with processing times of 2.93 s for PCA and 92 s for the ANN training phase (off-line stage), while the whole processing of each new measured BGS (on-line stage) will only take a few milliseconds. Here, it is possible to find a drawback of this kind of solutions: these systems need a training phase before the on-line stage. This implies to replicate in the most reliable way the real conditions that the sensor will finally encounter in a field application.

The other proposal is an alternative processing technique to the well-known Lorentz curve fitting typically employed in Brillouin distributed sensors to retrieve the BFS along the fiber from the measured BGS. The selected algorithm belongs to the group of subpixel algorithms and it is one of the most widely used. It is the centroid detection algorithm (CDA) and its operating principle basis on the estimation of the mass centre of a peak under analysis, in this case, the BGS. The results obtained when estimating the BFS along a 50 km length sensing fiber with the proposed algorithm show the improved performance of this approach in some specific scenarios. BOTDA measure-

ments have been done using different scanning granularities, giving rise to the expected degradation in the BFS estimation. For the worst case scenario, considering a 20 MHz frequency step, the CDA subpixel algorithm has exhibited a clearly improved performance, showing a lower frequency error and a lower computational time in comparison to the Lorentz curve fitting. In accordance with these results, the employment of the suggested algorithm in addition to bigger frequency steps may be of special interest for faster distributed measurements where fast acquisition and processing is required at the expense of having a slightly greater error.

## Chapter 5

---

# Contributions to laboratory demonstrations of field applications using BOTDA sensors

---

As previously stated, optical fiber distributed sensors have generated a great amount of contributions due to their unique features and their potential use in a wide variety of sectors [1].

Among the diverse uses of these systems there are several applications based on the estimation of temperature along the fiber cable: solutions for the detection of fires[2], leakages in large oil, gas or water infrastructures [3] or failures in power cables [4] have been proposed. Raman-based distributed systems have also been employed as distributed temperature sensors (DTSs). Among other differences, they are based on intensity-detection schemes in comparison to the frequency detection implemented in SBS approaches. Moreover, higher optical powers are required to allow a suitable performance and they are not capable of strain monitoring. Other application fields of these systems inside structural health monitoring (SHM) environments are the temperature/strain monitoring of different infrastructures such as roads [5] or bridges [6, 7], their employment in geotechnical applications [8] or the corrosion monitoring at different scenarios, such as reinforced concrete [9] or pipeline corrosion [10], among others.

In this chapter, some laboratory scale demonstrations have been performed to evaluate the feasibility of employing the proposed solutions in real applications. The first proposal is a distributed system based on a Brillouin optical time domain analysis sensor in addition to a multimode gold-coated fiber capable of measuring temperatures up to 600°C without affecting the mechanical properties of the sensing fiber, allowing its employment in high-temperature field scenarios. The second is the demonstration of a monitoring tool allowing the estimation of the location of mechanical changes in an aluminum composite panel via modal analysis. It is based on retrieving the mode shapes of the first bending modes of the panel. The results confirm that it is possible to locate the position of the defect from the changes in strain mode shapes, with a resolution determined by the disposition of the fiber across the structure, as well as by the spatial resolution of the interrogation unit. Finally, the last contribution is an experimental demonstration of a leakage monitoring system designed for large diameter water pipes. In this study, the design and implementation of a specific infrastructure simulating the conditions to be found in field tests have allowed to carry out a comprehensive set of experiments that will show the feasibility of the proposed approach.

## **5.1. High temperature monitoring with gold-coated fibers**

This section describes a proposal allowing distributed measurements at high-temperature scenarios using a distributed fiber sensor based on a Brillouin optical time domain analysis (BOTDA) and a multimode gold-coated fiber. The proposed solution via the gold-coated fiber allows a feasible deployment in field applications such as industrial environments.

High-temperature distributed sensing (above 300°C), required for applications such as the monitoring of oil wells or industrial sectors like the manufacturing of heavy components for nuclear power stations, has been explored in Raman-based solutions [11]. Ge-doped and pure silica core multimode optical fibers have been used for temperature measurements up to 600°C [12]. High-temperature distributed sensing via BOTDAs has also been recently demonstrated by Wang et al. using a BOTDA system to measure temperatures up to 1000°C, with 5 m spatial resolution, although the optical fiber

employed in this work was not specified [13]. Dong et al. have presented 1100 and 1200°C distributed measurements with a BOTDA configuration using single-mode fiber (SMF) and a pure-silica photonic crystal fiber (PCF) and measurement accuracies of  $\pm 2$  and  $\pm 4^\circ\text{C}$ , respectively [14].

The deployment of these distributed systems in real field scenarios implies the necessity of considering special coated fibers able to resist harsh environments. For temperatures under 300°C, polyimide-coated fibers can be considered, but higher temperatures will require the employment of other solutions, such as metal coatings like aluminium, gold [15] or nickel [16]. The manufacturing of these special coated fibers can be performed after drawing in a separate process (off-line) or during drawing (in-line). The so-called freezing method is applied when the latter option is chosen. In this case, the fiber is passed through a layer of a few millimeters of molten metal. Provided that the melt exhibits a temperature close to the melting point of the metal and that the temperature of the fiber is somewhat lower, a layer of metal can freeze on the surface of the fiber. The duration of the contact of the fiber with the molten metal should be shorter than the time of the fiber heating to the metal melting point. If this condition is not fulfilled, the frozen layer will melt again and the fiber will exit the metallizer without any coating [17]. These metal coated fibers allow high-temperature measurements, but they exhibit high attenuation, especially at low temperatures, due to both hydrogen ingress and microbending losses due to thermal stress [15]. This may be a problem for Raman-based systems where the measurement of temperature is based on the detection of the intensity of the scattered signals, due to the considerable attenuation decrease for higher temperatures, which can give rise to errors in the measurements. However, distributed systems based on the Brillouin scattering perform a frequency-based detection, thus being more suitable to scenarios where attenuation can be very dependent with temperature. In a previous work, a gold-coated fiber was used to achieve centimeter spatial resolution over a 1 meter fiber using a system based on swept wavelength interferometry and Rayleigh scattering [18]. In comparison to the fibers employed in previous works dealing with distributed high-temperature measurements via BOTDAs [13, 14], the fiber considered here is suitable for its deployment in real field scenarios and endure a wide range of temperatures (from -269 to 700°C), and also harsh environments due to the mechanical properties of the gold-coated protection.

### 5.1.1. Fundamentals

As stated in Section 2.5.3.5, BOTDA sensors are based on the stimulated Brillouin scattering (SBS) generated via the interaction of the counter-propagating pump and probe waves. The frequency difference between both signals is fundamental, as the maximum Brillouin gain will be achieved when they are separated  $\nu_B$ . To acquire the whole Brillouin gain spectrum (BGS) it is necessary to scan a certain frequency range by modifying the frequency difference between pump and probe waves. Provided that the BGS has been acquired, the Brillouin frequency shift (BFS) can be estimated via Lorentzian fitting.

The BFS exhibits a linear dependence, as explained in Section 2.5.2 on the local temperature variation  $\Delta_T$  and the applied strain  $\Delta\epsilon$  that for low temperatures that can be expressed as follows [19]

$$\nu_B(T, \epsilon) = C_\epsilon \Delta\epsilon + C_T \Delta_T + \nu_B(T_0, \epsilon_0), \quad (5.1)$$

where  $C_\epsilon$  and  $C_T$  are the strain (MHz/ $\mu\epsilon$ ) and temperature (MHz/ $^\circ\text{C}$ ) coefficients and  $T_0$  and  $\epsilon_0$  the reference temperature and strain. These values are mainly determined by the fiber composition and external protections (coatings and jackets) [20].

However, results provided by other authors suggest that the best fitting when dealing with high-temperature measurements may be accomplished by means of a negative exponential [14].

When single-mode fibers are used as the sensing element, part of the energy of the higher frequency pump (if a gain configuration is considered) will be transferred to the chosen lower frequency probe sideband via the acoustic wave. The use of a multimode fiber enables the appearance of several optical and acoustic modes. This implies that the resulting BGS will be formed by the addition of the contributions of various pairs of counter-propagating optical modes interacting through a given acoustic mode [21]. Although this broaden and even non-symmetrical BGS may affect the final system accuracy, if a lateral offset in the splicings between the optical fiber transitions is avoided, the contribution of higher-order modes will be suppressed [22], thus favoring the system performance. The vast majority of BOTDA implementations reported in the literature has considered single-mode fibers, given their superior features for long distance sensing. However, the study of the performance of multimode fibers may prove

interesting, for example, to achieve bend-insensitive solutions or to explore the possible use of the multiple mode interactions to enable the discrimination between strain and temperature measurements.

### 5.1.2. Experimental setup

The fiber under test (FUT) designed and employed in the experimental tests is shown in Figure 5.1. It can be observed how the multimode gold-coated fiber is accessed via conventional silica graded-index multimode fiber and, additionally, two short sections of single-mode fibers have also been spliced at both ends to allow a straightforward connection to the BOTDA system access ends. The gold-coated section (FiberGuide AFS50/125/155G) is formed by 78 m, where the last 4 m are placed within a furnace chamber. Longer lengths of this fiber might be employed in the proposed system, with the only limitation of the fiber attenuation (around 20 dB/km). This high attenuation is mainly due to the microbendings generated by the metal coating. The gold fiber is a 50  $\mu\text{m}$  pure fused silica core and 125  $\mu\text{m}$  fluorine doped silica cladding.

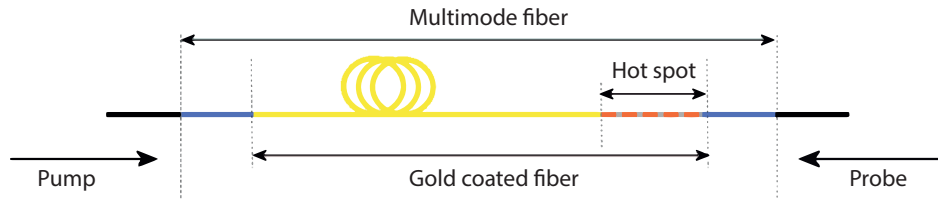


Fig. 5.1. Fiber under test configuration employed with standard single-mode fiber on both sides (black), multimode graded-index fiber (blue) and gold-coated fiber of 74 m length (yellow) and 4 m length (red dashed line).

Conventional BOTDA systems are typically implemented using single-mode optical fibers as FUT, mainly due to their higher performance in terms of attenuation. There are a few works where multimode fibers are used for distributed measurements based on SBS. Minardo et al. [21] carried out a numerical and experimental study with graded-index multimode fibers and Xu et al. [22] developed a bend-insensitive distributed BOTDA sensor using a graded-index multimode fiber as sensing fiber.

The experimental setup employed to carry out the experimental tests is described in Figure 5.2. The BOTDA system is formed by a distributed feedback laser (DFB) source, whose output is divided by a coupler into two branches. The upper branch

generates the pulsed pump wave (10 ns) via a semiconductor optical amplifier (SOA) (connected to a pulse generator) providing an extinction ratio above 40 dB. An Erbium-doped fiber amplifier (EDFA) is used to boost the pump pulse power and a polarization scrambler (PS) is used to avoid the polarization dependence of the SBS gain along the fiber. The probe wave is formed in the lower branch by an electro-optic modulator (EOM) driven by a microwave generator. Its power is fixed with an EDFA and a variable optical attenuator and then launched into the FUT. The system works in a balanced configuration, i.e. both Stokes and anti-Stokes signals enter the FUT and participate in their corresponding SBS processes. At the output of the system, once the SBS interaction has taken place within the FUT, the resulting optical signal is filtered by a narrow fiber Bragg grating (FBG) and only the Stokes component is directed to a 125 MHz photodetector by an optical circulator, thus a gain configuration is considered. Finally, an oscilloscope is employed to acquire and perform 1024 averaging of the BOTDA traces. In this system, a probe power of 8 mW and a pump peak power of 2 W are used to obtain an optimal signal at detection. It is worth noting that Raman distributed systems typically use pump powers of around tens of W, i.e. in a 40 km long Raman sensor a pump pulse of 10 ns and 20 W was employed [23].

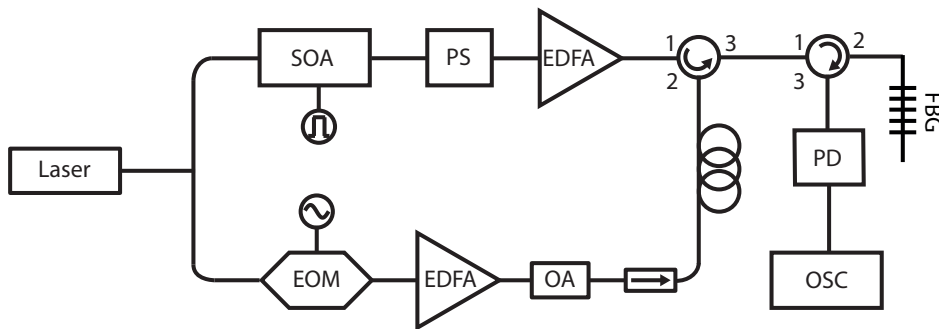


Fig. 5.2. Schematic setup of the BOTDA system used in the experimental tests to monitor the gold-coated fiber.

### 5.1.3. Experimental issues

A set of experimental tests was carried out to study the ability of the designed system to perform distributed high-temperature measurements. A 4 m section of the gold-coated fiber (at the end of the FUT) was placed within a furnace chamber and different temperatures between 50°C and 600°C were analyzed (with temperature steps of 50°C), with the temperature provided by the furnace thermocouple used as a reference. 4

measurements were performed at each temperature. Figure 5.3 presents these results, where the estimated BFS (after the Lorentzian fitting process) has been represented against the FUT distance. It can be clearly observed how the temperature differences give rise to different BFSs that are clearly distinguishable at the hot spot section.

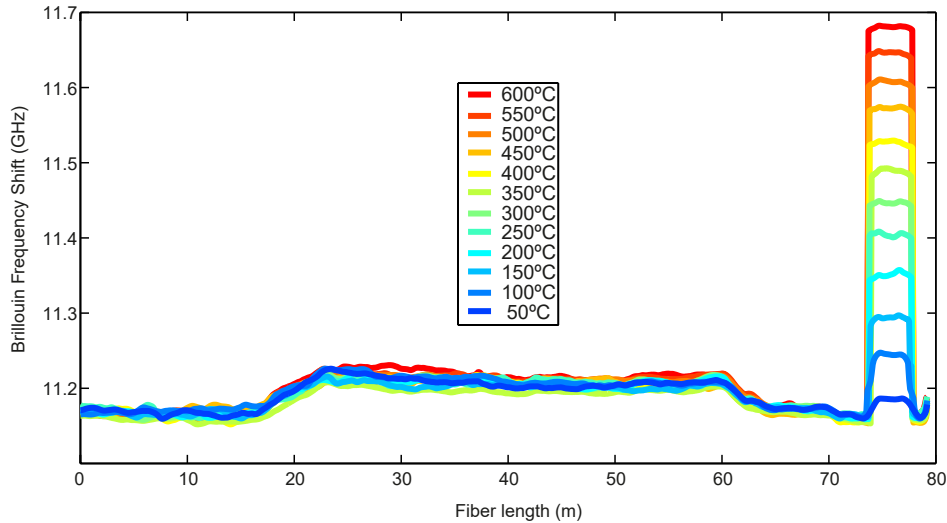


Fig. 5.3. Brillouin frequency shift distribution along the fiber for temperatures at the hot spot section from 50 to 600°C.

Figure 5.4 shows the same results previously discussed but considering descending temperatures from 600 to 50°C. This study is important to verify that a similar response is obtained and that the measurement system is free from hysteresis. Again, it can be validated how the temperature differences clearly appear at the hot spot section with a behavior similar to the one presented in Figure 5.3.

Figure 5.5 shows the resulting fitting of the BFS measured for each considered temperature at the hot spot section of the FUT. 8 different measurements were carried out for each temperature. The blue markers in this figure are associated with a cycle of increasing temperature from 50 to 600°C, while the green markers are associated with the corresponding decreasing cycle. These markers show the mean of the BFS at different temperatures for each spatial point at the hot spot section when the temperature of the furnace is stable. It is also worth noting that no temperature hopping appears [14] given that the considered temperatures are below 800°C. A fitting of these data gives rise to an exponential fitting expressed via the following expression

$$\nu_B = -1269e^{-0.00107T} + 12390 \quad (5.2)$$

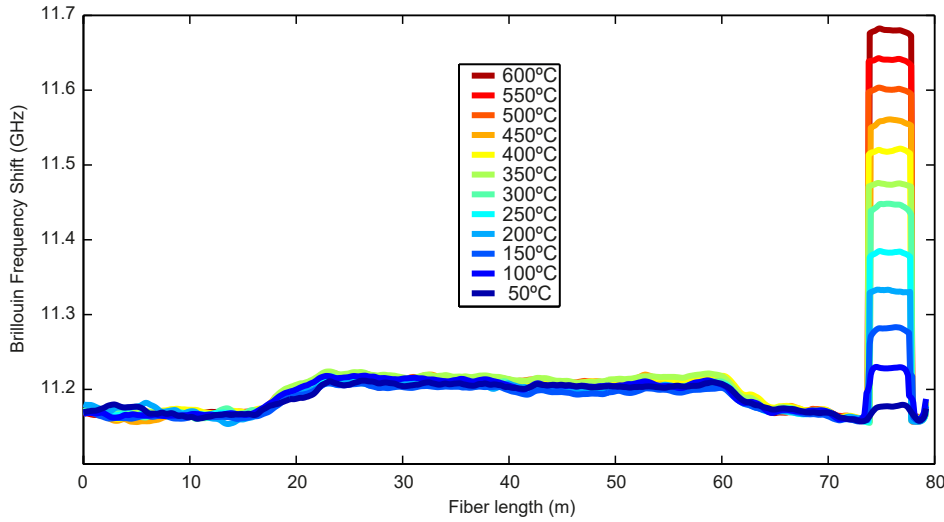


Fig. 5.4. Brillouin frequency shift distribution along the fiber for temperatures at the hot spot section from 600 to 50°C.

Using this exponential curve the value of  $R^2$  is 0.9976 and the mean error between the measured data and the real temperature is  $\pm 7.7^\circ\text{C}$ .

To validate the fitting equation obtained employing the previous data, additional temperature measurements have been carried out. Given that the process of changing and stabilizing the temperature of the furnace chamber is very slow, several measurements have been done for each temperature. In this case, a new cycle of increasing temperatures has been considered. The differences between the measured temperatures (applying Eq.5.2 to the measured Brillouin frequency) and the temperatures provided by the furnace thermocouple are presented in Table 5.1. The temperature error of Table 5.1 is calculated subtracting the average of the different measurements for each temperature and the reference temperature of the furnace.

The analysis of the evolution of the BGS for each scenario has been represented in Figure 5.6 for increasing and decreasing temperatures. It can be appreciated that no significant distortions appear in the BGS as the temperature varies. In both cases, a constant gain appears at a fixed frequency (natural Brillouin frequency of the fiber) away from the one associated with the measured temperature. This effect is provoked by the leakage signal generated during the pulse formation at the SOA due to the high pump power required.

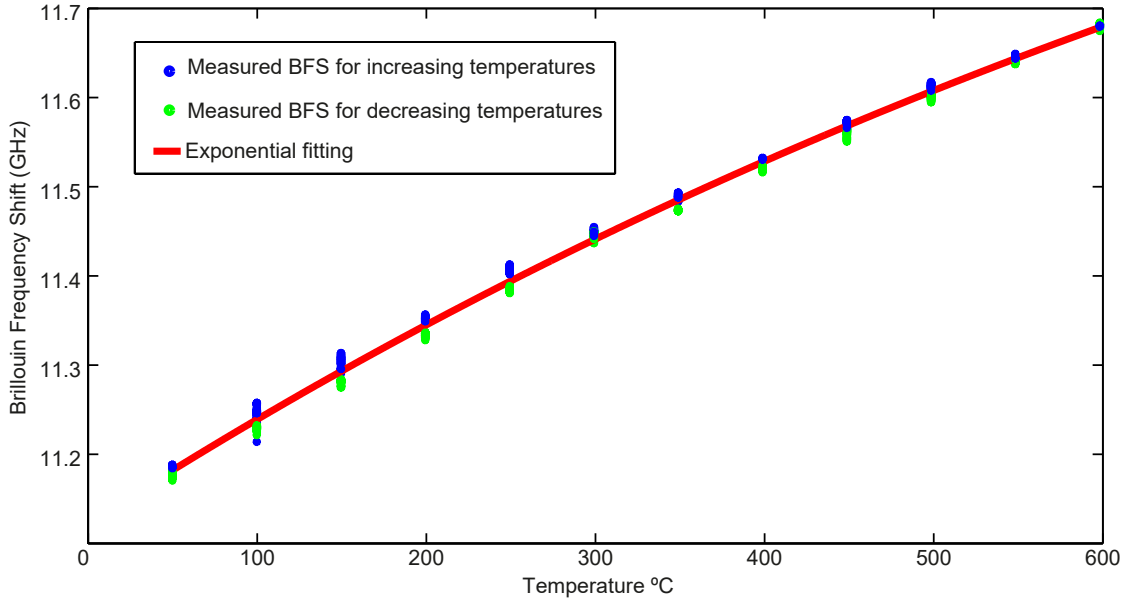


Fig. 5.5. Brillouin frequency shift vs. temperature at the hot spot section. The red line shows the fitting of BFS for the temperature between 50 to 600°C. Blue/green markers show the measured BFS for the increasing/decreasing temperatures.

Table 5.1.: Averaged BFS values, estimated temperature and mean error for each temperature.

Reference Temperature (°C)	Measured BFS (GHz)	Measured Temperature (°C)	Temperature error (°C)
50	11.187	55.69	5.69
100	11.239	101.95	1.95
150	11.295	152.93	2.93
200	11.346	202.72	2.72
250	11.394	251.17	1.17
300	11.443	304.35	4.35
350	11.483	349.15	0.85
400	11.525	397.41	2.59
450	11.566	447.84	2.15
500	11.602	493.78	6.21
550	11.636	540.00	9.99
600	11.672	590.46	9.53

These results demonstrate the potential of gold-coated fiber in addition to BOTDA sensors to be employed in real high-temperature scenarios. A few previous works have

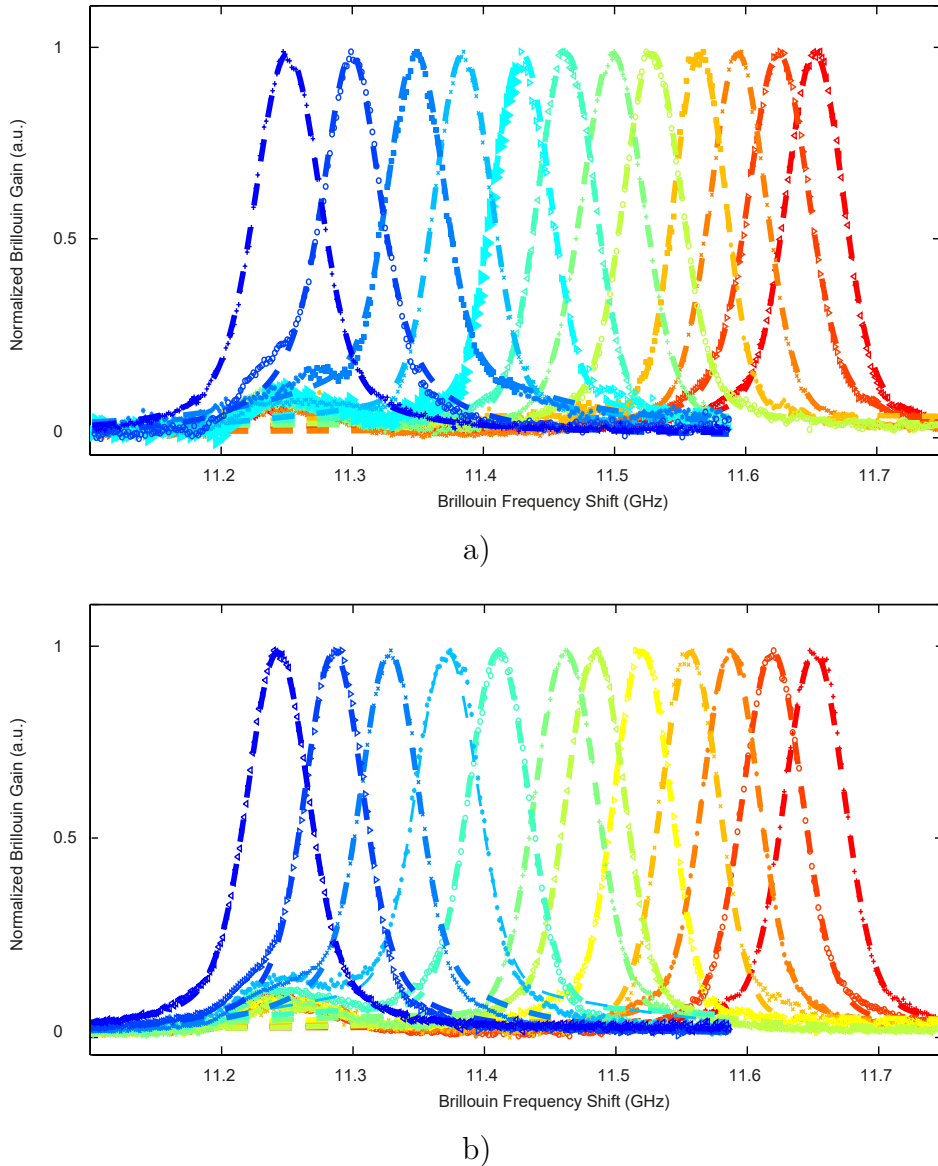


Fig. 5.6. Evolution of the BGS for a) increasing and b) decreasing temperatures.

dealt with high-temperature sensing via BOTDAs [13, 14], but the gold-coated fiber ensures a feasible fiber deployment in field applications for temperatures up to  $600^{\circ}\text{C}$ . The experimental tests carried out show a good agreement between the measurements performed for both increasing and decreasing temperatures between  $50$  and  $600^{\circ}\text{C}$ . The response of the system can be modeled via exponential fitting, obtaining a good temperature mean accuracy of about  $10^{\circ}\text{C}$ , showing a suitable system performance.

## 5.2. Modal analysis of a composite panel by means of slope-assisted BOTDA

In SHM, the experimental modal analysis (EMA) is the most common approach to retrieve dynamic parameters of a structure. This approach determines modal parameters of the structure (mode shapes, natural frequencies and modal damping) through the responses induced by known and sometimes unknown excitations [24]. Vibration-based modal analysis, typically using acceleration measurements, has the limitation that the resonant frequencies do not allow to detect accurately damage location, while the precision of identified mode shapes is often not sufficient for effective damage identification [25]. In contrast, curvature (strain) is more sensitive to damage, but unfortunately fails to work unless the area where strain sensor is fixed covers the damaged region. Therefore, an SHM strategy based on distributed strain sensing is particularly attracting, as it allows detecting arbitrary and unforeseen damages.

In this regard, Brillouin scattering offers the opportunity to perform fully distributed strain measurements with a single-mode optical fiber. In particular, the slope-assisted BOTDA configuration allows distributed strain acquisitions at a rate as high as several tens of Hz. In brief, as explained in Section 2.5.3.5, the method relies on the measurement of the interaction between a probe signal and a counter-propagating pump pulse, with the spectral shift between the two lightwaves biased at the midgain point of the BGS [26, 27]. This method have already been applied to perform experimental modal analysis of a cantilever beam [28] and a small rectangular plate [29].

The slope assisted BOTDA method is employed here to perform the modal analysis of an aluminium composite plate. Compared to other previous works, such as [29], the analysis presented here is aimed at detecting and localizing small changes (defects) of the mechanical structure.

### 5.2.1. Experimental demonstration

Modal shape measurements were carried out by using the slope assisted BOTDA system described in Figure 5.7.

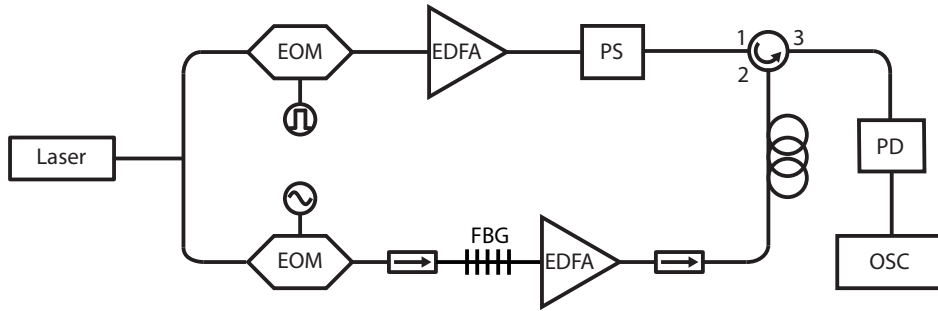


Fig. 5.7. Experimental slope assisted BOTDA setup.

The BOTDA setup employed for dynamic strain measurements is a configuration very similar to previous one explained in Section 5.1.2. The main differences are the employment of a FBG right next to the EOM of the probe branch to select the lower sideband (Stokes component) of the probe wave, and the use of an EOM instead of a SOA to generate the pump pulses. The pump pulse duration was fixed to 2 ns, resulting in a  $\sim 20$  cm spatial resolution. Moreover, two EDFAs are used to amplify the probe and pump beams before they enter the sensing fiber. Another difference lies in the photodetector employed to detect the Stokes wave emerging directly from the sensing fiber, it is a 1 GHz bandwidth InGaAs photodiode instead of a 125 MHz one. The response of the photodetector is sampled at 2 GS/s. Based on this sampling rate, a measurement point is available every 5 cm along the sensing fiber.

Note that the method requirement of small static and dynamic Brillouin frequency shift changes, compared to the BGS bandwidth, is easily verified when using 2 ns pulses [26–29]. The mode shapes were measured by acquiring the strain profiles at a maximum rate of 24 profiles/s. The structure chosen for the tests was a 1220 mm x 1220 mm x 2 mm (LxWxH) composite aluminum plate, made by a polymer layer sandwiched between two 0.3 mm thick aluminum foils. The panel was kept in vertical position and fixed to a wall using four clamps distant 2 cm from the plate corners in both x - and y - directions. A single-mode optical fiber was glued on the front surface of the plate, following the path shown in Figure 5.8. In detail, the fiber was disposed along the x direction so as to form 24 horizontal strands spaced 5 cm along the y direction as shown in Figure 5.8.

The plate was mechanically excited by using a voice coil characterized by a maximum continuous force of 28 N and a force constant of 8 N/A, and positioned close to the middle of the plate. The natural frequencies of the plate in the range 1 to 10 Hz were

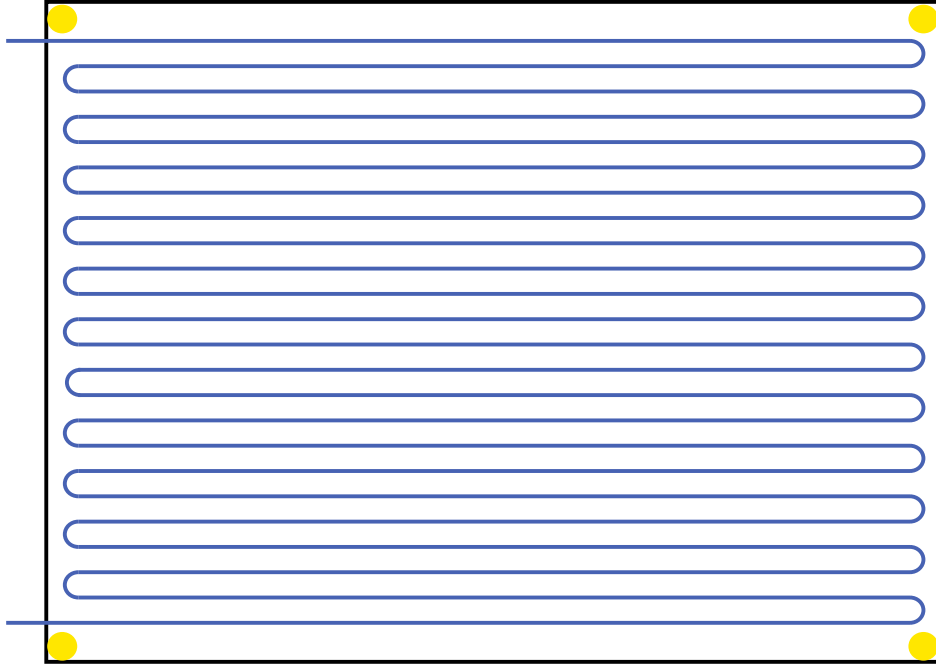


Fig. 5.8. Schematic view of the aluminum composite plate employed for the experiments. The blue line represents the path of the optical fiber glued on the plate front surface.

identified by applying a chirped current to the voice coil, while recording the intensity of the detected Brillouin signal. For each identified resonance, the corresponding mode shape was retrieved by exciting the plate at resonances for a time interval of 4 minutes, and taking the real part of the fast Fourier transform (FFT) of the Brillouin signal acquired at each fiber position [28, 29].

The mode shapes acquired in the free of defects (i.e. uniform) plate, for the first three resonances identified in the chosen frequency range are shown in Figure 5.9. The 3D maps were built by mapping each sampled position along the fiber to the corresponding plate location, across a grid of  $25 \times 24 = 600$  points. From power spectral density analysis of the various measurements, a dynamic strain resolution of  $\sim 132\mu\varepsilon/\sqrt{Hz}$  was estimated. The three experimental modal shapes were compared with the corresponding simulated modal shapes obtained with the software COMSOL multiphysics®. In the 3D maps it is possible to observe the similar shape between the experimental modes and the simulated ones.

Moreover in the Table 5.2, it is also possible to see and compare the numerical value of the resonance frequency of the plate.

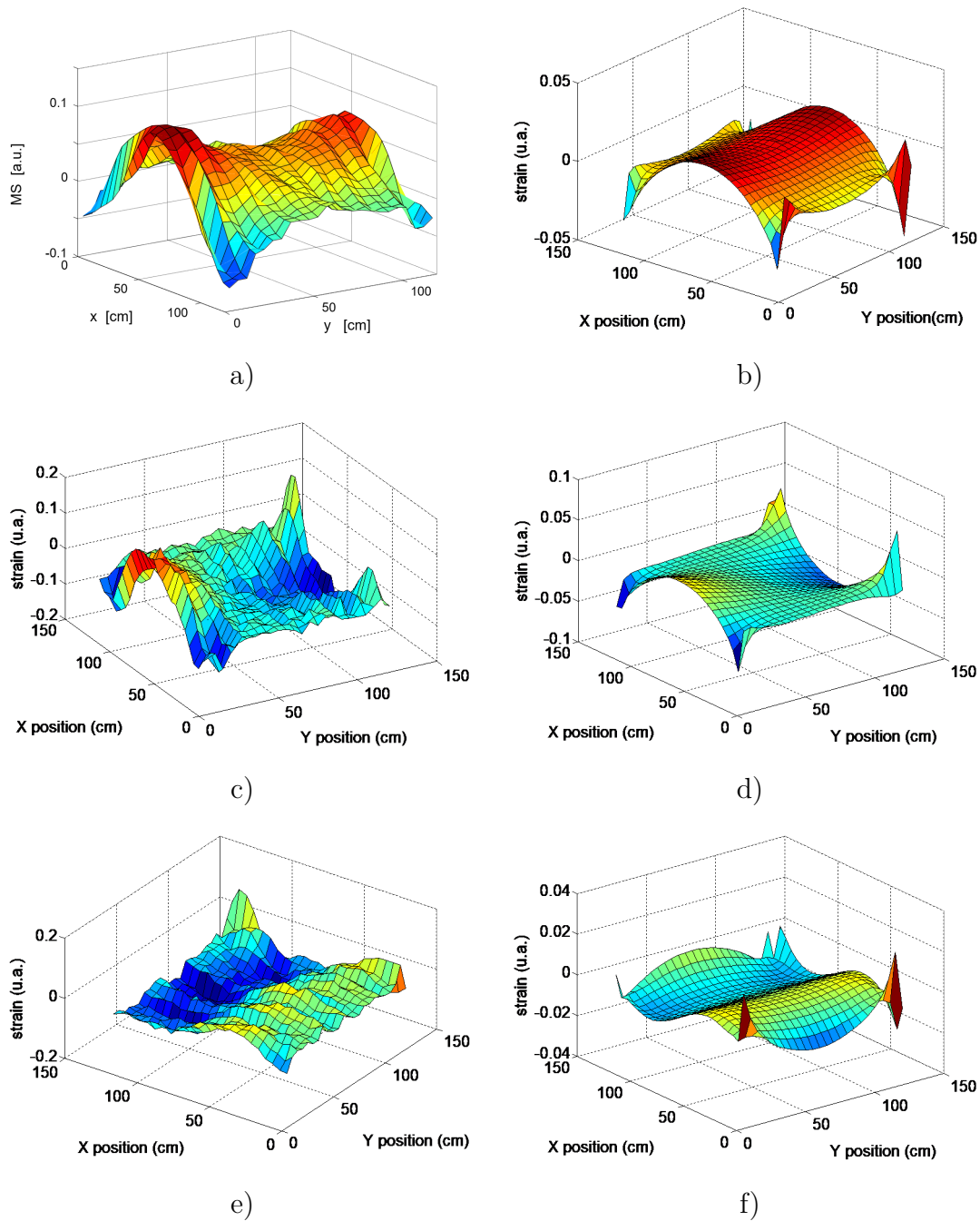


Fig. 5.9. First three strain modal shapes of the plate. Experimental and simulated shapes. a) Experimental shape first mode; b) Simulated shape first mode; c) Experimental shape second mode; d) Simulated shape second mode; e) Experimental shape third mode; f) Simulated shape third mode.

Table 5.2.: Experimental and simulated resonance frequencies.

	<b>Experimental frequency (Hz)</b>	<b>Simulated frequency (Hz)</b>
Mode 1	3.3	3.9
Mode 2	7.3	7.5
Mode 3	9	7.6

After the validation of the measurement system to obtain the bending shape of the plates, the same procedure was applied inducing a local change in the plate geometry. In particular, the plate was locally stiffened by bolting a  $200 \text{ mm} \times 200 \text{ mm} \times 4 \text{ mm}$  (L×W×H) aluminum composite element to its rear surface. Different tests were performed by varying the position of the added element. The coordinates of the center of the added mass, for each test case, are listed in Table 5.3, where the origin coincides with the lower-left corner of the plate. For each test, the mode shapes of the first two bending modes were compared to the ones previously acquired on the uniform plate, in order to verify the capability of the method to localize the changes in the plate mechanical properties.

Table 5.3.: Defect localization (the coordinates refer to the center of the added element).

<b>Defect case</b>	<b>Actual position (x)</b>	<b>Actual position (y)</b>	<b>Estimated position (x)</b>	<b>Estimated position (y)</b>
A	60	60	70	62
B	40	60	45	62
C	20	60	25	62
D	20	80	30	77
E	60	15	50	12

The method used to identify and localize the added mass is the following: the norm of the difference between the mode shapes for free of defects and with defects is calculated, for each one of the 24 strands shown in Figure 5.8. The vertical position of the added mass was then estimated as the y-coordinate of the fiber strand along which the maximum difference was observed. After fiber identification, the x-coordinate of the defect was estimated by determining the fiber location at which the maximum change

(in terms of absolute value) of the two modes occurred. The results are summarized in Table 5.3. It can be observed that the error in the estimation of the vertical position of the added mass, in all cases, is less than 5 cm, which corresponds to the vertical spacing between the various fiber strands (see Figure 5.8). On the other hand, the error in the estimation of the x-position of the added element is always less than 20 cm, which is the spatial resolution of the BOTDA unit.

To best illustrate the achieved results, Figure 5.10 a) shows the first mode shape ( $f_{res} = 3.3\text{Hz}$ ) acquired along the fiber segment disposed at  $y = 62.5\text{ cm}$ , with and without the added mass centered at (60cm, 60cm). Similarly, Figure 5.10 b) shows the first mode shape acquired along  $y = 12.5\text{ cm}$ , with and without the added mass centered at (60cm, 15cm). In both cases, the added element produces a local change in the modal strain, because of the modified local stiffness, which is recorded by the BOTDA sensor.

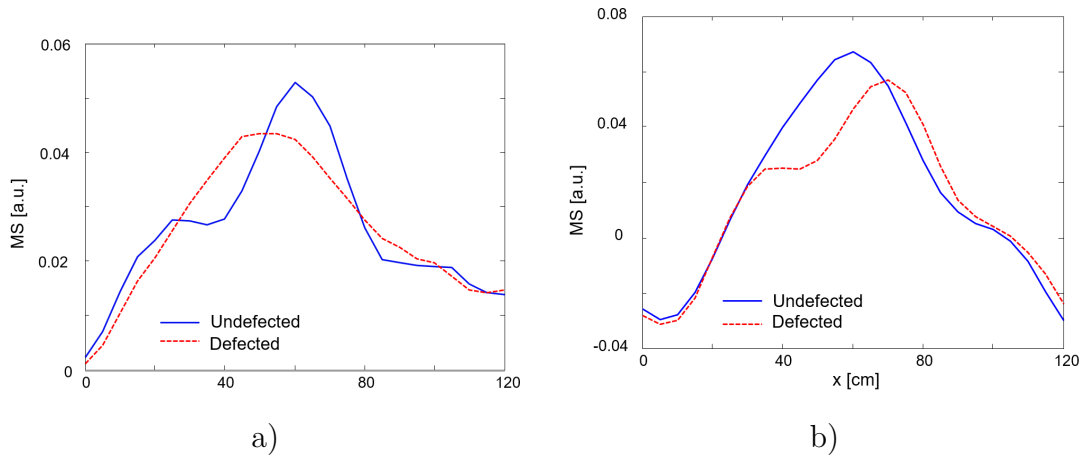


Fig. 5.10. Strain modal shape of the first bending mode of the plate, evaluated along a)  $y = 62\text{ cm}$ , or b)  $y = 12\text{ cm}$ . In (a), the red line refers to defect case (A) while in (b) the red line refers to defect case (E).

Experimental tests have demonstrated that the technique is capable of localizing plate stiffness changes with good resolution. The damage detection has been demonstrated on an aluminum composite plate by evaluating the changes in the shapes of the first two modes by a slope-assisted BOTDA sensor, demonstrating that local changes of plate geometry can be detected and localized.

### 5.3. Experimental demonstration of a leakage monitoring system for large diameter water pipes

The increasing relevance of saving water and other resources nowadays has given rise to the requirement of new monitoring systems capable of detecting and locating leakages on large water pipelines. This can enable a leakage reduction that is considered of primary relevance in terms of the management of water demand. Due to their unique characteristics, distributed fiber sensors are thought to be good candidates to be employed in this field. In this framework, it is worth noting that the losses associated with these water infrastructures are significant; thus making it necessary to find a suitable solution for this problem.

Leak detection on pipes using optical fiber technology, in particular, distributed sensor systems based on Brillouin scattering [30], has already been proposed in order to monitor the health of pipes and detect leakages of brine, gas or oil. Nikles et al. installed a distributed temperature sensor based on Brillouin scattering for leakage detection along a 55 km pipe [3]. The system was able to detect brine leakage due to the temperature change that the optical fiber suffers when the leakage appears. Another example of the employment of this technology is the monitoring of a 500 m gas pipe detailed in [31], where a DITEST (Omnisens ®) system was used with a spatial resolution of 1.5 m and a strain and temperature resolution of 20  $\mu\text{m}$  and 1°C, respectively. However, not all the monitoring systems used in leakage detection use the temperature surrounding the optical fiber to identify and detect leaks. Zou et al. developed a sensor based on Brillouin for detecting pipeline buckling in an energy pipe under internal pressure [32].

Here, the proposed solution for detecting and locating leakages in large diameter water pipes is a distributed optical fiber sensor system based on Brillouin scattering. The design and implementation of a specific infrastructure simulating the conditions to be found in field tests have allowed to carry out a comprehensive set of experiments that will show the feasibility of the proposed approach.

### 5.3.1. Experimental setup

The measurement system is formed by a DITEST interrogator unit [33] and 750 m of a BRUGG optical fiber cable. This cable has been designed to avoid strain effects in the measurements. Within the framework of the project FASO (Detection of leakages in large water pipelines by means of optical sensors), funded by the regional government of Cantabria, a laboratory was designed and implemented to perform the experimental tests. 3 different scenarios were considered using different filling materials in an attempt to emulate the conditions to be found in real field environments.

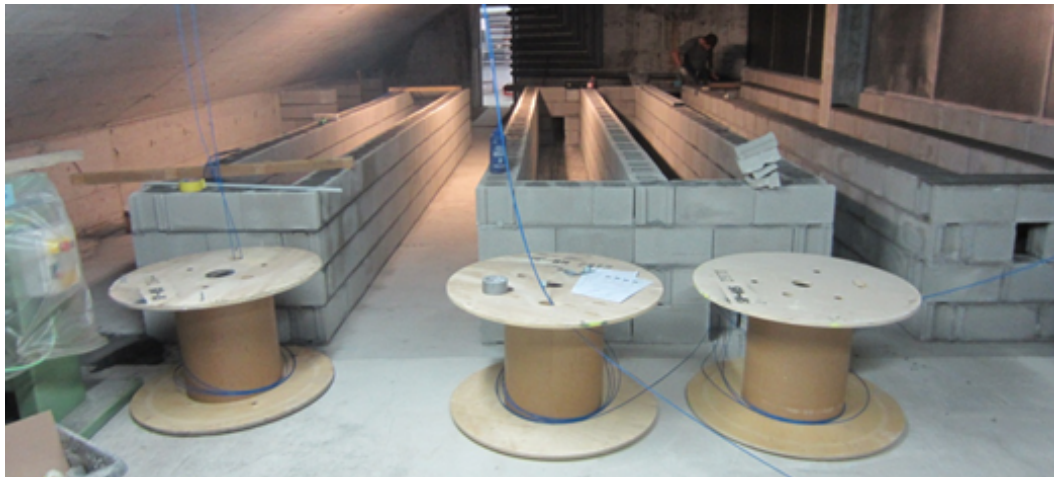
These three scenarios (E1 to E3) are depicted in Figure 5.11 a). Moreover, a 3D model of the scenarios showing the distribution of the optical fiber in the scenarios has also been included in Figure 5.11 b), and also, the detail view of the fiber location in c).

It should be noted that all three scenarios, filled with different materials, exhibit the same sensing configuration. As it can be appreciated in Figure 5.11 b) and c), the same optical fiber was deployed along the scenarios under the pipe in sections of 8 m (length of each scenario) at different vertical and horizontal positions to allow a more comprehensive analysis. This implies that instead of using only one fiber, 8 fibers sections (from the same fiber cable) were installed in each scenario.

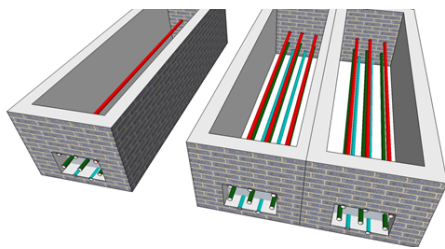
This kind of deployment is shown in Figure 5.12, where the first two fiber sections have been depicted in a), and an example of one of the scenarios has also been included in b). Given that the DITEST unit was located in an adjacent room, the initial length of the cable was not located within the mentioned scenarios, but guided to the experimental laboratory. In particular, the cable length associated with scenario 1 goes from 201 to 272 m, from 274 to 345 m for scenario 2 and from 351 to 422 m for scenario 3.

### 5.3.2. Experimental results

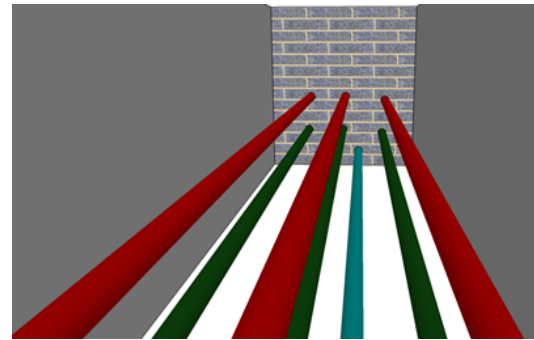
To verify the feasibility of the system, leakages were simulated using a water hose buried near the pipes and different experiments were carried out using different spatial



a)



b)



c)

Fig. 5.11. Images illustrating the experimental facility employed: a) detail of the laboratory developed for the experimental demonstration of the proposed system; b) distribution of the optical fiber deployed for leakage detection and c) detail view of the fiber location.

resolutions and leakage localizations to verify the proposed solution. Figure 5.13 depicts an experimental test performed in the first scenario, with a spatial resolution of 1 m. As it could be observed, the signal is rather noisy, but it is possible to detect some “hot” peaks where the leakage was performed. It should be noted that the cable length associated with scenarios E1 to E3 ranges from 201 to 422 m. In this range the only remarkable temperature variations are associated with the leakage simulated in scenario 1. The temperature variations also become noticeable at the end of the fiber channel, but in this case, the fiber is not within the experimental laboratory and, therefore, subjected to possible temperature changes provoked by a variety of situations.

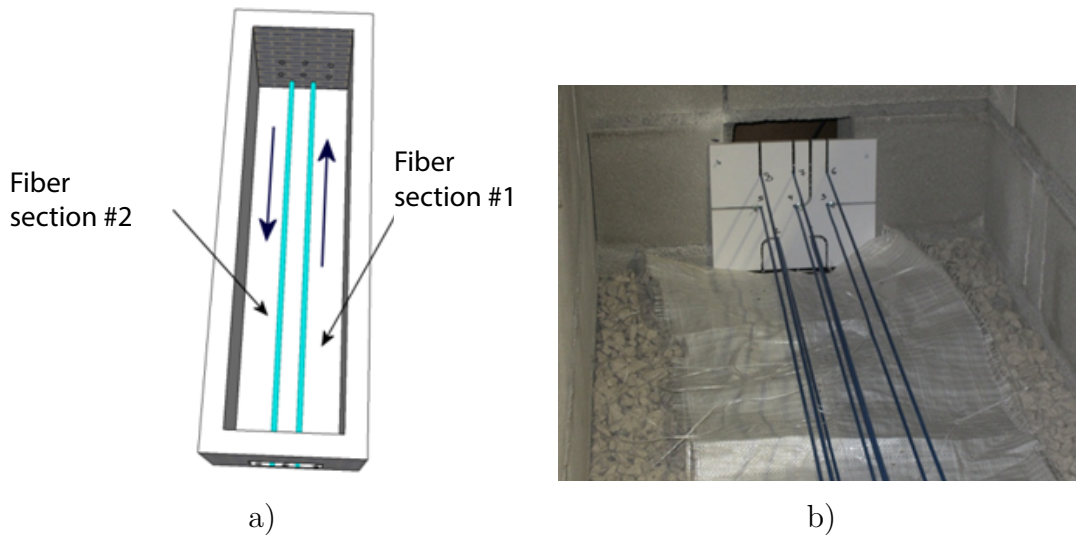


Fig. 5.12. Sensing fiber installation in each laboratory scenario: a) Scheme of the fiber installation and b) example of fiber deployment.

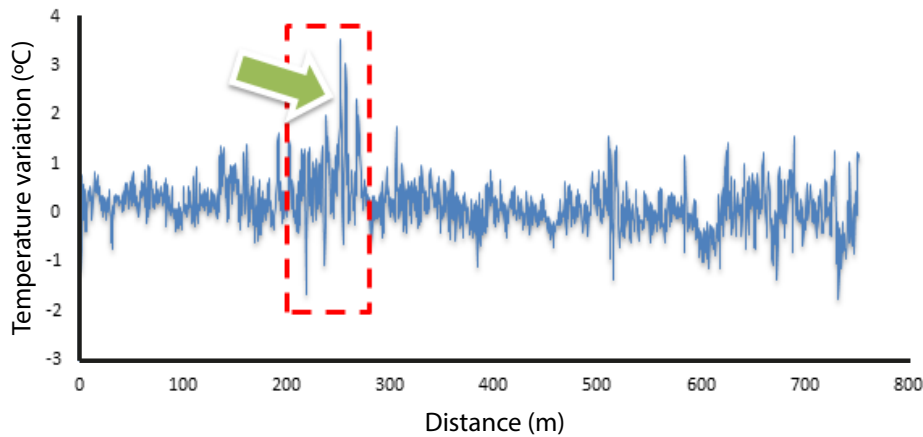


Fig. 5.13. Water leakage detection in the first scenario with 1 m spatial resolution.

Another interesting experiment is depicted in Figure 5.14. In this case, a leakage was simulated in scenario 1 to analyze the temporal evolution of the temperature profiles. The different measurements exhibit the expected behavior of the system. In the first measurement (blue line) three peaks associated with temperature variations can be detected at  $x \simeq 250$ ,  $x \simeq 260$  and  $x \simeq 268$  m. The following series (red line), taken 30 minutes afterwards, shows detection of the leakage in the 8 fibres, with increasing intensity for fibers located close to the pipe (greater cable length). Finally, the green series also exhibits eight peaks, one for each fiber, but with somewhat higher peak intensities. It should be mentioned that the water flow (approximately 4 liters

per minute) used for the simulation of the leakage was cut before the measurements took place. In this case, the temperature variations detected with the system were of approximately 6°C.

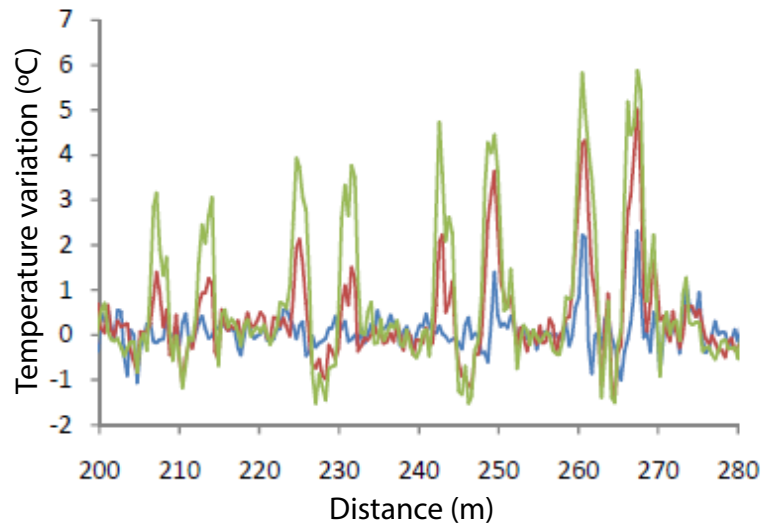


Fig. 5.14. Water leakage detection in the first scenario (temporal evolution)

One of the effects that can be expected when a leakage takes place is the expansion (in the longitudinal axis of the pipe) of the water escaping the pipe with time, thus involving a lateral expansion of the temperature change. A more detailed graph of this situation is shown in Figure 5.15, where five series present the evolution of the leakage detection every 10 minutes. The width of the associated peak clearly increases with time, being the blue series the first one and the violet (dashed line) the latest. The temperature deviation associated with the leakage detection is 8°C in this case.

Figure 5.16 shows the result of an experiment designed to verify the ability of the system to discriminate between events situated very close in terms of their spatial location. 2 water hoses were situated in scenario E2 separated 2 m. After the simulation of the leakage, the recorded temperature profiles are depicted in Figure 5.16, again showing their temporal evolution. The peaks associated with both leakages can be clearly distinguished. It is worth noting that the spatial resolution of the system can be configured in the interrogation unit, being its practical limit 1 m. For this test the spatial resolution was set at 2 m, as this parameter also affects the performance of the system in terms of the signal to noise ratio, for example (lower spatial resolutions

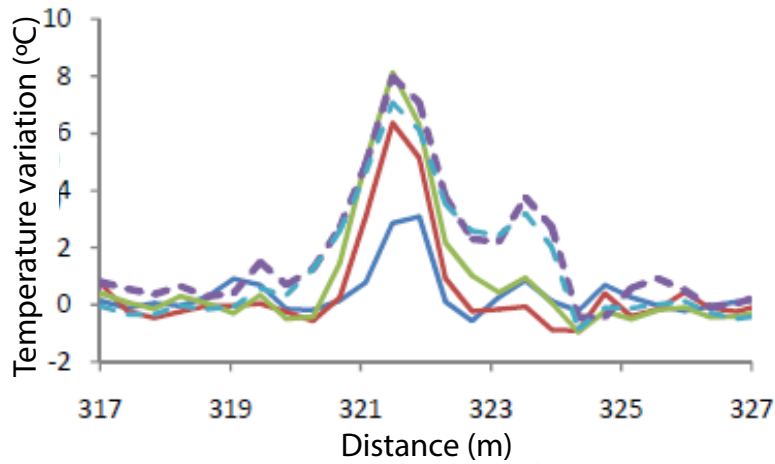


Fig. 5.15. Longitudinal expansion of the temperature variation with time.

typically imply a noisier acquisition signal, what can also give rise to higher acquisition times associated with higher number of averages).

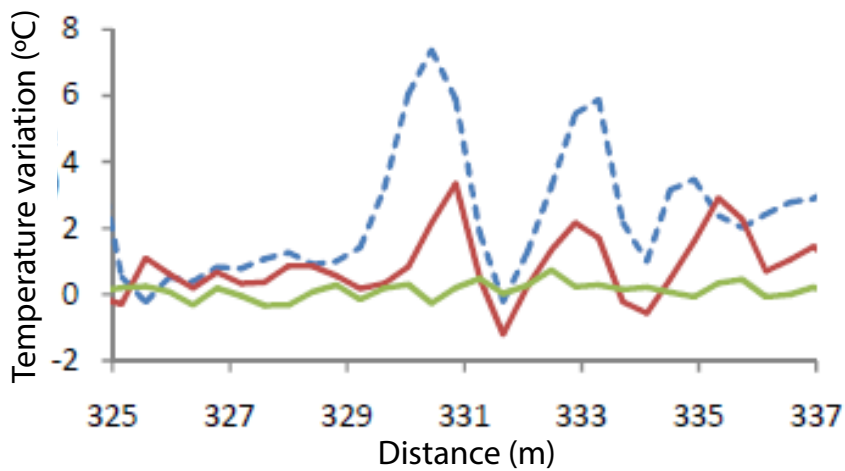


Fig. 5.16. Verification of the spatial resolution by means of multiple leakage detection.

These results demonstrate the feasibility of the proposed solution based on a distributed fiber sensor system via Brillouin scattering. Once the chosen optical cable was installed under the pipes and the different filling materials situated in the three considered scenarios, several studies were conducted to verify the suitability of this proposal. Analyses regarding the ability of the system to detect water leakages, the differences

in performance offered by the fiber sections installed in each scenario, the achievable spatial resolution or the longitudinal diffusion of the water were also performed. This study has clearly indicated the feasibility of using an optical fiber distributed sensor for water leakage monitoring. This system should be checked in field, and a processing stage should be developed to avoid false alarms derived from, for instance, specific weather conditions. This might be also combined with a model considering data acquired from weather stations reporting in real time.

## 5.4. Conclusions

In this chapter, the feasibility of employing Brillouin distributed sensors in different real applications has been demonstrated at lab-scale. Three different approaches have been proposed to demonstrate their possibilities in various sectors such as high-temperature environments, modal analysis in SHM and leakage detection.

The first contribution is a distributed measurement system based on a BOTDA sensor and a multimode gold-coated fiber especially thought to be employed in high-temperature applications. Other previous works have dealt with high-temperature sensing approaches in Brillouin distributed sensors. The main advantage of using gold-coated fibers is that their mechanical properties do not suffer degradations when employed in high-temperature environments for temperatures up to 600°C. This ensures a feasible fiber deployment in field applications, such as industrial boilers, as long as the maximum temperature is below this mentioned value. The experimental results obtained at the laboratory have demonstrated the feasibility of the proposed approach, obtaining a system response for both increasing and decreasing temperatures between 50 and 600°C that can be modeled via exponential fitting and showing a temperature mean accuracy of about 10°C.

The second contribution presented in this chapter is a solution capable of estimating the location of mechanical changes in an aluminum composite panel with good resolution. The proposed approach is based on the use of slope-assisted BOTDA to perform modal analysis in the specimen under study. This distributed sensing configuration is employed to retrieve the mode shapes of the first three bending modes of the plate. The position of the defect is estimated by evaluating the changes in the shapes of the

first two strain mode shapes. The spatial resolution achieved by the sensing system to locate the damages on the panel depends on two factors: the spatial resolution employed by the sensor and the deployment of the fiber on the panel.

Finally, the third contribution is an experimental demonstration of a leakage monitoring system designed for large diameter water pipes employing a Brillouin distributed fiber sensor. To verify the feasibility of the proposed solution to detect leakages, a comprehensive set of experiments was carried out in a specific infrastructure that simulates the conditions to be found in field tests. The deployed optical cable, a free fiber inside a protective cable, was installed under three different pipes buried in different filling materials. To verify the suitability of this proposal several studies were conducted. The main objective was demonstrated, verifying the ability of the system to detect water leakages. Moreover, the achievable spatial resolution or the longitudinal diffusion of the water were also analysed.

## **Part III**

### **Conclusions and open lines**

This is the final part of this thesis dissertation. This part summarizes the main conclusions obtained during the development of the thesis work and the open lines that have appeared.

The chapters included in this part are:

- Chapter 6: Conclusions
- Chapter 7: Open lines



## Chapter 6

---

### Summary and conclusions

---

This final chapter summarized all the conclusions derived from the works detailed in the previous chapters of this thesis dissertation. As previously mentioned, the main objective is to contribute to the performance enhancement of distributed sensors based on Brillouin effect, specially those based on stimulated Brillouin scattering (SBS). In this way, almost all the contributions presented in this thesis are based on the use of a Brillouin optical time domain analysis (BOTDA) sensor, with one exception focused on an alternative variation of Brillouin distributed sensors based on spontaneous Brillouin scattering (SpBS) and working in the frequency domain.

The first part of this thesis presents the theoretical fundamentals of the Brillouin scattering processes, both spontaneous and stimulated. First, a brief introduction to optical fiber sensors has been presented, especially those based light scattering effects. Some concepts have been introduced here, such as the linear and non-linear effects and the distinction between elastic and inelastic scattering processes, introducing the main scattering effects (Rayleigh, Brillouin and Raman). Once the fundamentals of the process have been explained, the different sensors based on Brillouin scattering are explained, devoting greater effort to explain the BOTDA sensor due to its relevant presence in this thesis dissertation. The main limitations of the technique have been detected and explained, including concepts such as non-local effects, modulation instability, the limited spatial resolution or the sensing range, and also providing the most

relevant solutions proposed in the literature to overcome such limitations.

The second part focuses on contributions designed to increase the performance of Brillouin distributed sensors. This has been divided into three chapters: the first for contributions based on modifications of the experimental setups; the second is about the application of processing techniques on the experimental data; and finally the third deals with some monitoring solutions for different applications.

In a detailed way, the third chapter contains proposals for new configurations of Brillouin distributed sensors that bring some advantages such as the overcoming of non-local effects or the possibility of measuring in the frequency domain using only one fiber end.

In this way, the first contribution is a frequency modulated BOTDA sensor that can perform distributed measurements using high probe powers, even higher than the Brillouin threshold of the deployed sensing fiber, without being affected by detrimental non-local effects. The proposed experimental setup employs a dual-probe sideband BOTDA setup, in which the probe waves are frequency modulated along the sensing fiber. Therefore, the interactions taking place within the fiber between the pump and the probe vary along the fiber, provoking that the broadband Brillouin gain and loss spectra are compensated. Directly related to this is the spectral shape of the pulse, that in this case does not suffer the distortion related to non-local effects. This employment of high probe powers has an evident advantage, the detected signal at the receiver is also higher, and therefore the signal-to-noise ratio (SNR). Experimental results have demonstrated the ability of the technique measuring along a 50 km sensing fiber when a probe power of 8 dBm is injected.

The second approach is an experimental configuration that employs the SpBS generated from a sinusoidally modulated pump light and the frequency domain to monitor a sensing fiber. This sensor is known as Brillouin optical frequency domain reflectometry (BOFDR). This system presents the typical advantages of frequency based sensors, such as the narrowband Brillouin spectrum of Brillouin optical frequency domain analysis (BOFDA) sensor, but also its capacity to perform distributed measurements along a sensing fiber using only one fiber end. Moreover, these sensors are free from a detrimental effect present in BOFDA that produces some distorting components related to acoustic wave modulation. Using the proposed configuration a hot spot of 1 m at the

---

end of a 5 km fiber length was clearly resolved.

The third and last contribution of this chapter is the feasibility analysis of using fiber ring lasers in BOTDA sensors. This proposal analysed the use of Erbium-doped fiber ring laser (EDFRL) as the laser source of a BOTDA sensor. The EDFRL was designed to work in the single longitudinal mode, avoiding some typical problems that this kind of fiber ring laser has, such as multimode operation. One advantage of this fiber laser is that it allows an easy change of its wavelength from 1500 to 1600 nm by only replacing the selected fiber Bragg grating (DFB). After a laser characterization, it was tested on dual-probe sideband BOTDA setup verifying its performance during the distributed measurement along a 50 km sensing fiber. At the end of the mentioned fiber, a hot spot was provoked. To compare the obtained experimental results, the same measurements were also done using a distributed feedback (DFB) laser. The results show that the proposed configuration presents more noise than the conventional system. However, the viability of using other types of laser sources have been demonstrated, opening the possibility of using other laser configurations that can improve the final performance.

The fourth chapter is focused on solutions that employ processing strategies to increase the performance of the sensors.

In this way, the first contribution of this chapter provides a solution to the problem of the discrimination between temperature and strain measurements. This new approach is based on processing the measurement performed using a dual-probe sideband BOTDA sensor with an artificial neural network (ANN) and other pre-processing techniques. This can enable an automatic tool to discriminate between simultaneous temperature/strain measurements. Using a pre-processing stage formed by principal components analysis (PCA) in addition to gain normalization and spatial filtering, a classification rate of around 90% for temperature and strain discrimination was achieved using the ANN solution. Besides the good classification rate obtained, this solution exhibits other advantages in comparison with other discrimination proposals. First, this solution does not imply modifications on the experimental setup that can drive to higher costs or an increase of the setup complexity and, in addition, it allows real-time operation, making the decision in only a few milliseconds. The main drawback of this artificial intelligence solutions is the need of a training stage before the real implementation of the discrimination tool. The deeper and more appropriate to the target application the training, the better the final performance of the discrimination

will be.

The other proposal of this chapter is the use of a subpixel algorithm instead of the commonly employed Lorentz curve fitting to estimate the Brillouin frequency shift (BFS) along a sensing fiber. This processing algorithm is directly applied to the measured Brillouin spectrum, and it is based on the estimation of the mass centre of the peak under analysis. The selected algorithm is known as the centroid detection algorithm (CDA), and it is one of the most employed subpixel algorithms. The main conclusion obtained after employing this algorithm to estimate the BFS along a 50 km length sensing fiber is that the proposed algorithm shows an improved performance when processing data measured using a big frequency step. For instance, if a 20 MHz frequency step is employed, the CDA subpixel algorithm provides better results than those derived from using Lorentz curve fitting, with a lower frequency error and also a lower computational time. This may be suitable for use in applications where it may be more relevant to have a fast acquisition and processing of the results than the associated accuracy.

Finally, the last chapter of the contribution part, chapter five, collects the contributions made seeking at lab-scale for future implementations in real applications. These could be high-temperature environments, such as industrial boilers, dynamic analysis of different structures or pipeline monitoring.

The first one of these last three contributions is the proposal of a BOTDA distributed sensor especially designed for high-temperature environments. This is achievable due to the employment of a metallic coated optical fiber, in this case, a multimode gold-coated fiber. To demonstrate the feasibility of the proposed approach, some experimental test were performed at the laboratory using a furnace chamber. The results obtained during a calibration show a dependence between the temperature and the BFS that can be modeled via exponential fitting. The main advantage of using this kind of fiber is that its mechanical properties are not affected by the high-temperature, as long as it is less than 600°C. This property makes this kind of fibers perfect to be employed in real industrial field scenarios.

The second application where these systems can be used is the dynamic analysis of some infrastructures. In this case, the proposal presented here is a slope-assisted BOTDA sensor designed to perform modal analysis in an aluminum composite panel

---

with a high resolution. The spatial resolution employed in this monitoring application is defined by two independent elements: the spatial resolution of the distributed interrogator and the fiber deployment on the panel. By using this dynamic sensor the mode shapes of the first three bending modes of the plate are retrieved. This recovered information can be employed to estimate the position of mechanical variations in the panel with good resolution. These defects that can appear on the panels can be located by evaluating and comparing the changes in the shapes of the first two strain mode shapes.

Finally, the last contribution of this thesis dissertation is a pipeline leakage monitoring system, specifically for large diameter water pipes. Some experimental tests have been conducted in a laboratory facility to check the capacity of the proposed Brillouin distributed sensor to detect and locate leakages. It is important to notice that the optical fiber employed is deployed in cable especially thought to be insensitive to strain variations, hence it is only affected by temperature changes. This cable was installed under three different pipes buried in different filling materials and several studies were carried out to check the capacity of the sensor to locate the water leakages, the achievable spatial resolution of the system or the longitudinal diffusion of the water in the filling materials.



# Chapter 7

---

## Open lines

---

The contributions presented in this thesis dissertation try to contribute in some research areas within the field of Brillouin distributed fiber sensors. However, these contributions are not completely closed and they can still be improved by applying some other complementary solutions.

For instance, the chapter that deals with the modifications of the experimental setup has some open lines. A possibility might be to try to increase the distance of the sensing fiber within the solution designed to avoid non-local effects. In this way, it could be possible to experimentally demonstrate its real potential given that in the performed measurements it was limited by the maximum power that the receiver can withstand. In the case of the proposal of a new Brillouin sensor based on the frequency domain, it shows the limitation of 1 m spatial resolution imposed by the vector network analyzer characteristics. However, the commercial availability of compact, multi-GHz vector network analyzers may push the development of sub-meter BOFDR configurations, which could compete with conventional BOTDR systems. Finally, in the case of the proposal of using the Erbium-doped fiber laser as a BOTDA source, it could be interesting to design other fiber ring lasers and compare their performance with the typical BOTDA sensor employing a DFB laser.

The future works related to Chapter 4 are basically the employment of other processing algorithms with the same purposes of those presented here, and compare their

response in terms of accuracy or processing time, among others. For instance, in the case of the employment of artificial intelligence solutions, such as the case of artificial neural networks, it could be very interesting to test other artificial intelligence solutions such as deep learning approaches or support vector machines. Moreover, to obtain a better classification rate it could be necessary to have a more convenient dataset, with more cases of study, and also employing alternative experimental setups not introducing so much inhomogeneity in the measured data. Also, it could be ideal to test the system with real data obtained in a field application. Future works associated with the use of subpixel algorithms to retrieve the BFS can be summarized indicating that it will be necessary to increase the measurement data to be analysed, including more measurements with different parameters, such as varying the number of averages, the spatial resolution employed, and also to verify the capability of detecting hot spot along the fiber. Moreover, it could be possible to compare the results obtained with the proposed algorithm with the obtained with other subpixel algorithms.

Finally, all the contributions of the last chapter have a common open line: to test the proposed solutions in real field applications. In addition to this shared idea, the main limitation of the solution regarding high-temperature measurement is that it employs a multimode fiber that has a lower performance in BOTDA sensors. Therefore it could be very interesting to make the analysis using a gold-coated single-mode fiber. Moreover, in this way it might prove interesting to study the influence of the coating by measuring strain at high temperature, thus verifying its mechanical properties. For the leakage detection system, it must be checked their performance in a real field scenario, being very interesting to develop a processing stage capable of locating the leakages, but also avoiding the false alarms derived, for instance, from specific weather conditions.

# **Part IV**

## **References**



# Chapter 8

---

## References by chapter

---

### 8.1. References of Chapter 2

- [1] Arthur H Hartog. *An Introduction to Distributed Optical Fibre Sensors*. CRC Press, 2017.
- [2] Avi Motil, Arik Bergman, and Moshe Tur. State of the art of brillouin fiber-optic distributed sensing. *Optics & Laser Technology*, 78:81–103, 2016.
- [3] Spillman W Udd E. *Fiber Optic Sensors: An Introduction for Engineers and Scientists*. John Wiley & Sons, 2011.
- [4] José Miguel López-Higuera. *Handbook of optical fibre sensing technology*. Wiley, 2002.
- [5] Robert W Boyd. *Nonlinear optics*. Academic press, 2003.
- [6] Govind P Agrawal. Nonlinear fiber optics. In *Nonlinear Science at the Dawn of the 21st Century*, pages 195–211. Springer, 2000.
- [7] David A Krohn, Trevor MacDougall, and Alexis Mendez. *Fiber optic sensors: fundamentals and applications*. Isa, 2000.
- [8] R Olshansky. Propagation in glass optical waveguides. *Reviews of Modern Physics*, 51(2):341, 1979.

- [9] Jake Bromage. Raman amplification for fiber communications systems. *Journal of Lightwave Technology*, 22(1):79, 2004.
- [10] Ander Zornoza, Rosa Ana Pérez-Herrera, César Elosúa, Silvia Diaz, Candido Bariain, Alayn Loayssa, and Manuel Lopez-Amo. Long-range hybrid network with point and distributed brillouin sensors using raman amplification. *Optics express*, 18(9):9531–9541, 2010.
- [11] Xabier Angulo-Vinuesa, Sonia Martin-Lopez, Javier Nuño, Pedro Corredera, Juan Diego Ania-Castañon, Luc Thévenaz, and Miguel González-Herráez. Raman-assisted brillouin distributed temperature sensor over 100 km featuring 2 m resolution and 1.2 c uncertainty. *Journal of Lightwave Technology*, 30(8):1060–1065, 2012.
- [12] Ozdal Boyraz and Bahram Jalali. Demonstration of a silicon raman laser. *Optics express*, 12(21):5269–5273, 2004.
- [13] JP Dakin, DJ Pratt, GW Bibby, and JN Ross. Distributed optical fibre raman temperature sensor using a semiconductor light source and detector. *Electronics letters*, 21(13):569–570, 1985.
- [14] Alessandro Signorini, Stefano Faralli, Marcelo A Soto, Giovanni Sacchi, Federico Baronti, Roberto Barsacchi, Andrea Lazzeri, Roberto Roncella, Gabriele Bolognini, and Fabrizio Di Pasquale. 40 km long-range raman-based distributed temperature sensor with meter-scale spatial resolution. In *Optical Fiber Communication Conference*, page OWL2. Optical Society of America, 2010.
- [15] Xiaoyi Bao and Liang Chen. Recent progress in brillouin scattering based fiber sensors. *Sensors*, 11(4):4152–4187, 2011.
- [16] RY Chiao, CH Townes, and BP Stoicheff. Stimulated brillouin scattering and coherent generation of intense hypersonic waves. *Physical Review Letters*, 12(21):592, 1964.
- [17] Léon Brillouin. Diffusion de la lumière et des rayons x par un corps transparent homogène-influence de l’agitation thermique. *Annales de physique*, 9(17):88–122, 1922.

- 
- [18] José Miguel López-Higuera, Luis Rodriguez Cobo, Antonio Quintela Incera, and Adolfo Cobo. Fiber optic sensors in structural health monitoring. *Journal of lightwave technology*, 29(4):587–608, 2011.
- [19] SP Smith, F Zarinetchi, and S Ezekiel. Narrow-linewidth stimulated brillouin fiber laser and applications. *Optics letters*, 16(6):393–395, 1991.
- [20] Jihong Geng, Sean Staines, Zuolan Wang, Jie Zong, Mike Blake, and Shibin Jiang. Highly stable low-noise brillouin fiber laser with ultranarrow spectral linewidth. *IEEE Photonics Technology Letters*, 18(17):1813–1815, 2006.
- [21] Javier Urricelqui, Mikel Sagues, and Alayn Loayssa. Brillouin optical time-domain analysis sensor assisted by brillouin distributed amplification of pump pulses. *Optics express*, 23(23):30448–30458, 2015.
- [22] Aldo Minardo. *Fiber-optic distributed strain/temperature sensors based on stimulated Brillouin scattering*. PhD thesis, Italy, Napoli: Seconda universita’ degli studi di Napoli, Dottorato di Ricerca in Ingegneria Elettronica XVI Ciclo, [cit. 21. 11. 2012]. Dostupné z URL < [http://www.dii.unina2.it/opto/publications/PhD\\_Thesis\\_Minardo.pdf](http://www.dii.unina2.it/opto/publications/PhD_Thesis_Minardo.pdf), 2003.
- [23] Luc Thevenaz. *Advanced fiber optics: concepts and technology*. EPFL press, 2011.
- [24] M Oskar Van Deventer and Andre J Boot. Polarization properties of stimulated brillouin scattering in single-mode fibers. *Journal of Lightwave Technology*, 12(4):585–590, 1994.
- [25] MK Barnoski and SM Jensen. Fiber waveguides: a novel technique for investigating attenuation characteristics. *Applied optics*, 15(9):2112–2115, 1976.
- [26] SD Personick. Photon probe—an optical-fiber time-domain reflectometer. *Bell Labs Technical Journal*, 56(3):355–366, 1977.
- [27] Tsuneo Horiguchi and Mitsuhiro Tateda. Optical-fiber-attenuation investigation using stimulated brillouin scattering between a pulse and a continuous wave. *Optics Letters*, 14(8):408–410, 1989.
- [28] D Culverhouse, F Farahi, CN Pannell, and DA Jackson. Potential of stimulated brillouin scattering as sensing mechanism for distributed temperature sensors. *Electronics Letters*, 25(14):913–915, 1989.

- [29] Toshio Kurashima, Tsuneo Horiguchi, and Mitsuhiro Tateda. Distributed-temperature sensing using stimulated brillouin scattering in optical silica fibers. *Optics letters*, 15(18):1038–1040, 1990.
- [30] Tsuneo Horiguchi, Toshio Kurashima, and Mitsuhiro Tateda. A technique to measure distributed strain in optical fibers. *IEEE photonics technology letters*, 2(5):352–354, 1990.
- [31] Tsuneo Horiguchi, Kaoru Shimizu, Toshio Kurashima, Mitsuhiro Tateda, and Yahei Koyamada. Development of a distributed sensing technique using brillouin scattering: Optical fiber sensors. *Journal of lightwave technology*, 13(7):1296–1302, 1995.
- [32] Carlos Augusto Galindez-Jamiroy and José Miguel López-Higuera. Brillouin distributed fiber sensors: an overview and applications. *Journal of Sensors*, 2012, 2012.
- [33] Yongkang Dong, Pengbai Xu, Cheng Fu, Chenglin Zhang, Dengwang Zhou, Taofei Jiang, Hongying Zhang, Zhiwei Lu, Liang Chen, and Xiaoyi Bao. 1200° c high-temperature distributed brillouin optical fiber sensing based on photonics crystal fiber. In *International Conference on Optical Fibre Sensors (OFS24)*, pages 963485–963485–4. International Society for Optics and Photonics, 2015.
- [34] Marc Nikles, Luc Thevenaz, and Philippe A Robert. Brillouin gain spectrum characterization in single-mode optical fibers. *Journal of Lightwave Technology*, 15(10):1842–1851, 1997.
- [35] Aldo Minardo, Agnese Coscetta, Romeo Bernini, and Luigi Zeni. Brillouin optical time domain analysis in silica fibers at 850-nm wavelength. *IEEE Photon. Technol. Letters*, 28(22):2577–2580, 2016.
- [36] Ester Catalano, Agnese Coscetta, Romeo Bernini, Luigi Zeni, and Aldo Minardo. Characterization of silica fibers for dual wavelength brillouin sensors. 2017.
- [37] Kazuo Hotate and Takemi Hasegawa. Measurement of brillouin gain spectrum distribution along an optical fiber using a correlation-based technique—proposal, experiment and simulation—. *IEICE transactions on electronics*, 83(3):405–412, 2000.

- [38] Kwang-Yong Song, Zuyuan He, and Kazuo Hotate. Distributed strain measurement with millimeter-order spatial resolution based on brillouin optical correlation domain analysis and beat lock-in detection scheme. In *Optical Fiber Sensors*, page ThC2. Optical Society of America, 2006.
- [39] Kazuo Hotate. Recent achievements in bocda/bocdr. In *SENSORS, 2014 IEEE*, pages 142–145. IEEE, 2014.
- [40] Kazuo Hotate. Fiber distributed brillouin sensing with optical correlation domain techniques. *Optical Fiber Technology*, 19(6):700–719, 2013.
- [41] Kazuo Hotate, Hiroshi Arai, and Kwang Yong Song. Range-enlargement of simplified brillouin optical correlation domain analysis based on a temporal gating scheme. *SICE Journal of Control, Measurement, and System Integration*, 1(4):271–274, 2008.
- [42] Yosuke Mizuno, Weiwen Zou, Zuyuan He, and Kazuo Hotate. Proposal of brillouin optical correlation-domain reflectometry (bocdr). *Optics express*, 16(16):12148–12153, 2008.
- [43] Sitthipong Manotham, Masato Kishi, Zuyuan He, and Kazuo Hotate. 1-cm spatial resolution with large dynamic range in strain distributed sensing by brillouin optical correlation domain reflectometry based on intensity modulation. In *Third Asia Pacific Optical Sensors Conference*, volume 8351, page 835136. International Society for Optics and Photonics, 2012.
- [44] Yosuke Mizuno, Zuyuan He, and Kazuo Hotate. Measurement range enlargement in brillouin optical correlation-domain reflectometry based on temporal gating scheme. *Optics express*, 17(11):9040–9046, 2009.
- [45] Yosuke Mizuno, Zuyuan He, and Kazuo Hotate. One-end-access high-speed distributed strain measurement with 13-mm spatial resolution based on brillouin optical correlation-domain reflectometry. *IEEE Photonics Technology Letters*, 21(7):474–476, 2009.
- [46] Dieter Garus, Katerina Krebber, Frank Schliep, and Torsten Gogolla. Distributed sensing technique based on brillouin optical-fiber frequency-domain analysis. *Optics letters*, 21(17):1402–1404, 1996.

- [47] Aldo Minardo, Genni Testa, Luigi Zeni, and Romeo Bernini. Theoretical and experimental analysis of brillouin scattering in single-mode optical fiber excited by an intensity-and phase-modulated pump. *Journal of Lightwave Technology*, 28(2):193–200, 2010.
- [48] Romeo Bernini, Aldo Minardo, and Luigi Zeni. Distributed sensing at centimeter-scale spatial resolution by bofda: Measurements and signal processing. *IEEE Photonics Journal*, 4(1):48–56, 2011.
- [49] D Garus, Torsten Gogolla, Katerina Krebber, and Frank Schliep. Brillouin optical-fiber frequency-domain analysis for distributed temperature and strain measurements. *Journal of lightwave technology*, 15(4):654–662, 1997.
- [50] H Ghafoori-Shiraz and Takanori Okoshi. Fault location in optical fibers using optical frequency domain reflectometry. *Journal of lightwave technology*, 4(3):316–322, 1986.
- [51] Aleksander Wosniok, Nils Nöther, and Katerina Krebber. Distributed fibre optic sensor system for temperature and strain monitoring based on brillouin optical-fibre frequency-domain analysis. *Procedia Chemistry*, 1(1):397–400, 2009.
- [52] Aldo Minardo, Romeo Bernini, and Luigi Zeni. A simple technique for reducing pump depletion in long-range distributed brillouin fiber sensors. *IEEE Sensors Journal*, 9(6):633–634, 2009.
- [53] Torsten Gogolla and Katerina Krebber. Fiber sensors for distributed temperature and strain measurements using brillouin scattering and frequency-domain methods. In *Chemical, Biochemical and Environmental Fiber Sensors IX*, volume 3105, pages 168–179. International Society for Optics and Photonics, 1997.
- [54] Thomas Kapa, Andy Schreier, and Katerina Krebber. 63 km bofda for temperature and strain monitoring. *Sensors*, 18(5):1600, 2018.
- [55] Thomas Kapa, Andy Schreier, and Katerina Krebber. A 100-km bofda assisted by first-order bi-directional raman amplification. *Sensors*, 19(7):1527, 2019.
- [56] Kaoru Shimizu, Tsuneo Horiguchi, Yahei Koyamada, and Toshio Kurashima. Coherent self-heterodyne detection of spontaneously brillouin-scattered light waves in a single-mode fiber. *Optics letters*, 18(3):185–187, 1993.

- 
- [57] Ander Zornoza Indart. *Contribution to the development of distributed fiber optic sensors based on stimulated Brillouin scattering*. PhD thesis, 2014.
- [58] Marcelo A Soto. Distributed brillouin sensing: time-domain techniques. *Handbook of Optical Fibers*, pages 1–91, 2018.
- [59] PC Wait and TP Newson. Landau placzek ratio applied to distributed fibre sensing. *Optics Communications*, 122(4-6):141–146, 1996.
- [60] Sally M Maughan, Huai H Kee, and Trevor P Newson. Simultaneous distributed fibre temperature and strain sensor using microwave coherent detection of spontaneous brillouin backscatter. *Measurement Science and Technology*, 12(7):834, 2001.
- [61] Qing Bai, Qinglin Wang, Dong Wang, Yu Wang, Yan Gao, Hongjuan Zhang, Mingjiang Zhang, and Baoquan Jin. Recent advances in brillouin optical time domain reflectometry. *Sensors*, 19(8):1862, 2019.
- [62] Rugang Wang, Liuying Zhou, and Xuping Zhang. Performance of brillouin optical time domain reflectometer with erbium doped fiber amplifier. *Optik-International Journal for Light and Electron Optics*, 125(17):4864–4867, 2014.
- [63] Muping Song, Qiaolan Xia, Kaibin Feng, Yan Lu, and Cong Yin. 100 km brillouin optical time-domain reflectometer based on unidirectionally pumped raman amplification. *Optical and Quantum Electronics*, 48(1):30, 2016.
- [64] Yongqian Li, Jun Wang, and Zhi Yang. A method for improving botdr system performance. In *2012 Symposium on Photonics and Optoelectronics*, pages 1–4. IEEE, 2012.
- [65] Feng Wang, Weiwei Zhan, Xuping Zhang, and Yuangang Lu. Improvement of spatial resolution for botdr by iterative subdivision method. *Journal of Lightwave Technology*, 31(23):3663–3667, 2013.
- [66] Wei Yang, Yuanhong Yang, and Mingwei Yang. Fast digital envelope detector based on generalized harmonic wavelet transform for botdr performance improvement. *Measurement Science and Technology*, 25(6):065103, 2014.

- [67] Fabien Ravet, Fabien Briffod, and Marc Niklès. Extended distance fiber optic monitoring for pipeline leak and ground movement detection. In *2008 7th International Pipeline Conference*, pages 689–697. American Society of Mechanical Engineers, 2008.
- [68] Branko Glisic, Jeremy Chen, and David Hubbell. Streicker bridge: A comparison between bragg-grating long-gauge strain and temperature sensors and brillouin scattering-based distributed strain and temperature sensors. In *Sensors and Smart Structures Technologies for Civil, Mechanical, and Aerospace Systems 2011*, volume 7981, page 79812C. International Society for Optics and Photonics, 2011.
- [69] Luigi Zeni, L Picarelli, B Avolio, A Coscetta, R Papa, G Zeni, C Di Maio, R Vassallo, and Aldo Minardo. Brillouin optical time-domain analysis for geotechnical monitoring. *Journal of Rock Mechanics and Geotechnical Engineering*, 7(4):458–462, 2015.
- [70] Aldo Minardo, Giuseppe Porcaro, Daniele Giannetta, Romeo Bernini, and Luigi Zeni. Real-time monitoring of railway traffic using slope-assisted brillouin distributed sensors. *Applied optics*, 52(16):3770–3776, 2013.
- [71] Romeo Bernini, Aldo Minardo, and Luigi Zeni. Reconstruction technique for stimulated brillouin scattering distributed fiber-optic sensors. *Optical Engineering*, 41, 2002.
- [72] Cheng Feng, Jaffar Emad Kadum, and Thomas Schneider. The state-of-the-art of brillouin distributed fiber sensing. In *Brillouin Distributed and Fiber-bragg-grating-based Fiber Sensing-Principle, Measurement and Applications*. In-techOpen, 2019.
- [73] Marc Nikles, Luc Thévenaz, and Philippe A Robert. Simple distributed fiber sensor based on brillouin gain spectrum analysis. *Optics letters*, 21(10):758–760, 1996.
- [74] Vincent Lecoecuche, David J Webb, Christopher N Pannell, and David A Jackson. Transient response in high-resolution brillouin-based distributed sensing using probe pulses shorter than the acoustic relaxation time. *Optics letters*, 25(3):156–158, 2000.

- 
- [75] Haritz Iribas, Jon Mariñelarena, Cheng Feng, Javier Urricelqui, Thomas Schneider, and Alayn Loayssa. Effects of pump pulse extinction ratio in brillouin optical time-domain analysis sensors. *Optics express*, 25(22):27896–27912, 2017.
- [76] Ander Zornoza, David Olier, Mikel Sagues, and Alayn Loayssa. Brillouin distributed sensor using rf shaping of pump pulses. *Measurement Science and Technology*, 21(9):094021, 2010.
- [77] Marcelo A Soto and Luc Thévenaz. Modeling and evaluating the performance of brillouin distributed optical fiber sensors. *Optics express*, 21(25):31347–31366, 2013.
- [78] Stella M Foaleng and Luc Thévenaz. Impact of raman scattering and modulation instability on the performances of brillouin sensors. In *21st International Conference on Optical Fiber Sensors*, volume 7753, page 77539V. International Society for Optics and Photonics, 2011.
- [79] Luc Thévenaz, Stella Foaleng Mafang, and Jie Lin. Effect of pulse depletion in a brillouin optical time-domain analysis system. *Optics express*, 21(12):14017–14035, 2013.
- [80] Dario Alasia, Miguel Gonzalez Herraiez, Laura Abrardi, Sonia Martin-Lopez, and Luc Thevenaz. Detrimental effect of modulation instability on distributed optical fiber sensors using stimulated brillouin scattering. In *17th International Conference on Optical Fibre Sensors*, volume 5855, pages 587–590. International Society for Optics and Photonics, 2005.
- [81] Ander Zornoza, Aldo Minardo, Romeo Bernini, Alayn Loayssa, and Luigi Zeni. Pulsing the probe wave to reduce nonlocal effects in brillouin optical time-domain analysis (botda) sensors. *IEEE Sensors Journal*, 11(4):1067–1068, 2010.
- [82] Yongkang Dong, Liang Chen, and Xiaoyi Bao. Extending the sensing range of brillouin optical time-domain analysis combining frequency-division multiplexing and in-line edfas. *Journal of Lightwave Technology*, 30(8):1161–1167, 2011.
- [83] Yongkang Dong, Liang Chen, and Xiaoyi Bao. Time-division multiplexing-based botda over 100km sensing length. *Optics Letters*, 36(2):277–279, 2011.

- [84] Javier Urricelqui, Mikel Sagues, and Alayn Loayssa. Botda measurements tolerant to non-local effects by using a phase-modulated probe wave and rf demodulation. *Optics express*, 21(14):17186–17194, 2013.
- [85] Alejandro Dominguez-Lopez, Zhisheng Yang, Marcelo A Soto, Xabier Angulo-Vinuesa, Sonia Martin-Lopez, Luc Thevenaz, and Miguel Gonzalez-Herraez. Novel scanning method for distortion-free botda measurements. *Optics express*, 24(10):10188–10204, 2016.
- [86] Alejandro Dominguez-Lopez, Xabier Angulo-Vinuesa, Alexia Lopez-Gil, Sonia Martin-Lopez, and Miguel Gonzalez-Herraez. Non-local effects in dual-probe-sideband brillouin optical time domain analysis. *Optics Express*, 23(8):10341–10352, 2015.
- [87] Yongkang Dong and Xiaoyi Bao. High spatial resolution and long-distance botda using differential brillouin gain in a dispersion shifted fiber. In *20th International Conference on Optical Fibre Sensors*, volume 7503, page 750384. International Society for Optics and Photonics, 2009.
- [88] Javier Urricelqui, Mehdi Alem, Mikel Sagues, Luc Thévenaz, Alayn Loayssa, and Marcelo A Soto. Mitigation of modulation instability in brillouin distributed fiber sensors by using orthogonal polarization pulses. In *24th International Conference on Optical Fibre Sensors*, volume 9634, page 963433. International Society for Optics and Photonics, 2015.
- [89] Marcelo A Soto, Jaime A Ramirez, and Luc Thevenaz. Intensifying the response of distributed optical fibre sensors using 2d and 3d image restoration. *Nature communications*, 7:10870, 2016.
- [90] Marcelo A Soto, Jaime A Ramírez, and Luc Thévenaz. Optimizing image denoising for long-range brillouin distributed fiber sensing. *Journal of Lightwave Technology*, 36(4):1168–1177, 2017.
- [91] X Bao, A Brown, M DeMerchant, and J Smith. Characterization of the brillouin-loss spectrum of single-mode fibers by use of very short ( $< 10$ -ns) pulses. *Optics letters*, 24(8):510–512, 1999.
- [92] Anthony W Brown, Bruce G Colpitts, and Kellie Brown. Distributed sensor based on dark-pulse brillouin scattering. *IEEE Photonics Technology Letters*, 17(7):1501–1503, 2005.

- [93] Anthony W Brown, Bruce G Colpitts, and Kellie Brown. Dark-pulse brillouin optical time-domain sensor with 20-mm spatial resolution. *Journal of Lightwave Technology*, 25(1):381–386, 2007.
- [94] K Kishida and CH Li. Pulse pre-pump-botda technology for new generation of distributed strain measuring system. *Structural health monitoring and intelligent infrastructure*, 1:471–477, 2005.
- [95] Wenhai Li, Xiaoyi Bao, Yun Li, and Liang Chen. Differential pulse-width pair botda for high spatial resolution sensing. *Optics express*, 16(26):21616–21625, 2008.
- [96] Aldo Minardo, Romeo Bernini, and Luigi Zeni. Numerical analysis of single pulse and differential pulse-width pair botda systems in the high spatial resolution regime. *Optics express*, 19(20):19233–19244, 2011.
- [97] Javier Urricelqui, Mikel Sagues, and Alayn Loayssa. Phasorial differential pulse-width pair technique for long-range brillouin optical time-domain analysis sensors. *Optics express*, 22(14):17403–17408, 2014.
- [98] Marcelo A Soto, Mohammad Taki, Gabriele Bolognini, and Fabrizio Di Pasquale. Optimization of a dpp-botda sensor with 25 cm spatial resolution over 60 km standard single-mode fiber using simplex codes and optical pre-amplification. *Optics Express*, 20(7):6860–6869, 2012.
- [99] Flavien Gyger, Etienne Rochat, Sanghoon Chin, Marc Niklès, and Luc Thévenaz. Extending the sensing range of brillouin optical time-domain analysis up to 325 km combining four optical repeaters. In *23rd International Conference on Optical Fibre Sensors*, volume 9157, page 91576Q. International Society for Optics and Photonics, 2014.
- [100] Félix Rodríguez-Barrios, Sonia Martín-López, Ana Carrasco-Sanz, Pedro Corredera, Juan Diego Ania-Castañón, Luc Thévenaz, and Miguel González-Herráez. Distributed brillouin fiber sensor assisted by first-order raman amplification. *Journal of lightwave technology*, 28(15):2162–2172, 2010.
- [101] Marcelo A Soto, Gabriele Bolognini, and Fabrizio Di Pasquale. Optimization of long-range botda sensors with high resolution using first-order bi-directional raman amplification. *Optics express*, 19(5):4444–4457, 2011.

- [102] Sonia Martin-Lopez, Mercedes Alcon-Camas, Felix Rodriguez, Pedro Corredera, Juan Diego Ania-Castañon, Luc Thévenaz, and Miguel Gonzalez-Herraez. Brillouin optical time-domain analysis assisted by second-order raman amplification. *Optics express*, 18(18):18769–18778, 2010.
- [103] Marcelo A Soto, Gabriele Bolognini, Fabrizio Di Pasquale, and Luc Thévenaz. Simplex-coded botda fiber sensor with 1 m spatial resolution over a 50 km range. *Optics Letters*, 35(2):259–261, 2010.
- [104] Marcelo A Soto, Sébastien Le Floch, and Luc Thévenaz. Bipolar optical pulse coding for performance enhancement in botda sensors. *Optics Express*, 21(14):16390–16397, 2013.
- [105] M Taki, Y Muanenda, CJ Oton, T Nannipieri, A Signorini, and F Di Pasquale. Cyclic pulse coding for fast botda fiber sensors. *Optics letters*, 38(15):2877–2880, 2013.
- [106] Marcelo A Soto, Mohammad Taki, Gabriele Bolognini, and Fabrizio Di Pasquale. Simplex-coded botda sensor over 120-km smf with 1-m spatial resolution assisted by optimized bidirectional raman amplification. *IEEE Photonics Technology Letters*, 24(20):1823–1826, 2012.
- [107] Romeo Bernini, Aldo Minardo, and Luigi Zeni. Dynamic strain measurement in optical fibers by stimulated brillouin scattering. *Optics letters*, 34(17):2613–2615, 2009.
- [108] Yair Peled, Avi Motil, Lior Yaron, and Moshe Tur. Slope-assisted fast distributed sensing in optical fibers with arbitrary brillouin profile. *Optics express*, 19(21):19845–19854, 2011.
- [109] Avi Motil, Orr Danon, Yair Peled, and Moshe Tur. Pump-power-independent double slope-assisted distributed and fast brillouin fiber-optic sensor. *IEEE Photonics Technology Letters*, 26(8):797–800, 2014.
- [110] Javier Urricelqui, Ander Zornoza, Mikel Sagues, and Alayn Loayssa. Dynamic botda measurements based on brillouin phase-shift and rf demodulation. *Optics express*, 20(24):26942–26949, 2012.
- [111] Yair Peled, Avi Motil, and Moshe Tur. Fast brillouin optical time domain analysis for dynamic sensing. *Optics express*, 20(8):8584–8591, 2012.

- [112] Asher Voskoboinik, Omer F Yilmaz, Alan W Willner, and Moshe Tur. Sweep-free distributed brillouin time-domain analyzer (sf-botda). *Optics express*, 19(26):B842–B847, 2011.
- [113] Mohsen Amiri Farahani, Michael TV Wylie, Eduardo Castillo-Guerra, and Bruce G Colpitts. Reduction in the number of averages required in botda sensors using wavelet denoising techniques. *Journal of Lightwave Technology*, 30(8):1134–1142, 2011.
- [114] Mohsen Amiri Farahani, Eduardo Castillo-Guerra, and Bruce G Colpitts. Acceleration of measurements in botda sensors using adaptive linear prediction. *IEEE Sensors Journal*, 13(1):263–272, 2012.
- [115] Yonas Muanenda, Mohammad Taki, and Fabrizio Di Pasquale. Long-range accelerated botda sensor using adaptive linear prediction and cyclic coding. *Optics letters*, 39(18):5411–5414, 2014.
- [116] Abul Kalam Azad, Liang Wang, Nan Guo, Hwa-Yaw Tam, and Chao Lu. Signal processing using artificial neural network for botda sensor system. *Optics express*, 24(6):6769–6782, 2016.
- [117] Jeff Smith, Anthony Brown, Michael DeMerchant, and Xiaoyi Bao. Simultaneous distributed strain and temperature measurement. *Applied optics*, 38(25):5372–5377, 1999.
- [118] Xiaoyi Bao, Qinrong Yu, and Liang Chen. Simultaneous strain and temperature measurements with polarization-maintaining fibers and their error analysis by use of a distributed brillouin loss system. *Optics letters*, 29(12):1342–1344, 2004.
- [119] Weiwen Zou, Zuyuan He, and Kazuo Hotate. Complete discrimination of strain and temperature using brillouin frequency shift and birefringence in a polarization-maintaining fiber. *Optics express*, 17(3):1248–1255, 2009.
- [120] CC Lee, PW Chiang, and S Chi. Utilization of a dispersion-shifted fiber for simultaneous measurement of distributed strain and temperature through brillouin frequency shift. *IEEE Photonics Technology Letters*, 13(10):1094–1096, 2001.
- [121] Lufan Zou, Xiaoyi Bao, Shahraam Afshar, and Liang Chen. Dependence of the brillouin frequency shift on strain and temperature in a photonic crystal fiber. *Optics letters*, 29(13):1485–1487, 2004.

## 8.2. References of Chapter 3

- [1] D Culverhouse, F Farahi, CN Pannell, and DA Jackson. Potential of stimulated brillouin scattering as sensing mechanism for distributed temperature sensors. *Electronics Letters*, 25(14):913–915, 1989.
- [2] Alejandro Domínguez-López, Alexia López-Gil, Sonia Martín-López, and Miguel González-Herráez. Signal-to-noise ratio improvement in botda using balanced detection. *IEEE Photonics Technology Letters*, 26(4):338–341, 2013.
- [3] Wenhai Li, Xiaoyi Bao, Yun Li, and Liang Chen. Differential pulse-width pair botda for high spatial resolution sensing. *Optics express*, 16(26):21616–21625, 2008.
- [4] Marcelo A Soto, Gabriele Bolognini, and Fabrizio Di Pasquale. Optimization of long-range botda sensors with high resolution using first-order bi-directional raman amplification. *Optics express*, 19(5):4444–4457, 2011.
- [5] Luc Thévenaz, Stella Foaleng Mafang, and Jie Lin. Effect of pulse depletion in a brillouin optical time-domain analysis system. *Optics express*, 21(12):14017–14035, 2013.
- [6] Aldo Minardo, Romeo Bernini, and Luigi Zeni. A simple technique for reducing pump depletion in long-range distributed brillouin fiber sensors. *IEEE Sensors Journal*, 9(6):633–634, 2009.
- [7] Javier Urricelqui, Mikel Sagues, and Alayn Loayssa. Botda measurements tolerant to non-local effects by using a phase-modulated probe wave and rf demodulation. *Optics Express*, 21(14):17186–17194, 2013.
- [8] Yongkang Dong, Liang Chen, and Xiaoyi Bao. Extending the sensing range of brillouin optical time-domain analysis combining frequency-division multiplexing and in-line edfas. *Journal of Lightwave Technology*, 30(8):1161–1167, 2012.
- [9] Yongkang Dong, Liang Chen, and Xiaoyi Bao. Time-division multiplexing-based botda over 100km sensing length. *Optics Letters*, 36(2):277–279, 2011.
- [10] Ander Zornoza, Aldo Minardo, Romeo Bernini, Alayn Loayssa, and Luigi Zeni. Pulsing the probe wave to reduce nonlocal effects in brillouin optical time-domain analysis (botda) sensors. *IEEE Sensors Journal*, 11(4):1067–1068, 2011.

- [11] Alejandro Dominguez-Lopez, Xabier Angulo-Vinuesa, Alexia Lopez-Gil, Sonia Martin-Lopez, and Miguel Gonzalez-Herraez. Non-local effects in dual-probe-sideband brillouin optical time domain analysis. *Optics Express*, 23(8):10341–10352, 2015.
- [12] Tomoya Shimizu, Kazuhide Nakajima, Kazuyuki Shiraki, Koji Ieda, and Izumi Sankawa. Evaluation methods and requirements for the stimulated brillouin scattering threshold in a single-mode fiber. *Optical Fiber Technology*, 14(1):10–15, 2008.
- [13] Asaf David and Moshe Horowitz. Low-frequency transmitted intensity noise induced by stimulated brillouin scattering in optical fibers. *Optics express*, 19(12):11792–11803, 2011.
- [14] Javier Urricelqui, Mikel Sagues, and Alayn Loayssa. Synthesis of brillouin frequency shift profiles to compensate non-local effects and brillouin induced noise in botda sensors. *Optics express*, 22(15):18195–18202, 2014.
- [15] James B Coles, BP-P Kuo, Nikola Alic, Slaven Moro, C-S Bres, JM Chavez Boggio, PA Andrekson, Magnus Karlsson, and S Radic. Bandwidth-efficient phase modulation techniques for stimulated brillouin scattering suppression in fiber optic parametric amplifiers. *Optics Express*, 18(17):18138–18150, 2010.
- [16] Toshio Kurashima, Tsuneo Horiguchi, Hisashi Izumita, Shin-ichi Furukawa, and Yahei Koyamada. Brillouin optical-fiber time domain reflectometry. *IEICE transactions on communications*, 76(4):382–390, 1993.
- [17] Hiroshi Naruse and Mitsuhiro Tateda. Trade-off between the spatial and the frequency resolutions in measuring the power spectrum of the brillouin backscattered light in an optical fiber. *Applied optics*, 38(31):6516–6521, 1999.
- [18] Yosuke Mizuno, Weiwen Zou, Zuyuan He, and Kazuo Hotate. Proposal of brillouin optical correlation-domain reflectometry (bocdr). *Optics express*, 16(16):12148–12153, 2008.
- [19] Yosuke Mizuno, Zuyuan He, and Kazuo Hotate. Measurement range enlargement in brillouin optical correlation-domain reflectometry based on temporal gating scheme. *Optics express*, 17(11):9040–9046, 2009.

- [20] Yosuke Mizuno, Zuyuan He, and Kazuo Hotate. Measurement range enlargement in brillouin optical correlation-domain reflectometry based on double-modulation scheme. *Optics Express*, 18(6):5926–5933, 2010.
- [21] Yosuke Mizuno, Neisei Hayashi, Hideyuki Fukuda, Kwang Yong Song, and Kentaro Nakamura. Ultrahigh-speed distributed brillouin reflectometry. *Light: Science & Applications*, 5(12):e16184, 2016.
- [22] D Garus, Torsten Gogolla, Katerina Kriebber, and Frank Schliep. Brillouin optical-fiber frequency-domain analysis for distributed temperature and strain measurements. *Journal of lightwave technology*, 15(4):654–662, 1997.
- [23] Mostafa Ahangrani Farahani and Torsten Gogolla. Spontaneous raman scattering in optical fibers with modulated probe light for distributed temperature raman remote sensing. *Journal of Lightwave Technology*, 17(8):1379–1391, 1999.
- [24] Romeo Bernini, Aldo Minardo, and Luigi Zeni. Distributed sensing at centimeter-scale spatial resolution by bofda: Measurements and signal processing. *IEEE Photonics Journal*, 4(1):48–56, 2012.
- [25] H Ghafoori-Shiraz and Takanori Okoshi. Fault location in optical fibers using optical frequency domain reflectometry. *Journal of lightwave technology*, 4(3):316–322, 1986.
- [26] Ken’ichi Nishiguchi, Che-Hsien Li, Artur Guzik, and Kinzo Kishida. Synthetic spectrum approach for brillouin optical time-domain reflectometry. *Sensors*, 14(3):4731–4754, 2014.
- [27] Marcelo A Soto and Luc Thévenaz. Modeling and evaluating the performance of brillouin distributed optical fiber sensors. *Optics express*, 21(25):31347–31366, 2013.
- [28] Aldo Minardo, Genni Testa, Luigi Zeni, and Romeo Bernini. Theoretical and experimental analysis of brillouin scattering in single-mode optical fiber excited by an intensity-and phase-modulated pump. *Journal of Lightwave Technology*, 28(2):193–200, 2010.
- [29] Robert W Boyd. *Nonlinear optics*. Academic press, 2003.

- 
- [30] Aydin Yeniay, Jean-Marc Delavaux, and Jean Toulouse. Spontaneous and stimulated brillouin scattering gain spectra in optical fibers. *Journal of lightwave technology*, 20(8):1425, 2002.
- [31] The Basis of Spectrum Analyzers. [http://www.naic.edu/~phil/hardware/Misc/anritsu/SpectrumAnalyzer\\_basis\\_of.pdf](http://www.naic.edu/~phil/hardware/Misc/anritsu/SpectrumAnalyzer_basis_of.pdf). Technical Note.
- [32] Yosef London, Yair Antman, Eyal Preter, Nadav Levanon, and Avi Zadok. Brillouin optical correlation domain analysis addressing 440 000 resolution points. *Journal of Lightwave Technology*, 34(19):4421–4429, 2016.
- [33] Xabier Angulo-Vinuesa, Sonia Martin-Lopez, Javier Nuño, Pedro Corredera, Juan Diego Ania-Castañón, Luc Thévenaz, and Miguel González-Herráez. Raman-assisted brillouin distributed temperature sensor over 100 km featuring 2 m resolution and 1.2 c uncertainty. *Journal of Lightwave Technology*, 30(8):1060–1065, 2012.
- [34] Javier Urricelqui, Mikel Sagues, and Alayn Loayssa. Brillouin optical time-domain analysis sensor assisted by brillouin distributed amplification of pump pulses. *Optics express*, 23(23):30448–30458, 2015.
- [35] K Kishida and CH Li. Pulse pre-pump-botda technology for new generation of distributed strain measuring system. *Structural health monitoring and intelligent infrastructure*, 1:471–477, 2005.
- [36] Romeo Bernini, Aldo Minardo, and Luigi Zeni. Dynamic strain measurement in optical fibers by stimulated brillouin scattering. *Optics letters*, 34(17):2613–2615, 2009.
- [37] Javier Urricelqui, Marcelo A Soto, and Luc Thévenaz. Sources of noise in brillouin optical time-domain analyzers. In *24th International Conference on Optical Fibre Sensors*, volume 9634, page 963434. International Society for Optics and Photonics, 2015.
- [38] Omer Shlomovits, Tomi Langer, and Moshe Tur. The effect of source phase noise on stimulated brillouin amplification. *Journal of Lightwave Technology*, 33(12):2639–2645, 2015.

- [39] A Minardo, R Bernini, and L Zeni. Analysis of snr penalty in brillouin optical time-domain analysis sensors induced by laser source phase noise. *Journal of Optics*, 18(2):025601, 2015.
- [40] Tsuneo Horiguchi and Mitsuhiro Tateda. Botda-nondestructive measurement of single-mode optical fiber attenuation characteristics using brillouin interaction: Theory. *Journal of lightwave technology*, 7(8):1170–1176, 1989.
- [41] Marc Nikles, Luc Thevenaz, and Philippe A Robert. Brillouin gain spectrum characterization in single-mode optical fibers. *Journal of Lightwave Technology*, 15(10):1842–1851, 1997.
- [42] Félix Rodríguez-Barrios, Sonia Martín-López, Ana Carrasco-Sanz, Pedro Corredera, Juan Diego Ania-Castañón, Luc Thévenaz, and Miguel González-Herráez. Distributed brillouin fiber sensor assisted by first-order raman amplification. *Journal of lightwave technology*, 28(15):2162–2172, 2010.
- [43] Sonia Martin-Lopez, Mercedes Alcon-Camas, Felix Rodriguez, Pedro Corredera, Juan Diego Ania-Castañón, Luc Thévenaz, and Miguel Gonzalez-Herraez. Brillouin optical time-domain analysis assisted by second-order raman amplification. *Optics express*, 18(18):18769–18778, 2010.
- [44] Diego Marini, Marco Iuliano, Filippo Bastianini, and Gabriele Bolognini. Botda sensing employing a modified brillouin fiber laser probe source. *Journal of Lightwave Technology*, 2017.
- [45] M Angeles Quintela, Rosa Ana Perez-Herrera, Irene Canales, Monserrat Fernandez-Vallejo, Manuel Lopez-Amo, and José Miguel López-Higuera. Stabilization of dual-wavelength erbium-doped fiber ring lasers by single-mode operation. *IEEE Photonics Technology Letters*, 22(6):368–370, 2010.
- [46] Shilong Pan and Jianping Yao. A wavelength-switchable single-longitudinal-mode dual-wavelength erbium-doped fiber laser for switchable microwave generation. *Optics express*, 17(7):5414–5419, 2009.
- [47] Jian Liu, Jianping Yao, Jian Yao, and Tet Hin Yeap. Single-longitudinal-mode multiwavelength fiber ring laser. *IEEE Photonics technology letters*, 16(4):1020–1022, 2004.

- [48] Li Zhang, Marcelo A Soto, Zinan Wang, and Luc Thévenaz. Optimization of detection schemes in botda. In *Asia-Pacific Optical Sensors Conference*, pages W4A–28. Optical Society of America, 2016.
- [49] T Okoshi, Ki Kikuchi, and A Nakayama. Novel method for high resolution measurement of laser output spectrum. *Electronics letters*, 16(16):630–631, 1980.

### 8.3. References of Chapter 4

- [1] Zhisheng Yang, Marcelo A Soto, and Luc Thévenaz. 200 km fiber-loop brillouin distributed fiber sensor using bipolar golay codes and a three-tone probe. In *24th International Conference on Optical Fibre Sensors*, volume 9634, page 96340J. International Society for Optics and Photonics, 2015.
- [2] Xabier Angulo-Vinuesa, Sonia Martin-Lopez, Javier Nuño, Pedro Corredera, Juan Diego Ania-Castañón, Luc Thévenaz, and Miguel González-Herráez. Raman-assisted brillouin distributed temperature sensor over 100 km featuring 2 m resolution and 1.2 c uncertainty. *Journal of Lightwave Technology*, 30(8):1060–1065, 2012.
- [3] Javier Urricelqui, Mikel Sagues, and Alayn Loayssa. Brillouin optical time domain analysis sensor assisted by a brillouin distributed amplifier. In *24th International Conference on Optical Fibre Sensors*, volume 9634, page 96344U. International Society for Optics and Photonics, 2015.
- [4] Marcelo A Soto, Jaime A Ramirez, and Luc Thevenaz. Intensifying the response of distributed optical fibre sensors using 2d and 3d image restoration. *Nature communications*, 7:10870, 2016.
- [5] Abul Kalam Azad, Liang Wang, Nan Guo, Hwa-Yaw Tam, and Chao Lu. Signal processing using artificial neural network for botda sensor system. *Optics express*, 24(6):6769–6782, 2016.
- [6] Xiaoyi Bao, David J Webb, and David A Jackson. Combined distributed temperature and strain sensor based on brillouin loss in an optical fiber. *Optics Letters*, 19(2):141–143, 1994.

- [7] Da-Peng Zhou, Wenhai Li, Liang Chen, and Xiaoyi Bao. Distributed temperature and strain discrimination with stimulated brillouin scattering and rayleigh backscatter in an optical fiber. *Sensors*, 13(2):1836–1845, 2013.
- [8] CC Lee, PW Chiang, and S Chi. Utilization of a dispersion-shifted fiber for simultaneous measurement of distributed strain and temperature through brillouin frequency shift. *IEEE Photonics Technology Letters*, 13(10):1094–1096, 2001.
- [9] Lufan Zou, Xiaoyi Bao, Shahraam Afshar, and Liang Chen. Dependence of the brillouin frequency shift on strain and temperature in a photonic crystal fiber. *Optics letters*, 29(13):1485–1487, 2004.
- [10] Xin Lu, Marcelo A Soto, and Luc Thévenaz. Temperature-strain discrimination in distributed optical fiber sensing using phase-sensitive optical time-domain reflectometry. *Optics express*, 25(14):16059–16071, 2017.
- [11] E Catalano, R Laiso, R Bernini, Luigi Zeni, and Aldo Minardo. Simultaneous strain and temperature measurements using dual-wavelength botda. In *2017 25th Optical Fiber Sensors Conference (OFS)*, pages 1–4. IEEE, 2017.
- [12] Weiwen Zou, Zuyuan He, and Kazuo Hotate. Investigation of strain-and temperature-dependences of brillouin frequency shifts in  $\text{ge}_{-}2$ -doped optical fibers. *Journal of Lightwave Technology*, 26(13):1854–1861, 2008.
- [13] Marc Nikles, Luc Thevenaz, and Philippe A Robert. Brillouin gain spectrum characterization in single-mode optical fibers. *Journal of Lightwave Technology*, 15(ARTICLE):1842–1851, 1997.
- [14] Rubén Ruiz-Lombera, Arianna Piccolo, Luis Rodriguez-Cobo, José Miguel Lopez-Higuera, and J Mirapeix. Feasibility study of strain and temperature discrimination in a botda system via artificial neural networks. In *2017 25th Optical Fiber Sensors Conference (OFS)*, pages 1–4. IEEE, 2017.
- [15] J Mirapeix, PB García-Allende, A Cobo, OM Conde, and JM López-Higuera. Real-time arc-welding defect detection and classification with principal component analysis and artificial neural networks. *NDT & e International*, 40(4):315–323, 2007.

- 
- [16] Abul Kalam Azad, Faisal Nadeem Khan, Waled Hussein Alarashi, Nan Guo, Alan Pak Tao Lau, and Chao Lu. Temperature extraction in brillouin optical time-domain analysis sensors using principal component analysis based pattern recognition. *Optics express*, 25(14):16534–16549, 2017.
- [17] Xuping Zhang, Yuangang Lu, Feng Wang, Hao Liang, and Yixin Zhang. Development of fully-distributed fiber sensors based on brillouin scattering. *Photonic Sensors*, 1(1):54–61, 2011.
- [18] Chuankai Zhang, Yuanhong Yang, and Anqi Li. Application of levenberg-marquardt algorithm in the brillouin spectrum fitting. In *Seventh International Symposium on Instrumentation and Control Technology: Optoelectronic Technology and Instruments, Control Theory and Automation, and Space Exploration*, volume 7129, page 71291Y. International Society for Optics and Photonics, 2008.
- [19] Romeo Bernini, Aldo Minardo, and Luigi Zeni. Dynamic strain measurement in optical fibers by stimulated brillouin scattering. *Optics letters*, 34(17):2613–2615, 2009.
- [20] Javier Urricelqui, Ander Zornoza, Mikel Sagues, and Alayn Loayssa. Dynamic botda measurements based on brillouin phase-shift and rf demodulation. *Optics express*, 20(24):26942–26949, 2012.
- [21] Pan Bing, Xie Hui-Min, Xu Bo-Qin, and Dai Fu-Long. Performance of sub-pixel registration algorithms in digital image correlation. *Measurement Science and Technology*, 17(6):1615, 2006.
- [22] Thomas Zeh, Hans Schweizer, Andreas Meixner, Andreas Purde, and Alexander W Koch. Enhancement of detection accuracy of fiber bragg grating sensors. In *Second European Workshop on Optical Fibre Sensors*, volume 5502, pages 540–543. International Society for Optics and Photonics, 2004.
- [23] J Mirapeix, A Cobo, C Jaúregui, and JM López-Higuera. Fast algorithm for spectral processing with application to on-line welding quality assurance. *Measurement Science and Technology*, 17(10):2623, 2006.

## 8.4. References of Chapter 5

- [1] José Miguel López-Higuera, Luis Rodriguez Cobo, Antonio Quintela Incera, and Adolfo Cobo. Fiber optic sensors in structural health monitoring. *Journal of lightwave technology*, 29(4):587–608, 2011.
- [2] Z Liu, G Ferrier, X Bao, X Zeng, Q Yu, and AK Kim. Brillouin scattering based distributed fiber optic temperature sensing for fire detection. *Fire Safety Science*, 7:221–232, 2003.
- [3] Marc Niklès, Bernhard H Vogel, Fabien Briffod, Stephan Grosswig, Florian Sauser, Steffen Luebbecke, André Bals, and Thomas Pfeiffer. Leakage detection using fiber optics distributed temperature monitoring. In *Smart Structures and Materials 2004: Smart Sensor Technology and Measurement Systems*, volume 5384, pages 18–26. International Society for Optics and Photonics, 2004.
- [4] Gunes Yilmaz and Sait Eser Karlik. A distributed optical fiber sensor for temperature detection in power cables. *Sensors and Actuators A: Physical*, 125(2):148–155, 2006.
- [5] Yi Bao, Fujian Tang, Yizheng Chen, Weina Meng, Ying Huang, and Genda Chen. Concrete pavement monitoring with ppp-botda distributed strain and crack sensors. *Smart Struct. Syst*, 18(3):405–423, 2016.
- [6] Aldo Minardo, Romeo Bernini, Lucio Amato, and Luigi Zeni. Bridge monitoring using brillouin fiber-optic sensors. *IEEE Sensors Journal*, 12(1):145–150, 2011.
- [7] Jinlong Xu, Yongkang Dong, Zhaohui Zhang, Shunlong Li, Shaoyang He, and Hui Li. Full scale strain monitoring of a suspension bridge using high performance distributed fiber optic sensors. *Measurement Science and Technology*, 27(12):124017, 2016.
- [8] Cheng-Yu Hong, Yi-Fan Zhang, Guo-Wei Li, Meng-Xi Zhang, and Zi-Xiong Liu. Recent progress of using brillouin distributed fiber optic sensors for geotechnical health monitoring. *Sensors and Actuators A: Physical*, 258:131–145, 2017.
- [9] Jianghong Mao, Jiayun Chen, Lei Cui, Weiliang Jin, Chen Xu, and Yong He. Monitoring the corrosion process of reinforced concrete using botda and fbg sensors. *Sensors*, 15(4):8866–8883, 2015.

- 
- [10] Liang Ren, Tao Jiang, Zi-guang Jia, Dong-sheng Li, Chao-lin Yuan, and Hongnan Li. Pipeline corrosion and leakage monitoring based on the distributed optical fiber sensing technology. *Measurement*, 122:57–65, 2018.
- [11] Glynn R Williams, George Brown, William Hawthorne, Arthur H Hartog, and Peter C Waite. Distributed temperature sensing (dts) to characterize the performance of producing oil wells. In *Industrial Sensing Systems*, volume 4202, pages 39–55. International Society for Optics and Photonics, 2000.
- [12] Sudeep Mandal, Sachin Dekate, Boon K Lee, Renato Guida, Michael Mondanos, Jackson Yeo, and Marc Goranson. Characterization and calibration of raman based distributed temperature sensing system for 600° c operation. In *Sensors for Extreme Harsh Environments II*, volume 9491, page 94910A. International Society for Optics and Photonics, 2015.
- [13] Jing Wang, Di Hu, Dorothy Y Wang, and Anbo Wang. Fully-distributed fiber-optic high temperature sensing based on stimulated brillouin scattering. In *Fiber Optic Sensors and Applications X*, volume 8722, page 87220E. International Society for Optics and Photonics, 2013.
- [14] Yongkang Dong, Pengbai Xu, Cheng Fu, Chenglin Zhang, Dengwang Zhou, Taofei Jiang, Hongying Zhang, Zhiwei Lu, Liang Chen, and Xiaoyi Bao. 1200° c high-temperature distributed brillouin optical fiber sensing based on photonics crystal fiber. In *24th International Conference on Optical Fibre Sensors*, volume 9634, page 963485. International Society for Optics and Photonics, 2015.
- [15] Thomas Reinsch and Jan Henniges. Temperature-dependent characterization of optical fibres for distributed temperature sensing in hot geothermal wells. *Measurement Science and Technology*, 21(9):094022, 2010.
- [16] T Grandal, E Piñeiro, A Asensio, and F Rodriguez. Metallic coating techniques for fiber bragg grating sensors. In *8th Iberoamerican Optics Meeting and 11th Latin American Meeting on Optics, Lasers, and Applications*, volume 8785, page 878538. International Society for Optics and Photonics, 2013.
- [17] Alexis Méndez and Ted F Morse. *Specialty optical fibers handbook*. Academic Press, 2011.
- [18] Alex K Sang, Mark E Froggatt, Dawn K Gifford, Stephen T Kreger, and Bryan D Dickerson. One centimeter spatial resolution temperature measurements in a

- nuclear reactor using rayleigh scatter in optical fiber. *IEEE Sensors Journal*, 8(7):1375–1380, 2008.
- [19] Tsuneo Horiguchi, Kaoru Shimizu, Toshio Kurashima, Mitsuhiro Tateda, and Yaehei Koyamada. Development of a distributed sensing technique using brillouin scattering. *Journal of lightwave technology*, 13(7):1296–1302, 1995.
- [20] Carlos Augusto Galindez-Jamioy and Jose M Lopez-Higuera. Brillouin distributed fiber sensors: an overview and applications. *Journal of Sensors*, 2012, 2012.
- [21] Aldo Minardo, Romeo Bernini, and Luigi Zeni. Experimental and numerical study on stimulated brillouin scattering in a graded-index multimode fiber. *Optics express*, 22(14):17480–17489, 2014.
- [22] Pengbai Xu, Yongkang Dong, Juwang Zhang, Dengwang Zhou, Taofei Jiang, Jinlong Xu, Hongying Zhang, Tao Zhu, Zhiwei Lu, Liang Chen, et al. Bend-insensitive distributed sensing in singlemode-multimode-singlemode optical fiber structure by using brillouin optical time-domain analysis. *Optics express*, 23(17):22714–22722, 2015.
- [23] Alessandro Signorini, Stefano Faralli, Marcelo A Soto, Giovanni Sacchi, Federico Baronti, Roberto Barsacchi, Andrea Lazzeri, Roberto Roncella, Gabriele Bolognini, and Fabrizio Di Pasquale. 40 km long-range raman-based distributed temperature sensor with meter-scale spatial resolution. In *Optical Fiber Communication (OFC), collocated National Fiber Optic Engineers Conference, 2010 Conference on (OFC/NFOEC)*, pages 1–3. IEEE, 2010.
- [24] Antonio Paolozzi and Paolo Gasbarri. Dynamic analysis with fibre optic sensors for structural health monitoring. Technical report, UNIVERSITA DI ROMA LA SAPIENZA ROMA (ITALY), 2006.
- [25] Suzhen Li and Zhishen Wu. Modal analysis on macro-strain measurements from distributed long-gage fiber optic sensors. *Journal of Intelligent Material Systems and Structures*, 19(8):937–946, 2008.
- [26] Romeo Bernini, Aldo Minardo, and Luigi Zeni. Dynamic strain measurement in optical fibers by stimulated brillouin scattering. *Optics letters*, 34(17):2613–2615, 2009.

- [27] Yair Peled, Avi Motil, and Moshe Tur. Fast brillouin optical time domain analysis for dynamic sensing. *Optics express*, 20(8):8584–8591, 2012.
- [28] Aldo Minardo, Agnese Coscetta, Salvatore Pirozzi, Romeo Bernini, and Luigi Zeni. Modal analysis of a cantilever beam by use of brillouin based distributed dynamic strain measurements. *Smart Materials and Structures*, 21(12):125022, 2012.
- [29] Aldo Minardo, A Coscetta, Salvatore Pirozzi, R Bernini, and Luigi Zeni. Experimental modal analysis of an aluminum rectangular plate by use of the slope-assisted botda method. *Smart Materials and Structures*, 22(12):125035, 2013.
- [30] Andrey Kobayakov, Michael Sauer, and Dipak Chowdhury. Stimulated brillouin scattering in optical fibers. *Advances in optics and photonics*, 2(1):1–59, 2010.
- [31] Daniele Inaudi and Branko Glisic. Long-range pipeline monitoring by distributed fiber optic sensing. *Journal of pressure vessel technology*, 132(1):011701, 2010.
- [32] Lufan Zou, Xiaoyi Bao, Fabien Ravet, and Liang Chen. Distributed brillouin fiber sensor for detecting pipeline buckling in an energy pipe under internal pressure. *Applied optics*, 45(14):3372–3377, 2006.
- [33] Marc Nikles. Long-distance fiber optic sensing solutions for pipeline leakage, intrusion, and ground movement detection. In *Fiber optic sensors and applications VI*, volume 7316, page 731602. International Society for Optics and Photonics, 2009.



---

## List of publications

---

## 1. Related to the thesis work

### 1.1. International journals

1. **R. Ruiz-Lombera, L. Rodriguez-Cobo, J. M. López-Higuera and J. M. Mirapeix.** “*Feasibility Study of a Fiber Ring Laser Working on the SLM Regime in a BOTDA Sensor*”, pp. 361–365, Optics and Laser Technology (June, 2018).
2. **R. Ruiz-Lombera, A. Fuentes, L. Rodriguez-Cobo, J. M. López-Higuera and J. M. Mirapeix.** “*Simultaneous Temperature and Strain Discrimination in a Conventional BOTDA via Artificial Neural Networks*”, pp. 2114–2121, Journal of Lightwave Technology (June, 2018).
3. **R. Ruiz-Lombera, I. Laarossi, L. Rodriguez-Cobo, M. A. Quintela-Incera, J. M. López-Higuera and J. M. Mirapeix.** “*Distributed High-Temperature Optical Fiber Sensor Based on a Brillouin Optical Time Domain Analyzer and Multimode Gold-Coated Fiber*”, pp. 2393-2397, IEEE Sensors Journal (April, 2017).
4. **A. Minardo, R. Bernini, R. Ruiz-Lombera, J. M. Mirapeix, J. M. López-Higuera and Luigi Zeni.** “*Proposal of Brillouin optical frequency-domain reflectometry (BOFDR)*”, pp 29994–30001, Optics Express (December, 2016).
5. **R. Ruiz-Lombera, J. Urricelqui, M. Sagues, J. M. Mirapeix, J. M. López-Higuera and A. Loayssa.** “*Overcoming Nonlocal Effects and Brillouin Threshold Limitations in Brillouin Optical Time-Domain Sensors*”, pp 1–11, IEEE Photonics Journal (November, 2015).
6. **A. Minardo, A. Coscetta, R. Bernini, R. Ruiz-Lombera, J. M. Mirapeix, J. M. López-Higuera and L. Zeni.** “*Structural Damage Identification in an Aluminum Composite Plate by Brillouin Sensing*”, pp 659–660, IEEE Sensors Journal (February, 2015).

## 1.2. International conferences

1. **R. Ruiz-Lombera, L. Rodriguez-Cobo, J.M. Mirapeix, J.M. López-Higuera.** “*Brillouin optical time-domain analyzer with a fiber ring laser working on the SLM regime*”, OFS25 (25th International Conference on Optical Fiber Sensors), Jeju (Korea), pp. 1032381-1/ 1032381-4; ISBN: 9781510610910, ISSN: 0277-786X; (April, 2017).
2. **R. Ruiz-Lombera, A. Piccolo, L. Rodriguez-Cobo, J.M. López-Higuera, J.M. Mirapeix.** “*Feasibility study of strain and temperature discrimination in a BOTDA system via artificial neural networks*”, OFS25 (25th International Conference on Optical Fiber Sensors), Jeju (Korea), pp. 103237Z-1/ 103237Z-4; ISBN: 9781510610910, ISSN: 0277-786X; (April, 2017).
3. **R. Ruiz-Lombera, A. Minardo, R. Bernini, J. M. Mirapeix, J.M. López-Higuera, L. Zeni.** “*Experimental demonstration of a Brillouin optical frequency-domain reflectometry (BOFDR) sensor*”, OFS25 (25th International Conference on Optical Fiber Sensors), Jeju (Korea), pp. 103238L-1 / 103238L-4; ISBN: 9781510610910, ISSN: 0277-786X; (April, 2017).
4. **R. Ruiz-Lombera, I. Laarossi, J.M. Mirapeix, M.A. Quintela-Incera, J.M. López-Higuera.** “*High-temperature distributed sensor system via BOTDA and multimode gold-coated fiber*”, EWOFSS2016 (European Workshop on Optical Fibre Sensors), Limerick, Ireland, pp. 991632-1 991632-4; ISBN: 9781510602199, ISSN: 0277-786X; (May, 2016).
5. **R. Ruiz-Lombera, J.M. Mirapeix, I. Laarossi, L. Rodríguez-Cobo, J.M. López-Higuera.** “*Brillouin Frequency Shift estimation in BOTDA via subpixel processing*”, EWOFSS2016 (European Workshop on Optical Fibre Sensors), Limerick, Ireland, pp. 99162L-1 99162L-4; ISBN: 9781510602199, ISSN: 0277-786X; (May, 2016).
6. **J. Urricelqui, R. Ruiz-Lombera, M. Sagues, J. M. Mirapeix, J. M. López-Higuera, A. Loayssa.** “*Overcoming nonlocal effects and Brillouin threshold imitations in Brillouin distributed sensors*”, OFS24 (24th International Con-

ference on Optical Fiber Sensors), Curitiba, Brazil, pp. 963487-1 - 963487-4; ISBN: 978162841839  
2, ISSN: 0277-786X; (September, 2015).

7. **R. Ruiz-Lombera, J. M. Mirapeix, O. Martínez, J. Domingo, J. M. López-Higuera.** "*Experimental demonstration of a leakage monitoring system for large diameter water pipes using a fiber optic distributed sensor system*", IEEE Sensors 2014, Valencia, Spain, pp. 1885-1888; ISBN: 978-1-4799-0161-6; (November, 2014).
8. **R. Ruiz-Lombera, J. M. Mirapeix, J. M. López-Higuera.** "*Automatic strain detection in a Brillouin Optical Time Domain Sensor using Principal Component Analysis and Artificial Neural Networks*", IEEE Sensors 2014, Valencia, Spain, pp. 1539-1542; ISBN: 978-1-4799-0161-6; (November, 2014).

## 2. Additional contributions

### 2.1. International journals

1. **F. J. Casas, D. Ortiz, B. Aja, L. de la Fuente, E. Artal, R. Ruiz-Lombera and J. M. Mirapeix.** "*A Microwave Polarimeter Demonstrator for Astronomy with Near-Infra-Red Up-Conversion for Optical Correlation and Detection*", pp. 1-17. Sensors (April, 2019).
2. **L. Rodriguez-Cobo, R. Ruiz-Lombera, M. A. Quintela-Incera, J. M. Mirapeix and J. M. López-Higuera.** "*Single longitudinal mode fiber ring laser*", pp. 361-365, Optics and Laser Technology (November, 2018).
3. **L. Rodriguez-Cobo, R. Perez-Herrera, M. A. Quintela-Incera, R. Ruiz-Lombera, M. López-Amo and J. M. López-Higuera.** "*Virtual FBGs Using Saturable Absorbers for Sensing with Fiber Lasers*", pp. 1-10, Sensors (October, 2018).
4. **D. Ortiz, F. J. Casas, R. Ruiz-Lombera and J. M. Mirapeix.** "*Electro-*

*optic correlator for large-format microwave interferometry: Up-conversion and correlation stages performance analysis*", pp 044702, Review of Scientific Instruments (April, 2017).

5. **I. Laarossi, R. Ruiz-Lombera, M. A. Quintela-Incera, J. M. Mirapeix, D. Lima, D. Solana, J. M. López-Higuera.** "*Ultrahigh Temperature Raman-Based Distributed Optical Fiber Sensor With Gold-Coated Fiber*", pp 296–301, Journal of Selected Topics in Quantum Electronics (March, 2017).
6. **J. M. Mirapeix, R. Ruiz-Lombera, J. J. Valdiande, A. Cobo and J. M. López-Higuera.** "*Colorimetric Analysis for On-Line Arc-Welding Diagnostics by Means of Plasma Optical Spectroscopy*", pp 3465–3471, IEEE Sensors Journal (May, 2016).
7. **L. Rodriguez-Cobo, J. M. Mirapeix, R. Ruiz-Lombera, A. Cobo and J. M. López-Higuera.** "*Fiber Bragg grating sensors for on-line welding diagnostics*", pp 839–843, Journal of Materials Processing Technology (April, 2014).
8. **L. Rodriguez-Cobo, R. Ruiz-Lombera, O. M. Conde and J. M. López-Higuera, A. Cobo and J. M. Mirapeix.** "*Feasibility study of Hierarchical Temporal Memories applied to welding diagnostics*", pp 58–66, Sensors and Actuators A: Physical (December, 2013).
9. **J. M. Mirapeix, R. Ruiz-Lombera, J.J. Valdiande, L. Rodriguez-Cobo, F. Anabitarte and A. Cobo.** "*Defect detection with CCD-spectrometer and photodiode-based arc-welding monitoring systems*", pp 2132–2139, Journal of Materials Processing Technology (December, 2011).

## 2.2. International conferences

1. **R. Ruiz-Lombera, T. Grandal, S. Fraga** "*Monitoring high thermal performance concrete for concentrated solar power plants with fiber optic sensors*", SMAR2019 (5th International Conference on Smart Monitoring, Assessment and Rehabilitation of Civil Structures), Potsdam (Germany); (August, 2019).

2. **L. Rodríguez-Cobo, M.A. Quintela-Incera, R. Ruiz-Lombera, R.A. Perez-Herrera, M. López-Amo and J.M. López-Higuera** “*Influence of saturable absorbers on fiber ring laser sensors*”, OFS25 (25th International Conference on Optical Fiber Sensors), Jeju (Korea), pp. 103232H-1 / 103232H-4; ISBN: 9781510610910, ISSN: 0277-786X; (April, 2017).
3. **I. Laarossi, R. Ruiz-Lombera, M.A. Quintela-Incera, J. M. Mirapeix, D. Lima, D. Solana, J.M. Lopez-Higuera.** “*Ultra-high temperature distributed sensor based on Raman and multimode gold-coated fiber*”. Optical Sensors 2016, Vancouver Canada, pp. 1-3; ISBN: 978-1-943580-14-9; (July, 2016).
4. **I. Laarossi, M.A. Quintela, R. Ruiz-Lombera, J. M. Mirapeix, D. Lima, D. Solana, J.M. López-Higuera.** “*High-temperature distributed sensor based on Raman and multimode standard telecom fiber*”, Optical Sensors 2016, Vancouver Canada, pp. 1-3; ISBN: 978-1-943580-14-9; (July, 2016).
5. **L. Rodríguez-Cobo, M. Lomer, R. Ruiz-Lombera, A. Cobo, J.M. López-Higuera.** “*Reflection-based Fiber Specklegram Sensor*”, EWOFSS2016 (European Workshop on Optical Fibre Sensors), Limerick, Ireland, pp. 99161Q-1 99161Q-4; ISBN: 9781510602199, ISSN: 0277-786X; (May, 2016).
6. **J. M. Mirapeix, R. Ruiz-Lombera, J. J. Valdiande, J. M. López-Higuera.** “*Colorimetric analysis for on-line arc-welding diagnostics by means of plasma optical spectroscopy*”, IEEE Sensors 2014, Valencia, Spain, pp. 637-640; ISBN: 978-1-4799-0161-6; (November, 2014).
7. **E. Real, J. Mirapeix, O.M. Conde, R. Ruiz-Lombera, A. Cobo, J.M. López-Higuera.** “*Species discrimination in plasma welding spectra by means of Principal and Independent Component Analysis*”, OFS23 (23rd International Conference on Optical Fibre Sensors), Santander, pp. 91570F-1 - 91570F4; ISBN: 9781628411751, ISSN: 0277-786X; (June, 2014).
8. **L. Rodríguez-Cobo, J. M. Mirapeix, R. Ruiz-Lombera, A. Cobo, J.M. López-Higuera.** “*Fiber Bragg Grating sensors for on-line welding diagnostic*”, EWOFSS 2013. 5th European Workshop on Optical Fibre Sensors, Krakow,

Poland, pp. 879441-1/879441-4; ISBN:9780819496348, ISSN: 0277-786X; (May, 2013).